Microstructural evolution of a 2.25Cr - 1 Mo steel during austenitization and temper : austenite grain growth, carbide precipitation sequence and effects on mechanical properties

Sylvain Dépinoy

ParisTech
INSTITUT DES SCIENCES ET TECHNOLOGIES
PARIS INSTITUTE OF TECHNOLOGY

MINES ParisTech

École doctorale n° 432 : Sciences des Métiers de l'Ingénieur

Doctorat ParisTech

T H È S E

pour obtenir le grade de docteur délivré par

l'École nationale supérieure des mines de Paris

Spécialité " Sciences et Génie des Matériaux "

présentée et soutenue publiquement par

Sylvain DÉPINOY

le 10 décembre 2015

Evolution microstructurale d'un acier 2.25 Cr – 1 Mo au cours de l'austénitisation et du revenu : croissance des grains austénitiques, séquence de précipitation des carbures et effets sur les propriétés mécaniques

Microstructural evolution of a 2.25 Cr - 1 Mo steel during austenitization and temper: austenite grain growth, carbide precipitation sequence and effects on mechanical properties

Directeur de thèse : **Anne-Françoise GOURGUES-LORENZON**
Co-directeur de thèse : **Ernst KOZESCHNIK**
Co-encadrante de la thèse : **Caroline TOFFOLON-MASCLET**

Jury

M. André PINEAU, Professeur Emérite, MINES ParisTech	Président
M. Stéphane GODET, Professeur, Université Libre de Bruxelles	Rapporteur
M. Mohamed GOUNÉ, Professeur, ICMCB, Université de Bordeaux	Rapporteur
Mme Catherine TASSIN, Maître de conférences, SIMAP, INPG	Examinatrice
Mme Anne-Françoise GOURGUES-LORENZON, Professeur, MINES ParisTech	Examinatrice
M. Ernst KOZESCHNIK, Professeur, IMST, Université Technologique de Vienne	Examinateur
Mme Caroline TOFFOLON-MASCLET, Docteur, CEA Saclay	Examinatrice
M. Bernard MARINI, Docteur, CEA Saclay	Invité
M. Francois ROCH. Docteur. AREVA	Invité

MINES ParisTech
Centre des Matériaux – UMR CNRS 7633
B.P. 87 – 91003 Evry Cedex, France

T H È S E

"It can now be said that the metallurgy of the chromium-molybdenum steels is almost completely understood and further work can only be aimed at assessing the effects of modern production processes, scrap control and minor refinements to composition"

- Orr et al, in *Ferritic steels for fast reactor steam generators*, 1978

Acknowledgement

En premier lieu, je tiens à remercier Stéphane Godet et Mohamed Gouné d'avoir accepté de relire cette thèse et d'en être les rapporteurs. Je remercie également André Pineau et Catherine Tassin d'avoir accepté d'être membres du jury.

Cette thèse a été encadrée par Caroline Toffolon et dirigée par Anne-Françoise Gourgues. Elles ont su me laisser la part d'autonomie dont j'ai besoin pour travailler tout en me recadrant quand je faisais n'importe quoi. J'ai beaucoup appris à leur contact, que ce soit en termes de connaissances scientifiques, de rigueur ou d'organisation. Je les remercie pour cela. Je remercie également François Roch pour son point de vue industriel qui me faisait totalement défaut en début de thèse, et que j'ai appris à intégrer dans mon raisonnement par la suite. Enfin, bien qu'il ne soit pas officiellement dans l'encadrement, Bernard Marini a été d'une très grande aide, particulièrement en ce qui concerne les propriétés mécaniques et l'algorithme de résolution des équations de croissance de grains.

Un grand merci à tous les docteurs, ingénieurs et techniciens qui m'ont beaucoup aidé au cours de ce travail, à savoir Thomas, Élodie, Stéphane, Didier, Françoise, Jean-Christophe, Denis, Justine, Dominique, Véronique, Marie-Pierre, Jean-Philippe, Jean-Luc, Louis au CEA, Mohamed, Cécilie, Régis et Abdennour aux Mines. Je tiens à remercier particulièrement Sylvain Gailliègue pour son super four trop bien sans qui l'étude du revenu n'aurait pas été possible, ainsi que Pierre Wident pour sa gestion des essais mécaniques.

Je souhaite également remercier légadulabo, Cyan et Freko, et les gars et les filles du labo. Afin d'éviter de froisser quiconque, j'ai décidé de les nommer dans le sens trigonométrique : Gilles "Mango", un mec en or (surtout change jamais champion), Nicolas "Kopom" et sa tendance à faire masse, Katia "Podzi" malgré sa géométrie euclidienne moralement répréhensible, Isabelle pour ses yeux qui ont une couleur normale, Bertrand pour sa constance à être assorti à lui-même en toutes circonstances et Baptiste, dont le père, pêcheur, a mis toutes les étoiles dans l'eau. Je remercie aussi Benjamin "Ben Hasher" pour m'avoir remercié dans son mémoire de stage (j'attends de lui qu'il me remercie dans sa thèse en retour), Vianney qui prend ma relève dans le photomontage ubique, Pierre pour arriver à avoir l'air encore plus nonchalant que moi, Marine qui partage ma passion pour les ruelles et Alexia "Cappadonna" pour son savoureux durian. Je n'oublie pas non plus Anne-Laure et Julie qui ont partagé mon bureau, Emma pour son aide concernant les répliques extractives, Pauline, Danny boy, William, Camille, Esther, Juan, Nesrine, Emilie, Mickael, Vincent et plusieurs Olivier (tout ça au CEA), de même que Guillaume, Alexandre, Lucie, Hubert et Victor (aux Mines). J'en place une dernière pour Breton, Paul et Bédouche pour ces longs débats intellectuels que nous avons menés à Bordeaux, Mathilde parce qu'elle est cool et Thomas pour l'intégralité de son œuvre (mais alors vraiment l'intégralité).

Je n'oublie bien évidemment pas mes parents qui m'ont soutenu tout au long de ces trois années avec des frites et du bœuf bourguignon, ainsi que mes frères Falzar et Scooter. Je dédie cette thèse à mon grand-père Gilbert, disparu en 2014, et à ma grand-mère Marie-Rose.

Enfin, je remercie Elisa pour son soutien au quotidien lors de la rédaction de ce manuscrit. Le résultat final aurait été très probablement de moins bonne qualité sans elle, et ma santé mentale bien plus dégradée.

En revanche, je ne remercie pas Freddy Mercury. Mon seul regret concernant cette thèse est de ne pas avoir étudié un acier inoxydable, tant cela m'aurait permis d'introduire ce manuscrit par une merveilleuse citation de Method Man. Mais bon, tant pis.

Résumé

Le travail qui suit porte sur l'optimisation des propriétés mécaniques et microstructurales d'une pièce épaisse d'acier 2.25 Cr – 1 Mo à travers l'utilisation des traitements thermiques. Ce manuscrit est découpé en 6 chapitres qui sont brièvement résumés ici.

Le premier chapitre est un résumé des propriétés générales de l'acier 2.25 Cr – 1 Mo que lui confère sa composition chimique et ses propriétés microstructurales. Afin de satisfaire aux exigences en terme de propriétés mécaniques en vigueur dans l'industrie nucléaire, cet acier doit préférablement être sous forme bainitique avec le moins de ferrite proeutectoïde possible. La précipitation de carbures qui a lieu au cours du traitement de revenu lui donne ses propriétés mécaniques finales et conditionne également sa durée de vie. De plus, l'acier 2.25 Cr – 1 Mo présente une bonne résistance aux phénomènes de fragilisation par vieillissement thermique et par irradiation susceptibles d'avoir lieu au cours de sa vie, que ce soit en conditions normales ou accidentelles. Il est également montré que l'utilisation de 2.25 Cr – 1 Mo enrichi en vanadium, bien que présentant des avantages certains pour l'application classique de cet acier (industrie pétrochimique), n'est pas intéressante dans le cas étudié ici. Enfin, les différents types de traitements thermiques sont présentés, ainsi que leurs influences sur la microstructure finale : l'austénitisation et la trempe à l'eau ont un effet sur la matrice, alors que le revenu n'influence que l'état de précipitation des carbures. Un dernier traitement thermique dit de détensionnement est appliqué à la fin du processus de fabrication de la pièce épaisse, et n'a *a priori* pas d'effet notable sur la nature des phases constituant le matériau.

Le second chapitre rassemble plusieurs études préliminaires nécessaires à la bonne conduite de l'étude à proprement parler. La composition chimique moyenne de la pièce servant à usiner les échantillons est étudiée, puis comparée à un matériau dit de référence avec lequel les propriétés mécaniques futures sont comparées. Ces deux matériaux sont issus de la même virole de 280 mm d'épaisseur. Il est à noter que la composition chimique moyenne est quasiment identique dans l'épaisseur de la pièce. Le diagramme de phase à l'équilibre tel que déterminé à l'aide des logiciels MatCalc et ThermoCalc est discuté. Il en ressort qu'à l'exception des carbures, auxquels un chapitre entier est dédié, les seules phases secondaires potentiellement intéressantes sont les AlN, susceptibles d'agir sur la croissance du grain austénitique, et les MnS, qui servent de site de germination pour la rupture ductile. Les vitesses de refroidissement au cours de la trempe à l'eau sont ensuite calculées en utilisant l'équation générale du transfert thermique. En effet, à cause de la forte épaisseur de la pièce considérée, des gradients thermiques apparaissent au cours du refroidissement et sont susceptibles d'aboutir à des hétérogénéités microstructurales, telles que celles illustrées par un diagramme TRC obtenu après une condition d'austénitisation particulière. Enfin, des hétérogénéités locales de composition, dites microségrégations, sont mises en évidence. Elles n'affectent toutefois que très légèrement les propriétés mécaniques locales du matériau. A l'issue de ce chapitre, il apparait donc d'une part que les échantillons étudiés sont bel et bien représentatifs de la pièce dans son ensemble, et d'autre part qu'il est nécessaire de déterminer une condition d'austénitisation

permettant une bonne homogénéité microstructurale de la pièce après trempe. Cette dernière problématique fait l'objet des chapitres 3 et 4.

Dans un premier temps, l'étude de la croissance du grain austénitique en fonction du temps et de la température d'austénitisation est abordée. Le but de ce chapitre est de développer un modèle permettant de calculer le diamètre moyen des grains austénitiques en prenant en compte la pression motrice due à la courbure du joint de grain et les pressions de freinage dues à des phénomènes d'épinglage et de trainage de soluté (*solute drag*). Avant de pouvoir développer le modèle, des mesures expérimentales pour des températures allant de 920°C à 1120°C et des temps d'austénitisation allant jusqu'à 2 heures sont effectués. Il apparait qu'à des températures inférieures ou égales à 970°C, un phénomène de croissance limitée intervient. Pour des températures supérieures ou égales à 1070°C, la croissance est dite parabolique, c'est-à-dire qu'elle ne dépend que de la pression motrice. Entre ces deux régimes, à 1020°C, la croissance est ralentie mais pas limitée. Une analyse statistique de la distribution en diamètre des grains montre que la croissance est normale quelle que soit la température. En utilisant le modèle cinétique de précipitation de MatCalc, il apparaît que l'épinglage dû aux particules d'AlN seules ne permet pas d'expliquer la croissance limitée aux basses températures. En revanche, l'ajout d'un terme correspondant au trainage d'atomes de molybdène piégés aux joints de grains donne des résultats proches de l'expérience, et ce pour des paramètres cohérents avec ceux trouvés dans la littérature. En conclusion, il est proposé que la croissance des grains austénitiques dans l'acier étudié soit principalement contrôlée par ce phénomène de trainage de soluté. Cette conclusion est toutefois à tempérer par le fait que le modèle ne prend en compte qu'un seul grain, et ne permet donc pas d'estimer les interactions existantes entre les différents grains.

L'étude de l'effet des conditions d'austénitisation sur les propriétés microstructurales et mécaniques après trempe et revenu fait l'objet du 4^{e} chapitre. Huit différentes conditions d'austénitisation sont étudiées pour trois différentes vitesses de refroidissement représentant des épaisseurs caractéristiques d'une pièce épaisse. En dehors de l'effet attendu de la taille du grain austénitique sur les transformations au refroidissement, il apparaît que les conditions d'austénitisation n'ont qu'un effet très limité sur les propriétés microstructurales telles que la taille du paquet bainitique ou l'état de précipitation. De même, il est impossible de mettre en évidence un effet de l'austénitisation sur les propriétés en traction et en résilience. Il est toutefois très intéressant de noter qu'à 920°C, le temps d'austénitisation a une influence considérable sur la fraction de ferrite transformée au refroidissement, et ce pour une taille de grain très similaire. L'explication proposée renvoie à la ségrégation du molybdène aux joints de grains lors du traitement d'austénitisation, potentiellement couplée à des phénomènes de *solute-drag like effect* (SDLE). En conclusion, une austénitisation à 970°C pendant 1 heure donne de bons résultats en termes d'homogénéité microstructurale et de propriétés mécaniques ; il est donc décidé de l'utiliser pour l'étude du traitement thermique de revenu.

L'effet du temps et de la température de revenu sur la précipitation des carbures est étudié dans le chapitre 5. Les températures étudiées vont de 650°C à 725°C pour des temps allant jusqu'à 24 heures. En raison d'une vitesse de chauffage très lente, une attention particulière a été portée aux

évolutions microstructurales ayant lieu lors du chauffage. Dans l'acier étudié, cinq différents types de carbures sont susceptibles d'être observés, dans l'ordre de leur stabilité thermodynamiques croissantes : M_3C, M_2C, M_7C_3, $M_{23}C_6$, M_6C. Ces carbures présentent chacun des propriétés morphologiques, cristallographiques et chimiques bien spécifiques. En particulier, la composition en éléments métalliques *M* est propre à chaque carbure : il est donc aisé de les différencier par une simple analyse EDX. Les évolutions microstructurales sont caractérisées par des observations au MET sur des répliques extractives. Des analyses par diffraction des Rayons X sur de la poudre de dissolution sélective sont également effectuées afin de déterminer la fraction massique de chaque type de carbure en fonction du temps et de la température de revenu. Il est important de souligner qu'aucun M_6C n'est observé, quelles que soient les conditions de revenu, en bon accord avec les calculs thermodynamiques qui prédisent un domaine de stabilité pour ces carbures à des températures bien plus faibles que celles étudiées. Au vu des résultats obtenus, la séquence de précipitation des carbures au cours du traitement thermique de revenu peut être décrite comme suit : lors du chauffage, l'austénite résiduelle présente entre les lattes bainitiques et aux anciens joints de grains austénitiques se décompose en ferrite et en cémentite M_3C. En chauffant à plus haute température, les carbures M_2C, $M_{23}C_6$ et M_7C_3 commencent à précipiter. Les deux premiers germent dans la matrice et dans les dislocations se trouvant à l'intérieur des lattes bainitiques, alors que les carbures M_7C_3 germent à l'interface entre la cémentite et la matrice et croissent aux dépens des M_3C. Lors du palier isotherme, les carbures d'équilibre $M_{23}C_6$ croissent et provoquent la dissolution des carbures les moins stables, M_2C d'abord et M_7C_3 ensuite. L'augmentation de la température augmente la cinétique de ces dernières transformations.

Le dernier chapitre s'emploie à mettre en évidence la relation entre le traitement thermique de revenu et les propriétés en dureté, en traction et en résilience. D'une manière générale, l'augmentation du temps et de la température de revenu provoque un adoucissement du matériau. Lors du chauffage et des premières heures de revenu, cet adoucissement est majoritairement dû à des phénomènes de restauration des dislocations. Pour des temps plus longs, le grossissement ou la dissolution des carbures M_2C non-cisaillables est tenu pour responsable. Il convient de préciser que l'adoucissement dû à la restauration de dislocations est bien plus important que celui résultant de l'évolution des carbures. Les conditions de revenu n'ont pas d'effet mesurable sur les propriétés en résilience. Toutefois, les courbes de transition ductile-fragile obtenues sont remarquables par l'étroitesse du domaine mixte ductile-fragile. L'effet du traitement de détensionnement a également été brièvement étudié : bien qu'il n'ait pas d'effet sur la dureté, un adoucissement est observé lors des essais de traction. Ce résultat contre-intuitif reste inexpliqué. Tout comme le revenu, le traitement de détensionnement n'a pas d'effet sur les propriétés en résilience.

Table of contents

Chapter I: Background, objectives and approach of the study

Light water reactors (PWRs, BWRs) are representing 80% of the world nuclear plants. In France, PWR constitutes the reference solution for the renewal of EDF reactors. This will lead to a massive use of PWRs at least until the end of the 21st century. Thus, there will be coexistence between those reactors and the 4th generation reactors. On an international level, the renewal of 2nd generation light water reactors may also be provided by PWR or BWR until at least the middle of the century. Thus, safety and technological improvements of light water reactors represent key issues.

In this framework, the 2.25 Cr – 1 Mo steel (15 CD9-10), designated by the ASTM A387/ASME SA387 and by ASME A508/A508M-14 Grade 22 standard (Table 1.1), is being considered as potential candidate pressure vessel material for future light water reactors. The two main reasons are its good fracture toughness (in particular low temperature value of the start of the upper shelf) and its very good resistance to radiation-induced embrittlement compared to usual pressure vessel steels. Moreover, its good weldability is interesting regarding the manufacturing of a thick-walled pressure vessel [1].

	C	Mn	P	S	Si	Cr	Mo
SA387	0.05-0.15	0.25-0.66	0.035 max	0.035 max	0.50 max	1.88-2.62	0.85-1.15
A508	0.11-0.15	0.30-0.60	0.015 max	0.015 max	0.35 max	2.00-2.50	0.90-1.10

Table 1.1: *Chemical composition as specified by the ASME SA387 and ASME A508 Grade 22 standard (wt%)*

These steels have been widely used in pressure vessels for the petrochemical industries for decades due to their good mechanical properties at high temperature [2, 3]. In such applications, the typical operating temperature ranges from 300 to 480°C under high hydrogen partial pressure, in the range of 15-200 bars. On the other hand, for nuclear applications, the operating temperature is around 300°C under irradiation due to thermal neutrons. These two different operating conditions require different specifications. The mechanical standards set by the RCC-M for nuclear pressure vessel steels is summarized in Table 1.2. These requirements for tensile properties are easily met for a 2.25 Cr – 1 Mo in the quenched and tempered condition [4].

Good properties of 2.25 Cr – 1 Mo are due to the chemical composition of the steel as well as to its microstructure. For instance, the presence of chromium gives satisfactory resistance to corrosion and oxidation [5] (although a stainless steel cladding remains needed for nuclear applications), while both chromium and molybdenum improve the creep resistance [6]. A low Sulphur content is also recommended, since this element reduces the upper shelf impact energy (USE) [7], and a low phosphorus content allows to prevent a thermal aging at the service temperature and to limit the irradiation embrittlement as it will be shown later.

Quenched and tempered 2.25 Cr – 1Mo steels are fully bainitic. It is worth mentioning that bainite after cooling in 2.25 Cr – 1 Mo steels is granular bainite [8–10]. This particular type of bainite is free from carbides before tempering, and austenite is retained along lath boundaries. A fully bainitic matrix gives an optimum for tensile and toughness properties, as well as creep resistance, compared to proteutectoid ferritic matrix [5, 11]. While the occurrence of 2% of proteutectoid ferrite does not change the mechanical properties [12], it is generally advised to minimize the proteutectoid ferrite fraction [13].

Test	Test temperature	Characteristics	Requirements	
			Axial direction	Azimutal direction
Tensile	RT	Min Rp0.2		400 MPa
		Rm		550/670 MPa
		Min A%		20
	350°C	Min Rp0.2		300 MPa
		Min Rm		497 MPa
KV Impact toughness	0°C	Min average	80 J	80 J
		Min individual value	60 J	60 J
	-20°C	Min average	40 J	56 J
		Min individual value	28 J	40 J
	20°C	Min individual value	104 J	120 J

Table 1.2: *Mechanical standards for nuclear pressure vessel steel as given by the RCC-M*

In the case of thick-walled component such as pressure vessels, it is thus mandatory that the microstructure remains homogeneous throughout the thickness, from the skin, where the cooling is very fast, to the mid-thickness, where the cooling is slower. 2.25 Cr – 1 Mo steels exhibit good bainitic hardenability due to their chemical composition. The two main alloying elements, chromium and molybdenum, are known to delay the ferritic transformation towards lower cooling rates upon continuous cooling, while the bainitic transformation critical cooling rates remain unaffected [10]. This effect is counter-intuitive when considering the ferrite-stabilizing nature of these elements, and is usually explained by their strong affinity with carbon, impeding carbon diffusion and therefore delaying the decomposition of austenite. On the other hand, austenite-stabilizing elements such as carbon and manganese are usually advised to be at the upper bound of the requirements, in order to improve the bainitic hardenability [12].

Final mechanical properties and their evolution at operating temperature are given by the carbides. In the general case of a quenched+tempered bainitic steel, carbide precipitation can occur during the decomposition of austenite upon cooling, or upon subsequent tempering. A detailed literature review and information regarding these carbides can be found in Chapter V. In chromium steels, several carbides can coexist: the cementite $(Fe,Cr)_3C$, and alloyed carbides $(Cr,Fe)_7C_3$ and $(Cr,Fe)_{23}C_6$. In molybdenum steels, possible carbides are $(Fe,Mo)_3C$, Mo_2C and $(Mo,Fe)_6C$. The precipitation sequence upon tempering in bainitic 2.25 Cr – 1 Mo steels is well-known, and has been determined by Baker & Nutting as [14]:

$$\begin{array}{ccccc} \varepsilon\text{-carbide} & \rightarrow & M_3C + M_2C & \rightarrow & M_7C_3 \\ & & \downarrow & & \downarrow \\ & & M_{23}C_6 & \rightarrow & M_6C \end{array}$$

where ε-carbide are the precursors of the cementite M_3C, and "M" stands for the metallic elements. M_2C carbides, due to their fine dispersion and their coherency with the matrix, are partially responsible for the good strength of the 2.25 Cr – 1 Mo steels. For instance, they are held responsible for the good creep properties [15] and possible secondary hardening [16]. Upon ageing, these metastable carbides are progressively replaced by M_6C with increasing time and temperature [14, 17], leading to a loss of mechanical properties over use. Precipitation of these Mo-rich carbides also reduces the amount of molybdenum in solid solution, leading to an increase in susceptibility to tempering embrittlement. However, since this sequence of precipitation is triggered by diffusion, these carbides can be considered as relatively stable at low working temperature: for instance, in petrochemical applications, the life service of 2.25 Cr – 1 Mo steel is beyond 20 years at an operating temperature in the range of 520-560°C [17]. At the end of its lifetime, the steel typically exhibits large, blocky M_6C carbides located at boundaries, providing pathways for crack propagation and thus leading to further embrittlement.

Along with this loss of mechanical properties due to the carbide evolution, four other embrittlement mechanisms can take place depending on the application. Under hydrogen atmosphere, hydrogen embrittlement and hydrogen attack are susceptible to occur. For nuclear applications, embrittlement due to neutron irradiation is of major concern. Furthermore, thermal ageing can induce temper embrittlement, depending on the steel purity.

Temper embrittlement is due to the segregation of chemical species at prior austenite grain boundaries, resulting in an increase in the fracture appearance transition temperature (FATT) and in a loss of toughness. It should be pointed out that the fully bainitic structure is more susceptible to temper embrittlement than a ferritic structure [18, 19]. Temper embrittlement depends on the chemical composition: phosphorus, tin, antimony and arsenic co-segregate with alloying elements, such as silicon and manganese. The susceptibility to temper embrittlement can be estimated through empirical factors like J-factor (expressed as a function of wt%) or the Bruscatto factor $\bar{X}$ (expressed as a function of wt-ppm), given respectively in equations (1.1) and (1.2).

$$J = (\mathrm{Mn} + \mathrm{Si}) \times (\mathrm{P} + \mathrm{Sn}) \times 10^4 \quad (1.1)$$

$$\bar{X} = (10\,\mathrm{P} + 5\,\mathrm{Sb} + 4\,\mathrm{Sn} + \mathrm{As})/100 \quad (1.2)$$

The fracture appearance transition temperature (FATT) of 2.25 Cr – 1 Mo type steels has been correlated to the J-factor: Low values of J-factor lead to very low values of FATT after in-service use, and thus after thermal ageing (Figure 1.1). Consequently J-factor has to be kept as low as possible mainly by controlling the impurity content of the steel.

In rather large quantity relatively to the other elements, phosphorus is the most deleterious element, since its segregation at parent austenite grain boundaries promotes intergranular fracture

and could lead to an increase in FATT. Manganese and silicon are only promoting phosphorus segregation. Thus, reducing their concentration leads to a decreased susceptibility to temper embrittlement [20]. It should be pointed out that chromium and nickel also promote phosphorus segregation. At the opposite, molybdenum is known for reducing phosphorus segregation upon thermal ageing when in appropriate content [21, 22]. Increase in parent austenite grain size also leads to increase in susceptibility to temper embrittlement. The temper embrittlement susceptibility of the 2.25 Cr – 1 Mo steel can be optimized by setting phosphorus and other embrittling elements, but also silicon and manganese at their lowest possible content allowed both by requirements and steelmaking process constraints. In the case of manganese, this advice is in conflict with the considerations on the bainitic hardenability, thus a good compromise has to be found.

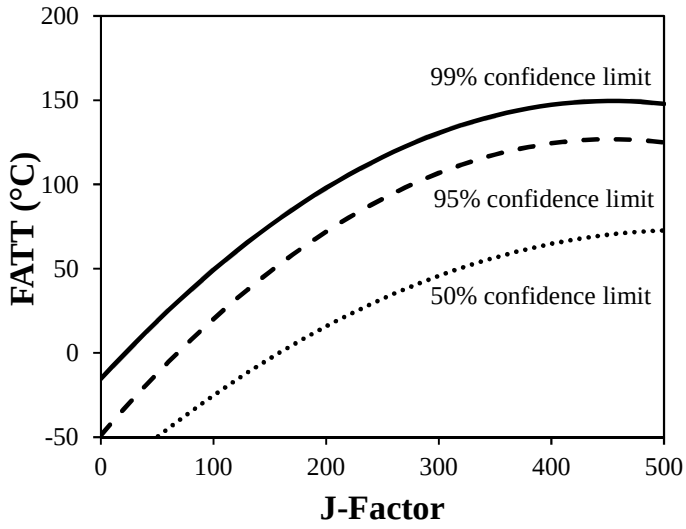

Figure 1.1: *Effect of impurities (J-factor) on the fracture appearance transition temperature (FATT). Probability curves based on historical data collection for base and weld metals, aged from 20 000 hours to 200 000 hours. From* [2]

Hydrogen embrittlement is a phenomenon that can occur below 300°C if the ingot is cooled below this temperature before the application of the de-hydrogeneization treatment. The defects that could appear are known as flakes. For chemical plant vessels, this phenomenon is also considered when the vessel is cooled too quickly upon shutdown, where the hydrogen dissolved in the steel during operation cannot escape and is therefore retained at lower temperatures. Hydrogen embrittlement leads to a lower threshold stress for crack propagation, and can also result in the loss of adherence of the stainless steel cladding to the wall of the pressure vessel [23].

This phenomenon is not possible in nuclear pressure vessel in nominal service conditions the hydrogen content remains low during operation (very small H uptake from the primary circuit coolant and H generation by transmutation ((n, p) reactions). Hydrogen embrittlement decreases the minimum value of stress intensity for crack propagation more significantly than temper embrittlement, and interactions between these two embrittlement phenomena results in further reduction of this minimum stress intensity factor [24].

Higher strength steels are more sensitive to this phenomenon than lower strength steels as shown in Figure 1.2 [6, 23], and 2.25 Cr – 1 Mo steels with a tensile strength lower than 100 ksi, i.e. 689 MPa, are considered as resistant materials to hydrogen embrittlement [6].

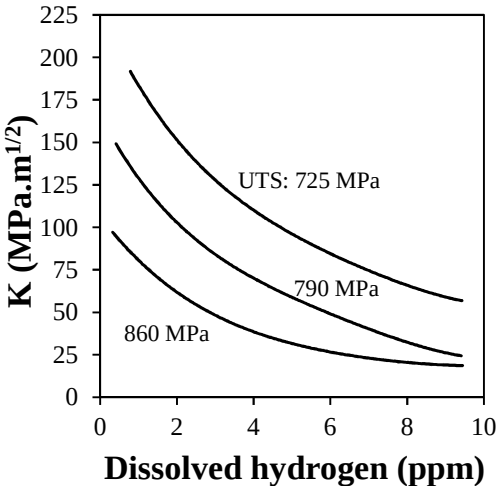

Figure 1.2: *Effect of dissolved hydrogen concentration on fracture toughness of 2.25 Cr – 1 Mo steel of various tensile strengths. From* [23]

Hydrogen attack is another degradation process due to the presence of hydrogen in solution in the material. Unlike hydrogen embrittlement, such phenomenon takes place at higher temperatures, above 300°C. Hydrogen attack occurs when dissolved hydrogen reacts with carbon and form methane bubbles, leading to an irreversible loss of strength, ductility and toughness, and even to blistering or cracking [24]. The safe operating limits in terms of pressure and temperature are assessed by the Nelson diagram, which is built from experience-based curves (Figure 1.3). For 2.25 Cr – 1 Mo steels, at 300°C, the maximal partial hydrogen pressure is approximately 1.5 MPa. A lacking parameter in such representation is the applied stress, which enhances the rate of bubble nucleation [25]. Thermal stress and residual stress have the same effect as that of applied stress.

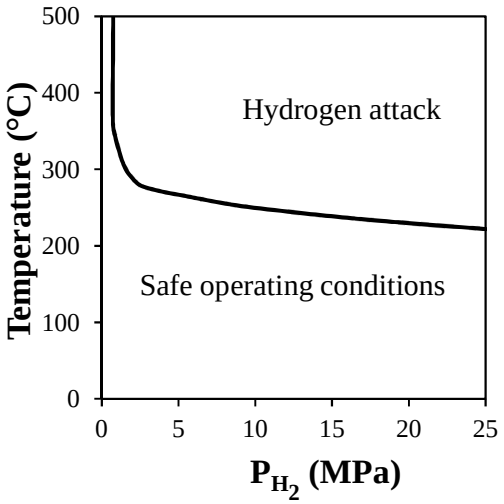

Figure 1.3: *Nelson curve for 2.25 Cr – 1 Mo steels. From* [23]

2.25 Cr – 1 Mo steels have typically a higher resistance to hydrogen attack than plain carbon steels, due to two factors that reduce the growth rate of methane bubbles: stable carbides and high creep strength. Stable carbides trap carbon atoms, which are then not available for the methanation reaction, while high creep strength induces elastic back-stress around isolated bubbles, impeding their growth. The presence of chromium and molybdenum improves the resistance to hydrogen attack for several reasons: they are strong carbide formers, they reduce the activity of nearby carbon atoms, and in the case of molybdenum, its segregation at grain boundaries tend to reduce the grain boundary energy, making the formation of new free surfaces more difficult [6]. Further addition of vanadium, tungsten, boron, titanium, niobium, tantalum, zirconium and yttrium reduces the susceptibility to hydrogen attack, either because they are strong carbide formers (V, W, Ti) or by acting as hydrogen traps (V, Ti, Nb, Ta, Zr). Other elements, such as Sn or Si, increase the methane density and bubble diameter.

Due to the susceptibility to hydrogen attack, the maximum operating temperature for 2.25 Cr – 1 Mo steels in hydrogen service is 454°C, as given by the API 941 standards. These requirements are largely met for the nuclear industry, where the nominal operating temperature does not exceed 300°C, for a much lower partial pressure of hydrogen.

Neutron irradiation upon service induces microstructural changes on low-alloy steels by creating structural defects, such as dislocation loops and cavities, and enhancing solute diffusion, leading to precipitation, formation of solute clusters and eventually phase transformations. These microstructural changes are responsible for evolution of mechanical properties, for instance increase of tensile strength and ductile to brittle transition temperature (DBTT), reduction in fracture toughness and loss in the upper shelf energy (USE). This embrittlement is correlated to chemical elements present in the steel. Nickel, manganese, silicon, as well as impurities like copper and phosphorus are known to segregate under irradiation, and tend to form nanoclusters in the matrix, along dislocation lines and at metallurgical interfaces. Among all these elements, only copper could be above its solubility limit and precipitates easily. Copper-enriched nanoclusters are often enriched in manganese, silicon, nickel and phosphorus. However, in the absence of copper, nanoclusters of manganese and nickel as well as of phosphorus are still observed. Neutron radiation is also known to favor phosphorus segregation to metallurgical interfaces and in particular to prior austenitic grain boundaries, possibly leading to intergranular fracture qualitatively comparable to temper embrittlement [26]. The average size and composition of nanoclusters does not change with the fluence, however their number density increases almost linearly with the fluence [27–29].

Copper, nickel and phosphorus are recognized as the most deleterious elements regarding radiation-induced embrittlement. Embrittlement due to irradiation can be divided in two categories: hardening and non-hardening effects. Hardening effects are due to the formation of point defects and solute clusters, while non-hardening effects are based on the same mechanisms as temper embrittlement, i.e. segregation at prior austenite grain boundaries. For instance, copper nanoclusters causes hardening embrittlement, while radiation induced phosphorus segregation falls in the second category as already stated regarding temper embrittlement. Nickel enhances radiation embrittlement by both mechanisms, since it forms nanoclusters but also nickel phosphides at grain boundaries, causing reduction in cohesive strength of grain boundaries and thus leading to grain boundary

embrittlement [30, 31]. Thus, nickel content in steels is clearly correlated to their sensitivity to radiation-induced embrittlement, as shown in Figure 1.4.

Recently, new Russian RPV steels (Modified 15Kh2MFA-A, close to 2.25 Cr – 1 Mo but with V), have been proposed. The authors of these works conclude to a better resistance of these steel to thermal ageing and irradiation embrittlement at 300°C because of their low Ni content. When clean, i.e. with low amounts of copper and phosphorus, the only mechanisms of radiation-induced embrittlement is due to hardening caused by creation of structural defects, and a low Ni content reduces the density of these defects, improving the radiation resistance of the steel. The standard V-free 2.25 Cr – 1 Mo provides a similar advantage with a wider industrial background.

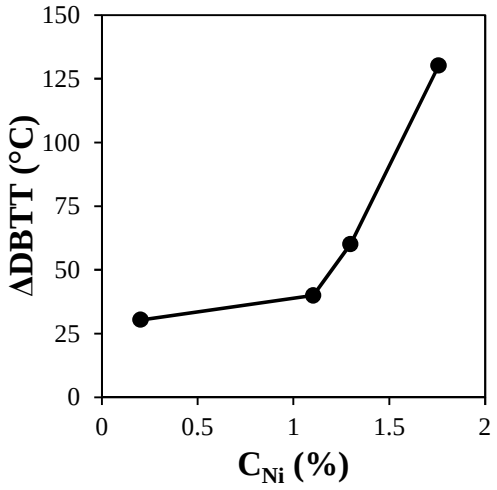

Figure 1.4: *Dependence of irradiation induced DBTT shift on nickel content. Phosphorus and copper contents are 0.010% and 0.05%, respectively. Irradiation temperature: 270°C, fluence: 10^{24} neutron/m². From* [30]

It is known that the amount of chromium also plays a role in radiation-induced embrittlement especially for high Cr content when α-α' decomposition is involved. However for 2.25 Cr – 1 Mo steel, this type of ageing mechanism is not expected. As an illustration of the effect of Cr, 5% Cr steels and 9% Cr steels experience less degradation of their toughness properties after irradiation at high doses at 365°C than 2.25% Cr steels, but 12% Cr steels exhibit less resistance to radiation-induced embrittlement than 2.25% Cr steels in the same irradiation conditions [32].

As a result, careful control of the chemical composition results in good resistance to embrittlement upon ageing. Low phosphorus and copper contents and reduced content of Ni compared to usual RPV steels makes the 2.25 Cr – 1 Mo steel less susceptible to temper embrittlement and radiation-induced embrittlement. In the considered operating conditions, hydrogen attack should not occur but limited hydrogen embrittlement could exist for long time of operation, and 2.25 Cr – 1 Mo has a good resistance to this type of damage.

A wide range of modified 2.25 Cr – 1 Mo chemistries have been designed since the first use of 2.25 Cr – 1Mo steels, to improve either the bainitic hardenability or the mechanical properties. The most widespread one is the 2.25 Cr – 1 Mo – 0.2 V, where some vanadium is added to the steel. Such

chemical modification improves the material strength and resistance to hydrogen attack, and allows the material to be used at temperatures up to 510°C against 454°C for conventional 2.25 Cr – 1 Mo steel, regarding the API 941 standard for hydrogen service [33]. Such improvement of mechanical properties is due to precipitation of relatively stable, fine vanadium carbides which stabilize a fine dislocation substructure within the bainite [34]. However, addition of vanadium only has little effect on the steel hardenability [12]. Other modified 2.25 Cr – 1 Mo steels for petrochemical applications include addition of niobium, titanium, manganese, nickel or even boron [12, 34–37]. Such additions tend to increase the bainitic hardenability as well as the mechanical properties. However, in the present industrial application, such modifications of the material composition do not appear mandatory. Operating conditions are by far less aggressive than in the petrochemical industry: partial pressure of H_2 is negligible compared to the petrochemical industries, and the working temperature, around 300°C, is well below the maximal operating temperature as given by the API 941 standard. Other chemical elements, such as nickel or boron also considered in modified chemistries are detrimental regarding the resistance to irradiation-induced phenomena.

In the present study, the chemical composition of the steel is already defined, as well as the steelmaking process. Thus, the only adjustable parameter leading to optimize the mechanical properties is the microstructure. Microstructural parameters are controlled through heat treatments conducted upon the industrial manufacturing of the component, after the forging stages. These heat treatments are summarized in Figure 1.5.

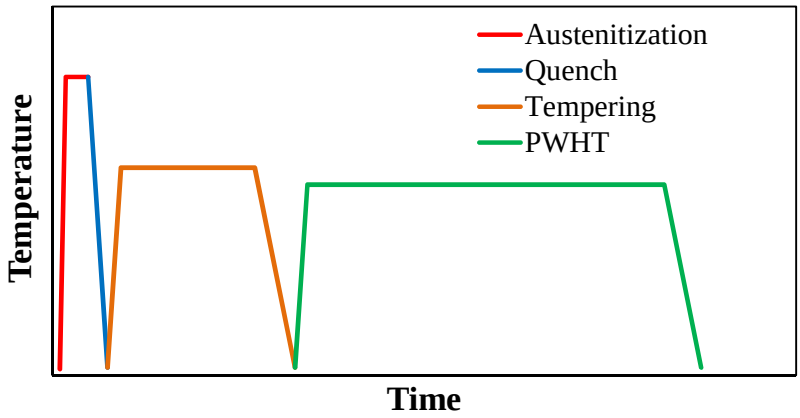

Figure 1.5: *Schematic diagram showing the different heat treatment applied on the material after forging. PWHT: Post-weld heat treatment.*

The first step is austenitization, where the steel is heated in order to transform its microstructure from a mixture of carbides and body-centered cubic ferrite into a single face-centered cubic austenite phase where all carbon atoms are in solid solution. After austenitization, the component is quenched; upon quenching, the austenite decomposes into the final matrix microstructure. A tempering heat treatment is then applied, where almost all carbon atoms in solid solution precipitate into carbides. The stress-relieving heat treatment, or post-weld heat treatment, is the last heat treatment applied on the material. It is typically conducted at lower temperatures than the tempering heat treatment, and aims at reducing the residual stresses in the material that have been introduced by welding. No

obvious microstructural changes are expected upon this last heat treatment compared to the microstructure before welding.

The aim of this work is to improve the understanding of the effects of heat treatments on phase transformations and microstructural evolution, as well as their effect on the mechanical properties. Microstructural evolution was experimentally investigated on various heat treatments, and models were used in order to quantify the contribution from different mechanisms on this evolution. In this manuscript, each heat treatment is investigated on after the other, as in the real targeted process.

Chapter II is dedicated to the study of the as-received material in terms of chemistry and microstructure. Comparison is made with a reference material. Thermodynamic equilibrium calculations, characterization of chemical variations throughout the component and determination of the cooling rates of interest is also made in order to prepare further experimentations. A first austenitization is applied in order to test the material bainitic hardenability, which does not give satisfactory results.

In the considered industrial application, the component is water quenched thus cooling rates after austenitization are not a process parameter. Under this constraint, bainitic hardenability can only be improved by increasing the austenite grain size upon austenitization. Thus, Chapter III and IV are dedicated to the study of microstructural evolution during austenitization, to optimize conditioning of austenite for further decomposition and tempering.

In Chapter III, the effect of austenitization on microstructural evolution of austenite is experimentally investigated as a function of temperature and time. Mechanisms controlling the austenite grain growth, such as Zener pinning and solute drag, are then postulated and discussed thanks to a modelling approach.

Chapter IV is dedicated to the effect of austenitization on microstructural and mechanical properties after cooling at different rates representative of different locations in the thickness of a large component. It should be pointed out that while the bainitic hardenability is of interest, the bainitic transformation mechanism itself has not been studied. This choice is justified by the fact that the final mechanical properties are mostly due to the precipitation of carbides within the bainite, and that a good bainitic hardenability is mandatory for the considered industrial application. On the other hand, several assumptions about the decomposition of austenite into proteutectoid ferrite, and more precisely on the means for delaying this transformation, are made. Based on the study of the grain growth mechanisms and the characterization of microstructures after cooling, an austenitization condition is selected for the subsequent study of carbide precipitation upon tempering.

The carbide precipitation sequence upon both heating up to the temperature of interest and the isothermal step of tempering is studied in Chapter V. Evolutions of size, phase fraction and chemical composition of carbides have been quantitatively determined. Based on these experimental data, mechanisms for nucleation and growth of carbides are then proposed; a thermokinetic modelling approach has been tested to discuss these mechanisms and is presented in Appendix D.

In the last Chapter VI, the effect of tempering conditions on the strength and toughness properties is reported, as well as the effect of the final stress-relieving heat treatment.

Chapter II: Materials under study

TABLE OF CONTENTS

Prior to the study of the effects of heat treatments on microstructural and mechanical properties, the material itself had to be characterized thoroughly.

The studied 2.25 Cr – 1 Mo steel was provided with two different states: the so-called as-received material, which was considered as the initial state, and the reference material, which had been industrially reheated and was used as a means of comparison. In a first part, the thermal history prior to this study is described for both states, as well as their chemical composition and microstructure. Moreover, the effect of the component thickness on these properties is briefly reported. In a second part, material properties useful to the study of microstructural transformations during heat treatments are described. Among them, the equilibrium state was estimated using thermodynamic simulations. The general behavior of the steel regarding austenitization and quench was studied. Equivalent cooling rates, corresponding to representative thicknesses in the ingot, were also determined. Finally, the chemical homogeneity in the material was studied in order to ensure that every sample is characteristic of the whole piece.

1. MATERIALS

Two different states of the studied material were supplied: the as-received state and the reference state, which was industrially reheated. This latter will be used as a mean of comparison, mostly for mechanical properties but also for microstructural properties in Chapter IV.

1.1 As-received material

The as-received material was a 280 mm thick cylindrical shell forged from a 186-ton hollow ingot fabricated at Industeel-Le Creusot (formerly Creusot-Loire Industries) in 1994. Heats were melted in an electric furnace and then underwent a heating ladle refinement. The hollow ingot was casted by bottom pouring of two heats. After hot forging, the hollow shell underwent an austenitization at 990°C for 10 hours followed by water quench, then several tempering heat treatments, the last one being at 660°C for 12 hours followed by air quenching. After these heat treatments, the piece of metal was cut into two halves through its center perpendicular to its axis. Both halves were then welded, joining the top and the bottom of the forged component. A final heat treatment at 690°C for 10 hours was then performed on the welded component. Samples used through this study were machined from a 420x450 mm² blank taken from the quarter-thickness and from the top of the as-received forged component.

Composition of the steel measured after different steps of its processing history is shown in Table 2.1, the "heat" chemical composition being the average of the two heats used for casting. The resulting microstructure is tempered bainite with carbides located at the interfaces, as shown in Figure 2.1. Since this material was to be reheated for the purpose of the present study, no detailed characterization of its microstructural and mechanical properties was conducted except for chemical homogeneity as described at the end of this chapter.

	C	**S**	**P**	**Si**	**Mn**	**Ni**	**Cr**	**Mo**	**V**	**Cu**	**Al**	**N**
Heat	0.14	0.004	0.004	0.22	0.53	0.16	2.43	1.07	N/A	0.04	0.014	N/A
Product	0.14	0.003	0.005	0.23	0.53	0.16	2.44	1.09	<0.01	0.06	0.012	N/A
¼ th	0.15	0.003	0.006	0.24	0.51	0.17	2.47	1.11	<0.01	N/A	0.008	0.007

Table 2.1: *As-received steel composition (wt%). Heat and Product compositions are given by AREVA, ¼ thickness composition is given from an independent analysis*

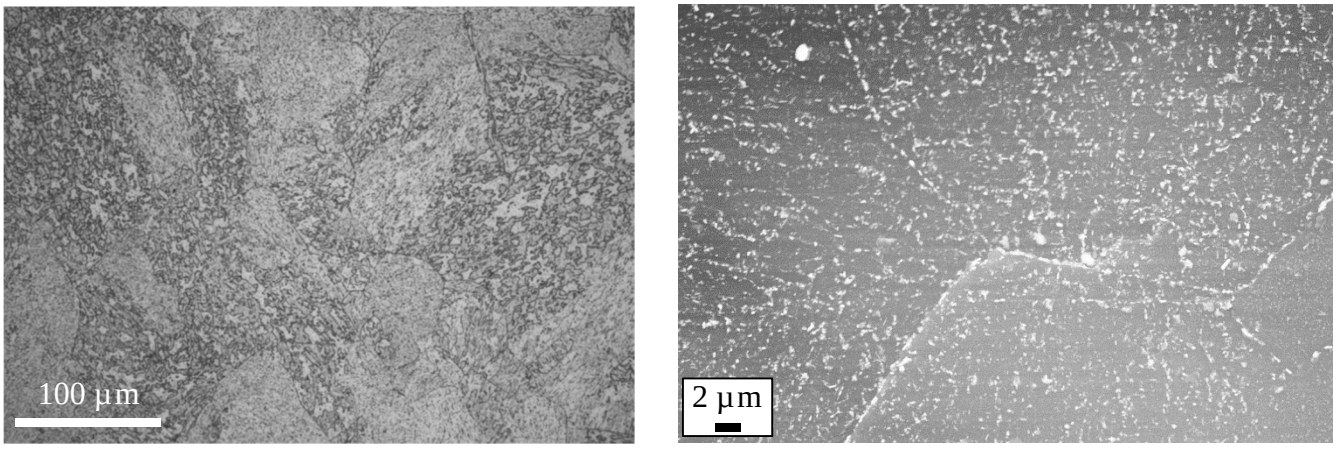

(a) (b)

Figure 2.1: *Microstructure of the as-received material, (a) optical microscopy (etchant: Nital 4%) and (b) SEM observation of carbides on a carbon extraction replica.*

1.2 Reference material

As already stated, all samples used in this study come from the quarter-thickness of the as-received material. In order to estimate their representability when compared to the whole hollow component, thorough analysis of thermal gradient during heat treatments and chemical composition across the thickness were done.

These studies were conducted on the so-called “reference material”, which comes from the same hollow component as the as-received material as schematized in Figure 2.2. In the hollow component, one must differentiate the quarter-thickness, located halfway between the inner skin and the mid-thickness, and the three quarter-thickness located halfway between the outer skin and the mid-thickness. Location in thickness might have an effect on the chemical composition due to possible segregations that happened during casting.

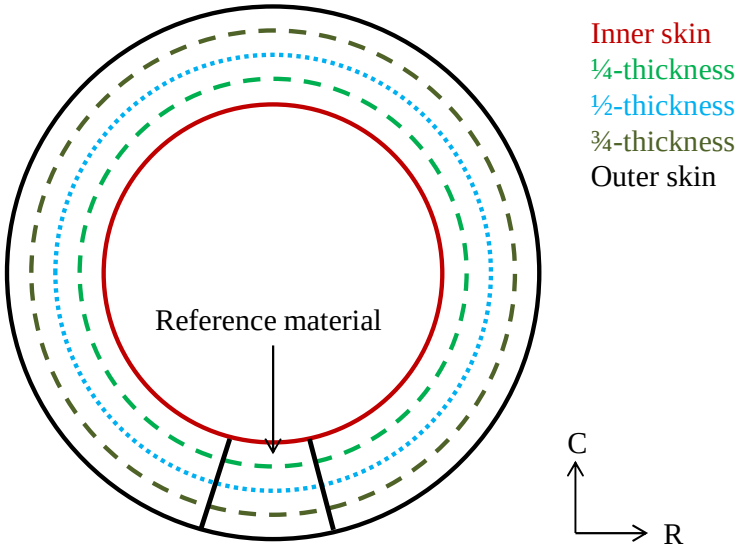

Figure 2.2: *Schematic diagram of the different locations of interest and geometry of the reference material component.*

The reference material has undergone the same thermomechanical processing and prior heat treatments as the as-received steel, as well as further heat treatments:

- Austenitization at 930°C, then water quenched.
- Tempering at 675°C. The heating rate was 2°C/min, and the component was then air cooled.
- Stress-relieving heat treatment at 645°C for 16 hours. The heating rate was 15°C/h, and the cooling rate was 20°C/h.

Due to the large thickness of the component, a thermal gradient occurs during the heating and cooling stages of the heat treatments. Temperatures at locations of interest, namely the skin, the quarter-thickness, the mid-thickness and the three-quarter thickness were monitored during each step of these heat treatments. K-type thermocouples were inserted into holes drilled from outer skin to quarter-thickness, mid-thickness and three-quarter thickness. Another set of thermocouples were welded at the skin; two thermocouples were used for each location. The stress-relieving heat treatment was carried out with only the skin thermocouples. It should be pointed out that the

geometry of the reference material part is not the same as that of the prior hollow component. Indeed, the first one has a symmetry axis corresponding roughly to the mid-thickness, thus the thermal gradient at quarter-thickness and three quarter-thickness is expected to be the same during all heat treatments. In the case of the prior hollow component, one could imagine that cooling rates would be different at inner and outer skins upon quenching (and by extension at the quarter-thickness and the three quarter-thickness), for instance because of local heating of the water inside the component. However, its large inner radius, namely 4360 mm, allows the water to behave the same way whether it is inside or outside the component. Thus, all thermal gradients measured in the reference material are considered representative of the industrial hollow component.

Heating rates are slow enough to be considered as homogeneous across thickness, so are the cooling rates after tempering and the stress relieving heat treatment. As expected considering the symmetry of the piece, no differences were found between the quarter-thickness and the three-quarter thickness during heat treatments. However, the isothermal steps durations and the cooling rates after austenitization change across the thickness, as shown in Table 2.2.

Location in the thickness	**Inner skin**	**¼ and ¾-thickness**	**½-thickness**
Austenitization time (h)	2	1.5	1
Cooling rates after austenitization (°C/s)	10	0.5	0.3
Tempering time (h)	6	5.5	5.5

Table 2.2: *Isothermal step durations for austenitization and tempering and cooling rates after austenitization at different locations of the forged component.*

After heat treatments, the resulting part was cut into four pieces corresponding to the four locations of interest in the component thickness. The chemical composition remains the same through the thickness, as shown in Table 2.3. Moreover, the average composition through thickness is similar to the one at the quarter-thickness of the as-received steel as shown in Table 2.1, thus this one can be considered as chemically representative of the whole component.

	C	**S**	**P**	**Si**	**Mn**	**Ni**	**Cr**	**Mo**	**Al**	**N**
Skin	0.14	0.003	0.007	0.23	0.52	0.16	2.47	1.13	0.011	0.007
¼ th	0.15	0.003	0.005	0.23	0.52	0.16	2.48	1.13	0.010	0.007
½ th	0.15	0.003	0.005	0.23	0.52	0.16	2.46	1.09	0.010	0.007
¾ th	0.14	0.003	0.006	0.23	0.54	0.16	2.51	1.13	0.010	0.007

Table 2.3: *Chemical composition of the reference material for four locations across the thickness (wt%).*

The microstructure is fully bainitic through the thickness, as shown in Figure 2.3, with very little proeutectoid ferrite. Vickers hardness values at the skin, the quarter-thickness, the mid-thickness and the three-quarter thickness are close to each other, respectively 216 HV, 215 HV, 218 HV and 216 HV with a standard deviation of 8 HV. More detailed information about hardness measurements can be found in Appendix A.

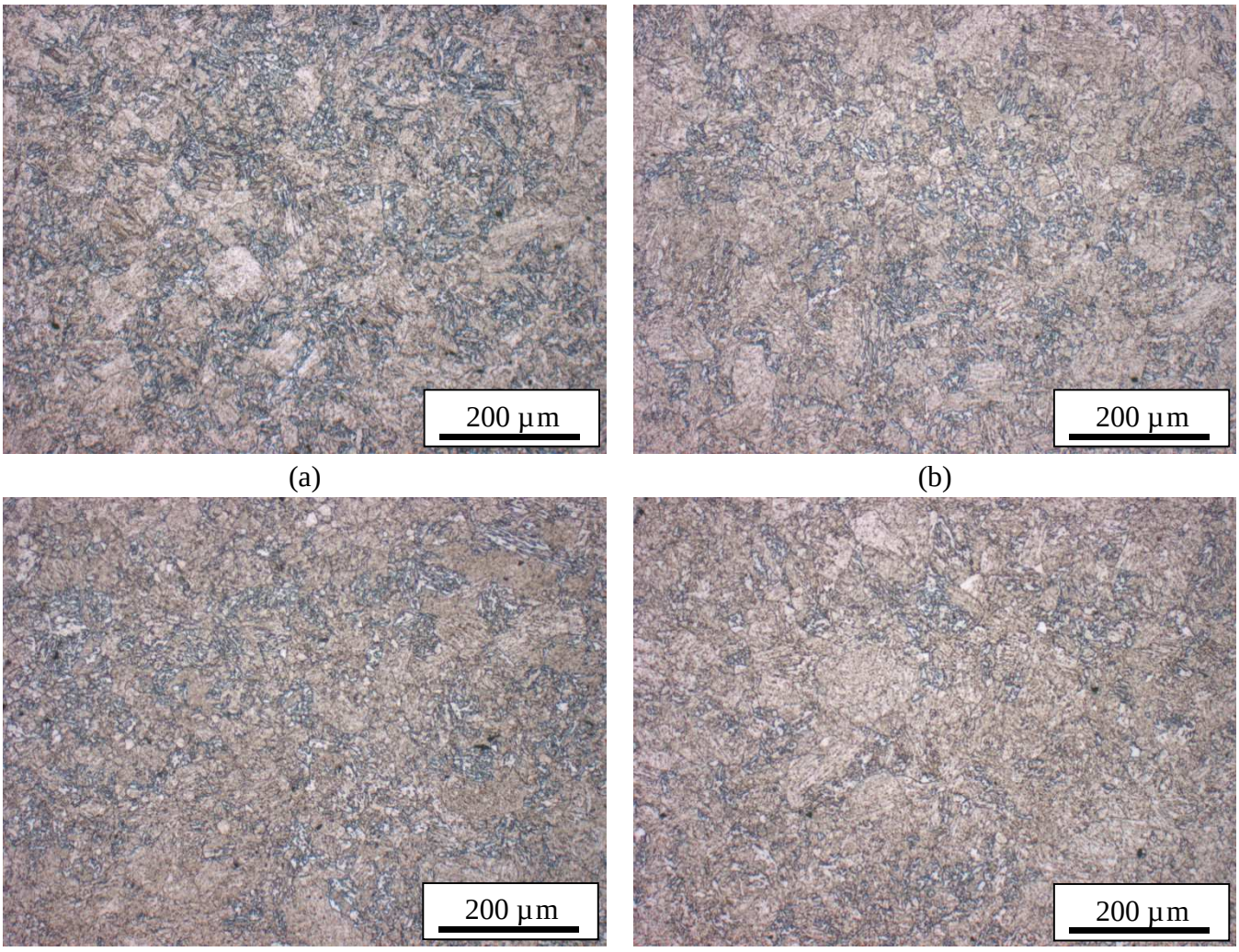

***Figure 2.3**:Microstructure of the reference material at (a) outer skin, (b) ¼ thickness, (c) ½ thickness and (d) ¾ thickness. Nital etching 2%, optical microscopy.*

Thus, the industrial component can be considered as chemically homogeneous and is expected to have the same physical properties (transformation temperatures, mechanical properties …) throughout its thickness. All further studies performed on the as-received samples can therefore be considered as representative of the whole material.

2. PHASE TRANSFORMATIONS AND EQUILIBRIUM

Several material parameters must be known in order to perform the study of heat treatments. The characterization of the steel in its thermodynamic equilibrium state is useful to assess phase transformation in the iron-based matrix and the evolution of secondary phases during heat treatments. The determination of austenitic transformation temperatures is a prerequisite for the study of austenitization, as is determination of cooling rates at different locations of the component for the study of bainitic hardenability through CCT diagrams. A first austenitization heat treatment is thus conducted in order to estimate the bainitic hardenability of the material.

2.1 Equilibrium calculations

The nature of secondary phases and the ferrite-to-austenite transformation temperatures were investigated using two different softwares: MatCalc v. 6.00, using the mc_fe_v2.029 database (Figure 2.4); and ThermoCalc, using the TcFe7 database (Figure 2.5). The input chemical composition is that determined at the quarter-thickness and given in Table 2.1. Both simulations give similar results. However, one should notice that the ThermoCalc calculation tends to give higher dissolution temperatures for the secondary phases when compared to MatCalc, as detailed below.

The ferrite-to-austenite transformation is similarly described in both simulations: austenite starts to form at 778°C and 780°C respectively from ThermoCalc and MatCalc, and the transformation is fully finished respectively at 841°C and 830°C. Predicted equilibrium carbides are $M_{23}C_6$, which dissolve in the intercritical temperature range, and M_6C, which are stable up to 625°C. This is consistent with literature data [14]. Predictions from both simulations are in good agreement with each other. The specific topic of carbide stability will be discussed in more detail in the chapter dedicated to precipitation (Chapter V).

Several other secondary phases coexist. AlN precipitates are well-known for pinning austenite grain boundaries during grain growth [38], and their actual effect will be discussed in Chapter III for the chemistry considered here. However, one should notice that MatCalc predicts dissolution of AlN at 930°C while ThermoCalc predicts it at 970°C.

Cr_2N particles precipitate due to the excess of nitrogen in the material; this excess is due to the low amount of aluminum. Interestingly, ThermoCalc calculations predict a change in crystallography from hexagonal to face-centered cubic structure for Cr_2N at the vicinity of 550°C while MatCalc calculations only show a stable face-centered cubic in the whole stability domain. However, these precipitates should not have any effect on the material properties: they cannot act as a pinning particles since they are not stable in the intercritical temperature range, and their overall phase fraction is low enough to be negligible in front of carbides for the study of the precipitation kinetics.

MnS particles are in very low concentration in the material (phase fraction of $\sim 10^{-4}$). This type of particle is unavoidable in steels and appears during the steelmaking process. They are stable up to 1300°C, and will not play any role in the chemical evolution of the material. They are typically spherical particles, 1 µm in diameter, and can act as void nucleation sites in ductile fracture as shown in Figure 2.6.

As a conclusion, several equilibrium secondary phases are of interest in this material. AlN particles might play a role in the austenite grain growth, while MnS particles can have an effect on the mechanical properties by acting as void nucleation sites. Most important secondary phases are the carbides, which precipitation and transformation, before equilibrium is reached, have a great role in the material properties. This topic will be addressed in Chapter V.

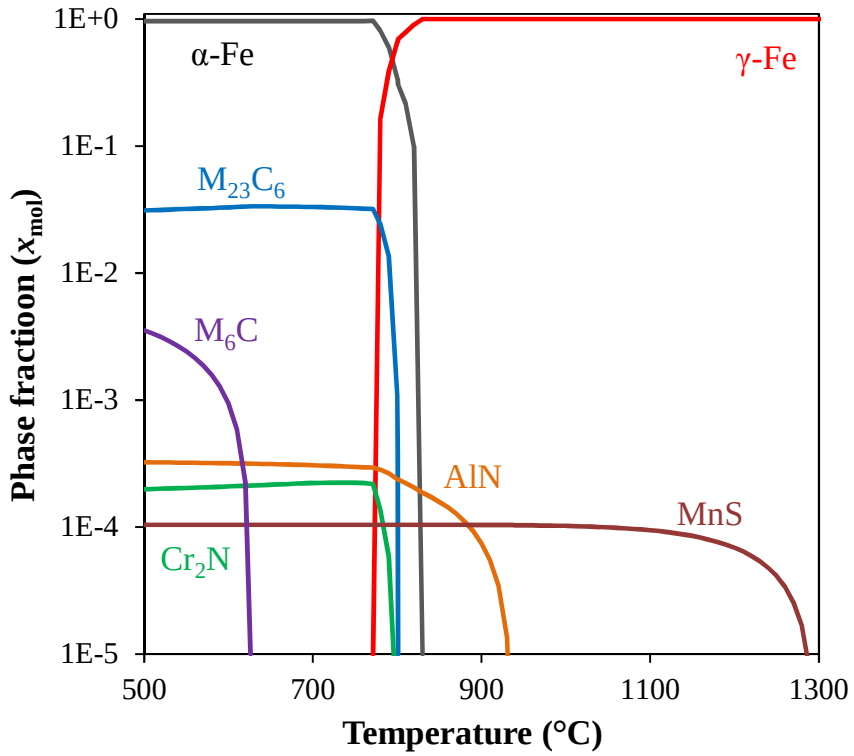

***Figure 2.4**: Phase stability diagram predicted using MatCalc software*

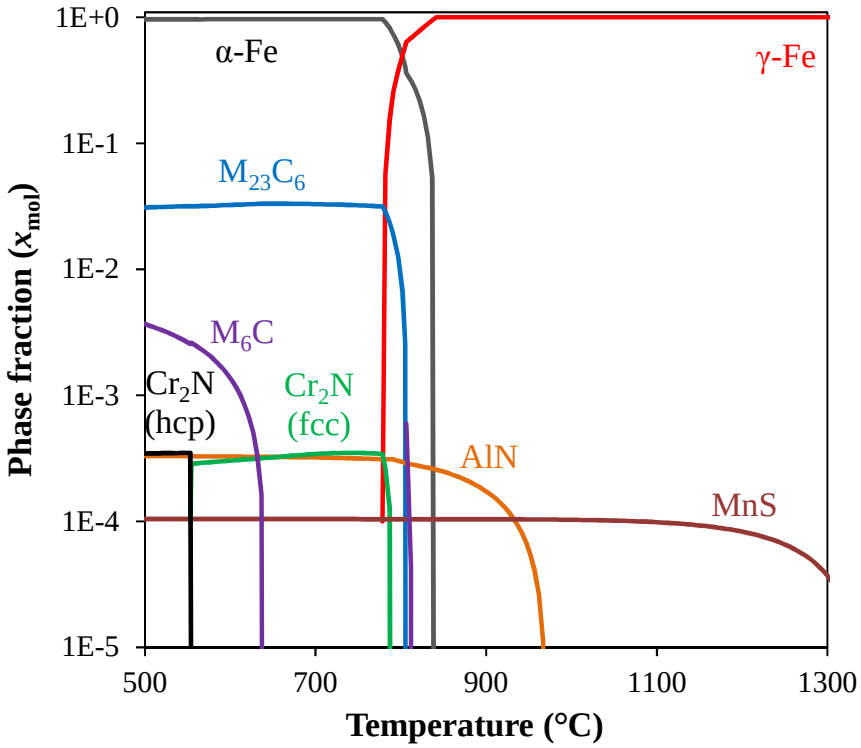

***Figure 2.5**: Phase stability diagram predicted using ThermoCalc software*

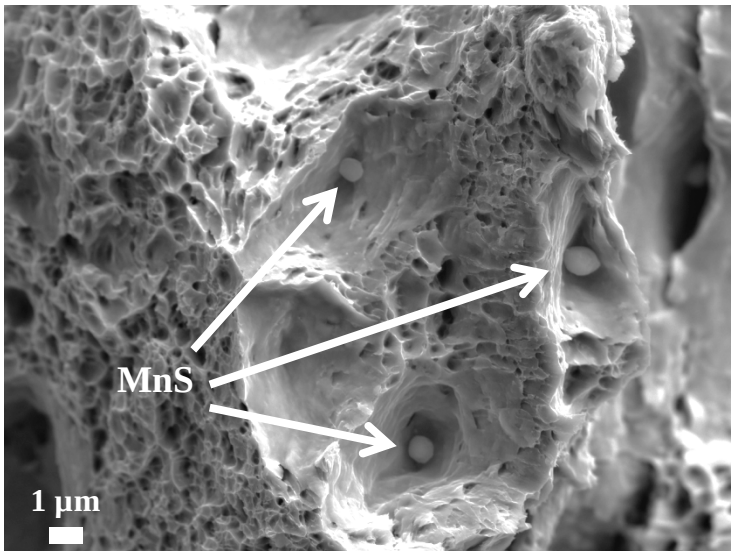

***Figure 2.6**: MnS particles inside fracture dimples. Heat treatments: 970°C – 1 hour + cooled at 0.5°C/s + tempering 675°C – 12h, fractured at -125°C. SEM observation, characterization made by EDX measurements.*

2.2 Transformations upon heating

Ferrite-to-austenite transformation temperatures in the material have been determined. These characteristic temperatures correspond to the beginning and the end of the austenitic transformation. They are respectively noted Ae_1 and Ae_3 at the thermodynamic equilibrium and Ac_1 and Ac_3 in real conditions since the heating rate has an impact on these transformation temperatures. However, for slow enough heating rates, one can consider that the experimentally measured temperatures are close to the equilibrium ones.

In order to study the material behavior in out-of-equilibrium conditions, characterizations of Ac_1 and Ac_3 temperatures have been conducted. Three different heating rates were used: 0.02°C/s, 0.2°C/s and 1°C/s; this latter is the reference heating rate for the austenitization step that will be used throughout this study. The two slower heating rates were applied by means of calorimetry, and the faster one by means of dilatometry. Estimated error is 10°C for both techniques. Equilibrium values are taken from MatCalc calculations which were discussed in part 2.1.

Results are shown in Table 2.4. Both temperatures strongly increase with the heating rate from 0.02°C/s to 0.2°C/s and stabilize around 800°C for Ac_1 and around 880°C for Ac_3, for heating rates from 0.2°C/s to 1°C/s. This increase is stronger for the Ac_3 temperature. Good agreement is found at slow heating rates with thermodynamic equilibrium calculations.

	Equilibrium	**0.02°C/s**	**0.2°C/s**	**1°C/s**
Ac_1 (°C)	780	780	800	810
Ac_3 (°C)	830	840	870	880

***Table 2.4**: Ferrite-to-austenite characteristic temperatures at thermodynamic equilibrium and at different heating rates. Equilibrium values are calculated with MatCalc.*

2.3 Equivalent cooling rates

Prior to estimate the bainitic hardenability of the steel for the manufacturing of a heavy component, one must determine the range of cooling rates that may occur in the piece, namely the slowest and fastest ones. In the considered hollow component, it corresponds to the cooling rates occurring at mid-thickness and at both skins, respectively. However, during industrial manufacturing, several machining steps are applied to the skin of the piece after the final tempering. Thus, the fastest cooling rate of interest is the one occurring at the so-called "machined skin", namely, 10 mm under the skin of the heat treated component. While the mid-thickness and the quarter-thickness equivalent cooling rates are already known from measurements during reheating of the reference material, calculations have to be done in order to determine the equivalent cooling rate at the machined skin.

In industrial applications, the cylindrical shell is water quenched after austenitization. Thermal shields are welded at its top and bottom, thus the cooling stage can be considered as a unidirectional problem as shown in Figure 2.7.

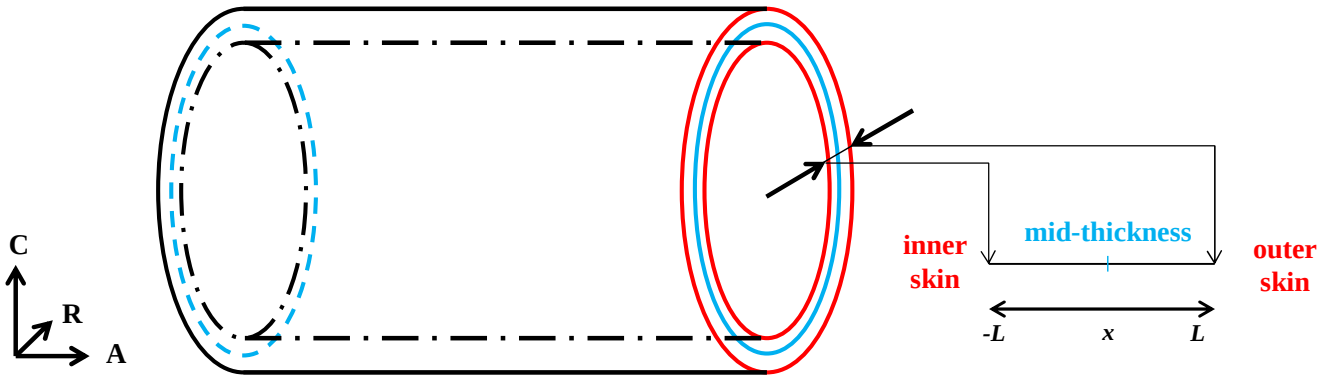

Figure 2.7: *Schematic diagram of the cylindrical shell. x: location in component thickness*

In these particular conditions, the general heat equation (2.1) can be developed into equation (2.2), where:

- $2L$ is the shell thickness, namely L = 0.014 m
- x is the length of interest, where positive x are towards the outer skin. Lengths of interest are x = 0 m for the mid-thickness, x = 0.07 m for the quarter-thickness and x = 0.013 m for the machined skin.
- a is the thermal diffusivity of the material, in $m^2.s^{-1}$. In equation (2.1), a is considered as constant for all x and thus independent of the temperature. Its actual dependency on temperature will be discussed later.

$$\frac{\partial T}{\partial t}(x,t) = a\,\frac{\partial^2 T}{\partial x^2}(x,t) \tag{2.1}$$

$$\frac{T(x,t)-T_0(x)}{T_\infty - T_0(x)} = \sum_{n=0}^{\infty}(-1)^n \left\{ \operatorname{erf} c\left[\frac{(2n+1)L-x}{2(at)^{1/2}}\right] + \operatorname{erf} c\left[\frac{(2n+1)L+x}{2(at)^{1/2}}\right]\right\} \tag{2.2}$$

Boundary conditions and assumptions for the calculations are the following:

- As already stated, the outer skin and the inner skin, and by extension the quarter-thickness and the three-quarter-thickness, are expected to experience the same cooling rate during the water quench, such as at each time step t, $T(x) = T(-x)$. Thus, inner and outer skins will be referred to as “skin”, and quarter-thickness and three-quarter-thickness as “quarter-thickness”.
- Before quenching, every point of the cylindrical shell is at the austenitization temperature, thus $T_0(x) = T_{aust}$ for any value $x \neq \pm L$.
- The cooling rate at the skin is considered to be infinite, such as $T(\pm L, t) = T_\infty$ at any time $t \geq 0$.
- The water temperature is considered to be constant and equal to room temperature, so that $T_\infty = 20°C$.

The thermal diffusivity of the material, a, was determined by a LaserFlash method under static helium with a heating rate of 0.1°C/s. More information about this technique can be found in Appendix A. In order to study the effect of the microstructure on thermal diffusivity, three samples containing different amounts of bainite were tested: 100% bainitic, (67% bainitic – 33% ferritic) and (25% bainitic – 75% ferritic). These microstructures were produced on a dilatometer based on the preliminary CCT diagram established in section 2.4. Heat treatments were as follows: austenitization at 920°C for 30 minutes, then cooling at 1°C/s, 0.3°C/s and 0.1°C/s, respectively. Measurements were done between room temperature and 980°C. Since the microstructure is fully austenitic at temperatures higher than 880°C, this range of temperature allows the thermal diffusivity of austenite to be determined. Measurements are shown in Figure 2.8. It appears that the fraction of bainite does not influence the thermal diffusivity of the material. For simplicity, an average temperature-independent value of 5 $mm^2.s^{-1}$ is chosen for the thermal diffusivity.

Predictions from equation (2.2) were compared to temperature measurements available for the reference material (see Table 2.2). The results are reported in Figure 2.9.

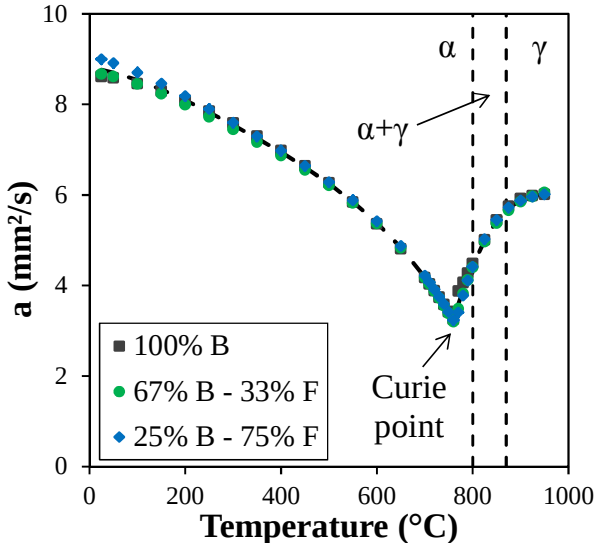

Figure 2.8: *Thermal diffusivity of the material as a function of temperature for different microstructures (F: ferrite, B: bainite). α and γ stand for ferrite and austenite domains, respectively. Ac_1 and Ac_3 temperatures correspond to a heating rate of 0.2°C/s (actual heating rate: 0.1°C/s)*

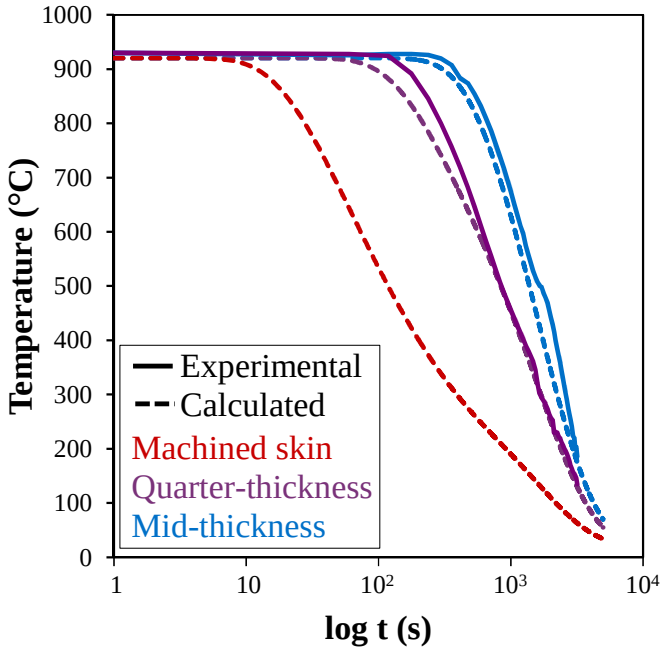

Figure 2.9: *Experimental and calculated cooling rates at machined skin (10 mm under skin), quarter-thickness and mid-thickness.*

Good correspondence between on-field measurements and model predictions is found, respectively -0.31°C/s and -0.38°C/s at the mid-thickness and -0.54°C/s and -0.55°C/s at the quarter-thickness between 800°C and 500°C. As a mean of comparison, cooling rates in the center of a 400-mm-thick plate and in a center of a 200-mm-thick plate between 800°C and 500°C during water quenching are respectively 0.15°C/s and 0.5°C/s [12].

As shown in Table 2.5, chosen equivalent cooling rates for the rest of this study were rounded to the inferior first decimal to be conservative with respect to the risk of getting a high fraction of proeutectoid ferrite.

Location in thickness	**Machined skin**	**Quarter-thickness**	**Mid-thickness**
Cooling rate	3°C/s	0.5°C/s	0.3°C/s

Table 2.5: *Equivalent cooling rates for the mid-thickness, the quarter-thickness and the machined skin (10-mm under the skin after the heat treatment) of a 280 mm-thick cylindrical shell during quenching after austenitization.*

2.4 Phase transformation behavior during cooling (CCT diagram)

In order to estimate the transformations upon cooling in a thick-walled component, a CCT diagram had to be established. A first study on austenitization was made at 920°C; the austenitization time was set to 30 minutes.

The CCT diagram was established by means of dilatometry on 2x2x12 mm^3 samples; studied cooling rates ranged from 100°C/s to 0.05°C/s and cooling rates representative of specific locations in the component thickness are highlighted in Figure 2.10. It should be pointed out that the ferrite

fractions were determined using the tangent method from dilatometer curves upon cooling (see Appendix A); thus the whole sample volume was taken into account. However, during high temperatures heat treatments, a decarburization layer can appear at the sample periphery. Upon slow cooling, the sample remains for longer times at high temperature and the decarburization layer becomes thicker. Since it is depleted in carbon, ferrite transformation tends to occur in this layer upon cooling. Considering the small dimension of the samples, the ferrite form in this layer are not negligible, and the given ferrite fractions are thus overestimated.

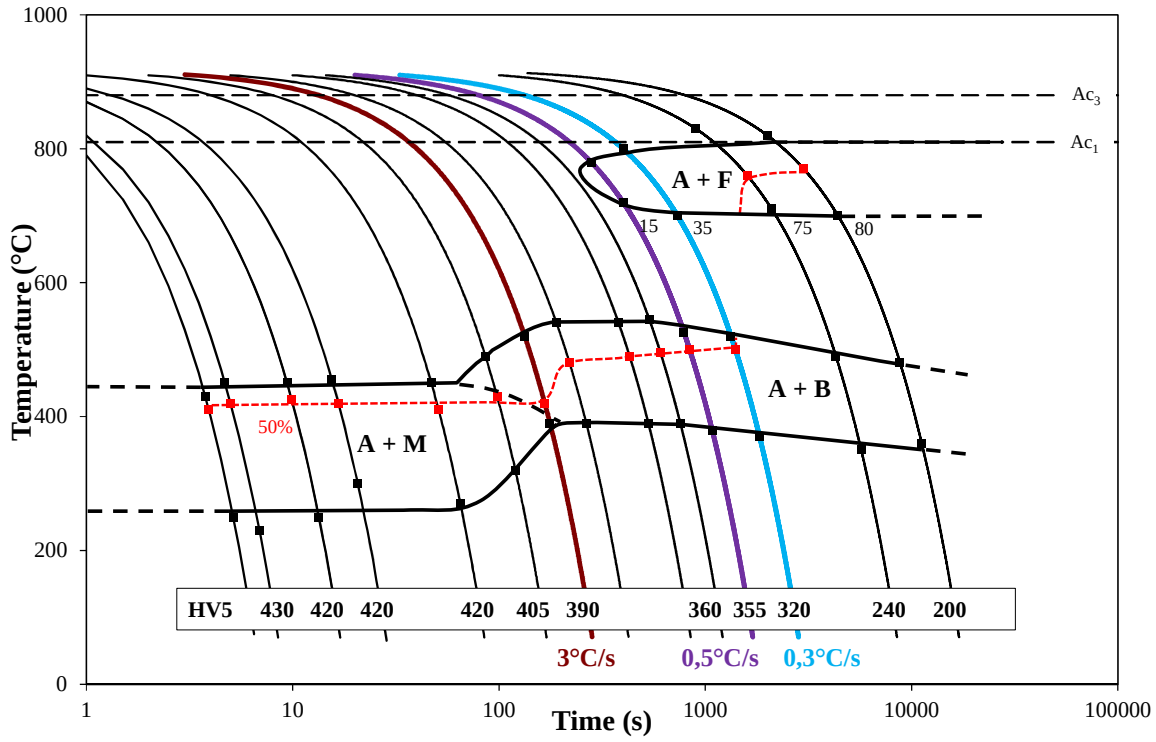

Figure 2.10: *CCT diagram after austenitization at 920°C for 30 minutes. Representative cooling rates of the targeted component are highlighted. A: Austenite, M: Martensite, B: Bainite, F: Ferrite.*

In the studied austenitization conditions, four different microstructures can be found at room temperature, depending on the cooling rate (Figure 2.10):

- **For cooling rates higher than 10°C/s**, the microstructure is fully martensitic. The martensite start transformation temperature M_s remains constant at 450°C. The hardness is close to 420 HV, independently of the cooling rate.
- **For cooling rates ranging from 5°C/s down to 3°C/s**, the microstructure consists of a mixture of bainite and martensite. The amount of martensite, as well as the hardness, decreases when decreasing the cooling rate.
- **For cooling rates ranging from 3°C/s down to 0.7°C/s**, the microstructure is fully bainitic. The hardness is around 350 HV, and the bainite start transformation temperature B_s remains constant at 520°C independently of the cooling rate.
- **For cooling rates lower than 0.7°C/s**, austenite decomposes into proeutectoid ferrite before final transformation into bainite. The amount of proeutectoid ferrite increases with lower cooling rates,

decreasing the general hardness from 350 HV to 200 HV for 15 vol% and 80 vol% of proeutectoid ferrite, respectively. The bainite start transformation temperature B_s decreases with increasing amount of proeutectoid ferrite, due to the enrichment of austenite in carbon induced by the formation of low-carbon ferrite.

These results are consistent with other CCT diagrams found in literature for similar steel compositions and austenitization conditions [1, 10]. Considering these results, the bainitic hardenability is too low for the considered thick piece since ferrite transformation significantly occurs at the quarter-thickness equivalent cooling rate (0.5°C/s). Thus, the material is not adapted for the targeted industrial application when using this austenitization condition and an optimal austenitization condition has to be determined. Comparison of these results with the reference material presented in section 1.2 is interesting: after austenitization at 930°C for 1 hour, then cooled at a similar cooling rate, its resulting microstructure is fully bainitic. Moreover, its chemical composition is the same as that of the as-received material used for this study. This indicates that, at temperatures ranging around 920°C - 930°C, increase of the duration of the austenitization heat treatment has an effect on the austenite itself, increasing its bainitic hardenability. Thus, a more extensive study of the microstructural evolution of austenite during austenitization and its decomposition during subsequent cooling is needed. These topics will be adressed in Chapters III and IV.

3. CHEMICAL HETEROGENEITIES

During the casting process, chemical segregation can occur in the ingot at different scales. Major segregations occur in the ingot thickness, and consist mostly in carbon content variations. As seen in the chemical composition analysis made at different thicknesses in part 1.2, no such segregations were observed in the studied part of the component, and thus in the studied material.

Millimeter-scale segregations can also be found in such heavy components, for example in manganese steels such as the ASTM A508 grade. These segregations are also known as “ghost lines” and show high enrichment in phosphorus as well as clustering of MnS particles, and are thus detrimental for the mechanical properties. No such segregations were observed in the studied material.

Another scale of segregations, much finer, is the interdendritic segregation, also known as microsegregation. Microsegregations result from freezing of solute-enriched liquid in the interdendritic regions. The chemical composition of a solidified dendrite is not uniform: the core is richer in iron atoms, since it is the first to solidify. Solidification then leads to progressive enrichment of the interdendritic liquid with solute elements. This results in a progressive increase in solute concentration in the dendrite from the core to its periphery. The typical length scale of this type of segregations is hundreds of micrometers in the case of slow solidification of a heavy ingot. Local chemical heterogeneities and their influences on mechanical properties were investigated in the as-received state, in order to assess whether samples of the study can be considered as chemically similar to each other.

3.1 Spatial distribution of chemical composition

A slight Nital etching was used to reveal heterogeneities in the material (Figure 2.11). These heterogeneities are ordered as millimeter-long, hundred micrometers-wide bands located along in the radial-circumferential plane. Interdendritic spacing, as deformed from the forging steps, is ranging between 0.2 mm and 0.4 mm.

The tendency of a chemical element to segregate is given by the Equilibrium Partition Coefficient K_e, $K_e = C_s/C_l$, where C_s and C_l are the element concentrations in solid and liquid, respectively. The lower the value of K_e, the higher the tendency towards segregation. Gosh summarized values of K_e for solidification of binary iron alloys into δ-iron [39]; values for 2.25 Cr – 1 Mo-related chemical elements are reported in Table 2.6. Theoretically, only slight variations in chromium content are expected. However, as the main alloying element, even slight variations of its content should be detected. On the other hand, a strong variation in carbon content should be observed, and it seems reasonable to assume that dark-etching areas observed in Figure 2.11 are carbon-enriched regions.

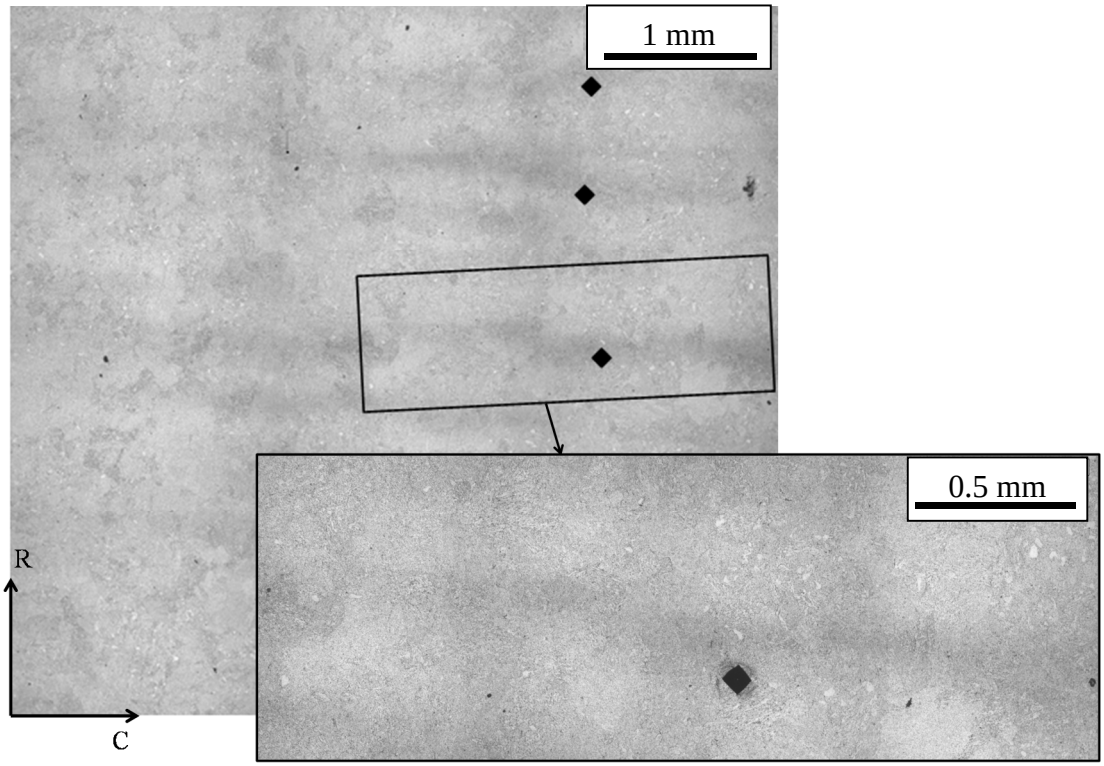

***Figure 2.11**: Optical observation of the as-received state. Microsegregations are horizontal alternately bright and dark regions. Black spots are indentation marks from hardness measurements. Vertical dark bands are artifacts due to interpolation of multiple images.*

Element	**Al**	**C**	**Cr**	**Mn**	**Mo**	**Ni**	**N**	**P**	**Si**	**S**
K_e	0.92	0.13	0.95	0.84	0.80	0.80	0.28	0.13	0.66	0.02

***Table 2.6:** Values of Equilibrium Partition Coefficient (K_e) for solidification of binary iron alloys intro ferrite. From* [39]

Qualitative WDS maps were performed on a Cameca SX100 electron microprobe. The analyzed area was set to 1000 µm x 800 µm, which is large enough to observe several microsegregated regions. Analyzed chemical elements were carbon, chromium, manganese, molybdenum, copper, nickel, phosphorus, sulfur and silicon. Amongst all these elements, only variations in amounts of chromium, molybdenum and manganese were found (Figure 2.12). Carbon content analysis was not possible due to sample contamination.

Segregations bands appear to be alternately chromium and molybdenum enriched and depleted. Local enrichments in manganese observed in segregated areas are likely MnS particles. Distances between microsegregated regions is ranging between 0.2 mm and 0.3 mm, which is consistent with the observations made in Figure 2.11.

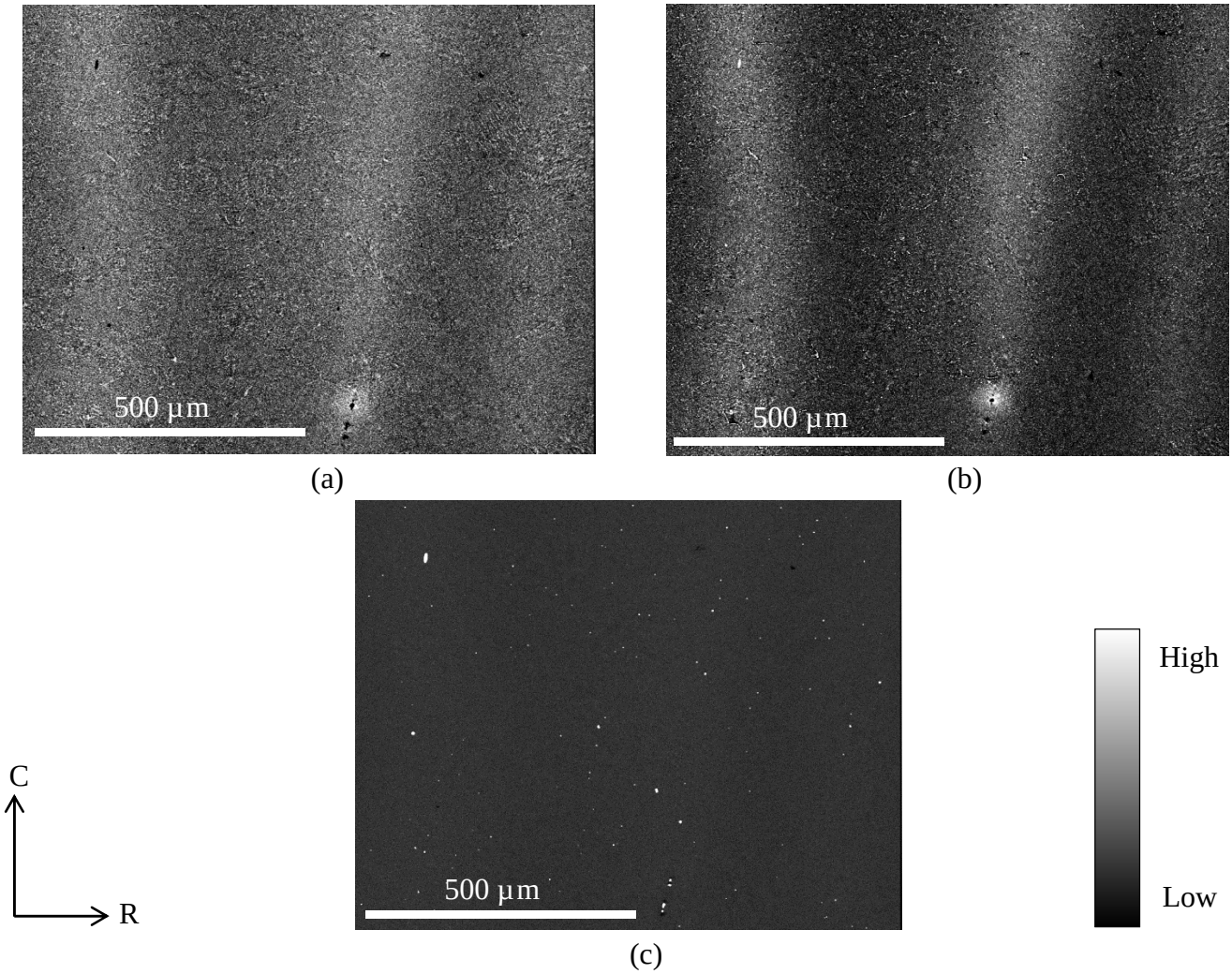

Figure 2.12: *X-ray elemental maps of (a) Cr, (b) Mo, (c) Mn*

In order to quantify variations of chemical composition, quantitative analyses were made across the two heterogeneities as shown in Figure 2.12 for these three elements. Analyses were done in bandscan mode with 50x1 µm² beam. The step size was 2 µm for a total length of 1 mm. Results are shown in Figure 2.13 and Figure 2.14. As expected, a chemical gradient is observed. Minimum and maximum contents, respectively from the center of dendrites and from the last liquid droplet to

solidify, are summarized in Table 2.7. These compositions are the average values over quantitative data sets corresponding to the straight lines drawn in Figure 2.13 and Figure 2.14, respectively.

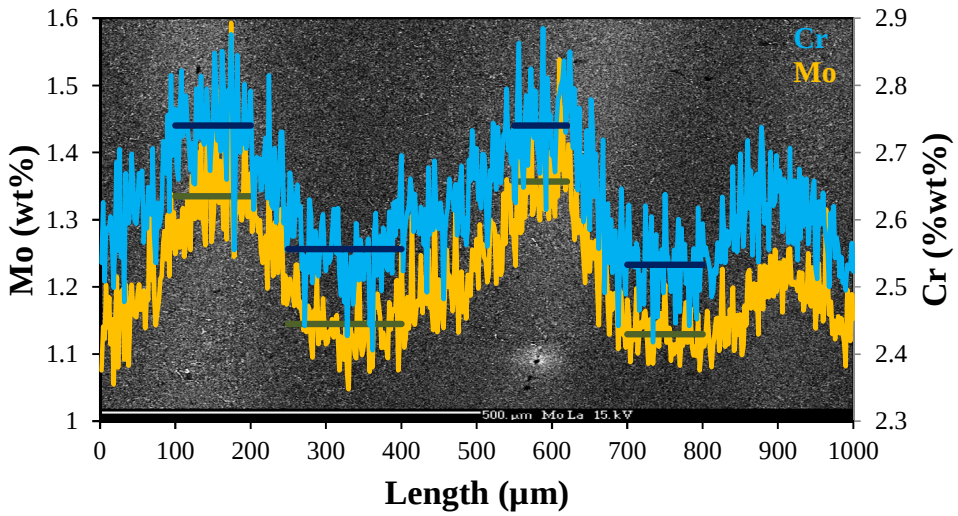

Figure 2.13: *Quantitative chemical analysis of Cr and Mo (wt%). Bandscan mode, 50x1 µm² beam, 2 µm step, total length: 1 mm.*

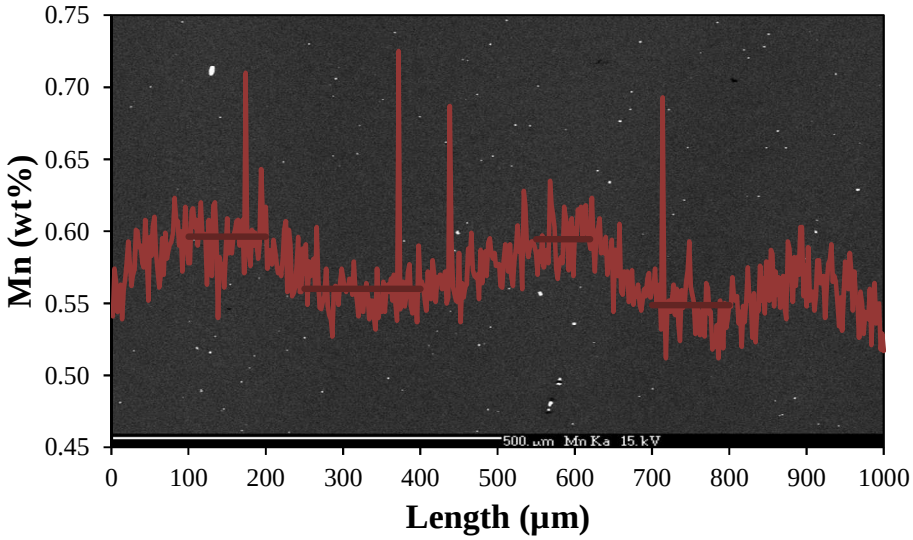

Figure 2.14: *Quantitative chemical analysis of Mn (wt%). Bandscan mode, 50x1 µm² beam, 2 µm step, total length: 1 mm.*

	Cr	Mo	Mn
Expected content (wt%)	**2.47** ± 0.03	**1.11** ± 0.03	**0.51** ± 0.01
Maximum	**2.74** ± 0.06	**1.34** ± 0.06	**0.59** ± 0.02
Minimum	**2.54** ± 0.06	**1.13** ± 0.04	**0.55** ± 0.01

Table 2.7: *Average alloy element content of the former dendrite core (Maximum) and of the region supposed to be the last liquid to solidify (Minimum), corresponding to straight lines drawn on Figure 2.13 and Figure 2.14. Expected content is the ¼-thickness chemical composition (Table 2.1)*

One should notice that chemical contents are always higher than the nominal composition (see Table 2.1). The overestimation of chromium content is due to a calibration problem on the EPMA. As expected in the presence of a systematic bias, interpretation is possible when only the difference between extremes is considered. Concerning molybdenum and manganese measurements, differences are more or less in the range of the standard deviation and the detection limit.

3.2 Effect on local mechanical properties

To assess microstructure-mechanical property relationships, mechanical tests, namely tensile and V-notch Charpy, were conducted in this study with small size specimens (Chapter VI). V-notch Charpy tests rely on a small plastic zone, namely several hundred micrometers in width, thus one could expect possible sampling effects on toughness properties if the plastic zone on several specimens would correspond to positive segregations while on other specimens it would correspond to negative segregations. Local mechanical properties as a function of chemical heterogeneity have then to be investigated. However, even if the composition variations in segregated regions have an effect on local elastoplastic or fracture properties, this would have little effect on the elastoplastic behavior evaluated with tensile tests since in such tests only the average response of the material is measured over a gauge volume of several cubic millimeters.

Nanoindentation measurements were performed on a CSM instruments nanoindenter, using a modified Berkovich indent with a 15 mN load. Investigated regions were positive and negative microsegregations resulting in fully bainitic microstructure, located with respect to WDS maps. For each region, a 3x20 mapping with a 10 µm step size was realized (Figure 2.15).

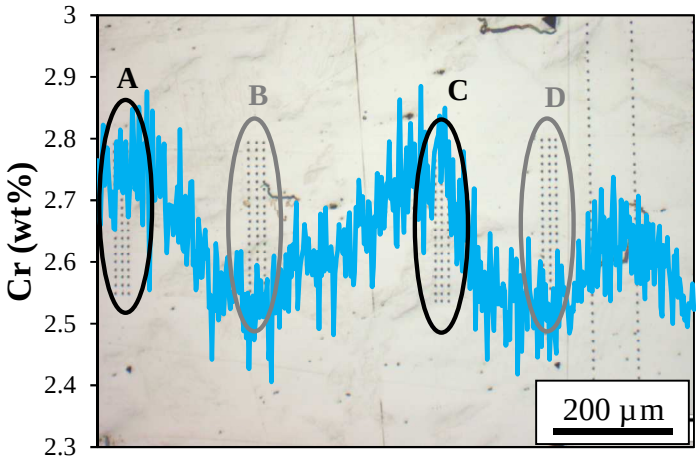

Figure 2.15: *Superposition of Cr WDS profile and nanoindentation measurements regions. Black dots are indentation marks. Regions A and C correspond to positive segregations while regions B and D are negative segregations.*

Results are given in Table 2.8. It should be noted that results were processed from data in H_{IT}, which unit is MPa, that were converted into HV numbers for comparison purpose with results presented in section 1. Original results and conversion equations can be found in Appendix A.

Depleted regions show hardness of 270-280 HV while enriched areas exhibit up to 290-300 HV. No variations of the Young modulus are observed, although the absolute values are higher than the

usual value of the Young's modulus for ferritic and bainitic steels. Considering the hardness measurement standard deviation, we can conclude that segregations only have little effect on hardness values. One should also notice that these hardness values are higher than those determined from macrohardness measurements, which is about 220 HV. This is due to the very low load used for nanoindentation measurements: a 15 mN load penetrates 0.5 µm deep into the material. Thus, surface effects and strain-hardening affect the measurements.

	A	**B**	**C**	**D**
Average hardness (HV)	277 ± 8	290 ± 10	271 ± 12	298 ± 10
Average Young modulus (GPa)	269 ± 13	269 ± 11	261 ± 12	268 ± 11

Table 2.8: *Results of nanoindentation: converted Vickers hardness and Young's modulus (load: 15 mN, average value over 60 measurements)*

Complementary measurements were done with a higher load (400 mN) in order to get rid of surface effects. This load corresponds to an indentation depth of 2.7 µm. Five additional points were done in regions A and B. Results are given in Table 2.9 and are consistent with macrohardness measurements, and the Young's moduli are within range of usual values.

	A	**B**
Average hardness (HV)	240 ± 10	250 ± 5
Average Young modulus (GPa)	225 ± 8	234 ± 3

Table 2.9: *Results of nanoindentation: converted Vickers hardness and Young's modulus (load: 400 mN, average value over 5 measurements)*

Differences in hardness and in Young's modulus between enriched and depleted zones are within standard deviations. Thus, microsegregations have no significant effect on local elastoplastic properties, with the exception of local concentrations of MnS that might have an effect on toughness.

3.3 Effect on phase transformations

Changes in composition can induce a shift of the ferritic transformation domain in CCT diagrams. In the case of 2.25 Cr – 1 Mo steel, any increase in amount of chemical elements such as nickel, manganese, boron or carbon is known to improve the bainitic hardenability [35–37]. In the case of microsegregations, the chemical enrichment may appear too slight to have a measurable effect. However, when considering a cooling after austenitization which rate is very close to the ferritic critical cooling rate, for instance cooling at 0.3°C/s after austenitization at 940°C for 1 hour, one can observe a change in microstructure as shown in Figure 2.16. Regions corresponding to positive microsegregations are fully bainitic, while the depleted regions consist of a mixture of ferrite (white patches in center of Figure 2.16) and bainite. The fully ferritic region observed at the periphery is the decarburization layer mentioned in section 2.4.

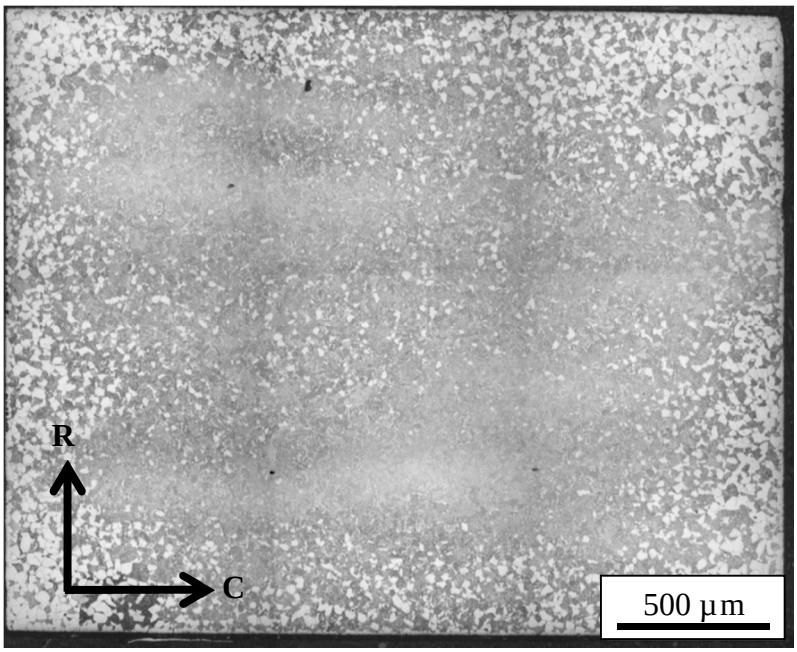

Figure 2.16: *Optical micrography showing change in microstructure due to microsegregations. Equiaxial ferrite is bright. The fully bainitic dark bands along the radial-circumferential plane correspond to the chemically enriched zones. Horizontal and vertical dark lines are artifacts due to stitching of multiple images.*

Based on all these results, we can then safely state that 2.25 Cr – 1 Mo steel microsegregations only have a minor impact on microstructure and elastoplastic properties. Chemical variations even increase bainitic hardenability locally. All heat treatments for the study of microstructural and mechanical properties of the material have been conducted on 30x3x4 mm^3 blanks, with the 30x4 mm^2 section in the A-C plane perpendicular to microsegregations, as shown in Figure 2.17. In this configuration, microsegregations are not expected to have an effect on toughness properties as several of them are sampled by the fracture process zone all along the crack initiation and propagation stages in a given specimen.

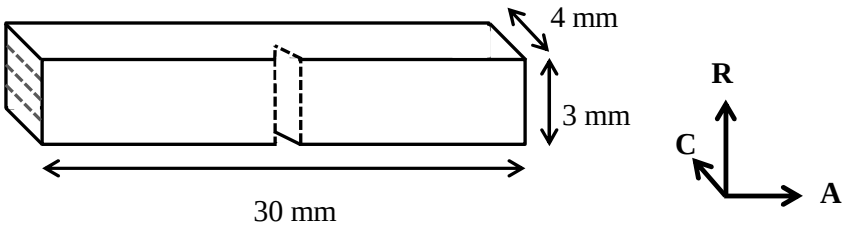

Figure 2.17: *Schematic drawing of the blanks used throughout this study with the location of the V-notch for Charpy tests. Grey dashed lines represent microsegregations on a given R-C plane.*

4. CONCLUSION

The as-received state of the studied material has been described in terms of chemistry and microstructural properties, as well as the reference state, which is used for comparison in the

following chapters. No major segregations or ghost lines have been highlighted in this material. Millimeter-long, hundred micrometer-wide bands stemming from minor segregations are located along the radial-circumferential plane, but are expected to have only little effect on both mechanical and microstructural properties, with the exception of possible local clustering of MnS particles. Thus, samples taken from the quarter-thickness material will be considered as chemically representative of the component.

Thermodynamic equilibrium calculations show that, with the exception of carbides which will be studied in Chapter V, the only secondary phases of interest for metallurgical evolution during heat treatments are aluminum nitrides AlN which might have an effect on austenite grain growth.

Moreover, with the austenitization conditions tested in this preliminary study, the bainitic hardenability proved to be insufficient for the industrial application since transformation of austenite into ferrite significantly takes place at the quarter-thickness equivalent cooling rate. This issue has to be elucidated, as the reference material is fully bainitic at quarter thickness for austenitization conditions similar (but no identical) to these used for this first experimental heat treatment in this study. Thus, optimal austenitization conditions have to be determined through a better understanding of the austenite grain growth mechanisms (Chapter III) and the effects of austenitization heat treatment on microstructural and mechanical properties after cooling (Chapter IV).

Chapter III: Experimental characterization and modelling of austenite grain growth

TABLE OF CONTENTS

For the considered industrial applications, the only way to improve bainitic hardenability is by increasing the austenite grain size, since the cooling rate after austenitization is prescribed by the wall thickness of the component. However, too coarse grains might result in a decrease in toughness and increase the susceptibility to temper embrittlement. Thus, austenite grain growth must be present and understood in order to control the austenite grain size through austenitization time and temperature. The present chapter is thus dedicated to the experimental characterization of austenite grain growth with time at various austenitization temperatures. Mathematical models are applied in order to determine the physical mechanisms controlling grain growth and for predicting the austenite grain size for a given couple of time and temperature.

In the first part of this chapter, the current state-of-the-art regarding the modelling of austenite grain growth is summarized. The general framework of the model assumes that growth of a single grain is controlled by the grain boundary curvature and can be slowed down, or even stopped, by retarding pressures induced by fine particles or by the presence of solute atoms. In the second part, the evolution of austenite grain size with time at various temperatures is experimentally determined. Limited growth occurs at lower temperatures, while at higher temperatures it is not affected by such phenomenon. Finally, model predictions are compared to experimental measurements in order to understand the different mechanisms controlling grain growth.

1. MODELLING AUSTENITE GRAIN GROWTH

1.1 General framework of modelling

For normal grain growth in polycrystalline materials, the simplest model describes the growth of a single grain, assuming that the mean grain diameter D is representative of all grains in the material.

Under this assumption, it is considered that the boundary of a grain of radius $D/2$ moves with a velocity v due to the net pressure P acting on it. It is generally assumed that the velocity is directly proportional to the pressure with the constant of proportionality being the mobility M of the boundary (equation (3.1)). The mobility is strongly temperature dependent and follows an Arrhenius-type relationship, as shown in equation (3.2).

$$\frac{1}{2}\frac{dD}{dt} = v = MP \tag{3.1}$$

$$M = M_0 \exp\left(-\frac{Q}{RT}\right) \tag{3.2}$$

where M_0 is the pre-exponential mobility factor, Q is the activation energy of the mobility, T is the temperature and R the gas constant. The value of Q will be discussed later in this chapter.

The net pressure P can be decomposed into the sum of all driving and retarding contributions, respectively, P_d and P_r. The driving pressure is responsible for the boundary movement while retarding pressures tend to inhibit it:

$$P = P_d - P_r \tag{3.3}$$

The driving pressure can be calculated as follows. In polycrystalline materials, atoms at the boundaries are less accommodated than atoms inside the grain lattice, therefore their energy is higher. Thus, the minimization of the energy of the system occurs by reducing the total grain boundary area per unit volume, which leads to grain growth. Let us consider a system with two different grains A and B separated by a boundary of area A, as shown in Figure 3.1. By assuming constant volume-stored energy, the Gibbs free energy G of this system can be written as:

$$G = G_0 + \gamma_g A \tag{3.4}$$

where G_0 is the energy inside the grains and γ_g is the grain boundary interfacial energy. By assuming that the shape of metal grains is the same as that of cell foams, then the change in Gibbs free energy ΔG associated with growth of grain B can be written using the Young-Laplace equation:

$$\Delta G = \gamma_g V_m \left(\frac{1}{\rho_1} + \frac{1}{\rho_2}\right) \tag{3.5}$$

where V_m is the molar volume and ρ_1 and ρ_2 are the two principal curvature radii of the boundary. The driving pressure P_d applied on the grain boundary is then defined as the free energy reduction per molar volume, and can be written as:

$$P_d = \gamma_g \left(\frac{1}{\rho_1} + \frac{1}{\rho_2} \right) \tag{3.6}$$

Equation (3.6) can also be written as a function of the grain equivalent diameter D_{eq}, such as:

$$P_d = k_d \frac{\gamma_g}{D_{eq}} \tag{3.7}$$

where k_d is a geometrical parameter linking the curvature radii and the equivalent diameter. Assuming a spherical grain, $\rho_1 = \rho_2 = \rho$. The curvature radius ρ and the diameter of a sphere D are related such as $\rho = D/2$. Thus, in this case, $k_d = 4$.

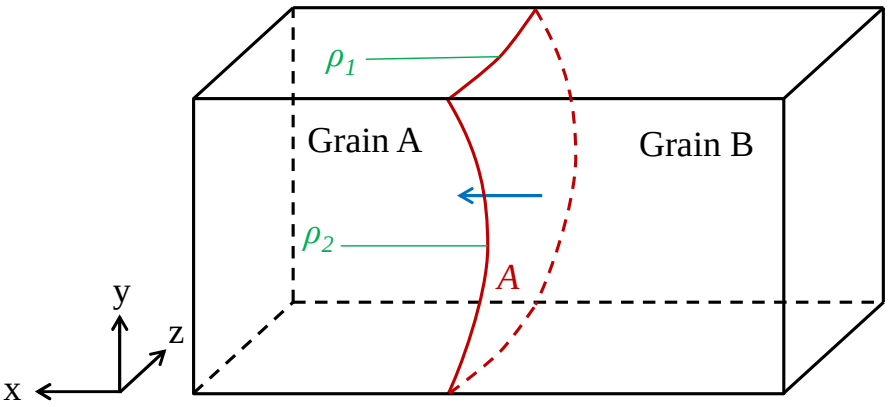

Figure 3.1: *Schematic diagram of a grain boundary of area A and principal radii of curvature ρ_1 and ρ_2 moving in order to reduce interfacial energy.*

The previous equation only describes the migration of the boundary due to the curvature of only one grain, therefore it does not take the interaction between grains into account. In reality, the boundary surface energy could reach equilibrium due to pressure exerted on both sides of that boundary. Abbruzzes & Lucke proposed a model where the grain distribution is taken into account [40, 41]. Under the assumption that a grain size of class *i* is surrounded statistically by grains of class *j*, the net driving force for the growth of grain *i* is given by the differential of driving pressure by considering only grain *i* and grain *j* such as equation (3.7) becomes:

$$P_d = k_d \gamma_g \left(\frac{1}{D_i} - \frac{1}{D_j} \right) \tag{3.8}$$

Large size differences between classes *i* and *j* can then lead to growth or shrinkage of grain *i*. These phenomena will not be considered in the further modelling.

1.2 Grain growth kinetic exponent: grain growth with no retarding pressure

1.2.1 The parabolic growth law

Burke and Turnbull [42] considered that when no retarding pressure is acting on a spherical grain boundary, the following differential equation could be derived by combining equations (3.1) and (3.7):

$$\frac{dD}{dt} = 2Mk_d\frac{\gamma_g}{D} \tag{3.9}$$

After integration, and by considering that the temperature remains constant (thus M being constant):

$$D^2 - D_0^2 = 4Mk_d\gamma_g t \tag{3.10}$$

which can be rewritten as follows:

$$D^2 - D_0^2 = Kt = K_0 \exp\left(-\frac{Q}{RT}\right) t \tag{3.11}$$

where D_0 is the initial grain size ($t = 0$). When D_0 is negligible with respect to D (typically, $D > 3\,D_0$ [43]), the grain size is given by a mean free path equivalent equation. Hence, equation (3.11) can be seen as a diffusion-controlled equation, where K is the diffusion coefficient governing the grain boundary mobility in the material.

This parabolic law can be seen as a specific case of the more general equation phenomenologically deduced by Beck et al. in [44]:

$$D^n - D_0^n = Kt \tag{3.12}$$

where n is a kinetic exponent and K is an effective mobility factor which is proportional to n. While n is supposed to be equal to 2 for grain growth in a pure material, experimental determinations show that its value is usually higher. In the case of heat-affected zones of a 2.25Cr - 1Mo steel, Miranda and Fortes found a kinetic exponent $n = 3.2$ for an activation energy $Q = 180$ kJ.mol^{-1} [45], using a non-isothermal form of equation (3.9).

1.2.2 The signification of the kinetic exponent

Hu and Rath [46] showed that a kinetic exponent n different from 2 implies a non-linear dependence between the boundary velocity and the net pressure, such as:

$$v = M P^m \tag{3.13}$$

where the driving-force exponent m is related to the kinetic exponent n:

$$m = (n - 1) \tag{3.14}$$

Thus, if one considers D_0 as negligible, then equations (3.7), (3.13) and (3.14) can be combined into the following equation [47]:

$$\frac{dD}{dt} = 2M_0(k_d\gamma_g)^{(n-1)} \exp\left(-\frac{Q}{RT}\right)\left(\frac{1}{D}\right)^{(n-1)} \tag{3.15}$$

And equation (3.15) can be formally simplified as:

$$\frac{dD}{dt} = M^*\left(\frac{1}{D}\right)^{(n-1)} \tag{3.16}$$

where M^* is an effective mobility factor, which unit is $m^n.s^{-1}$.

For n = 2, equation (3.13) reduces to equation (3.1), and time integration of equation (3.15) reduces to the parabolic growth law (3.11). When different from 2, the kinetic exponent appears to be a phenomenological parameter, useful to describe the grain growth kinetics rather than a physical parameter. It can be regarded as a gross estimate of the resistance of the grain boundary motion in the presence of defects, precipitates or solute atoms.

1.2.3 Activation energy associated to the effective grain boundary mobility

It is generally assumed that the activation energy for boundary migration is often close to that of grain boundary self-diffusion, which is about half that of the bulk self-diffusion [48]. Thus, in austenite, the activation energy for grain growth is expected to be in the range of 145-170 $kJ.mol^{-1}$. For metallic alloys, empirical activation energies derived experimentally from equation (3.12) are usually higher than the above values, typically, between 250 and 500 $kJ.mol^{-1}$ [49]. This deviation is believed to be due to the diffusion of impurity atoms, or to the fact that the diffusion of atoms happens *across* a *moving* grain boundary, and not necessarily *along* a *static* one.

1.3 Retarding pressures

Retarding pressures can be due either to particles impeding the grain boundary movement (pinning effect) or to the segregation of solute atoms at the grain boundary (solute drag effect).

1.3.1 Pinning effect

General framework

Modelling of the pinning effect, theorized by Zener and published by Smith [50], assumes that particles exert a pressure on the grain boundary and thus counteract the driving pressure for grain growth. If assuming incoherent spherical particles of radius r_p and energy of the particle/matrix interface per unit area γ_p, as shown in Figure 3.2, the pinning force F_z exerted by a single particle on the grain boundary is expressed as the product of the total line of contact between the particle and the boundary and the component of the interfacial energy in the direction opposite to the movement of this boundary (equation (3.17)).

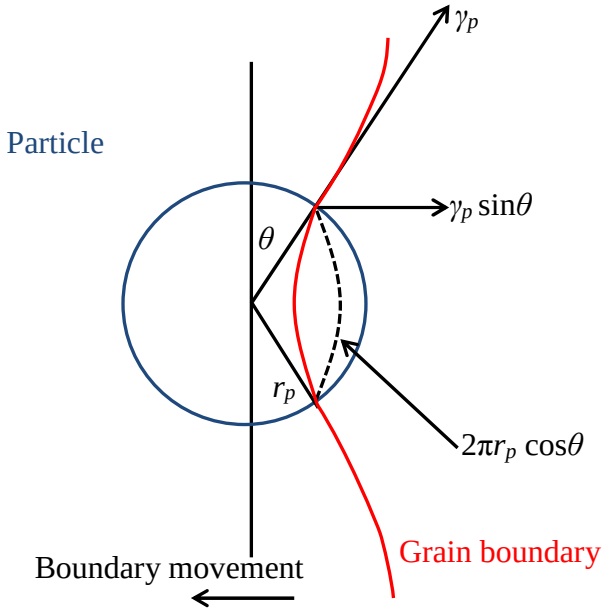

Figure 3.2: *Schematic diagram of the interaction of a spherical particle with a moving grain boundary (from* [51]*).*

$$F_z = 2\pi r_p \gamma_p \sin\theta \cos\theta \tag{3.17}$$

where θ is the angle between the particle and the moving grain boundary as shown in Figure 3.2. The maximal force is obtained for $\theta = 45°$, such as:

$$F_z = \pi r_p \gamma_p \tag{3.18}$$

By assuming that all particles are randomly distributed, then the total number of particles per unit volume (i.e. number density), N_t, is given by the volume fraction of particle f divided by the volume of one particle. For spherical particles with a unique radius r_p, N_t is given by equation (3.19).

$$N_t = \frac{3f}{4\pi r_p^3} \tag{3.19}$$

From this total number density, only particles within a distance r_p of a planar boundary are supposed to interact with the latter, as shown in Figure 3.3. Thus, the number of particles interacting with the grain boundary N_{int} is the product of the number density and twice the particle radius r_p, as given by equation (3.20).

$$N_{int} = N_t \times 2r_p = \frac{3f}{2\pi r_p^2} \tag{3.20}$$

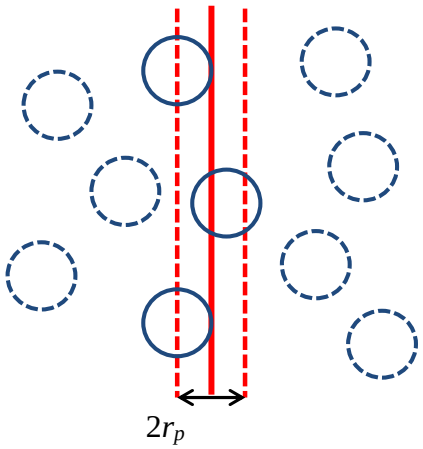

Figure 3.3: *Schematic diagram of the interaction of a planar boundary with immobile particles*

Assuming that all particles exert the maximal Zener force F_z on the boundary, then the pinning pressure P_z is given by multiplying equations (3.18) and (3.20), as reported in equation (3.21):

$$P_z = F_z \times N_{int} = \frac{3\,\gamma_p f}{2r_p} \tag{3.21}$$

The general expression for P_z is given by equation (3.22), where k_r is a constant called the pinning parameter, which is a function of the coherency of the particle with the matrix and its shape, but also from the physical interaction mechanisms between the particle and the matrix, as well as the interaction geometry between the particle and the matrix in the case of non-spherical particle. In the case of non-spherical particle, the particle size is given by the equivalent radius regarding the volume $r_{p,eq}$.

$$P_z = k_r \frac{\gamma_p f}{r_{p,eq}} \tag{3.22}$$

From equation (3.22), it appears clearly that the Zener pressure is higher when particles are smaller and in higher number density.

Pinning parameter: influence of the shape and of the coherency of the particle with respect to the matrix

For the previous example of incoherent spherical particles, $k_r = 3/2$ as seen above. For coherent spherical particles, Ashby et al found that the maximal Zener force F_z is twice larger than for incoherent particles, therefore $k_r = 3$ [52].

Ringer et al [53] determined parameter k_r for cubic particles, regarding their orientation relative to the grain boundary and the particle coherency with the matrix grains. It should be pointed out that for cubic particles, equation (3.22) is obviously written as a function of the cube side a_p. However, in order to compare the pinning parameter corresponding to a cubic particle and a spherical particle, k_r was calculated using the equivalent radius regarding the volume, i.e:

$$r_{p,eq} = \sqrt[3]{\frac{3}{4\pi}}\, a_p \tag{3.23}$$

As shown in Figure 3.4, the orientation of the particle with respect to the grain boundary only depends on two angles, ω and φ, which are respectively the rotation around the x-axis and the y-axis, assuming that the grain boundary is in the x-y plane. Rotation around the z-axis does not affect the orientation of the particle with respect to the boundary plane.

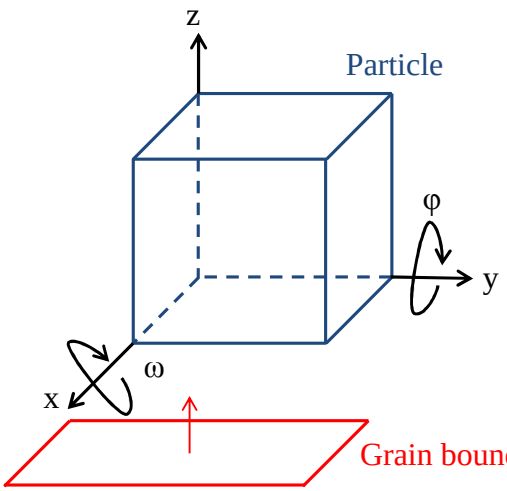

Figure 3.4: *Schematic diagram of a cubic particle. The orientation relative to the grain boundary is described by angles ω and φ*

The coherency of the particle is assumed as follows: Let us consider a migrating grain boundary interacting with a coherent cubic particle, as shown in Figure 3.5. Assume that the migrating boundary wraps around the particle such as the coherency with grain 1 (growing grain) may be lost, while coherency is maintained with grain 2. Tension forces due to interfacial energies of the grain boundary close to the particle γ_p, and particle/matrix interfacial energies regarding grains 1 and 2 (respectively γ_1 and γ_2) should remain in equilibrium. Thus, the contact angle between the particle and the grains, β, depends on the balance between these tension forces, as given in equation (3.24). If $\gamma_1 = \gamma_2$, $\beta = 90°$ and coherency is lost. If $\beta = 0°$, the particle is coherent with both grains.

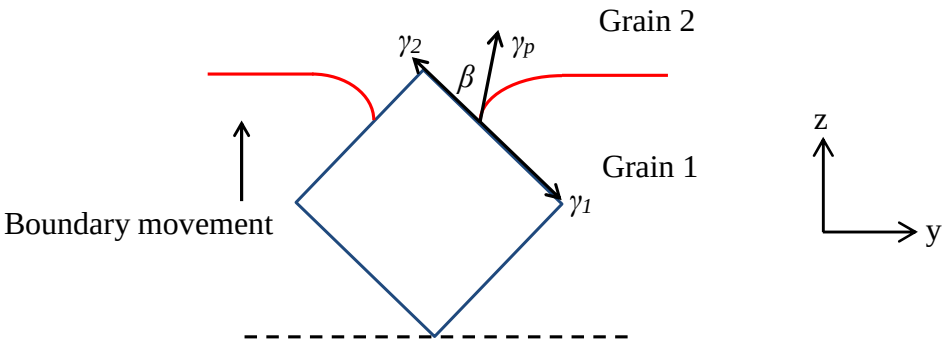

Figure 3.5: *Geometry of surface energy interactions between a migrating grain boundary and a cubic precipitate*

$$\cos\beta = \frac{\gamma_1 - \gamma_2}{\gamma_p} \tag{3.24}$$

Effect of the orientation: Assuming that $\gamma_1 = \gamma_2 > 0$ ($\beta = 90°$) and maximum Zener force, the pinning parameter as a function of ω and φ may be analytically derived, according to equations (3.25) to (3.29). It should be noted that a symmetry exists for φ = 90° and ω = 45°, therefore it is only necessary to consider cases in which φ ≤ 90° and ω ≤ 45°. The value of k_r as a function of φ for various values of ω is given in Figure 3.6, along with that in case of a spherical particle.

ω = 0°, φ= 0° or φ= 90°
$$k_r = \sqrt[3]{\frac{3}{4\pi}} \times 2\sqrt{2}[(\cos\omega + \sin\omega)\cos\varphi + \sin\varphi] \tag{3.25}$$

ω = 0°, 0 < φ < 90°
$$k_r = \sqrt[3]{\frac{3}{4\pi}} (\cos\varphi + \sin\varphi)[(\cos\omega + \sin\omega)\cos\varphi + \sin\varphi] \tag{3.26}$$

$0 < \omega \leq 45°$
$0 \leq \varphi < \arctan(\sin(\omega))$
$$k_r = \sqrt[3]{\frac{3}{4\pi}} \times \boldsymbol{B} \times [(\cos\omega + \sin\omega)\cos\varphi + \sin\varphi] \tag{3.27}$$

$0 < \omega \leq 45°$
$\arctan(\sin(\omega)) \leq \varphi < 90°$
$$k_r = \sqrt[3]{\frac{3}{4\pi}} \times \boldsymbol{B}\frac{\sin\omega}{\tan\varphi} \times [(\cos\omega + \sin\omega)\cos\varphi + \sin\varphi] \tag{3.28}$$

where *B* is given by equation (3.29).

$$\boldsymbol{B} = \tan\omega\sqrt{(1 - \cos^2\varphi\sin^2\omega)} + \cot\omega\sqrt{(1 - \cos^2\varphi\cos^2\omega)} + \frac{\tan\varphi\sin\varphi}{\sin\omega\cos\omega} \tag{3.29}$$

For each angle ω there is a corresponding φ resulting in a maximal pinning parameter. For ω = 0, the maximum is obtained at φ = 0° (see discontinuity in Figure 3.6), i.e. when the cube face is parallel the boundary. For ω = 45°, the maximum is obtained for φ = 35.3°, i.e. when the cube is standing with its longest diagonal perpendicular to the boundary. Thus, the pinning parameter can vary from 0.7 to 2.6 regarding the particle orientation.

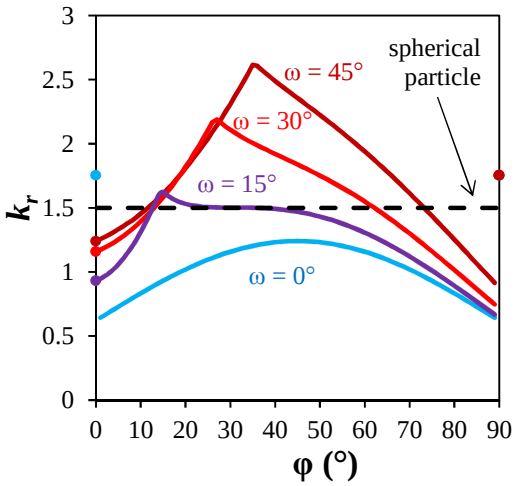

Figure 3.6: *Evolution of the pinning parameter k_r as a function of the relative orientation of a cubic particle with the grain boundary plane. The spherical case is also represented.*

Effect of the coherency: Figure 3.7 shows different possible orientations between the particle and the grain boundary, along with the case of a spherical particle. Case (d) represents a cube standing with its longest diagonal perpendicular to the boundary. Assuming maximum Zener force, the pinning parameter k_r for these four cases as a function of the contact angle β is given by calculating the derivatives of k_r with respect to ω and φ. These results are shown in equation (3.30) to equation (3.34). More details on these calculations can be found in reference [53].

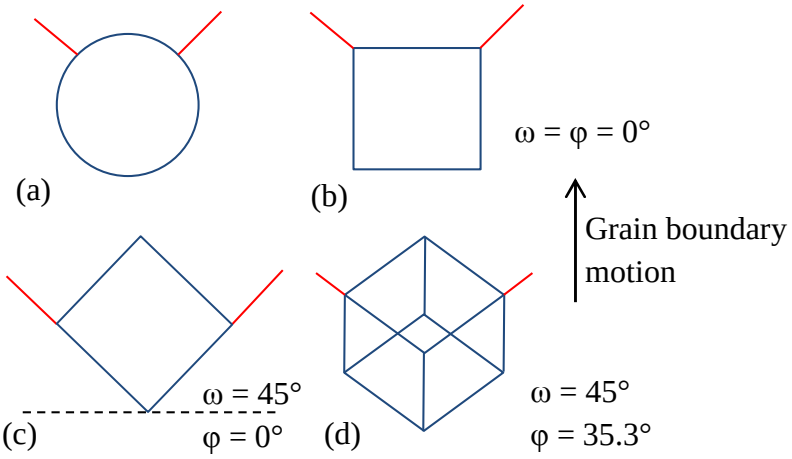

Figure 3.7: *Schematic diagram of several orientations between cubic particles and the grain boundary, as well as a spherical particle.*

Values of pinning parameter k_r for all four cases as a function of the degree of coherency are shown in Figure 3.8. One should notice that for the spherical particle, k_r is respectively equal to 3/2 and to 3 for incoherent and coherent particles, as already stated. For a cubic particle, depending on its orientation, the pinning parameter ranges from 1.5 to 4.5.

case (a) $$k_r = \frac{3\cos\beta}{2} \tag{3.30}$$

case (b) $$k_r = 2 \times \sqrt[3]{\frac{3}{4\pi}} \times \left(\cos\beta + \sqrt{2 - \cos^2\beta}\right) \tag{3.31}$$

case (c) $$k_r = \sqrt[3]{\frac{3}{4\pi}} \times 1.41 \times \left[1.41 \times (\cos\beta + \sin\beta) + \frac{2\cos\beta}{0.7}\right] \tag{3.32}$$

case (d) $$k_r = \sqrt[3]{\frac{3}{4\pi}} \left(6\cos\beta + \sqrt{18}\sin\beta\right) \tag{3.33}$$

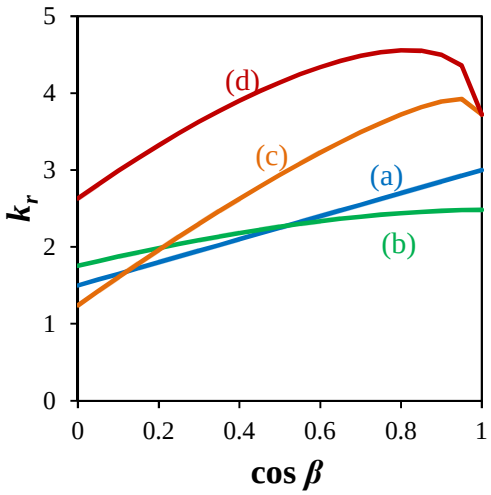

Figure 3.8: *Influence of the coherency on the pinning parameter k_r as a function of the degree of coherency for several particle orientations as shown in Figure 3.7. Degree of coherency increases from left to right.*

Thus, both particle orientations and relative coherency with shrinking and growing grains have a critical impact on the pinning parameter, and should be taken into account for further calculations. It should be pointed out that these cases are only an example of the large variety of values that can be taken for this parameter, which have been extensively summarized by Manohar et al. [51].

1.3.2 Solute drag

Solute element atoms can segregate from the bulk lattice to the grain boundary where they can be better accommodated. This yields to a molar concentration profile $C(z)$ of these atoms, were z is the distance to the boundary, that is a function of the solute element diffusion coefficient profile $X(z)$ and of the binding energy profile $E(z)$ between the solute atom and the boundary. In the case of a moving boundary, solute atoms may be dragged along and the grain boundary migration rate can be limited by the diffusivity of these dragged solute atoms. Therefore, $C(z)$ and the grain boundary velocity, v, become interrelated. In practical cases, this solute drag effect can decrease the grain growth kinetics by several orders of magnitude [54]. Concerning modelling of this effect, the following considerations are based on the papers by Lücke and Detert [55], Hillert [56, 57] and Cahn [58].

Assuming that the temperature remains constant, that the boundary moves with a steady state velocity and that the considered system is a dilute solution of solute atoms, the composition profile $C(z)$ is expected to reach a steady-state form obeying the following equation [58], where k_B in the Boltzmann constant:

$$X(z)\frac{\partial^2 C(z)}{\partial z^2} + \left[\frac{\partial X(z)}{\partial z} + \frac{X}{k_B T}\frac{\partial E(z)}{\partial z} + v\right]\frac{\partial C(z)}{\partial z} + \frac{C(z)}{kT}\left[\frac{\partial X(z)}{\partial z}\frac{\partial E(z)}{\partial z} + X\frac{\partial^2 E(z)}{\partial z^2}\right] = 0 \tag{3.34}$$

A solute atom exerts a force –(dE(z)/dz) on the boundary, and the total pressure P_{drag} exerted by all solute atoms is therefore:

$$P_{drag} = -N_v \int_{-\infty}^{+\infty} \left[C(z) - C_0\right]\frac{\partial E(z)}{\partial z}\, dz \tag{3.35}$$

where N_v is the number of atoms per unit volume, given as $N_v = 4/a^3$, where a is the lattice parameter assuming a fcc crystal structure, and C_0 is the bulk concentration of solute atoms. One should notice that the pressure P_{drag} exerted by the solute atoms is dependent on the composition profile, thus on the grain boundary velocity. This dependency is schematically shown in Figure 3.9.

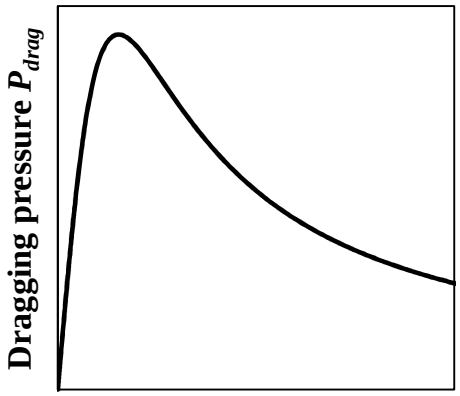

Figure 3.9: *Schematic relationship between the dragging pressure P_{drag} and the grain boundary velocity v for a given energy and diffusivity profile E(z) and X(z).*

For low values of v, the dragging pressure increases proportionally with the velocity, due to the increasing concentration of solute atoms at the boundary, and reaches a maximal pressure for a critical velocity. For higher velocities, solute atoms find it more and more difficult to keep pace with the migrating boundary, resulting in their desorption from the grain boundary. The dragging pressure thus starts to decrease and then finally vanishes when no more solute atoms are segregating at the moving grain boundary.

Equation (3.35) can be approximated as equation (3.36), which mathematical resolution is easier, as proposed by Cahn:

$$P_{drag} = \frac{C_0 \, \alpha \, v}{1 + \beta^2 v^2} \tag{3.36}$$

where α and β are given by equations (3.37) and (3.38):

$$\alpha = 4 N_v k T \int_{-\infty}^{+\infty} \frac{\sinh^2 \left(E(z) / 2 k_B T \right)}{X(z)} dz \tag{3.37}$$

$$\beta^2 = \frac{\alpha k T}{N_v} \left[\int_{-\infty}^{+\infty} \left(\frac{dE(z)}{dz} \right)^2 X(z) \, dz \right]^{-1} \tag{3.38}$$

Assuming a triangular profile for $E(z)$ and that X is constant across a grain boundary of thickness δ, as shown in Figure 3.10, equations (3.37) and (3.38) can be written as equations (3.39)[1] and (3.40), respectively:

$$\alpha = \frac{N_v (kT)^2 \delta}{E_0 X} \left(\sinh \left(\frac{E_0}{kT} \right) - \frac{E_0}{kT} \right) \tag{3.39}$$

$$\beta^2 = \frac{\alpha k T \delta}{2 N_v E_0^2 X} \tag{3.40}$$

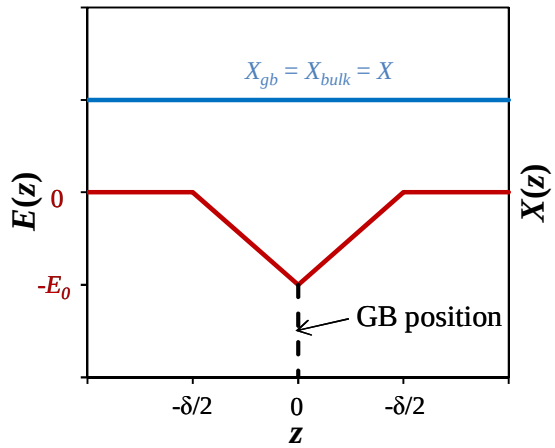

***Figure 3.10**: Diffusivity profile and binding energy profiles across a grain boundary as a function of the distance to the grain boundary z. At the grain boundary, the solute diffusivity and binding energy are increased, δ being the grain boundary thickness and E_0 the binding energy between a solute atom and the boundary.*

[1] In the original article, Cahn wrote equation (3.39) as $\alpha = \frac{N_v (kT)^2}{E_0 X} \left(\sinh \left(\frac{E_0}{kT} \right) - \frac{E_0}{kT} \right)$. However, such equation is not dimensionally homogeneous with equation (3.36). Therefore, this equation has been multiplied by the grain boundary thickness δ in order to obtain the right dimension for α. Similar correction has already been made by Fu et al [132].

In order to represent the effect of E_0 and X on the dragging pressure for the considered profile, let us assume that C_0 = 0.1 at%, a = 0.36 nm, δ = 0.5 nm and T = 1000°C. Figure 3.11 shows the dragging pressure as a function of the grain boundary velocity when varying the binding energy E_0 and the diffusion coefficient X.

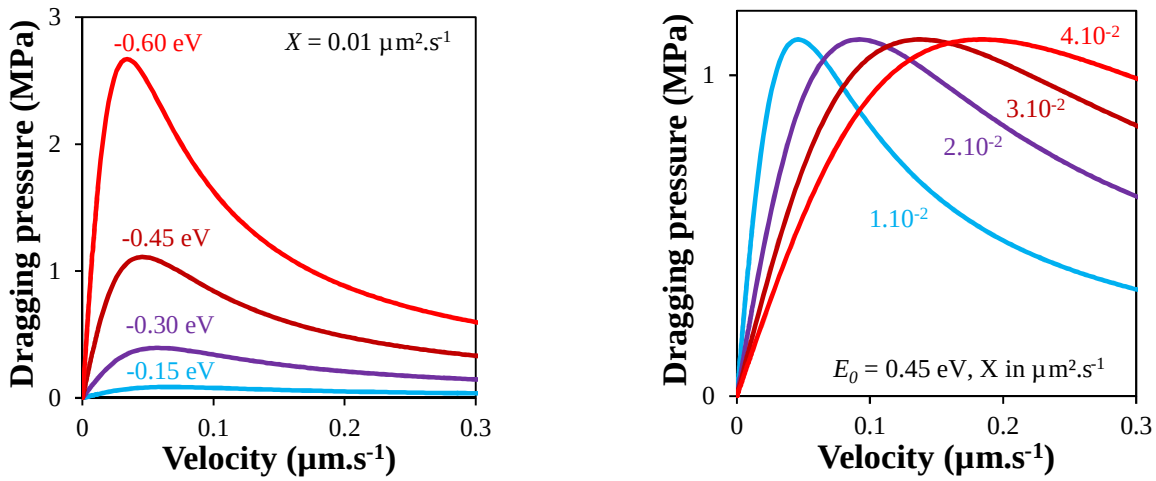

Figure 3.11: *Effect of the binding energy E_0 and of the diffusion coefficient X on the dragging pressure as a function of the grain boundary velocity.*

Increase in the binding energy leads to an increase in the maximal dragging pressure, while increasing the solute diffusivity shifts the critical velocity towards higher values. In other words, solute atoms induces more dragging when they are well accommodated in the boundary, and the boundary needs to move faster to break free from solute atoms when their diffusivity in the grain lattice close to this grain boundary is higher.

All these models will be used at the end of this chapter in order to discuss the austenite grain size as a function of the austenitization time and temperature as experimentally determined. Determination of the kinetic exponent n is used for a simple, phenomenological description of grain growth, while the driving pressure, the pinning pressure and the solute pressure are used to understand the mechanisms responsible for grain growth.

2. EXPERIMENTAL INVESTIGATIONS

2.1 Experimental approach

Prior austenite grains (PAGs) were measured for austenitization temperatures ranging from 920°C to 1120°C and for durations up to 2 hours. The lower temperatures correspond to acceptable industrial austenitization temperatures (below 1000°C); higher temperatures were also selected in order to fully investigate the thermal dependence of grain growth (for instance, the influence of temperature on the mobility M). The maximal duration, 2 hours, corresponds to the austenitization duration at the mid-thickness of a targeted thick component as stated in Chapter II. The heating rate

was set to 1°C/s, and the assumption was made that no grain growth occured upon heating. As already stated, the Ac_3 temperature for this heating rate is 880°C, therefore upon heating the material is fully austenitic for 40 seconds at 920°C and 240 seconds (4 minutes) at 1120°C before the beginning of the holding stage. While these durations are significant regarding the grain growth after soaking for 1 second and, in the latter case, for 5 minutes after, it can be considered as negligible for durations longer than 15 minutes. Thus, the grain size after 1 second of isothermal holding will be considered as the initial grain size.

PAG boundaries were revealed by ferrite decoration, as explained in Appendix A. An example of the microstructure obtained after heat treatment, polishing and etching is given in Figure 3.12. The prior austenite grain size (PAGS) was then determined using the Visilog software. Each grain was measured individually and then the average PAGS was calculated. The evolution of the PAGS with holding time at various austenitization temperatures is shown in Figure 3.13. The uncertainty associated with measurements was estimated around 5 µm, due to the size of ferrite nodules.

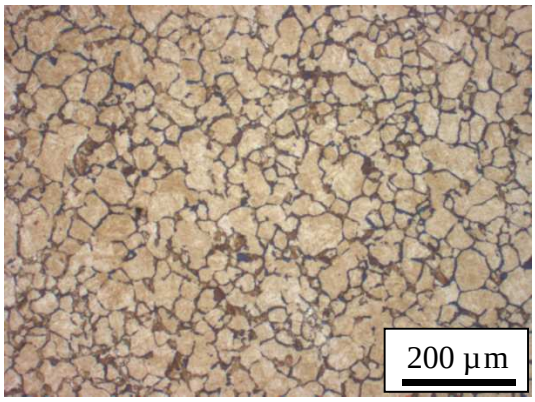

Figure 3.12: *Prior austenite grains revealed by ferrite decoration. Dark brown regions are small ferritic nodules while light brown areas are martensite. Austenitization conditions are 1020°C for 1 hour.*

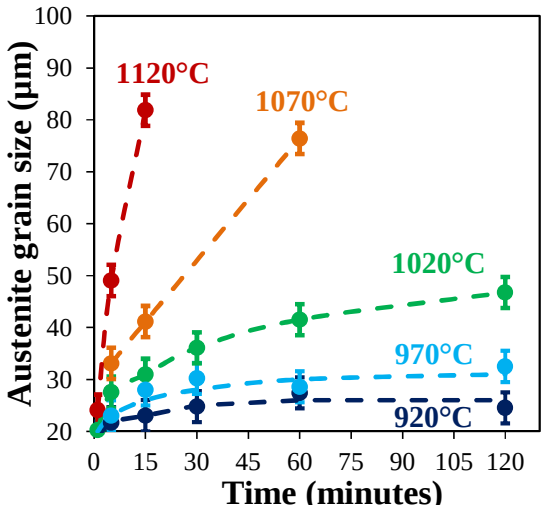

Figure 3.13: *Evolution of austenite grain size with holding time at different holding temperatures*

Before commenting the growth behavior, the physical significance of the average PAGS has to be discussed, with respect to the size distribution of austenite grains.

2.2 Grain size homogeneity

Characterization of the grain size homogeneity was made through the study of the grain size distributions. Typically, when no abnormal growth occurs, grain size distribution (GSDs) can be approximated by a unimodal log-normal distribution. Fitted log-normal distributions were calculated for every austenitization condition; an example for a 15 minute-austenitization is shown in Figure 3.14. Good agreement is found between these log-normal distributions and experimental distributions for every austenitization condition.

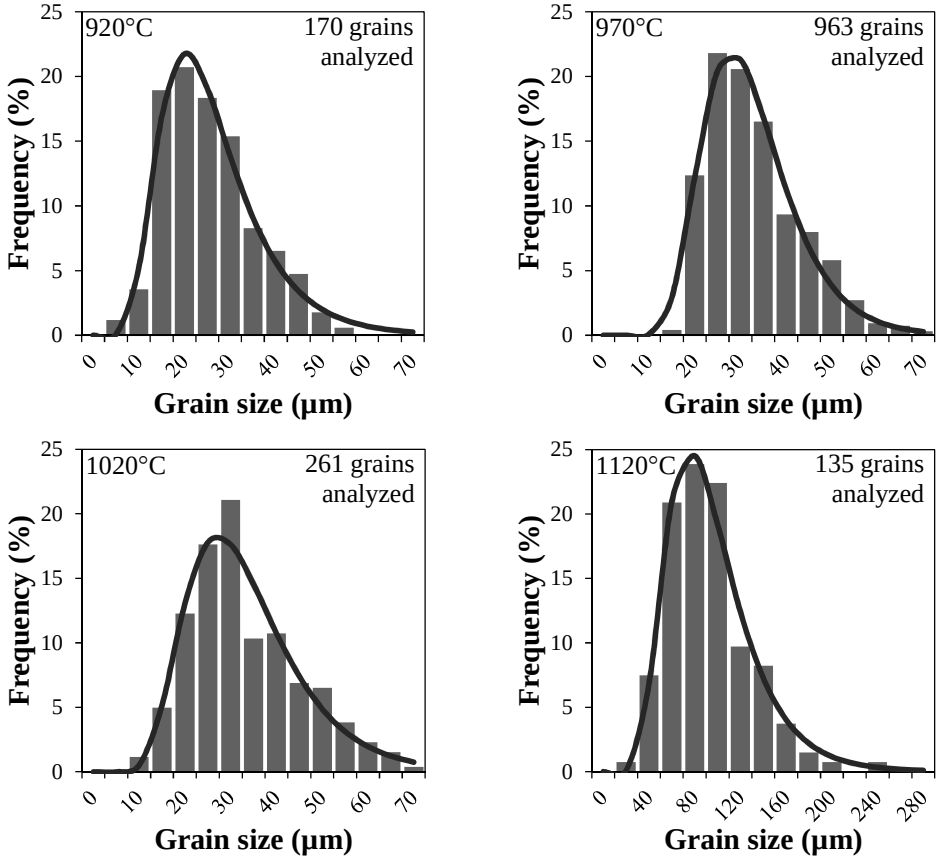

Figure 3.14: *Austenite grain size distributions after 15 minutes austenitization at 920°C, 970°C, 1020°C and 1120°C.*

Two important parameters can be extracted from these fitted log-normal distributions: the expected value, which is the probability weighted average, and the standard deviation, which indicates the broadness of the distribution. The evolution of these two parameters with austenitization holding time and temperature is shown in Figure 3.15.

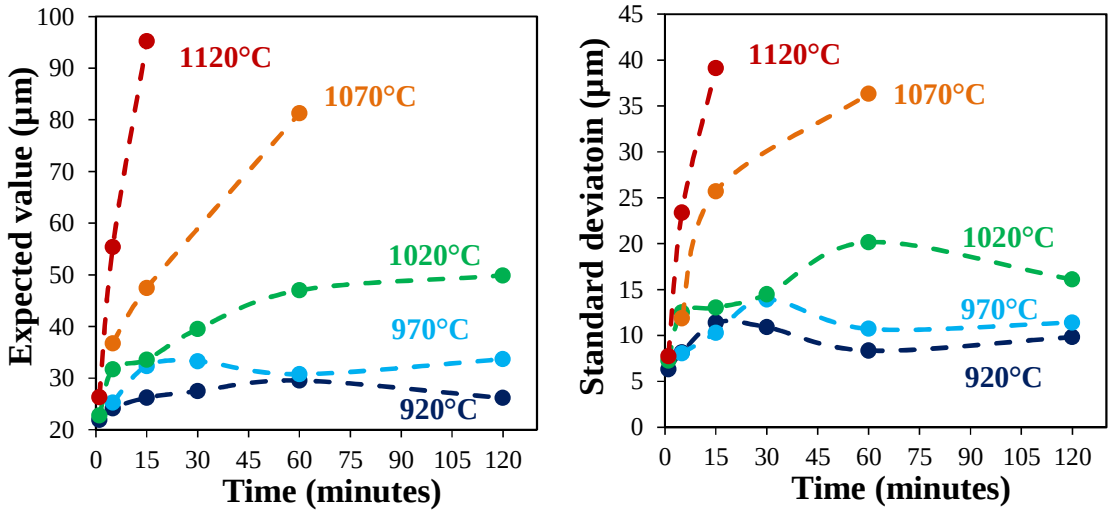

(a) (b)

Figure 3.15: *Evolution of (a) expected value and (b) standard deviation with austenitization time and temperature*

At temperatures equal to or lower than 1020°C, the expected value evolves in the same way as the average PAGS, and their value are similar when taking the standard deviations into account. The standard deviation reaches a maximum for a given holding time, then starts to decrease; this maximum being delayed towards longer durations when increasing the temperature. At higher temperatures (equal to or higher than 1070°C), the expected values remain similar to the average PAGS, and the standard deviation increases strongly with time.

Hence, high temperatures have a strong impact on the PAGS homogeneity: for example, grains as large as three times the average diameter appear at 1120°C after 15 minutes, while the largest observed grain for the same time at 920°C is only twice as large.

Since expected values are slightly higher than the average PAGS and since the variance is very high at higher temperatures, unimodal representation might not be the most adapted mean to describe GSD. Abnormal growth is susceptible to take place at high temperature, and scattered unimodal distribution could mask bimodal distributions.

In order to better visualize this phenomenon, the distribution of the grain diameter as log-normalized by the average grain diameter has been plotted. Normal distributions, well-centered around the average diameter satisfactory describe the data, which are typical of unimodal distribution [59]. As an example, Figure 3.16 shows four different austenitization for 15 minutes at 920°C, 970°C, 1020°C and 1120°C, which logarithmic representations are centered respectively at 0.03, 0.02, 0.01 and 0.03.

Thus, no abnormal grain growth can be significantly evidenced even at higher temperatures. Since normal grain growth takes place at every tested temperature, the austenite grain size distribution can be characterized in a representative way by using the average PAGS.

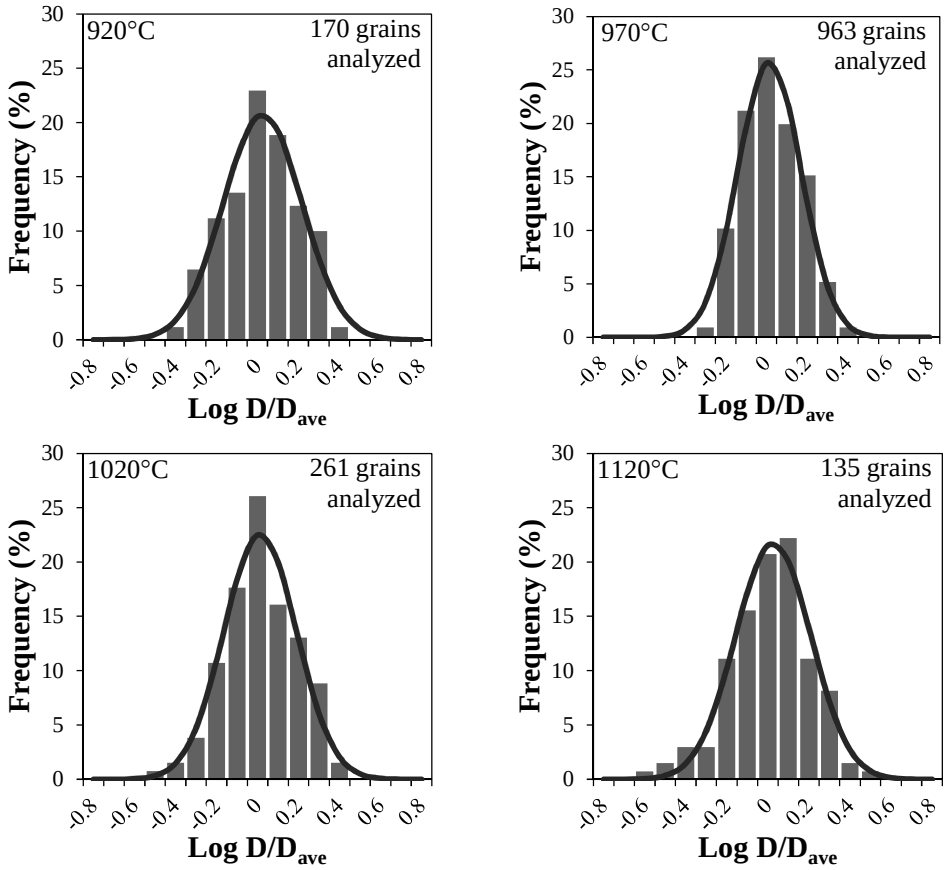

Figure 3.16: *Logarithmic representation of the normalized grain size distribution after 15 minutes austenitization at 920°C, 970°C, 1020°C and 1120°C.*

2.3 Analysis of the phenomenological kinetic exponent

A rapid method to qualitatively analyze the growth kinetics is to determine the kinetic exponent n in equation (3.12). Figure 3.17 shows the evolution of the correlation coefficient between the predictions from equation (3.12) and experimental measurements for various values of $1/n$. When the correlation coefficient is close to 1, good agreement is found between model predictions and experimental measurements. Optimal kinetic exponents for each temperature are gathered in Table 3.1. As a result, the kinetic exponent increases with decreasing temperature, thus growth becomes slower. Analysis of the kinetic exponents shows that two different growth modes occur according to the holding temperature.

At low temperatures, i.e. equal to or lower than 1020°C, grain growth kinetics decreases with decreasing temperature. At 920°C, almost no growth occurs. At high temperatures, i.e. equal to or higher than 1070°C, the kinetic exponent $n = 2$; the growth law is parabolic, as stated in section 1.2.1. However, the maximal studied austenitization time at these temperatures is 1 hour, and limited growth is still susceptible to appear for longer austenitization durations. The above results suggest the existence of a temperature dependent phenomenon which is responsible for limited growth and becomes less efficient with increasing temperature.

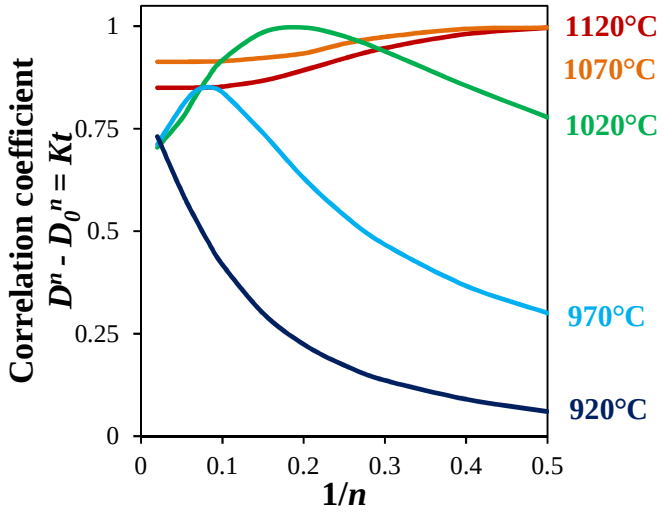

Figure 3.17: *Evolution of the correlation coefficient for equation (3.12) for various values of n.*

	920°C	970°C	1020°C	1070°C	1120°C
n	19	11	5	2	2

Table 3.1: *Values of the optimal kinetic parameter n for each temperature (rounded to the nearest unit).*

As a conclusion, since no abnormal growth occurs, the average grain size is considered to be representative of the material. Thus, equations presented in section 1 can be used in order to understand the limited growth phenomenon evidenced in this section and its apparent relation with temperature.

3. MODELLING LIMITED GROWTH MECHANISMS

In this study, two physical phenomena potentially leading to limited growth are investigated: Zener pinning and solute drag. Both phenomena are reasonable in view of the temperature dependency of grain growth kinetics: assuming that limited growth is due to Zener pinning, this dependency would be due to the dissolution of pinning particles at higher temperatures. In the case of solute drag, variation of the binding energy with temperature could be the source of variation. In this section, these two potential retarding pressures are investigated by using the formalism reported in section 1 and calibrating parameters to represent experimental data.

3.1 Driving pressure versus Zener pinning

3.1.1 Modelling approach

Assuming that limited growth is only due to the Zener pinning as a source for retarding pressure, grain growth can be expressed as equation (3.43) by combining equations (3.1), (3.7) and (3.22).

$$v = M\left(k_d \frac{\gamma_g}{D} - k_r \frac{\gamma_p f}{r_p}\right) \tag{3.41}$$

In such case, grain growth is stopped (v = 0) when $P_d = P_z$, thus the maximal grain diameter D_c can be expressed as:

$$D_c = \frac{k_d}{k_r}\frac{\gamma_g}{\gamma_p}\frac{r_p}{f} \tag{3.42}$$

At 920°C and 970°C, this maximal grain diameter as experimentally determined is 25 µm and 30 µm, respectively. The maximal grain size at higher temperatures, if existing, has not been experimentally determined. The following calculations lead to investigate the potential limiting effect of the Zener pinning in the studied material, regarding the experimental measurements.

3.1.2 Determination of the driving pressure

Driving pressure parameters are the geometrical constant k_d and the grain boundary energy γ_g. Assuming spherical grains, k_d = 4 as already stated.

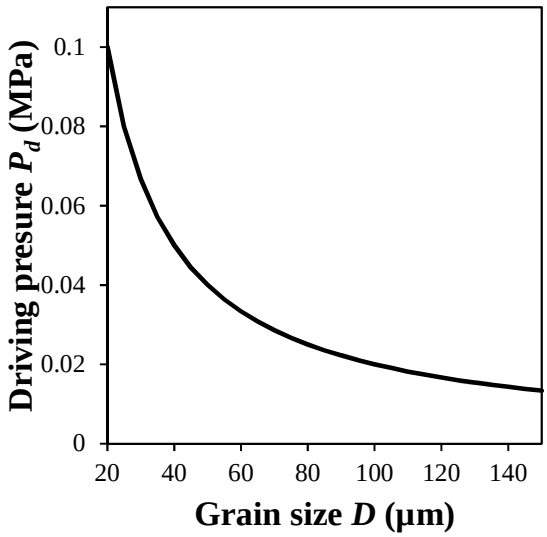

Figure 3.18: *Evolution of the driving pressure P_d as a function of the grain diameter D for γ_g = 0.5 J.m^{-2} and k_d = 4.*

Let us assume that the grain boundary interfacial energy, γ_g, is not temperature-dependent in the considered temperature range. Gjostein et al. determined that the grain boundary energy in plain steels decreases with increasing the bulk carbon content because of increasing carbon grain-boundary segregation. It results in the following empirical relationship between the grain boundary energy and the carbon content C in this steel (in wt%) [60]:

$$\gamma_g = (0.8 - 0.35\, C^{0.68}) \tag{3.43}$$

For the studied 0.15 wt% carbon steel, the grain boundary energy γ_g = 0.7 J.m^{-2}. Shahandeh & Militzer determined γ_g = 0.69 J.m^{-2} using 2D phase field simulations, which is in good agreement with the previous result [61]. A lower value, γ_g = 0.5 J.m^{-2}, has been suggested by Humphreys [48] and used successfully in various calculations [62–64]. The choice was made to use the latter value: γ_g = 0.5 J.m^{-2}.

Figure 3.18 shows the evolution of the driving pressure as a function of the grain diameter for γ_g = 0.5 J.m^{-2}. For a grain size of 20 µm, which corresponds to the experimental initial grain diameter D_0, the driving pressure is 0.10 MPa and decreases down to 0.02 MPa for a grain size of 100 µm.

3.1.3 Estimate of the Zener pinning effect

According to the considerations exposed in section 1.3.1 leading to equation (3.21), particles must be fine and numerous to induce a significant pinning effect. In the case of austenite grain growth, they also have to be stable in the austenitic domain, which is above 830°C for the studied material for the considered heating rate. Typically, pinning particles in steels are nitrides such as AlN or TiN or carbonitrides such as Nb(N,C) or V(N,C). Impacts of AlN and Nb(N,C) particles on austenite grain growth in 2.25Cr – 1Mo steel were respectively outlined by Swift [38] and Nieuwland et al. [65]. Some authors also suggested that residual alloy carbides [10] or impurity particles, such as MnS [66], could act as pinning particles. However, as seen in Chapter II (section 2.1), the low amount of residual carbides after the austenitic transformation and the large size of MnS particle make them unlikely to contribute to any potential pinning effect. Therefore, potential pinning effect in the studied steel could only be induced by AlN precipitates.

The volume fraction f, the average radius r_p and the particle energy γ_p of AlN precipitate were calculated by using the precipitation kinetics module of MatCalc. More detailed information on the MatCalc precipitation kinetics model can be found in Appendix B. The following thermal cycles were used for the numerical simulations:

(i) Cooling from 1200°C down to 20°C. This step simulates cooling after forging. The cooling rate proved to have no impact on both phase fraction and diameter of AlN precipitates, thus it was set up to 1°C/s in order to limit the calculation time.

(ii) Heating at 1°C/s from 20°C up to T_{aust}.

(iii) Isothermal step at T_{aust} for 100 hours. This very long time allows reaching the equilibrium regarding the volume fraction and the average radius of precipitates at austenitization temperature T_{aust}.

Matrix phase transformations cannot be taken into account in the software, thus the precipitation matrix domain is shifted from austenite to ferrite upon cooling and from ferrite to austenite upon heating, both at 800°C. AlN nucleation sites were set at grain boundaries and dislocations for both austenite and ferrite matrix. Austenite grain size during the first cooling, ferrite grain size and austenite grain size during the isothermal step were set up to 200 µm, 20 µm and 20 µm respectively. Dislocations densities in austenite and ferrite were assumed to be in the range of 10^{11} m^{-2} and 10^{12} m^{-2}, respectively. Results showed that a large majority of AlN, more than 95%, nucleated at the dislocations within the ferritic grains. Therefore, the following considerations are made when considering only this type of precipitate.

Figure 3.19 shows the resulting evolution of the volume fraction f and the particle radius r_p of AlN particles at 920°C, 970°C and 1020°C, respectively. As expected from the thermodynamic calculations performed in Chapter II, AlN precipitates are only stable at temperatures lower than 930°C. Thus, when soaking at 920°C, the volume fraction and the radius of AlN particles decrease over time before reaching an equilibrium value after 360 minutes (6 hours) of 7.10^{-5}% and 10 nm, respectively. At 970°C and 1020°C, the phase fraction and the radius decrease with time, until no more AlN is found. The dissolution times are predicted to be 75 minutes and 7 minutes at 970°C and 1020°C, respectively. At even higher temperatures, namely 1070°C and 1120°C, AlN particles are dissolving during the first seconds of austenitization, and are thus not represented in Figure 3.19. The interfacial energy γ_p is not time-dependent, however it slightly changes with temperature, from 0.47 J.m^{-2} to 0.49 J.m^{-2} at 920°C and 1020°C, respectively.

From these results alone, it appears clearly that the limited growth at 970°C and the slow growth at 1020°C cannot be induced by Zener pinning, since AlN particles dissolve during soaking at these temperatures. In particular, no change in grain growth kinetics can be associated to the end of dissolution of AlN at 970°C.

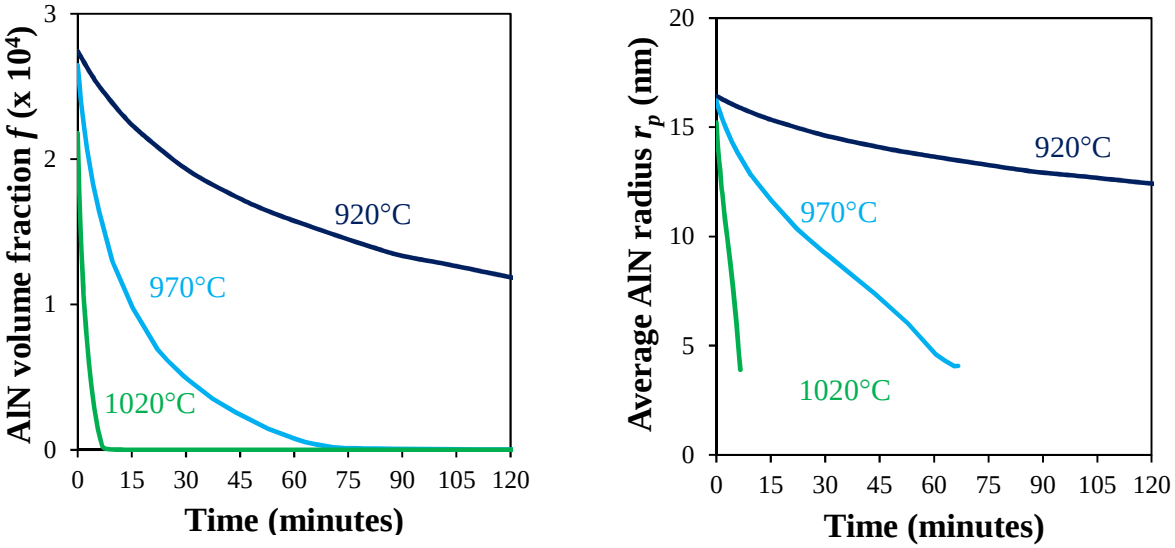

Figure 3.19: *Evolution with time and temperature of the volume fraction f and the particle radius r_p of AlN particles as predicted by calculations.*

3.1.4 Results and discussions

AlN particles are assumed to be cuboid shaped [67], therefore parameter k_r can range from 0.5 to 4.5 depending on their orientations with respect to the grain boundary and their coherency with both the shrinking and the growing grains, as reported in section 1.2.1. Figure 3.20 shows the evolution of the Zener pressure for these two limiting value of the pinning parameter, with holding time at 920°C, 970°C and 1020°C.

As expected from Figure 3.19, the pressure decreases with increasing holding temperature and time. At 970°C and 1020°C, no more Zener pressure due to AlN is effective after 7 minutes and 75 minutes, respectively, due to dissolution of AlN particles. One should notice that even with the highest possible value of the pinning parameter, the Zener pressure at 920°C ranges from 0.035 MPa

to 0.02 MPa at t = 0 and t = 120 minutes, respectively. As seen in Figure 3.18, the driving pressure corresponding to the maximal grain diameter at 920°C, i.e. 25 µm, is 0.08 MPa, twice as high as the maximal possible Zener pressure. Thus, limited growth at this temperature is not induced by a Zener pinning effect.

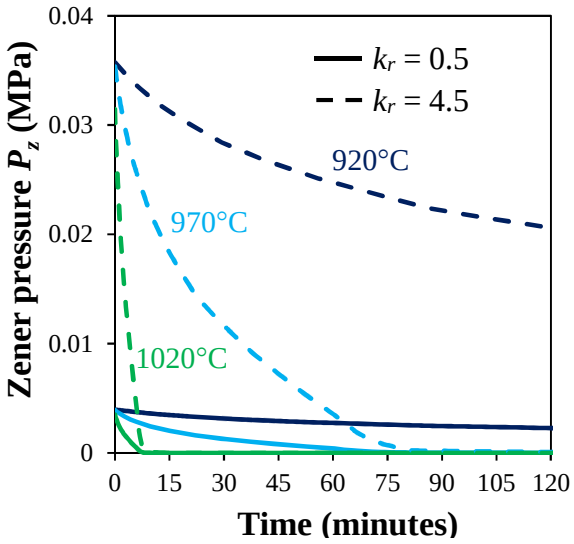

Figure 3.20: *Evolution with time of the Zener pressure for the two extreme values of the pinning parameter k_r at 920°C, 970°C and 1020°C.*

To further illustrate this result, it is interesting to apply equation (3.42) at this temperature using the equilibrium values of f and r_p at 920°C. For pinning parameters ranging from 0.5 to 4.5, the maximal grain size ranges from 140 µm to 1.2 mm.

As a conclusion, Zener pinning is not responsible alone for the limited austenite grain growth observed at 920°C and 970°C. However, at 920°C, this contribution is not negligible and must be taken into account for further modelling of grain growth. In the next section, the effect of solute drag is now taken into account in order to investigate its contribution to the grain growth kinetics.

3.2 Modelling solute drag during austenite grain growth

3.2.1 Selection of values of diffusivity X and binding energy E_0

Molybdenum is commonly seen as an element that can induce solute drag [68] due to its large atomic mismatch with the austenite matrix, and is known for segregating at austenite grain boundaries [69–71]. In 2.25 Cr – 1 Mo steels, an average concentration of 2 at% Mo was measured at the prior austenite grain boundaries after austenitization at 1150°C for 2 hours followed by water quench [22]. While the authors suppose that a large amount of this segregation occurred upon quenching, at least some of this molybdenum may have segregated during austenitization.

The diffusion coefficient of molybdenum in austenite and the binding energy of molybdenum with the austenite grain boundary have to be determined in order to determine α and β from

equations (3.37) and (3.38). The diffusion coefficient for molybdenum in austenite in $cm^2.s^{-1}$ is given by Ham as [72]:

$$X_{Mo/\gamma} = 0.482 \exp\left(-\frac{269833}{RT}\right) \tag{3.44}$$

where T is in Kelvin and R is the gas constant. Reported values for the binding energy are summarized in Table 3.2 and can range from 0.01 eV to 1 eV. However, Enomoto et al [73] showed that segregation of molybdenum atoms at austenite grain boundaries was enhanced by the presence of carbon, as shown in Figure 3.21. Thus, in the following study the binding energy of molybdenum should account for this interaction, and therefore the effective binding energy is likely in the range of 0.2 eV up to 0.5 eV.

The other model parameters are the atomic solute concentration of Mo in the bulk, C_0 = 0.006 (1.11 wt%), the lattice parameter of austenite, a = 0.36 nm, and the effective boundary thickness which is assumed to be δ = 0.5 nm.

Source	Binding energy E_0 (eV)	Note
[21]	0.01 0.2	Extracted from literature data on Mo-P interaction. The first value corresponds to the binding energy of molybdenum alone, while the second one is an effective energy accounting for the carbon interaction.
[73]	0.15 ± 0.03 (0.18 ± 0.03)	Extracted from experimental measurements on Fe-C-Mo steels, using a binding energy for carbon of 0.2 eV (0.1 eV). Austenitic matrix.
[74]	0.17	Used in the modelling of the SDLE in a Fe-C-Mo system (See Chapter IV). Austenite/ferrite boundary
[70]	0.29 ± 0.02	Effective binding energy extracted from experimental measurements in Fe-C-Mo steel at 800°C. Ferritic matrix.
[75]	0.31	Predicted for 11% Cr – 0.5 Mo steel. Ferritic matrix.
[76]	0.43	Predicted using strain-fields arguments. Austenitic matrix.
[77]	0.5	Effective binding energy accounting for the interaction with carbon at 600°C. Austenite/ferrite boundary
[78]	From 0.45 to 1.3	Ab-initio calculations at different locations on a grain boundary. Austenitic matrix.

Table 3.2: *Summary of available literature data on the binding energy of molybdenum with a grain boundary*

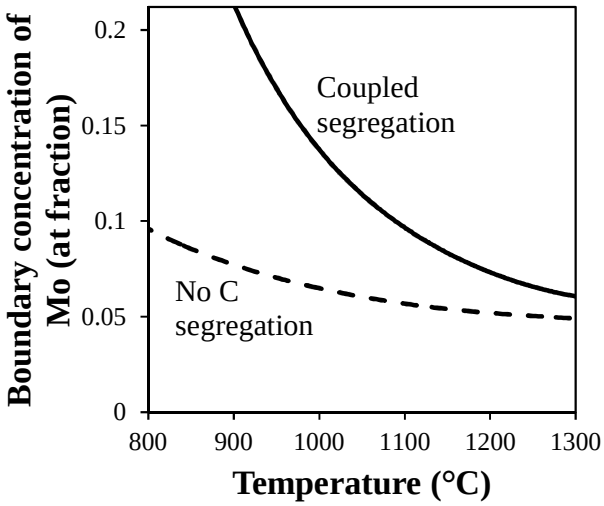

***Figure 3.21**: Equilibrium amount of molybdenum segregated at austenite grain boundary with and without the effect of Mo-C interaction. From* [73].

3.2.2 Setting up the model

By combining equations (3.1), (3.7), (3.22) and (3.36) the grain boundary migration rate can be calculated as follows:

$$\frac{1}{2}\frac{dD}{dt} = \upsilon = M\left(P_d - P_z - P_{drag}\right) \tag{3.45}$$

$$\upsilon = M\left(k_d\gamma_g\frac{1}{D} - k_r\,\gamma_p\frac{f}{r_p} - \frac{C_0\,\alpha\,\upsilon}{1+\,(\beta\,\upsilon)^2}\right) \tag{3.46}$$

One should notice that among the total pressure contributions, the Zener pressure P_z is the only one which value is not dependent of grain size or on its time derivative, although it evolves with time due to an evolution of pinning particles themselves. Assuming that for each time step i, the grain diameter $D_i = D_{i-1} + 2v_i dt$ and that $P_z = P_z(i)$, then equation (3.46) can be written as a fourth degree polynomial of the grain boundary velocity v_i for each time step i, such as:

$$V_4 v_i^4 + V_3 v_i^3 + V_2 v_i^2 + V_1 v_i + V_0 = 0 \tag{3.47}$$

where the expressions of V_0, V_1, V_2, V_3 and V_4 are given in equations (3.48), (3.49), (3.50), (3.51) and (3.52), respectively.

$$V_0 = k_d\gamma_g - P_z(i)D_{i-1} \tag{3.48}$$

$$V_1 = -2P_z(i)dt - D_{i-1}\left(C_0\alpha + M^{-1}\right) \tag{3.49}$$

$$V_2 = \left(k_d\gamma_g - P_z(i)D_{i-1}\right)\beta^2 - 2dt\left(C_0\alpha + M^{-1}\right) \tag{3.50}$$

$$V_3 = -\beta^2\left(D_{i-1}M^{-1} + 2dtP_z(i)\right) \tag{3.51}$$

$$V_4 = -2\beta^2 dtM^{-1} \tag{3.52}$$

Parameters k_d and γ_g remain the same as discussed in the Zener pinning model. The Zener pressure P_z is calculated with a pinning parameter k_r = 3, which is the average value for cubic particles considering the results from section 1.3.1. Results from MatCalc were fitted using an exponential law as a function of time in order to have a value of P_z for each time i. The time step dt was set to 0.1 second. The initial austenite grain size was set to D_0 = 20 µm based on experimental measurements, and the initial velocity was assumed to be 0.01 µm.s^{-1}. The mobility M was taken as an adjustable parameter with temperature.

An algorithm was developed in order to resolve equation (3.47) for each time step t_i, $i \geq 1$, using the Newton's method. Since equation (3.47) has four possible roots, the algorithm was told to select the root closer to that of time step (i-1). As a mean of verification, the equality (3.45) was checked once the calculation was finished. The relative departure from equality is in the range of 10^{-5} %, thus considered as negligible.

3.2.3 Results and discussion

Results

Comparison between model predictions using the values of M and E_0 summarized in Table 3.3, and experimental measurements is shown in Figure 3.22. Very good agreement is found. The model can thus be used to examine the contribution of solute drag to the grain growth kinetics.

Temperature	**920°C**	**970°C**	**1020°C**	**1070°C**	**1120°C**
***M* (10^{-12}.m^4.J^{-1}.s^{-1})**	0.05	0.12	0.19	0.4	0.75
***E*$_0$ (eV)**	-0.45	-0.43	-0.42	-0.30	-0.10

Table 3.3: *Mobility M and binding energy E_0 adjusted on experimental data for each temperature*

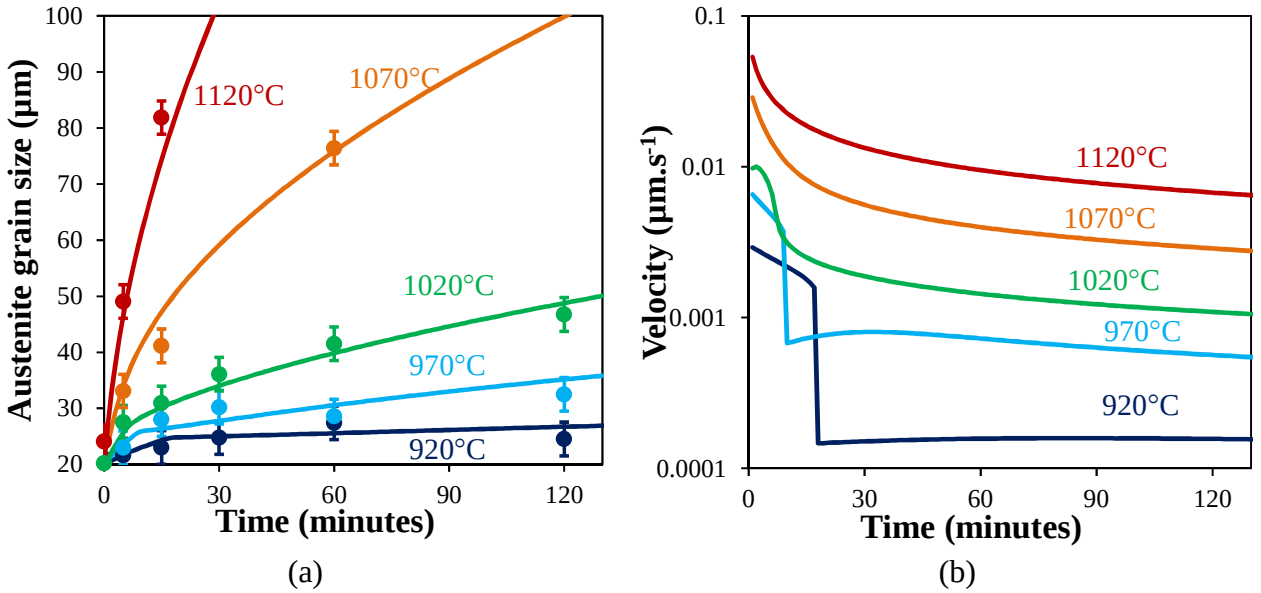

(a) (b)

Figure 3.22: *(a) Comparison between austenite grain size as predicted from equation (3.47) (plain lines) and experimental measurements (symbols), (b) evolution of grain boundary velocity with time for all temperatures.*

One should notice the abrupt change in regime in Figure 3.22 at 920°C and 970°C from high to low velocity, resulting in limited growth. This change happens sooner at 970°C, since the diffusivity of molybdenum is higher at this temperature and therefore shifts the critical velocity towards higher values, as seen above. At higher temperatures, no such change in regime is observed, since the binding energies are too low to induce limited growth.

Figure 3.23 shows the contributions of each different pressure on the total pressure exerted on the grain boundary at 920°C, 970°C, 1020°C and 1070°C. The case at 1120°C is not represented since growth is only linked to the driving pressure. At 920°C and 970°C, a brutal increase in pressure due to solute drag is observed, resulting in a drop in the total pressure which becomes very low. At 1020°C, the solute drag pressure increases quickly with time then decreases, leading to a decrease in total pressure and thus slowing down of growth. The same phenomenon occurs at 1070°C, but the solute drag pressure is lower.

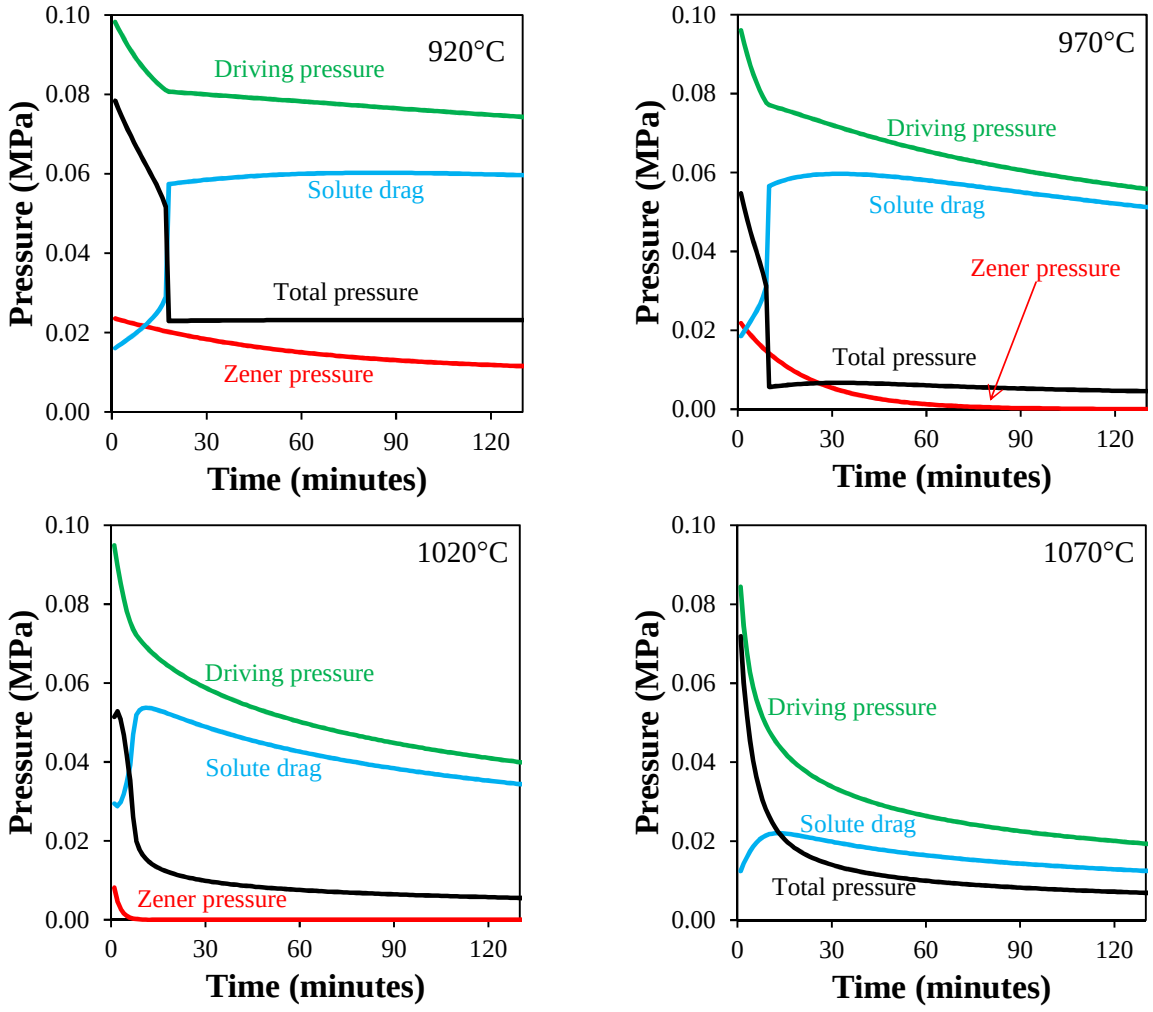

Figure 3.23: *Contributions from the different pressures exerted on the grain boundary at different temperatures.*

Mobility

The adjusted values of mobility are in the same order of magnitude as those reported for austenite grain growth accounting for solute drag and Zener pinning in an oxide dispersed strengthened Fe-Cr at 1350°C, namely, 0.4×10^{-12} $m^4.J^{-1}.s^{-1}$ [79].

The temperature dependency of the obtained values is well fitted by an Arrhenius equation as predicted by equation (3.2), where $M_0 = 4.67 \times 10^{-6}$ $m^4.J^{-1}.s^{-1}$ and $Q = 182$ $kJ.mol^{-1}$, with a correlation coefficient of 0.99. As already stated in section 1.1, this activation energy is usually assumed to be within the range of 170 $kJ.mol^{-1}$, i.e. the activation energy for boundary diffusion of iron atoms in austenite, which is in rather good agreement with the value deduced from calculations.

Binding energy

Binding energies used in the calculations are in the upper limit of the expected range, which is consistent with the assumption that they represent effective binding energies accounting for the co-segregation of carbon and molybdenum. Best results were obtained with a binding energy varying with temperature, namely, the binding energy decreases for temperature equal to or higher than 1070°C. This can be explained using different assumptions:

- As shown in Figure 3.21 in section 3.2.1, the amount of molybdenum segregating increases with the amount of carbon. Similarly, the carbon segregation at austenite grain boundaries increases due to the co-segregation of carbon and molybdenum, as shown in Figure 3.24. Moreover, this amount of segregated carbon and molybdenum decreases with temperature. Assuming that effective binding energy of molybdenum to grain boundaries is a function of the amount of segregated carbon, the decrease in binding energy with increasing temperature appears credible.

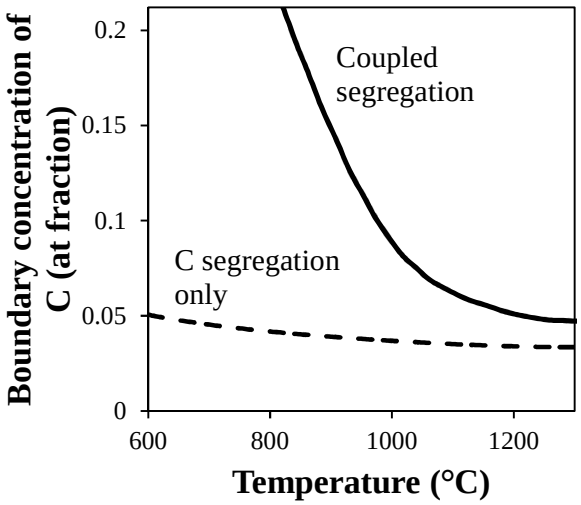

Figure 3.24: *Equilibrium amount of carbon segregated at austenite grain boundary with and without the effect of Mo-C interaction. From* [73].

- One of the strong uncertainties in these calculations is the grain boundary energy, since the considered value is an approximate one. Moreover, Enomoto et al showed that the boundary

energy decreases when the amount of carbon and molybdenum segregating at boundaries increases [73]. Thus, the boundary energy is likely to decrease with decreasing temperature. As a result, the driving pressure would decrease too, as well as the retarding pressure needed to induce limited growth. Accounting for these considerations, the variation of binding energy with temperature might only be an artifact from calculations, necessary for counterbalancing the assumption about temperature-independent boundary energy.

- Another possibility is that, as already stated, the interactions between neighboring grains are not taken into account. Such interactions lead to a decrease in the driving pressure, thus the binding energy inducing limited growth would be lower, as already discussed.

All these three considerations are likely to contribute to the rather high binding energies at lower temperatures and their strong evolution with temperature. Nevertheless, the solute drag of molybdenum cannot be neglected in the limited or slowed down growth of austenite grain, and the current model gives satisfactory results.

4. CONCLUSION

The equations describing austenite grain growth have been summarized and applied to the studied material in order to understand the experimentally determined evolution of austenite grain size.

Experimentally, limited growth is observed at 920°C and 970°C, while at 1020°C the growth is only slowed down. At higher temperatures, the growth kinetics appears to be parabolic, i.e. only driven by the diffusion of iron atoms across the boundary. No abnormal growth is observed. While some Zener pinning induced by AlN particles exists at 920°C, this phenomenon is not responsible for the observed limited grain growth due to their too low phase fraction. More likely, the solute drag of molybdenum atoms is responsible for the limited and slowed down growth. The scale of this solute drag phenomenon is temperature-dependent, either due to the co-segregation of molybdenum and carbon at grain boundaries or is a result of the misestimation of the grain boundary interfacial energy. Nevertheless, grain growth as predicted by accounting for Zener pinning and solute drag gives satisfactory results.

However, the effect of the growth of surrounding grains on the driving pressure is not taken into account, while this effect is obviously not negligible. Such phenomenon would result in a decrease in the driving pressure, and thus in a decrease in the necessary binding energy inducing limited growth due to solute drag. It would be interesting to account for these topological effects in further work. A possible result would be that no more solute drag would be necessary to induce limited growth, thus the binding energies at lower temperatures would also be lower.

An interesting observation from these results is that austenitization at 920°C for 30 minutes and at 930°C for 1 hour result in a similar austenite grain size, around 25 µm. Thus, the change in bainitic hardenability observed between these two conditions is triggered by something else. This phenomenon will be discussed in the next chapter.

Chapter IV: Effect of austenitization conditions on the material properties after cooling and tempering

TABLE OF CONTENTS

In this chapter, the decomposition of austenite upon different cooling conditions representative of an industrial hollow component is studied. The microstructural and mechanical properties after cooling are investigated, as well as the effect of both austenitization and cooling on subsequent tempering.

In a first part, a literature review is presented on the effect of austenitization conditions, and therefore the austenite grain size, on the resulting microstructure after cooling and tempering as well as the tensile and impact toughness properties. In a second part, the material behavior upon cooling at different rates of interest after different austenitization conditions is studied. In particular, two mechanisms are proposed in order to explain the difference in the ferrite phase fraction formed from a similar austenite grain size during cooling under the same conditions, but for different austenitization durations as already reported in Chapter II. From the eight studied austenitization conditions, a first selection of three most promising conditions is done regarding the industrial requirements, i.e. the homogeneity of properties throughout the thickness for a hollow component. The microstructures obtained after a quarter thickness equivalent cooling from these three austenitization conditions are then more thoroughly investigated, as well as their tensile and toughness properties. From these investigations, one austenitization condition is eventually selected for the subsequent study of tempering, which is reported in the next chapters.

1. LITERATURE REVIEW

This review aims at summarizing the effects of austenitization conditions, and therefore the austenite grain size, on final microstructures of 2.25 Cr – 1 Mo steels after cooling. Its effect on tensile and toughness properties is also considered.

1.1 Effect of austenitization temperature on austenite decomposition upon cooling

An increase in austenite grain size results in a shift of the ferritic and 100% martensitic transformation domains towards slower cooling rates [10, 20][2,3], as shown in the CCT diagram in Figure 4.1. Lower critical cooling rates resulting in a fully bainitic microstructure are respectively 1.5°C/s, 0.3°C/s and 0.2°C/s, respectively after austenitization at 975°C, 1100°C and 1200°C.

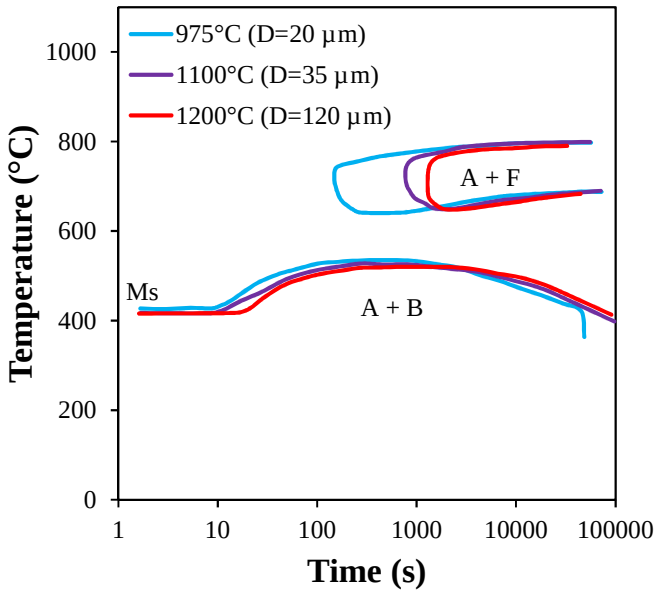

Figure 4.1: *Effect of austenitization temperature on 2.25Cr-1Mo steel[1] CCT diagram (from* [10]*). Austenitization time: 30 minutes. D: Austenite grain size, A: Austenite, B: Bainite, F: Ferrite, Ms: Martensitic transformation start temperature.*

During the austenite-to-ferrite transformation, the most favorable nucleation sites for ferritic germs are the austenite grain triple junctions. Coarser austenite grains decrease the area of grain boundaries per volume of material, thus the density of nucleation sites.

This shift of the ferritic domain allows understanding the extension of the 100% martensitic domain: since the rate of diffusion-controlled transformations of austenite is reduced, martensite can be formed at slower cooling rates. However, the shift in the ferritic transformation domain is usually

[2] Steel composition of reference [10], in wt% : 0.09 C, 0.93 Mn, 0.25 Si, 0.006 S, 0.010 P, 2.35 Cr, 1.05 Mo, 0.008 N.

[3] Steel composition of reference [20], in wt%: 0.14 C, 0.15 Mn, 0.26 Si, 0.004 S, 0.004 P, 2.48 Cr, 1.02 Mo, 0.20 Ni, 0.12 Cu, 0.010 Al, 0.0075 N

more pronounced than the one for the martensitic transformation, thus increase in the austenite grain size generally leads to an increase in bainitic hardenability.

1.2 Morphology of cooled microstructures

The austenite grain size can influence the size of microstructural units after cooling, such as bainitic packets or martensitic laths. First of all, it should be pointed out that two kinds of bainitic packets can be differentiated: so-called “morphological” packets and so-called “crystallographic” ones. The first ones correspond to packet of parallel laths of ferrite or martensite and may be characterized by optical microscopy, while the second ones correspond to packet of laths which share similar crystallographic orientation. From metallographic cross-sections, the crystallographic packet size can be up to 3 times smaller than the morphological one [80]; Figure 4.2 shows a comparison between both kinds of packets on a 2.25 Cr – 1 Mo steel close to that of the present study. The crystallographic packet is a key material parameter regarding toughness properties since such packets are the microstructural units controlling cleavage crack propagation [81]. However, it should be pointed out that the bainitic lath size is more representative for the tensile properties.

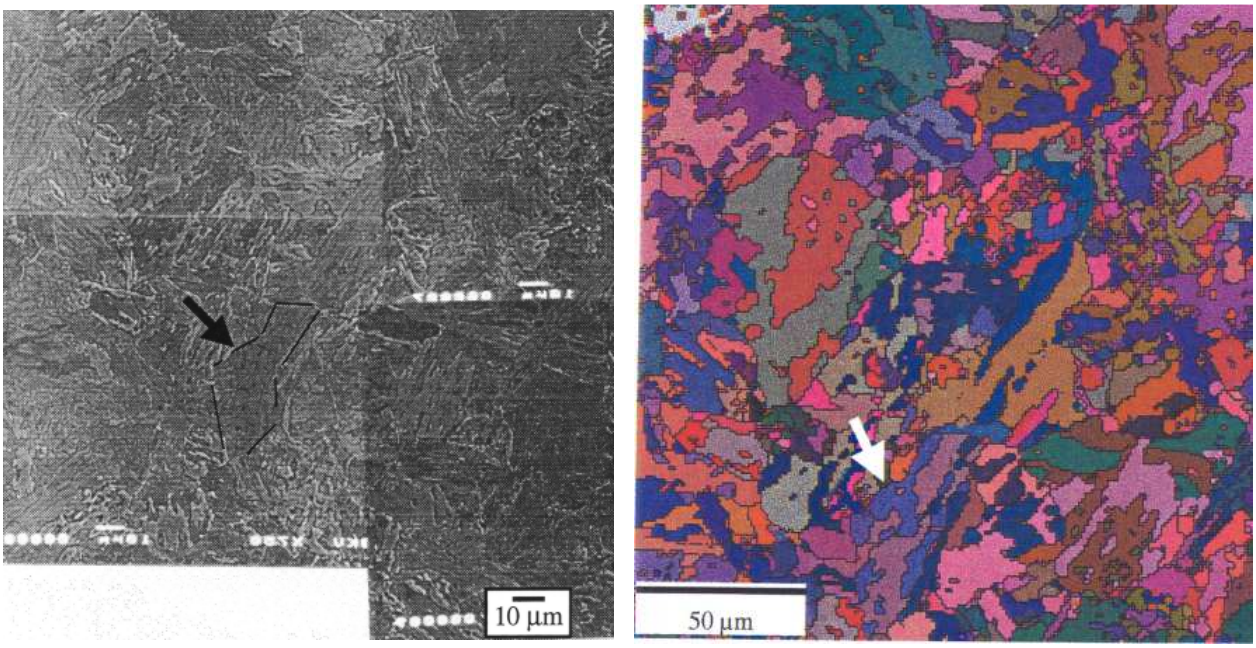

(a) (b)

Figure 4.2: *Comparison between (a) SEM observations of morphological packet and (b) EBSD mapping of crystallographic packets in the same region. Arrows show the same location on both images. From* [82]

As a general rule, the bainitic packet size decreases with the austenite grain size until both sizes coincide. In other words, a large enough austenite grain can be transformed into several bainitic packets, while a bainitic packet cannot be bigger than its parent austenite grain [83], unless it grows into several parent grains simultaneously. The influence of austenite grain size on the bainitic packet size has been reported by Bouyne in 2.25 Cr – 1Mo steels [82]. Increasing the austenite grain size

tends to raise the bainitic packet size, but no clear correlation was found: the average crystallographic bainitic packet diameter is respectively 7.6 µm and 8.5 µm for a prior austenite grain diameter of 25 µm and 105 µm, respectively[4]. However, these values have to be carefully considered since the 3D morphology of a bainitic packet is complex. Thus, in a cross section analysis, what appears to be several packets can actually be a single packet. Moreover, a slight increase in crystallographic packet size might be sufficient to decrease toughness properties. This issue will be addressed in more detail in section 1.4.

1.3 Carbide precipitation

No literature results were found on the effect of austenite grain size on the microstructural evolution during tempering for bainitic microstructures. However, Chang & Kai [84] measured the amount of metallic elements in cementite Fe_3C precipitated into tempered martensitic 2.25Cr - 1Mo steel[5] after tempering at 500°C, 600°C and 700°C for 1 hour after different austenitization conditions. It appears that the austenitization temperature only has little effect on the chemical composition of carbides for a given tempering condition.

1.4 Effect on mechanical properties

Several authors reported the effect of the austenitization conditions on the yield strength (YS), the ultimate tensile strength (UTS) and the elongation at fracture of fully bainitic 2.25 Cr – 1 Mo steels [20, 82, 84]. Parameters for each study are summarized in Table 4.1. They all concluded that the austenitization conditions have no direct impact on these mechanical properties. However, Ishiguro concluded that, with an addition of vanadium[6], an increase in the austenitization temperature results in a slight decrease in ductility, i.e. an increase in tensile and yield strengths and a decrease in elongation and reduction of area at fracture [35]. This was attributed to larger amounts of vanadium available for precipitation during subsequent tempering due to dissolution of V(C,N) precipitates when the austenitization temperature increases.

Sato et al. also conducted a study on the effect of austenite grain size on the impact toughness of a 2.25 Cr – 1 Mo steel [20]. The Fracture Appearance Transition Temperature (FATT), at which 50% of the fracture surface is ductile, was determined by V-notch Charpy tests. Tests were performed at 10°C or 20°C intervals, using two or three specimens per temperature, for a total amount of 15 specimens. A low FATT leads to best impact toughness properties. The heat treatments are the ones given in Table 4.1. Unlike UTS or YS, the austenite grain size and impact toughness are interrelated, as the FATT increases from -30°C to -15°C when the austenite grain size increases from 90 µm to 310 µm. While such small variations might not appear significant, similar results were obtained for a 2.25 Cr – 1 Mo – 0.2 V steel [35] and Bouyne found a DBTT of -30°C and -20°C for an austenite

[4] Steels composition of reference [82], in wt%:
- 25 µm PAG size steel: 0.14 C, 0.10 Si, 0.54 Mn, 0.003 S, 0.004 P, 2.25 Cr, 1.01 Mo, 0.07 Ni, 0.05 Cu, 0.002 Al, 0.005 V
- 105 µm PAG size steel: 0.14 C, 0.24 Si, 0.24 Mn, 0.003 S, 0.003 P, 2.49 Cr, 1.08 Mo, 0.15 Ni, 0.06 Cu, 0.012 Al, 0.008 V

[5] Steel composition of reference [84], in wt% : 0.10 C, 0.24 Si, 0.47 Mn, 2.12 Cr, 0.90 Mo, 0.025 Ni, 0.006 V

[6] Steel composition of reference [35], in wt%: 0.10 C, 0.02 Si, 0.54 Mn, 0.007 S, 0.009 P, 2.30 Cr, 0.97 Mo, 0.11 Ni, 0.21 V, 0.010 Al, 0.022 Ti, 0.002 B, 0.009 N

grain size of 25 µm and 105 µm, respectively [82]. A general conclusion is that mechanical properties are better when the austenite grain size is smaller. This influence is explained by changes in the unit cleavage crack path.

Ref	Heat treatments	PAG size (µm)	Testing conditions
[20]	1050°C/1200°C - 2h Cooling at 5°C/min Tempering 690°C - 19h	90 / 310	Tested at room temperature 1 test per condition
[82]	925°C – 5h40 Water quench 665°C – 7h40 + 635°C - 6h	25	Tested at 9 temperatures ranging from -200°C to room temperature 1-2 tests per condition per temperature
	1100°C – 1h Air quench 685°C – 7h20 + 645°C – 15h	105	
[84]	950°C/1000°C - 0.5h Water quench As-quenched or 400°C / 500°C / 600°C / 700°C – 1h	Unknown	Tested at 300°C 1 test per condition

Table 4.1: *Heat treatments, prior austenite grain size and testing conditions for the reported tensile tests.*

Based on all these considerations, the choice of the austenite grain size must be a compromise: small grains might lead to lower bainitic hardenability, while coarser grains could be detrimental to the toughness properties of the material. Moreover, as already stated, the austenite grain size must be constant for austenitization durations ranging from 1 hour to 2 hours in order to ensure homogeneous microstructural and mechanical properties through the thickness.

2. EXPERIMENTAL STUDY

2.1 Choice of experimentally studied austenitization conditions

The choice of austenitization conditions to be investigated was based on several considerations, explained as follows.

During industrial manufacturing, the austenitization time is not the same throughout the thickness. To get a homogeneous grain size, one should expect that the optimal austenitization temperatures are the one where limited growth occurs, i.e. lower than 1000°C as seen in Chapter III. Thus, it was decided to conduct the study at austenitization temperatures of 920°C and 970°C; this first temperature was selected as a reference, since the CCT diagram after austenitization at 920°C for 30 minutes had already been studied as reported in Chapter II. Besides that, this temperature is close to the austenitization temperature used for the reference material, namely, 930°C. Two additional austenitization temperatures, 1020°C and 1070°C, were also chosen in order to emphasize the effect of higher austenite grain size on the microstructure after cooling.

It was shown in Chapter II that the microstructure quenched at the mid-thickness equivalent cooling rate after an austenitization at 920°C for 30 minutes was different compared to the microstructure of the actual mid-thickness of the reference material, which had been austenitized at 930°C for 1 hour. This observation is quite startling since the austenite grain size of both austenitization conditions is expected to be similar, around 25 µm as seen in Chapter III. This suggests that the austenitization time has an effect on the austenitic phase, which is not directly reflected in the austenite grain size. Thus, two austenitization durations were systematically studied for the four temperatures in order to investigate this phenomenon: 30 minutes and 1 hour. As a result, a total amount of eight different austenitization conditions were studied. The corresponding values of austenite grain size, as experimentally determined in Chapter III, are summarized in Table 4.2.

	920°C	**970°C**	**1020°C**	**1070°C**
30 minutes	25 µm	30 µm	35 µm	55-60 µm
1 hour	25 µm	30 µm	40 µm	75-80 µm

Table 4.2: *Average austenite grain size diameter as experimentally measured for the eight austenitization conditions investigated in this chapter*

Industrially, optimal austenitization conditions must lead to fully bainitic microstructures for cooling rates ranging from 0.3°C/s to 3°C/s. The cooling rate experienced by the mid-thickness region of the component (0.5°C/s) was not used in this study since it is too close to the value of 0.3°C/s one. Instead, an intermediate cooling rate of 1°C/s was chosen because it was expected to lead to a fully bainitic structure independently of austenitization conditions, since it is in the middle of the bainitic transformation domain in the CCT diagram as determined in Chapter II. Since the mechanical properties of the material are tested after tempering, each cooled microstructure was investigated before and after a tempering heat treatment at 675°C for 5.5 hours followed by a stress-relief heat treatment at 625°C for 16 hours. Samples were air cooled after both heat treatments. These heat treatments are similar to the ones conducted on the reference material, thus comparison between the studied conditions and the reference material can be made regarding only the austenitization step. Samples that underwent such heat treatments will be called quenched+tempered, in opposition with the as-quenched samples. All further investigations were made using blank specimens as described in Chapter II. Austenitization and cooling were performed in a dilatometer in order to ensure a precise control of the temperature. Tempering and stress-relieving heat treatments were performed in batches in an electrical furnace.

2.2 First investigation: effect of austenitization conditions on the decomposition of austenite upon cooling

The microstructure after cooling from the eight different austenitization conditions was characterized by means of optical microscopy and hardness measurements. The austenite decomposition upon cooling was studied thanks to the dilatometric curves. It should be pointed out that these dilatometric measurements were done on large samples at the limit of the extensometer range, thus dilatometric curves are not available for all studied austenitization conditions.

Additionally, kinetics of transformation are not presented since several experimental errors were susceptible to take place upon these tests. Thus, dilatometric curves were only used in order to assess the presence of ferrite in the material and an estimation of the bainite start temperature B_s.

To address the industrial part of this project, focus was made on characterization of partial decomposition into proteutectoid ferrite. For the same reason, hardness values after tempering were compared to those of the reference material.

2.2.1 Lowest cooling rate (0.3°C/s)

Figure 4.3 shows the dilatometric curves upon cooling at 0.3°C/s from different austenitization temperatures for 30 minutes and 1 hour. The 1020°C – 1 hour curve was not available due to abovementioned technical issues. With the exception of austenitization at 1070°C, which leads to fully bainitic microstructures independently of the austenitization duration, samples cooled at 0.3°C/s consist of a mixture of ferrite and bainite.

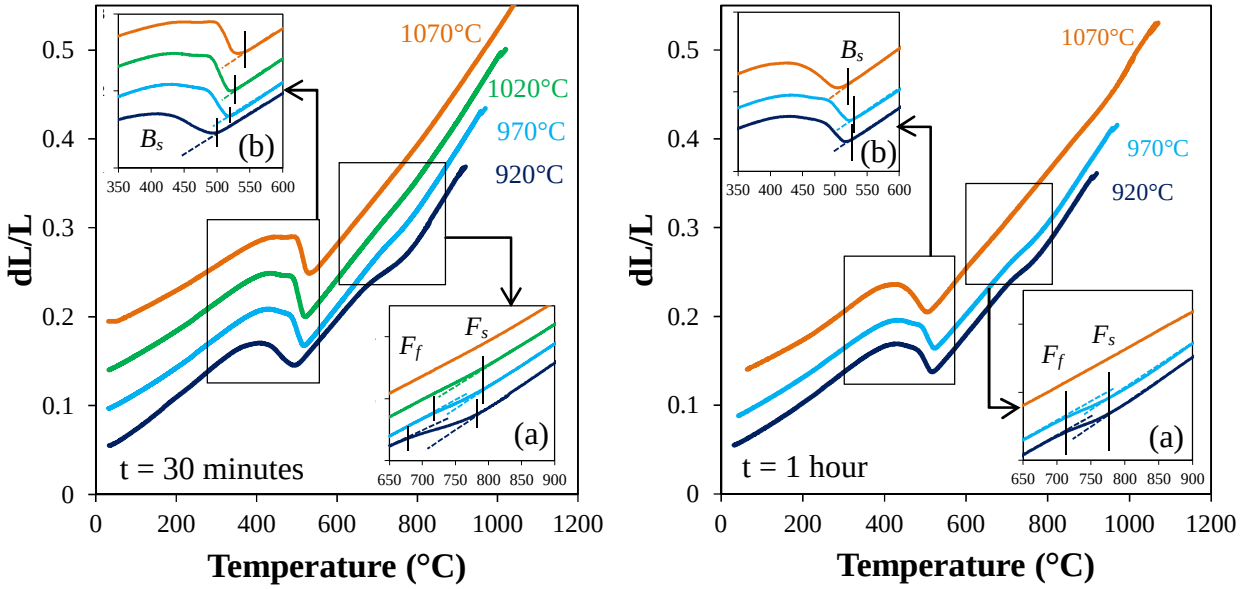

Figure 4.3: *Dilatometric curves upon cooling at 0.3°C/s from different austenitization temperatures for 30 minutes and 1 hour. Insets (a) and (b) are enlarged views of ferritic and bainitic transformations, respectively.*

One should notice that for this cooling rate, the ferritic transformation temperature range becomes narrower with increasing the austenitization temperature: at 1020°C for 30 minutes only a slight deviation is observed. The austenite-to-ferrite start transformation temperature F_s is the same for all conditions where ferrite precipitation occurs, around 790°C, and the transformation end temperature F_f remains the same for the 920°C – 1 hour, 970°C – 1 hour and 970°C – 30 minutes conditions, namely, 720°C. For these three conditions, the amount of ferrite formed, i.e. variation of length dL/L between these two temperatures appears to be similar. When considering the curve resulting from an austenitization at 920°C for 30 minutes, the F_f temperature drops to 680°C, lower than for the sample austenitized for 1 hour at this temperature. Moreover, the amount of ferrite formed is clearly higher than the one for the sample austenitized for 1 hour at this temperature. Thus,

at 920°C, the austenitization time has an influence on the ferritic transformation while the austenite grain size is similar, as hinted in Chapters II and III. The values of the B_s temperature are consistent with these observations: they remain the same for all conditions (520-530°C) with exception of the 920°C – 30 minutes conditions for which it drops down to 500°C. This is more likely due to the formation of ferrite which leads to carbon enrichment in austenite. One should also notice that, whatever the austenitization conditions except for 920°C – 30 minutes and 1070°C – 1 hour, the slope of the curve is steep at the beginning of the transformation, but abruptly decreases before the end, indicating a drop in transformation rates (which is almost a stasis in certain cases, e.g., 1020°C – 30 minutes and 1070°C – 30 minutes).

To confirm the interpretations made on the ferrite transformation, the area fraction of proeutectoid ferrite was determined from optical micrographs by image processing using ImageJ software. Samples were etched using Nital 2%; micrographs were taken at an intermediate magnification at the core of samples, far from the decarburization layer. Image size is 650 µm x 875 µm with 0.42 µm/px; one representative picture was taken by condition. Images were then binned and a threshold was applied in order to separate bainite (dark) from ferrite (bright), as shown in Figure 4.4. The choice of the threshold value is a key-parameter since the wide range in grey levels exhibited by bainitic ferrite can induce deviations in measurements. By using a high threshold, one only takes the proeutectoid ferrite into account, but one also underestimates the total ferrite area fraction by eroding the ferrite grains. On the other hand, using a low threshold leads to overestimating the ferrite fraction since the bainitic ferrite is partly taken into account in the estimation.

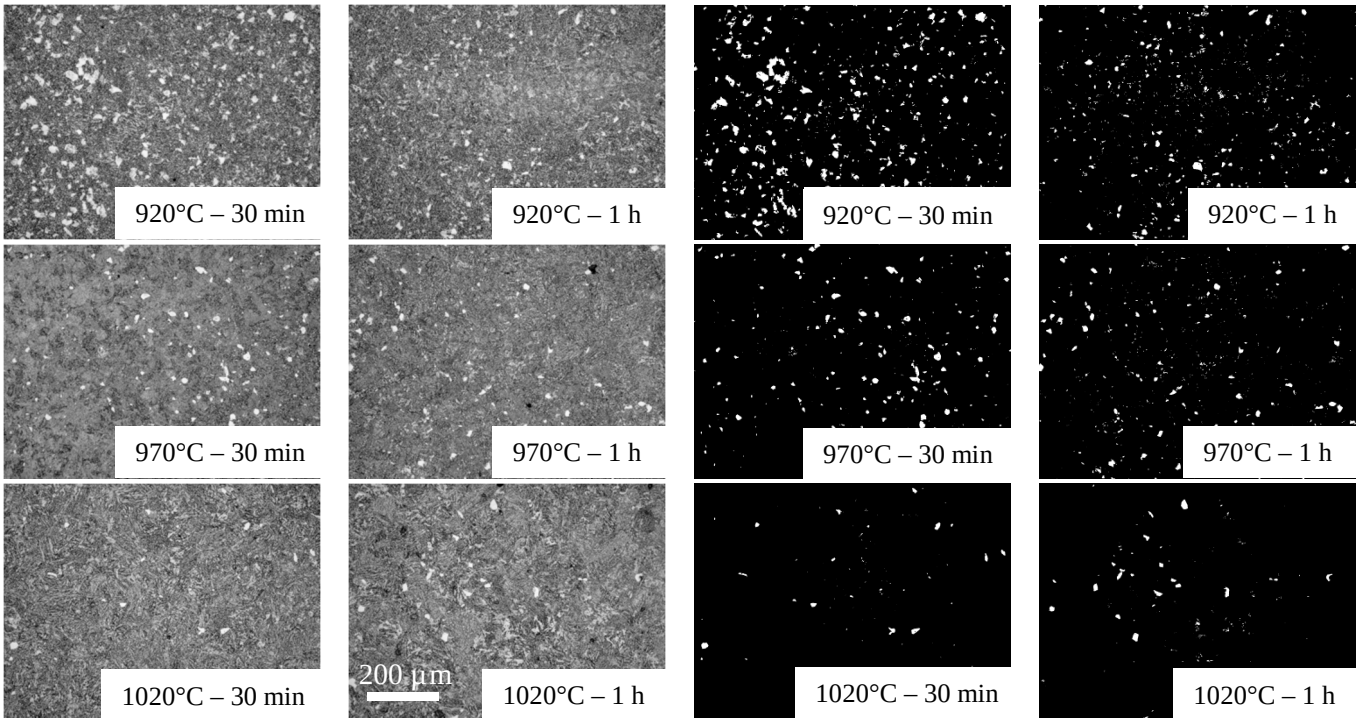

Figure 4.4: *Optical micrographs after cooling at 0.3°C/s for different austenitization conditions. (a) Optical micrographs, (b) Binned images using the lower threshold.*

The influence of austenitization condition on the proeutectoid ferrite fraction is shown in Figure 4.5. The two values per condition correspond to results obtained using the two abovementioned thresholds. One should also notice that the fractions given in Figure 4.5 are lower compared to the one indicated in the CCT diagram in Chapter II. This is due to the fact that the decarburization layer did not significantly influence the current measurement, since the samples size was much larger than that of samples used in Chapter II.

As expected from the dilatometric curves, the area fraction of ferrite decreases with increasing the austenitization temperature, e.g. with increasing the austenite grain size: at 1070°C, no ferrite was observed after cooling, while between 3-4% ferrite were found after an austenitization at 970°C, independently of the austenitization time. Moreover, image analysis confirmed that more ferrite had formed upon cooling after austenitization at 920°C for 30 minutes compared to the 1 hour austenitization, which confirm the strong effect of austenitization time already reported.

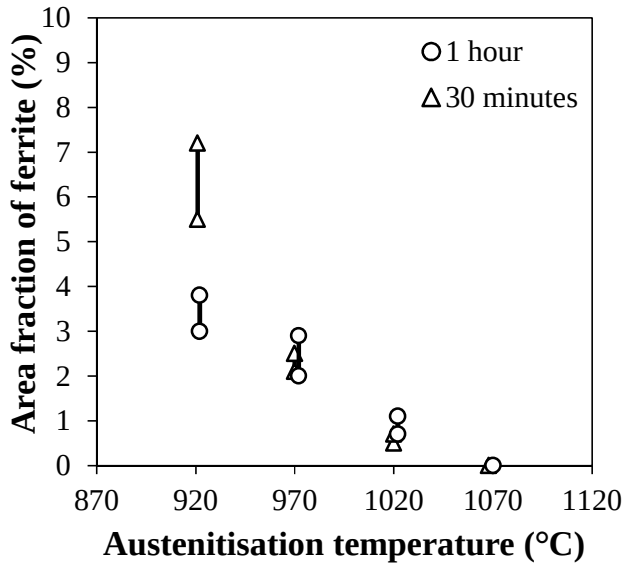

Figure 4.5: *Variation of ferrite area fraction with austenitization temperature and time after cooling at 0.3°C/s as determined by image analysis. Experimental points are slightly shifted for a given austenitization temperature for more clarity.*

This difference in the ferrite fraction while starting from similar austenite grain size could be induced by a change in the grain boundary chemistry. A conclusion of Chapter III was that austenite grain growth was limited at low temperature by a solute drag effect due to the segregation of molybdenum atoms at austenite grain boundaries. Despite being a ferrite-stabilizer, molybdenum is well-known for increasing the bainitic hardenability of steels [85, 86] by impeding ferrite nucleation and growth.

As already postulated when discussing the binding energy of molybdenum with the grain boundary, a co-segregation of both molybdenum and carbon atoms likely takes place at austenite grain boundaries due to their strong affinity with each other. As already stated in Chapter III, Enomoto et al. calculated the segregated amount of molybdenum and carbon at austenite grain boundaries in a Fe-0.44C-1.95Mo at several temperatures [73] as summarized in Figure 4.6. Different hypotheses were tested in these calculations: equilibrium concentration with carbon-

molybdenum-boundary interactions (solid curves) and paraequilibrium composition during quenching from 1300°C to room temperature (dashed curves). Atomic bulk fraction of carbon and molybdenum are respectively 0.02 and 0.01. As already stated, the molybdenum concentration in boundaries at equilibrium decreases with increasing temperature. Molybdenum tends to reduce the activity of nearby carbon, thus decreasing its diffusion coefficient [87], explaining the large amount of segregating carbon. The paraequilibrium curve is interesting, since it shows that the boundaries become slightly enriched in carbon upon cooling.

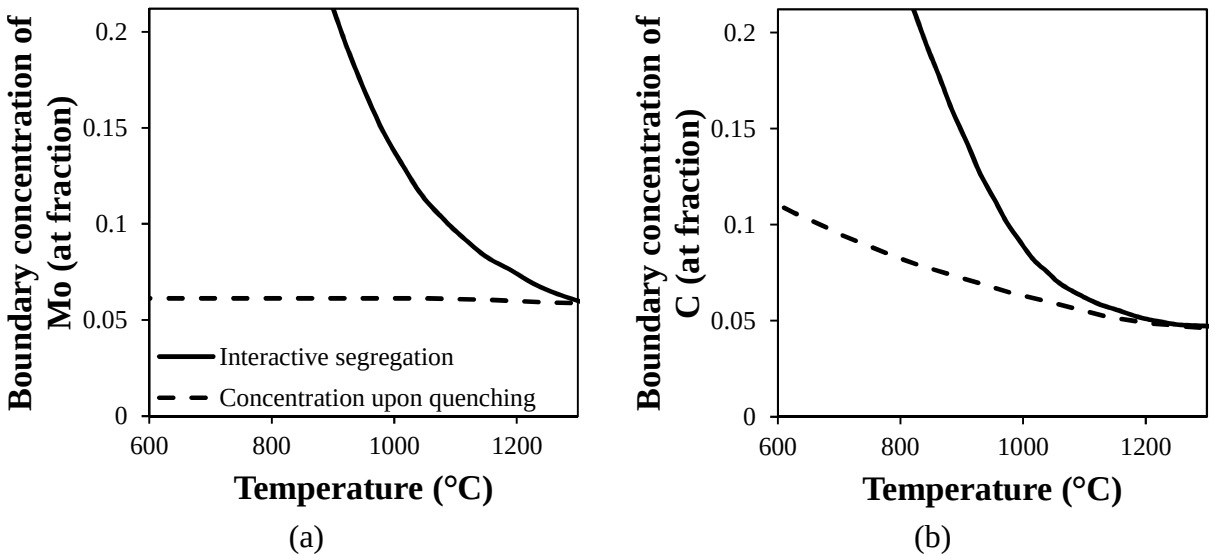

Figure 4.6: *Concentration in (a) molybdenum and (b) carbon at austenite grain boundaries as a function of the temperature. Plain lines are equilibrium concentration when accounting for the co-segregation of molybdenum and carbon, dashed lines are the concentration assuming paraequilibrium composition upon cooling from 1300°C. From* [73].

Let us now consider that this co-segregation equilibrium is not reached after 30 minutes at 920°C in the studied steel, although enough molybdenum atoms have segregated to induce limited austenite grain growth, as shown in Chapter III. After 1 hour at 920°C, the grain boundary would then become richer in molybdenum and carbon, the half free-mean path of molybdenum in austenite after 30 minutes at this temperature being 0.4 µm, using the diffusion coefficient used in Chapter III. Thus, grain boundaries would exhibit different chemical compositions regarding the austenitization time at this temperature. Assuming a paraequilibrium cooling, these assumptions would remain true when the ferrite transformation occurs. On the other hand, at temperatures equal to or higher than 970°C, this co-segregation equilibrium is reached sooner due to the higher half free-mean path of molybdenum and the lower equilibrium concentration. Thus, at these temperatures, the grain boundary chemistry would not evolve between 30 minutes and 1 hour of austenitization.

Based on these considerations, two mechanisms can be proposed to explain the observed difference in ferrite fraction with austenitization time at 920°C:

- Since ferrite nucleates preferentially at austenite grain boundaries, one could imagine that this increase in carbon content at these sites inhibits ferrite nucleation.

- In the case of ferrite growth into austenite, which is driven by carbon diffusion, an accumulation of molybdenum at the ferrite/austenite boundaries will decrease the diffusivity of carbon atoms located in the nearby austenite, until the growth becomes only driven by molybdenum diffusion [88]. This phenomenon, i.e. the solute drag-like effect (SDLE), can take place in Fe-C-Mo steels as postulated by Kinsman & Aaronson [89]. It differs from the solute-drag in the way that atoms do not diffuse toward boundaries, but the boundaries sweep atoms in the matrix that then remain segregated, hence its name. It has since then been widely studied and experimentally confirmed [69, 74, 90, 91], and for instance is held responsible for the bainitic stasis upon step-cooling in Fe-C-Mo steels, assuming that the bainitic transformation is diffusive. SDLE has also been highlighted during the ferritic transformation upon continuous cooling at 1°C/s in Fe-C-Mn steels [92] and Fe-C-Nb steels [93]. Limited growth of ferrite is expected to happen when the steady-state concentration of molybdenum is reached at austenite/ferrite interphases. Since ferrite nucleates preferentially at austenite grain boundaries, an initially large amount of molybdenum at these interfaces implies an initial enrichment at austenite/ferrite interphases after nucleation. Thus, the steady-state concentration, and therefore the limited growth regime of ferrite grains, is likely to be reached sooner as more molybdenum has segregated at austenite grain boundaries.

These two mechanisms reduce the ferrite transformation at two different steps: the first one impacts ferrite nucleation, while the second one limits ferrite growth. However, the similar F_s and different F_f temperatures determined after austenitization at 920°C for 30 minutes and 1 hour suggest that the variation in ferrite fraction is due to change in growth rate rather than in nucleation rate [92]. In either way, segregation of molybdenum and carbon at prior austenite boundary is likely to be considered as responsible for the change in hardenability. No chemical quantifications were made to support these hypotheses on the ferritic transformation due to the complexities of such analyses. However, if the previous assumptions are true, one should find a strong enrichment of molybdenum at the prior ferrite/austenite interphases after cooling interrupted by quenching.

However, observations of the bainitic stasis upon cooling are consistent with the occurrence of SDLE. According to the SDLE theory, the maximal fraction of formed bainite upon step cooling increases when the temperature of the isothermal step decreases [69]. Given the low cooling rate, the material stays in the temperature range for bainitic transformation for more than 10 minutes. A continuous cooling can be seen as a succession of short isothermal steps, thus one might assume that at some point upon cooling the bainite transformation is controlled by the molybdenum diffusion, leading to the stasis. When the temperature continues to decrease, the maximal possible bainite fraction thus increases and the transformation restarts. After austenitization at 920°C – 30 minutes and 1070°C – 1 hour, no such phenomenon is observed. When looking at the dilatometric curves, these two conditions result in a B_s similar or lower to the temperature at which the stasis is observed; thus this latter cannot occur.

For all conditions, hardness values range from 325 HV to 345 HV in the as-quenched states; values are between 200 HV and 220 HV after tempering (Figure 4.7). One should notice that the hardness values are slightly lower for the austenitization at 920°C, due to the non-negligible amount of ferrite. Other austenitization conditions seem to have little effect on hardness both after quenching and after tempering.

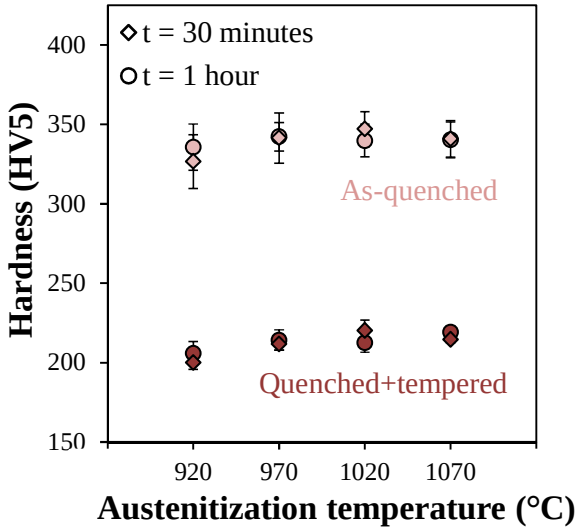

Figure 4.7: *Evolution of hardness with austenitization conditions after cooling at 0.3°C/s, for both as-quenched and quenched+tempered states.*

As a conclusion, the material exhibits good bainitic hardenability with a ferrite fraction inferior to 5% with the exception of the austenitization at 920°C for 30 minutes, possibly due to a change in the chemistry of the prior austenite grain boundaries between 30 minutes and 1 hour at 920°C.

2.2.2 Intermediate cooling rate (1°C/s)

Figure 4.8 shows the dilatometric curves for both lower temperature and higher temperature austenitization; all other curves are not available due to technical issues.

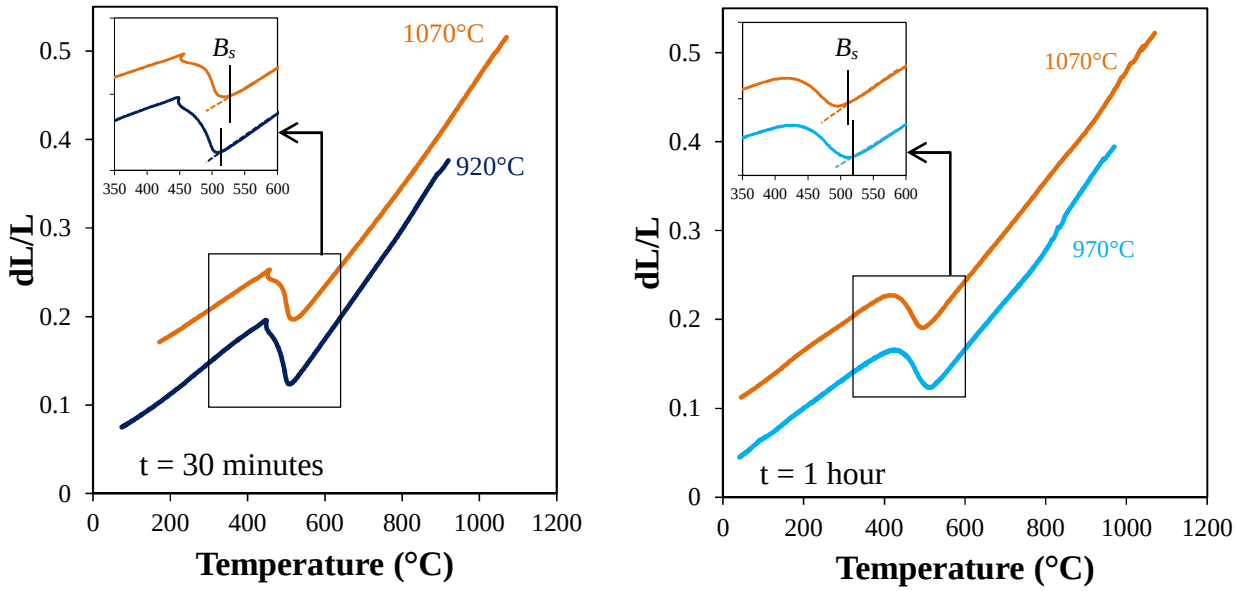

Figure 4.8: *Dilatometric curves upon cooling at 1°C/s from different austenitization temperatures for 30 minutes and 1 hour. Insets are enlarged views of bainitic transformation.*

No ferrite was ever observed, regardless the austenitization conditions. The deviation from thermal expansion at high temperatures for the 970°C – 1 hour condition cannot be due to ferrite transformation, since a contraction is observed instead of expansion. The abrupt contraction at the end of the bainitic transformation after austenitization for 30 minutes is likely another experimental artifact, since a similar curve obtained for the CCT diagram presented in Chapter II does not exhibit the same features. The bainite start temperature B_s ranges between 510°C and 530°C, the difference being within the experimental error (namely, ±10°C). These values are consistent with the CCT diagram proposed in Chapter II, where B_s equals 520°C upon such cooling.

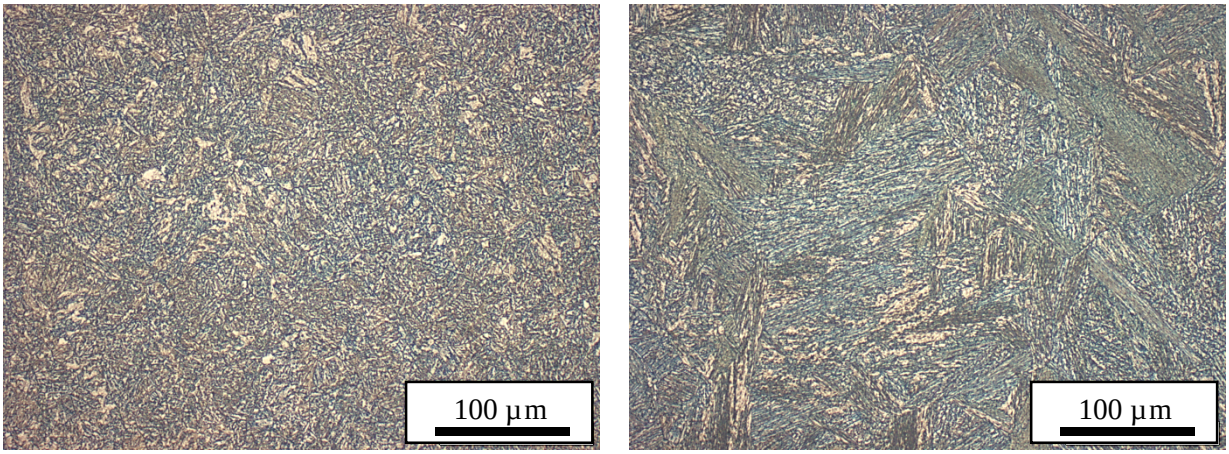

(a) (b)

Figure 4.9: *Optical micrographs after cooling at 1°C/s after an austenitization (a) at 920°C for 30 minutes, (b) at 1070°C for 1 hour.*

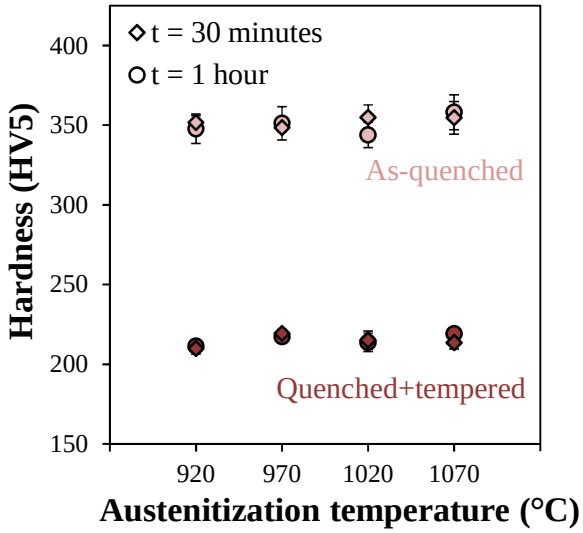

Figure 4.10: *Evolution of hardness with austenitization conditions after cooling at 1°C/s, for both as-quenched and quenched+tempered states.*

Microstructures resulting from extreme austenitization conditions are shown in Figure 4.9. The microstructure is coarser for larger austenite grains, but as expected from the literature review this phenomenon does not impact hardness: it ranges between 340 HV and 360 HV after quenching and

between 210 HV and 220 HV after tempering (Figure 4.10). As-quenched and quenched+tempered hardness values are respectively consistent with the ones given for fully bainitic microstructures by the CCT diagram and by the reference material studied in Chapter II, namely, 360 HV and ~215 HV.

As a conclusion, the austenite grain size has an effect on the bainitic packet size but neither on the B_s temperature nor on hardness. However, for the reason explained in section 1.4, the increase in packet size is expected to have an effect on toughness.

2.2.3 Higher cooling rate (3°C/s)

Microstructures after cooling at 3°C/s are mostly bainitic as shown by the dilatometric curves upon cooling in Figure 4.11, however larger austenite grains lead to a mixture of martensite and coarse bainite (Figure 4.12). When taking into account the CCT diagram given in Chapter II, one should notice that the 3°C/s cooling rate is the lowest limit of the bainitic domain. Thus, any increase in the austenite grain size might lead to martensite transformation upon cooling, as stated in the literature review (section 1.1). It should be specified that one cannot differentiate bainite from the martensite from dilatometric curves when both transformations occur during cooling, as already stated in Chapter II.

However, the bainitic start transformation temperature B_s is lower than the one at 1°C/s and ranges from 500°C to 520°C. This decrease in the B_s temperature was already observed in the martensite/bainite intercritical domain in the CCT diagram from Chapter II. Thus, all metallurgical states cooled at 3°C/s, even from the lowest temperatures, are expected to contain some martensite.

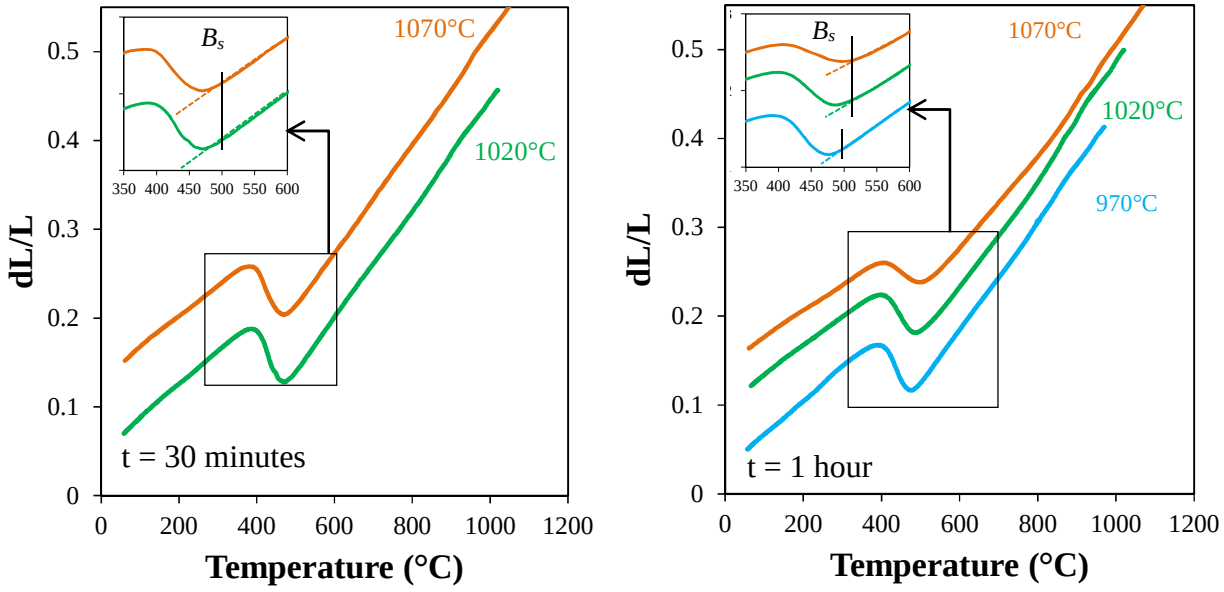

Figure 4.11: *Dilatometric curves upon cooling at 3°C/s from different austenitization temperatures for 30 minutes and 1 hour. Insets are enlarged views of bainitic transformation.*

Hardness values after cooling at 3°C/s are slightly higher than for lower cooling rates, between 365 HV and 390 HV (Figure 4.13). This increase in hardness in the as-quenched samples is

consistent with the presence of martensite. Some differences are observed between hardness values after austenitization for the two durations at a given temperature. However, all variations are within standard deviations which are due to the dual-phase nature of the material, which suggest that the martensite is not homogeneously distributed in the material.

After tempering, the hardness ranges from 215 HV to 230 HV, which is very similar to hardness after tempering for the fully bainitic state (cooled at 1°C/s). This can be explained by a similar precipitation of carbides in bainite and in martensite upon tempering; Chang & Kai have found similar carbides in martensitic 2.25 Cr – 1 Mo steel than in a bainitic one [84]. Moreover, dislocation recovery is likely to happen during a temper at 675°C and could result in a similar softening for both bainite and martensite.

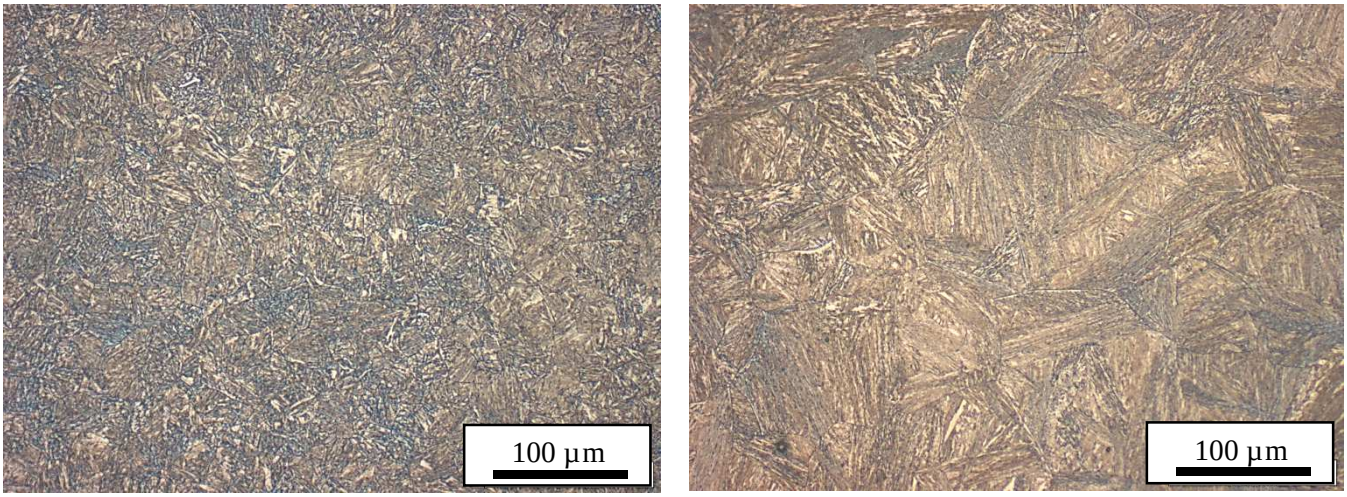

(a) (b)

Figure 4.12: *Optical micrograph of structures cooled at 3°C/s after an austenitization at (a) 920°C for 1 hour, (b) 1070°C for 1 hour.*

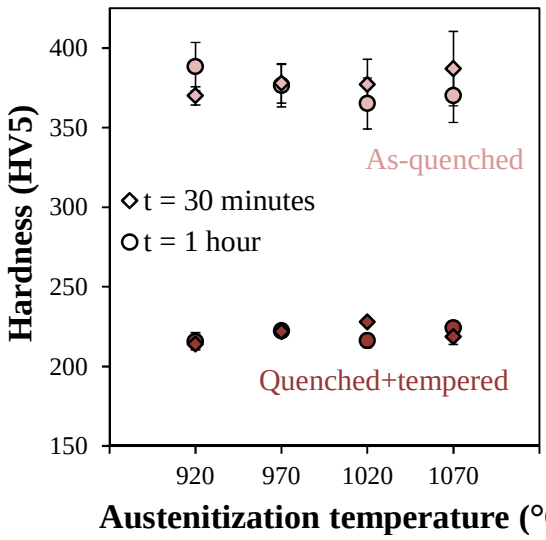

Figure 4.13: *Evolution of hardness with austenitization conditions after cooling at 3°C/s, for both as-quenched and quenched+tempered states.*

2.2.4 Summary: austenite decomposition upon cooling

Based on the previous results, the following conclusions can be drawn:

- At 0.3°C/s, the microstructure is mainly bainitic with some ferrite. Except after austenitization at 920°C for 30 minutes, the ferrite fraction is lower than 5% and therefore within industrial requirements. The difference in ferrite fraction after cooling between samples austenitized at 920°C respectively for 30 minutes and for 1 hour can be explained by the molybdenum segregation at austenite grain boundaries.
- At 1°C/s, the microstructure is fully bainitic for all studied metallurgical states. While the bainitic laths seem to enlarge with increasing austenitization temperature, this latter has no effect on the bainite transformation temperature B_s or on the hardness after quenching and/or tempering. However, a decrease in toughness properties is expected for the bainite resulting from coarser austenite grain size, thus cooled from higher temperatures.
- A 3°C/s the microstructure mostly consists of bainite with martensite heterogenesouly distributed within the material. The increase in hardness induced by the presence of martensite after quenching is reduced after tempering. This might be explained by a similar microstructural evolution upon tempering for both bainite and martensite in the investigated microstructures.

2.2.5 Selection of austenitization conditions for further microstructural characterizations and assessment of mechanical properties

When considering the impact of microstructure on hardness, it appears that while the increase in hardness due to martensite transformation seems more significant than the loss of hardness due to the appearance of some proeutectoid ferrite, measurements after tempering show that tempered martensite exhibits hardness values close to those of tempered bainite. On the other hand, the hardness of tempered ferrito-bainitic states remains below that of tempered bainite. As a result, the presence of some martensite is whether less problematic in term of strength than the presence of some ferrite. In either case, the main parameter for the selection of optimal austenitization conditions is thus the ferrite fraction at mid-thickness, i.e. for a cooling rate close to 0.3°C/s.

Based on these considerations, three austenitization conditions seem to satisfy the previously mentioned requirements (section 2.1):

- **(A) 920°C – 1 hour**, even with the lower hardness after quench and tempering, this condition is close to those used for the reference material. This justifies further study of the metallurgical behavior of the steel in these conditions.
- **(B) 970°C – 1 hour**, since only little ferrite is found after cooling at 0.3°C/s and that the three tested cooling rates yield hardness after tempering similar to that of the reference material. This condition is the most promising one regarding industrial requirements, since the austenite grain size does not evolve with longer austenitization time, ensuring similar properties across the component thickness.
- **(C) 1020°C – 30 minutes**, for its weak ferrite fraction at mid-thickness and its satisfactory hardness after tempering. One should notice that this temperature is not relevant for the

industrial application; however this austenitization condition will be further investigated in order to study the mechanical properties in the case of an over austenitized component.

These three austenitization conditions will be called (A), (B) and (C) throughout the following of this chapter.

2.3 Further investigations on selected austenitization conditions

2.3.1 Effect of austenitization conditions on microstructures cooled at the quarter-thickness equivalent cooling rate

Further metallographic studies and hardness measurements were done for the three selected conditions followed by cooling at the quarter thickness equivalent cooling rate (0.5°C/s)); this cooling rate being the one used for further studies on the tempering heat treatment (Chapters V and VI). Microstructures were fully bainitic. Hardness values for as-quenched and quenched+tempered microstructural states are gathered in Table 4.3, along with the PAG size and the B_s temperature. They are similar to those of a fully bainitic as-quenched material and of the reference material, respectively.

Studied microstructural properties are the crystallographic bainite packet size and carbide precipitation after tempering. Tensile and toughness properties are then investigated after the same tempering heat treatments as those used previously, and compared with the reference material. Finally, a single austenitization condition will be determined and used for further studies on tempering.

	(A)	**(B)**	**(C)**
PAG size (µm)	25	30	35
B_s (°C)	520	520	520
As-quenched (HV)	338	351	353
Quenched+tempered (HV)	214	219	215

Table 4.3: *Hardness values for as-quenched and quenched+tempered microstructures resulting from cooling at 0.5°C/s after all three selected austenitization conditions.*

Bainitic packet size

The crystallographic bainitic packet size for the three selected austenitization conditions cooled at 0.5°C/s was measured by means of EBSD. Two maps of 1200x900 pixels, where 1 pixel = 0.21 µm, were taken for each sample. The misorientation between two neighboring pixels was then calculated by the OIM analysis software. The indexation rate was higher than 90%.

Theoretical orientation relationships between parent austenite and bainitic ferrite approximatively follows those proposed by Kurdjumov-Sachs (KS) and Nishiyama-Wasserman (NW). The KS orientation relationship implies 24 distinct variants, and the NW orientation relationship allows 12 different variants in terms of crystallographic orientation. In the case of bainitic ferrite, this orientation relationship falls between KS and NW relationships [82]. As an approximation, bainitic

ferrite can therefore be described as following either KS or NW relationships, i.e. 24 + 12 different variants. Under this assumption, the misorientation between two different bainitic packets follows either a KS/KS, a NW/NW or a KS/NW relationship. The lowest possible misorientation angle between two bainitic variants is then 5.25°, thus any misorientation angle higher than 5.25° was supposed to be a packet boundary.

Only regions larger than 50 pixels (~2 µm²) were taken into account. The packet size is given in terms of equivalent circle diameter, although it is not the best suited value for bainitic packets since their shape factors are usually higher than 1. The mean bainitic packet size is given in Table 4.4 and size distributions are reported in Figure 4.14.

Austenitization condition	(A)	(B)	(C)
Mean bainitic packet size (µm)	4.7	4.8	4.6

Table 4.4: *Mean bainitic packet size for the three selected austenitization conditions*

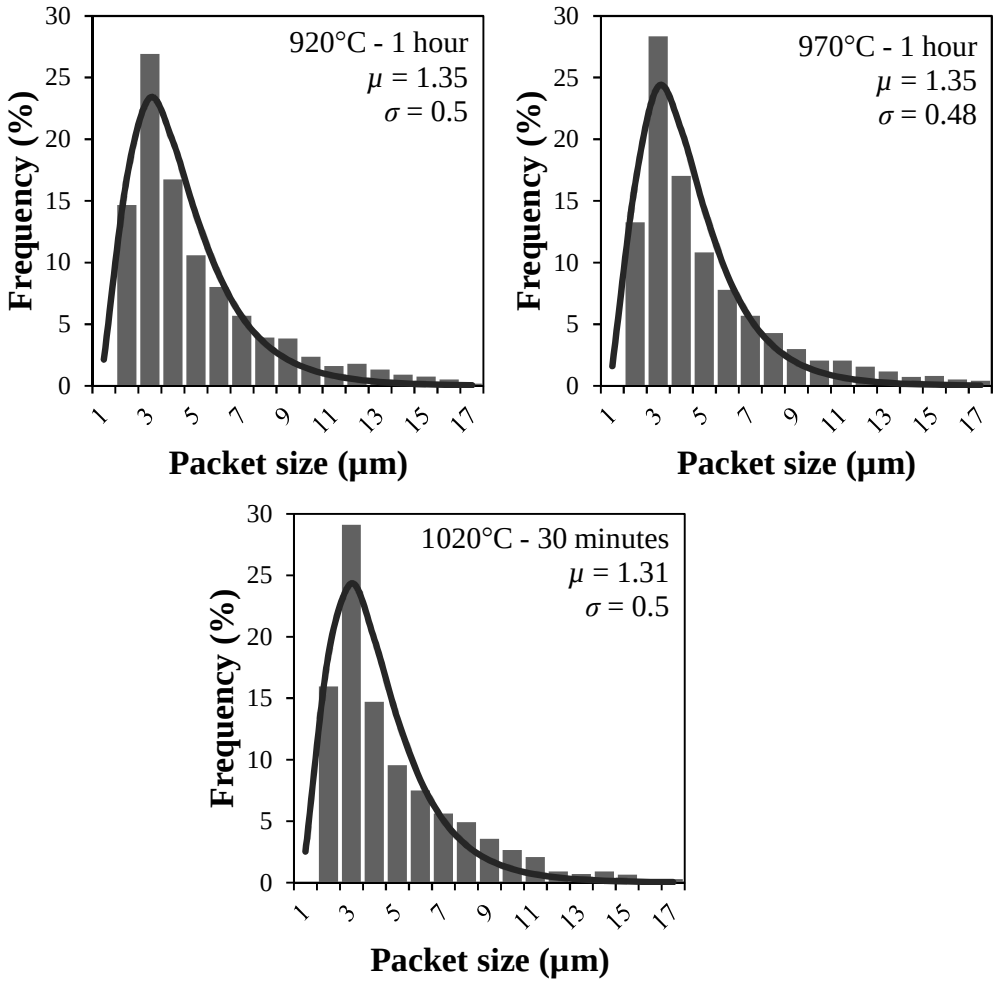

Figure 4.14: *Bainitic packet size distribution for the three selected austenitization conditions followed by a cooling at 0.5°C/s. Continuous lines are lognormal fits of the distributions which corresponding parameters* μ *and* σ *are given.*

Packet size distributions are almost identical, as well as the mean packet diameter. These results are consistent with reports from Bouyne showing the very weak influence of the austenitization conditions on the bainitic packet size (see part. 1.2). Potential factors influencing the bainitic packet size are the prior austenite grain size D and the bainitic start transformation temperature B_s [83], and these two parameters are similar for the three studied conditions (Bs = 520°C for all three conditions, D = 25 µm, 30 µm and 35 µm for conditions (A), (B) and (C) respectively).

Carbide precipitation upon tempering

The influence of austenitization conditions on carbide precipitation after tempering was investigated by means of SEM observations on carbon extraction replicas. The following considerations are purely indicative and more detailed investigations of chemical composition of carbides can be found in Appendix C, using the methodology described in Chapter V.

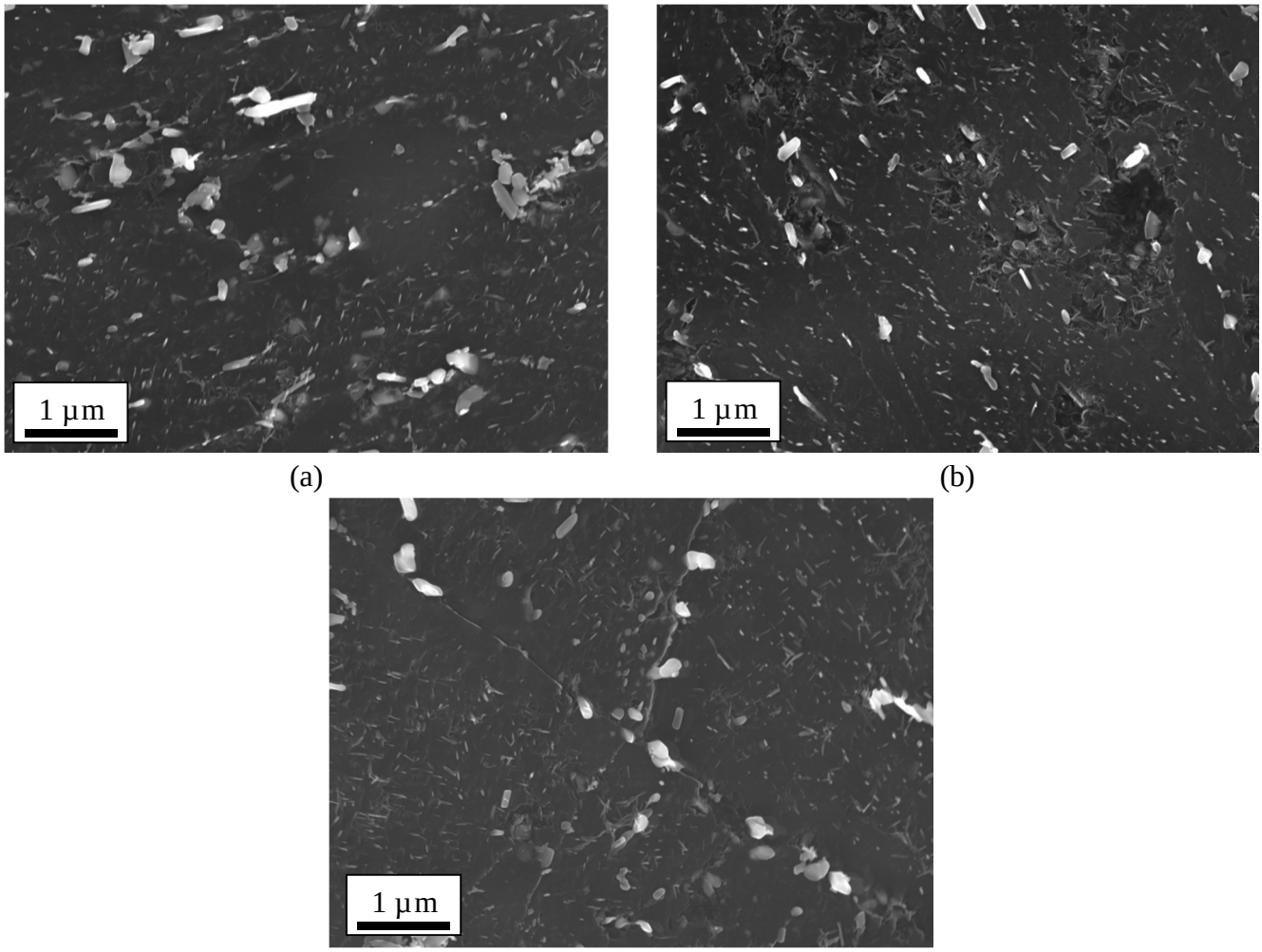

(a) (b)

(c)

Figure 4.15: *SEM Observations on carbon extraction replicas. Tempering condition is 675°C – 5.5 h + 625°C – 16h. Austenitization conditions are (a) 920°C - 1 hour, (b) 970°C – 1 hour, (c) 1020°C – 30 min.*

All three investigated austenitization conditions show similar spatial distribution and morphology of carbides (Figure 4.15). The austenitization conditions do not seem to have an influence on carbide precipitation after tempering under these conditions, which is consistent with the hardness values after tempering.

2.3.2 Influence of the austenitization conditions on mechanical properties

Specimens heat treated with the three selected austenitization conditions and cooled at the quarter-thickness equivalent cooling rate (0.5°C/s) were tested mechanically, by tensile and impact toughness tests on miniature specimens. More information on the testing conditions can be found in Appendix A. Tensile tests were conducted at room temperature, while impact toughness tests were done at -125°C, i.e. the lowest temperature of the brittle-to-ductile transition range of the reference material. For each austenitization condition, four Charpy specimens and two tensile specimens were tested. These specimens were machined from blanks samples as detailed in Chapter II. Results and discussion reported here are only preliminary, general assessments, and a more complete discussion on the tensile and impact toughness properties for the studied steel can be found in Chapter VI.

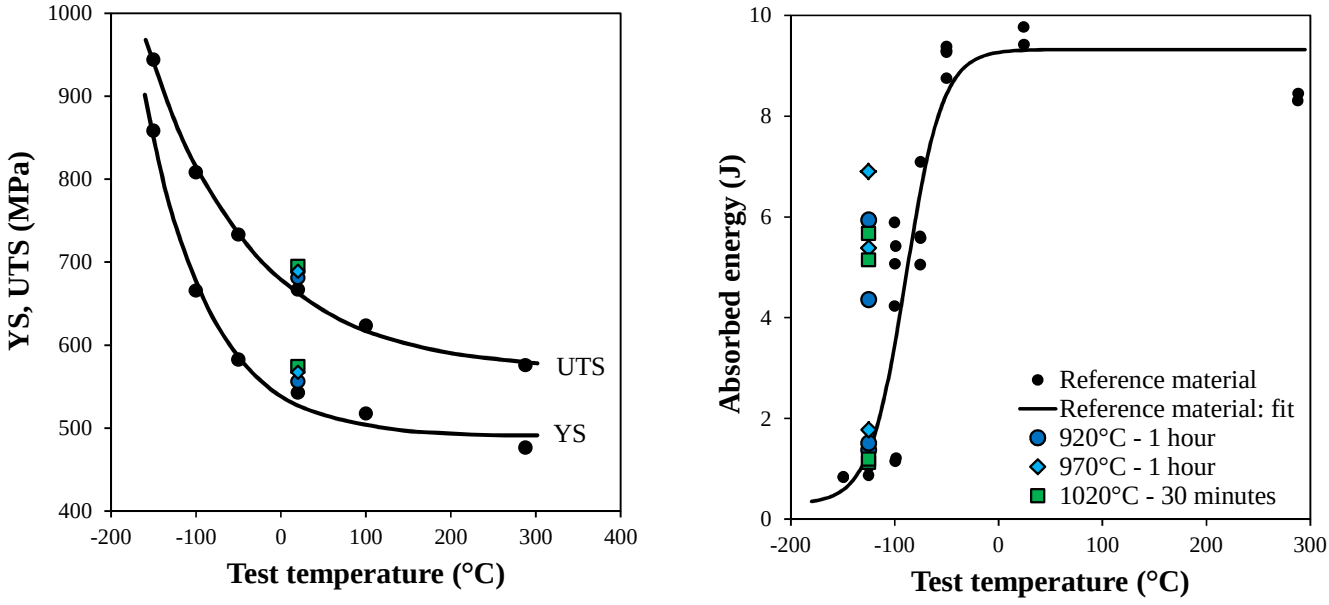

(a) (b)

Figure 4.16: *Effect of austenitization conditions (a) on Yield Strength (YS) and Ultimate Tensile Strength (UTS) and (b) on absorbed energy after tempering at 675°C for 5h30 + 625°C for 12h. Reference material specimens had been austenitized at 930°C for 1 hour and were machined from the quarter- thickness of the cylindrical shell.*

Figure 4.16 shows the comparison of the tensile and impact properties between all three selected austenitization conditions and the reference heat treatment. Austenitization conditions have nearly no influence on the tensile properties and impact energy, and no difference was found when compared to the reference material. The impact energy of heat-treated specimens is distributed into two groups, namely 0.5-2 J (fully brittle fracture) and 4-7 J (mixed brittle-ductile fracture). Such scatter is

observed on the reference material. On the other hand, four tests were done at -125°C on the reference material, all resulting in fully brittle fracture with an impact energy ranging from 0.9 to 1.3 J. Assuming that this difference is statistically representative, then reheated specimens seem to exhibit better toughness properties compared to the reference material.

The overall negligible effect of selected austenitization conditions on mechanical properties could be expected when considering microstructures after tempering. Indeed, all three metallurgical states have close PAG sizes, similar B_s temperature during cooling, a comparable fully bainitic microstructure with the same mean bainitic packet size, and similar precipitation state after tempering. Moreover, since only one tempering condition was used, one can imagine that the recovery of the dislocation structure inside bainitic laths is also the same for all three metallurgical states.

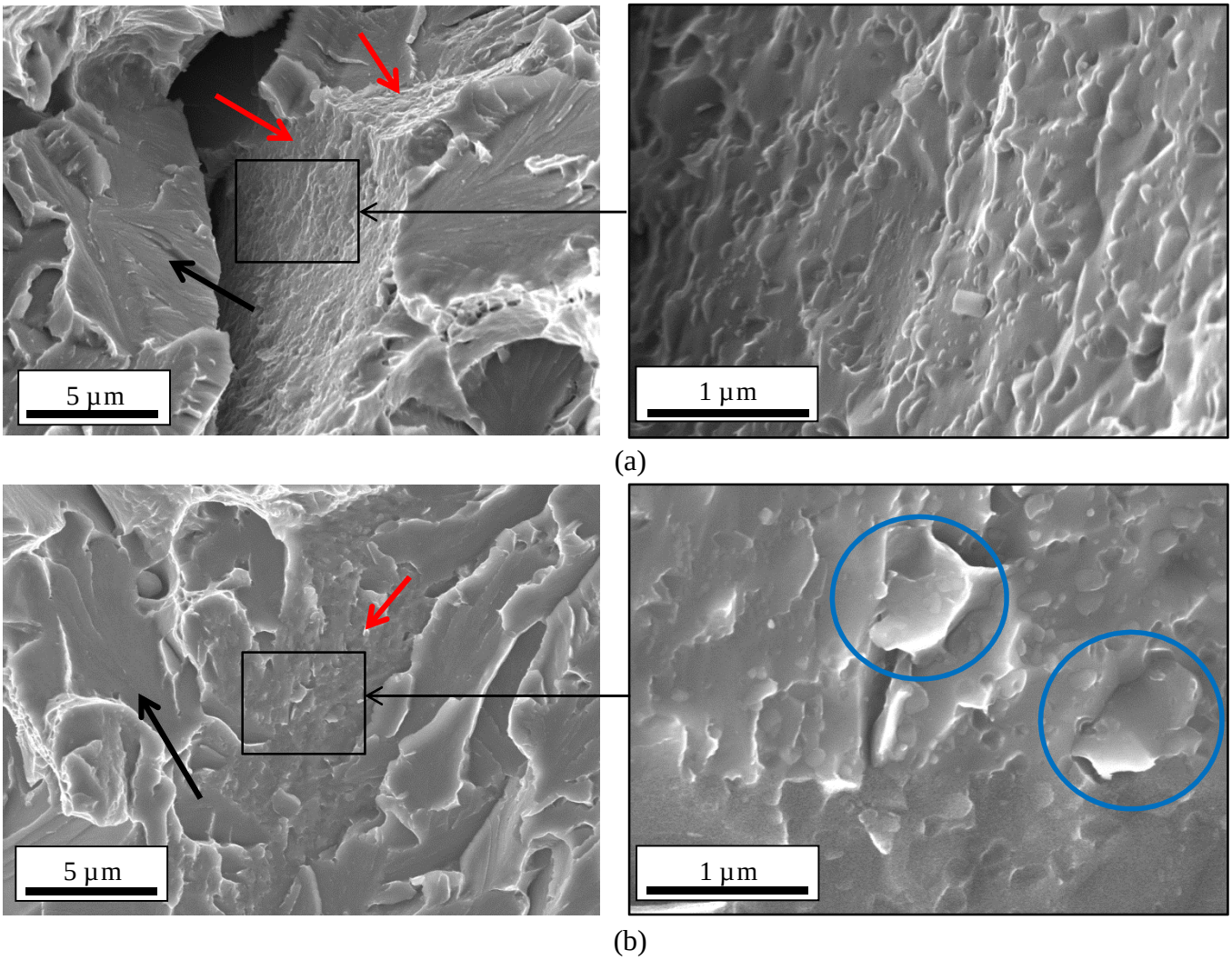

Figure 4.17: *Evidence of intergranular fracture patches (a) 970°C – 1 hour, impact toughness: 5.38 J, (b) 1020°C – 30 minutes, impact toughness: 1.19 J. Red arrows indicate intergranular patches, black arrows indicate cleavage surface, blue circles indicate ductility*

Intergranular fracture was observed from place to place on various specimens (Figure 4.17), sometimes close to the crack initiation site, however no correlation with either the austenitization conditions or the impact energy was found. These intergranular facets seem to be covered by small particles that could be precipitates located at prior austenite grain boundaries. It seems unlikely that these intergranular facets are induced by phosphorus segregation at boundaries, given the very low amount of phosphorus in the studied material and the relatively low tempering time compared to the ones necessary to induce temper embrittlement. On the other hand, the intergranular facet shown in Figure 4.17.b seems to exhibit flat dimples (blue circles), indicating that the intergranular rupture may be ductile. In both cases, since these regions are not systematically found at either of the two fracture surfaces of a given specimen, it seems unlikely that they act as the only crack initiation site.

3. CONCLUSION

This chapter addressed effects of austenitization heat treatment on transformations upon cooling. The major result is that the austenite grain size is not the only variable to be taken into account. The amount of molybdenum and carbon atoms segregated at austenite grain boundaries during the austenitization step can improve the bainitic hardenability by impeding ferrite nucleation or limiting ferrite grain growth.

Moreover, ferrite precipitation has higher influence on hardness compared to martensite, since the presence of the latter does not affect hardness after tempering.

As a conclusion, and with the exception of an austenitization at 920°C for 30 minutes, PAG size ranging from 25 µm to 35 µm gives satisfactory results. In other words, austenitization temperatures ranging from 920°C to at least 970°C for an austenitization time of 1 hour can be considered to yield similar results for the investigated tempering conditions. The 1020°C – 30 minutes austenitization could also be potentially interesting, but the grain size is not expected to be homogeneous through the thickness. Although this temperature is too high to be industrially realistic, it shows that the final microstructure and precipitation after tempering are rather robust with respect to the austenitization conditions. Among the two lower austenitization temperatures, the temperature of 920°C appears to be slightly less adapted to the desired properties. Ferrite is found for the mid-thickness equivalent cooling rate, and microstructural homogeneity through thickness could be a concern since an austenitization for only 30 minutes at this temperature results in ferrite precipitation at the quarter thickness. The robustness of the metallurgical behavior of this steel for an austenitization at 920°C for 1 hour is thus questionable. Thus, the chosen austenitization condition for further investigations is 970°C – 1 hour, and has been used as a basis for the study of the metallurgical behavior during tempering.

Chapter V: Carbide precipitation during tempering

TABLE OF CONTENTS

Once the material cooled after austenitization, a tempering heat treatment is conducted in order to precipitate excess carbon in solid solution and tune final mechanical properties. In 2.25 Cr – 1 Mo steels, various type of carbides with different stabilities can be found depending on the tempering time and temperature: M_3C, M_2C, M_7C_3, $M_{23}C_6$ and M_6C [14]. The size, nature and phase fractions of these carbides have a direct influence on the mechanical properties of the material, for instance by improving creep properties [15] or by inducing secondary hardening [16]. Thus, tight control of carbide precipitation through tempering is a key point for the targeted industrial application.

This chapter is divided in four main parts. First, a thorough literature review is conducted on the topic of carbide precipitation upon tempering. Carbide properties such as their crystal structure, chemical composition (metallic elements) and morphology, as well as their nucleation sites, are summarized. It appears that each type of carbide exhibits specific properties, in particular a specific amount of metallic elements that could be used for easy identification.

In the second part of this chapter, the carbides in the material are characterized, using an experimental and a theoretical way. Carbide stability and chemical composition at equilibrium are first estimated by means of thermodynamic calculations. Using literature data, a methodology for experimental characterization of carbides is set up by determining relative amounts of metallic elements in carbides by means of EDX measurements on carbon extraction replicas. Preferential nucleation sites and typical morphologies of carbides are also characterized using this methodology. Typical features are thus associated to each kind of carbides. The nature of carbides is then confirmed by electronic diffraction.

This methodology, coupled with XRD analyses on electroetching residues, is then used in order to study the evolution of carbides during the tempering heat treatment. Precipitation upon heating is

first investigated, and the effect of tempering time and temperature on the evolution of carbides is then discussed. The influence of the stress-relieving heat treatment is also investigated.

1. LITERATURE REVIEW: CARBIDE PRECIPITATION IN 2.25 Cr – 1 Mo STEELS

A literature review on the topic of carbides precipitation in 2.25 Cr – 1Mo steel was conducted, particularly on the carbides precipitation sequence, carbide characteristics and on their nucleation mechanisms. This review is used as a basis for the experimental characterization of carbides and will also be used to discuss further experimental results.

1.1 Precipitation sequence

In chromium-molybdenum steels, carbide precipitation occurs in a specific order: during tempering, metastable carbides precipitate before the most stable carbides. This is due to difference in interfacial energies with the matrix promoting nucleation of less stable carbides, such as M_3C and M_2C, over more stable ones. Moreover, since metastable carbides have a greater ratio of carbon/metallic elements, their precipitation or enrichment removes a non-negligible proportion of solute atoms from the matrix, thus delaying the precipitation of more stable carbides [94].

The pioneering work on carbide precipitation in 2.25 Cr – 1 Mo steel was published by Baker & Nutting in 1959 [14], who proposed a time-temperature-precipitation (TTP) diagram for this material[7]. An updated version of this diagram was released by Nutting[8] [95] and is shown in Figure 5.1. The chemical composition of the steel and the prior heat treatments were unfortunately not reported.

According to these authors, the generic precipitation sequence in bainitic and martensitic 2.25 Cr - 1 Mo steels can be written as follows:

$$\begin{array}{ccccc} \varepsilon\text{-carbide} & \rightarrow & M_3C + M_2C & \rightarrow & M_7C_3 \\ & & \downarrow & & \downarrow \\ & & M_{23}C_6 & \rightarrow & M_6C \end{array}$$

Equilibrium carbides are M_6C, however, $M_{23}C_6$ carbides take a very long time to dissolve (more than 1000 hours at 750°C) and are thus commonly referred as equilibrium carbides too. It should be pointed out that the heating step is not taken into account in Baker & Nutting's work. In ferritic 2.25 Cr – 1 Mo steels, the precipitation sequence is not the same, and only M_2C and M_6C were found.

[7] Steel composition of reference [14], in wt% : 0.15 C, 0.50 Mn, 0.18 Si, 0.012 S, 0.018 P, 2.12 Cr, 0.94 Mo, 0.17 Ni, 0.077 Cu, 0.009 Sn

[8] No information are given on the steel composition, however due to the similarities between the TTP diagrams reported by [14] and [95], one can assume that it is the same material.

The generic precipitation sequence, or more precisely the order in which carbides precipitate, has been widely confirmed by almost all work reported (for instance, [16, 17, 94, 96]) for martensitic, pearlitic and bainitic 2.25 Cr – 1 Mo steels. Notable exceptions are Vyrostokova et al. who found that $M_{23}C_6$ dissolve to the benefit of M_7C_3 in vanadium bearing 2.25 Cr – 1 Mo [97] and Yang et al. who did not found any M_6C carbides even after 18 years of service exposure in pearlitic 2.25 Cr – 1 Mo steels, allegedly due to the low concentration of Si in their studied steel [98]. As a general rule, the steel chemical composition impacts the carbide domain of stability: Mn was reported to accelerate M_7C_3 carbide precipitation while Si was reported to accelerate the precipitation of M_2C and to stabilize M_6C carbides [99]. While the effects of Mn on M_7C_3 carbides and of Si on M_2C remain unclear, it is assumed that Si increases the driving force for formation of M_6C carbides [100]. Increase in the material carbon content also tends to favor the M_6C carbides at the expense of $M_{23}C_6$ carbides [101].

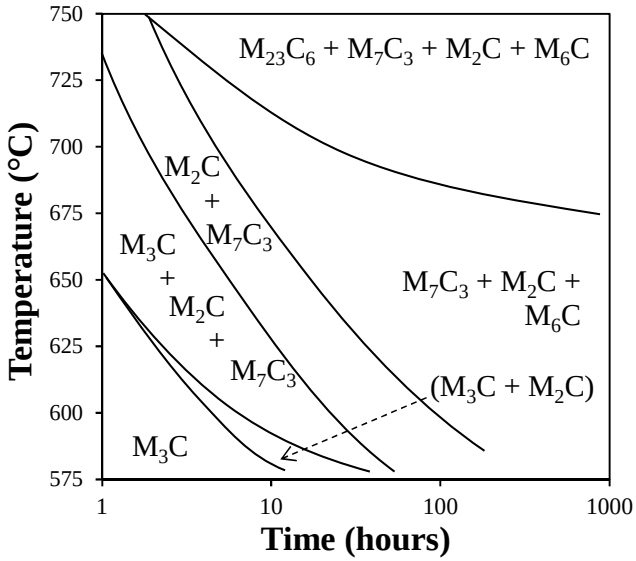

Figure 5.1: *Time-temperature-precipitation diagram in 2.25 Cr – 1Mo steel. From* [95]

1.2 Carbide characteristics

All kinds of carbides susceptible to precipitate in 2.25Cr – 1Mo steel exhibit specific characteristics, such as their crystallographic structure, chemical composition, morphology and nucleation sites. Here, their chemical composition is considered regarding the amount of iron, chromium and molybdenum only. It is important to notice that the following data were gathered over a wide range of studies about martensitic, pearlitic and bainitic 2.25 Cr – 1 Mo steels, regardless their thermal history and their average chemical composition. Thus, since the thermal history has an impact on the relative amount of metallic elements in carbides, only trends are reported here. For the same reason, no mention of the size of carbides is made here.

The various properties of carbides are summarized in this section in order to set up a method for characterizing carbides in the present experimental work. No mention of ε-carbides will be made here due to their very fine size and their rapid transformation into cementite expected at the beginning of tempering.

1.2.1 M_3C carbides

Cementite is the most common carbide in many steels, its crystal structure is orthorhombic with a = 5.07 Å, b = 6.74 Å and c = 4.52 Å. Morphological features of cementite depend on the temperature and time of tempering: at low temperatures, i.e. less than 600°C, clusters of "branch-like" cementite resulting from the decomposition of retained austenite are reported [14, 96, 102] (Figure 5.2). With further heating or tempering, these clusters spheroidize and form lenticular or globular shaped particles [102–105]. Cementite is commonly considered as iron-based carbide (Fe_3C); EDX analysis shows that cementite particles are rich in iron with some chromium and very little molybdenum [24, 96, 104, 106].

1.2.2 M_2C carbides

The M_2C crystal structure is usually described using an hexagonal cell where a = 2.99 Å and c = 4.72 Å [94, 107]. However, it has been proved that Mo_2C is more accurately described by an orthorhombic cell where a = 4.72 Å, b = 6.00 Å and c = 5.19 Å [108]. Here, the orthorhombic description will be used. They are found as fine needle-shaped particles [15, 17, 94, 98, 103, 105] following a regular Widmanstätten pattern in the matrix [96, 102], as shown in Figure 5.3. Gope et al. measured an orientation relationship between the M_2C carbides and the bainitic matrix of $(101)_\alpha$ ~ 5 deg from $(\bar{1}\bar{1}.\bar{1})M_2C$ and $(233)_\alpha$ ~ 5 deg from $(11.0)M_2C$ [103] assuming an hexagonal structure for the carbide. These carbides are molybdenum-based and their chemistry is close to Mo_2C. EDX analysis shows that their composition in metallic elements consists mostly of molybdenum with some chromium and very little iron [17, 24, 96, 101, 104]; moreover they tend to get enriched in molybdenum with time [96, 101]. Fine dispersions of coherent or semi-coherent M_2C carbides are held responsible for the material good mechanical properties, such as resistance to creep [15, 102] and strengthening due to secondary hardening [16].

Some authors mentioned that face-centered-cubic Mo-rich M_2C carbides can also be found, however very few reports were found about these carbides. These precipitates are located at prior austenite grain boundaries or within bainitic laths and exhibit a fine globular morphology [107, 109] (Figure 5.4). Their lattice parameter was experimentally determined as a = 4.21 Å [109]. No extra data on their composition was found.

Cubic M_2C carbides are coherent with the ferritic matrix. They are stable at low temperatures and progressively transform into orthorhombic M_2C with increasing temperature. Swift reported that only very fine cubic M_2C particles are found after tempering at 370°C while a mix of cubic and orthorhombic M_2C is observed around 580°C [109]. Moreover, Nagakura & Oketani reported that cubic $MoC_{0.54}$ formed by reactions between evaporated films of molybdenum and carbon turned to be orthorhombic upon heating at temperatures higher than 600°C [110]. These evidences suggest that the cubic structure is the most stable form of M_2C at low temperature which then transforms into orthorhombic M_2C when increasing temperature. It was also proposed that cubic M_2C can precipitate from decomposition of M_6C at temperatures lower than 580°C [94, 107].

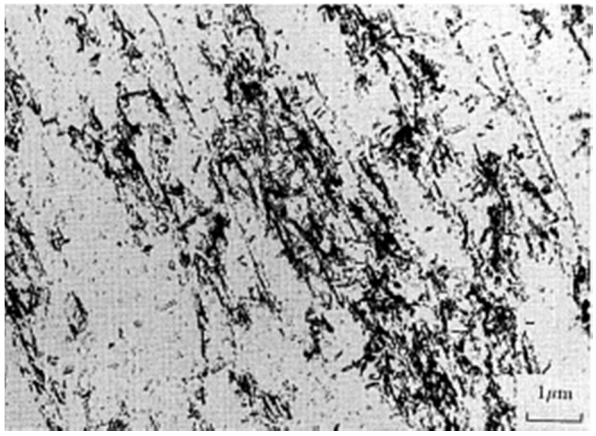

Figure 5.2: *TEM observation of carbon extraction replicas showing branch-like cementite in 2.25 Cr – 1 Mo steel. From* [96]

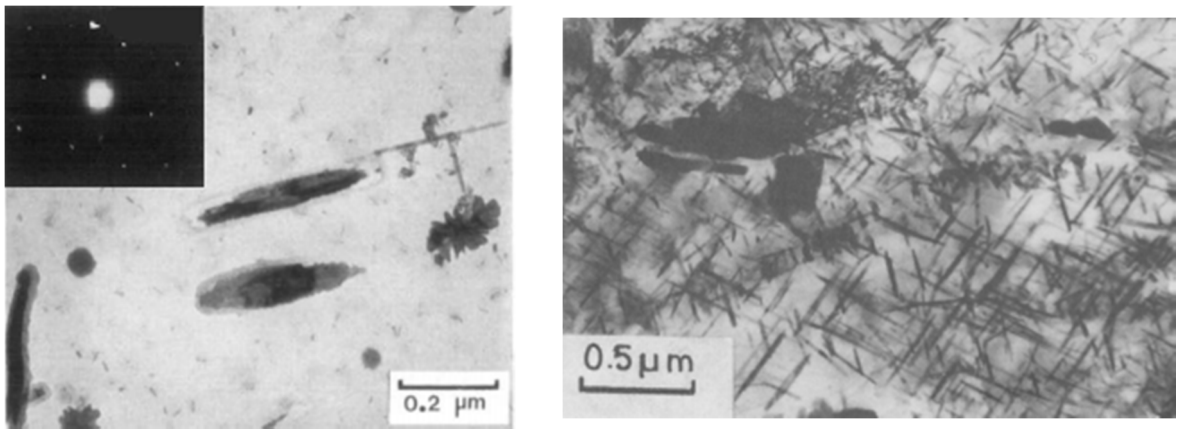

(a) (b)

Figure 5.3: *TEM observations on carbon extraction replicas: (a) M_2C carbides with the corresponding electron diffraction pattern. B = $(10\bar{1}1)$ (from* [98]*), (b) Numerous M_2C carbides forming a Widmanstätten pattern in the matrix (from* [103]*).*

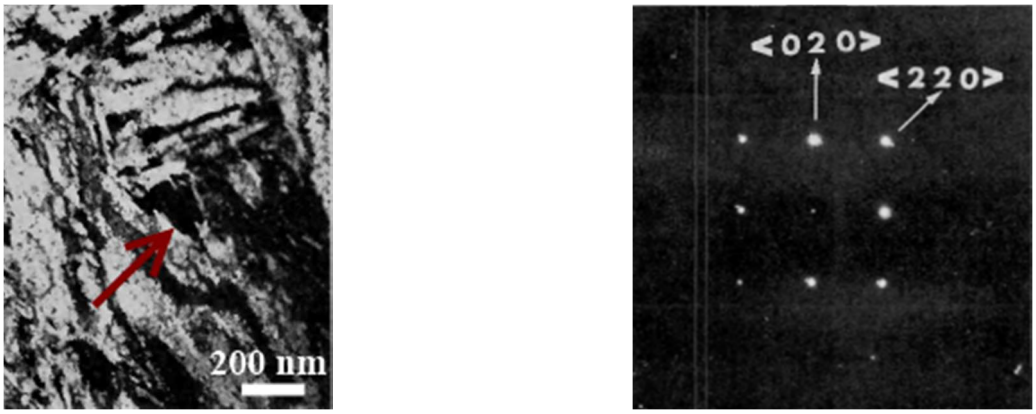

(a) (b)

Figure 5.4: *(a) TEM thin foil observation of cubic M_2C within bainitic laths (b) Corresponding electron diffraction pattern. B = (001). From* [109].

1.2.3 M_7C_3 carbides

The M_7C_3 carbide is often considered to have a pseudo-hexagonal structure with lattice parameters a = 13.98 Å and c = 4.51 Å [111]. It is better described with an orthorhombic structure, with a = 4.53 Å, b = 7.02 Å and c = 12.15 Å [112]. M_7C_3 carbides can be easily identified thanks to their typical streaky electron diffraction patterns due to the presence of stacking faults in planes perpendicular to the basal plane when considering the hexagonal structure, as shown in Figure 5.5.a [111]. These carbides are found at interfaces and can exhibit rhombus-shaped [84, 101] or rod-like [84, 94, 101, 105] morphologies (Figure 5.5.b).

M_7C_3 carbide can exist either as an iron carbide, Fe_7C_3 or a chromium carbide, Cr_7C_3. In 2.25 Cr - 1 Mo steels, M_7C_3 carbides are typically chromium-rich with iron and some molybdenum [17, 84, 96, 101, 104] and tend to get richer in chromium with time [17, 96]. Thus, M_7C_3 is considered here as a chromium-based carbide which equilibrium composition is expected to be close to Cr_7C_3.

1.2.4 $M_{23}C_6$ carbides

The $M_{23}C_6$ crystal structure is face-centered cubic, where a = 10.60 Å (Figure 5.6.a). These carbides precipitate at prior austenite grain boundaries [15, 103] but can also be found within the bainitic laths [101, 104]. In the latter case, they are lying parallel to the longitudinal axis of the laths. Their typical morphology is rod-like [98, 101, 103–105] (Figure 5.6.b).

The chemistry of $M_{23}C_6$ carbides can be expressed as $Fe_{21}Mo_2C_6$ in steels that contain molybdenum and as $Cr_{23}C_6$ in chromium steels [113]. Reported measurements in 2.25 Cr – 1 Mo steels show their chemical composition is rich in iron with chromium and some molybdenum [17, 24, 96, 101, 104, 113]. Enrichment in chromium with time is also reported [94, 104, 114], suggesting that the $Cr_{23}C_6$ could be the equilibrium composition.

1.2.5 M_6C carbides

M_6C carbide crystal structure is face-centered cubic where a ~ 11.0 Å. This lattice parameter is very similar to that of the $M_{23}C_6$ one, thus these two carbides are not differentiable by XRD [101, 106]. However, they can be easily differentiated by EDX analysis since M_6C are typically molybdenum rich with some iron and little chromium [17, 24, 104, 107, 113].

These carbides exhibit a lenticular or a globular morphology [94, 103–105] and are generally found in grain boundaries, as shown in Figure 5.7.

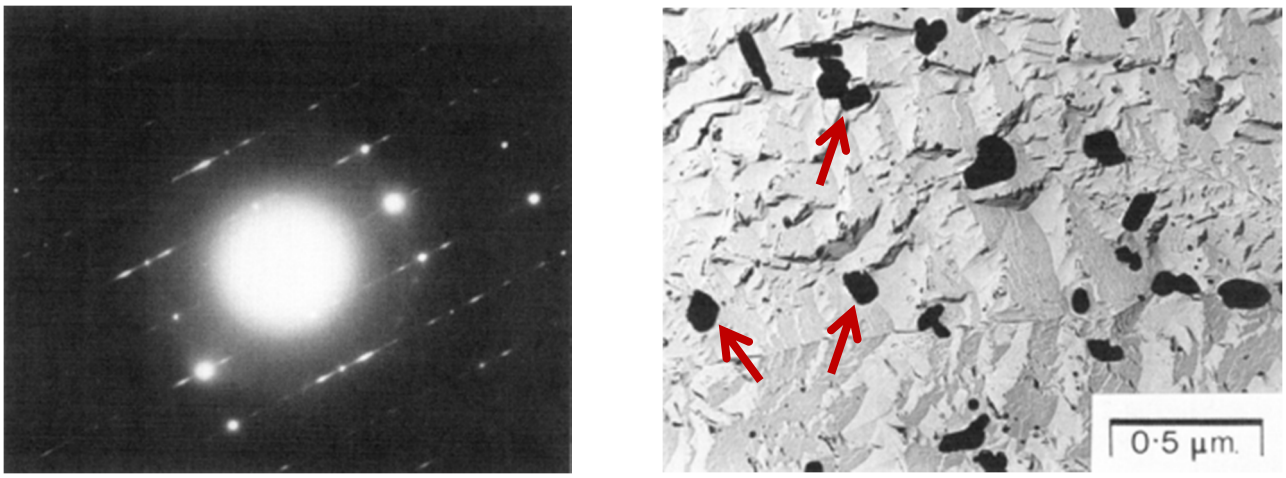

(a) (b)

Figure 5.5: *(a) M_7C_3 carbide electron diffraction pattern exhibiting streaks due to stacking faults, (b) TEM observations on carbon extraction replica showing rhombus-shaped M_7C_3 carbides. From* [101]

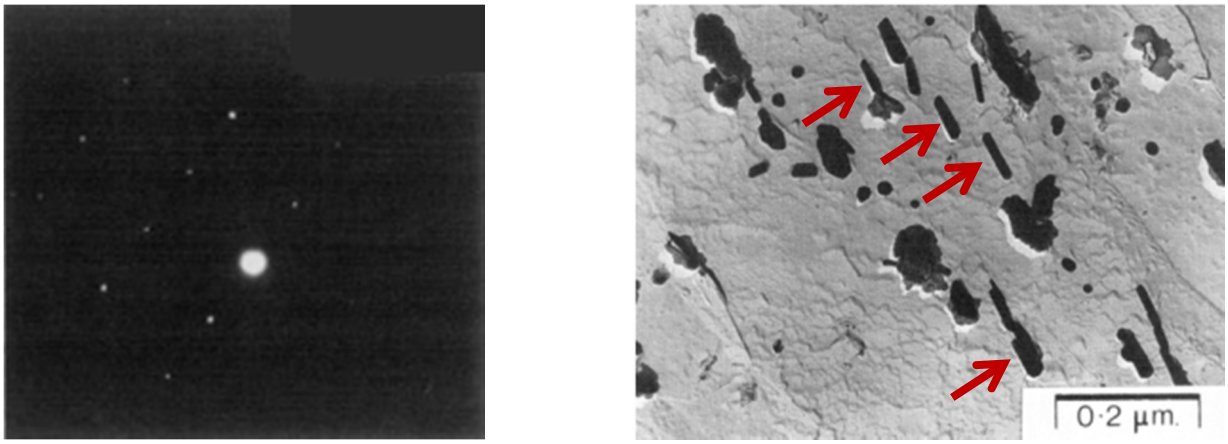

(a) (b)

Figure 5.6: *(a) Electron diffraction pattern of $M_{23}C_6$, B = (122) (from* [98]*), (b) TEM observations of a carbon extraction replica showing rod-shaped $M_{23}C_6$ carbides (from* [101]*)*

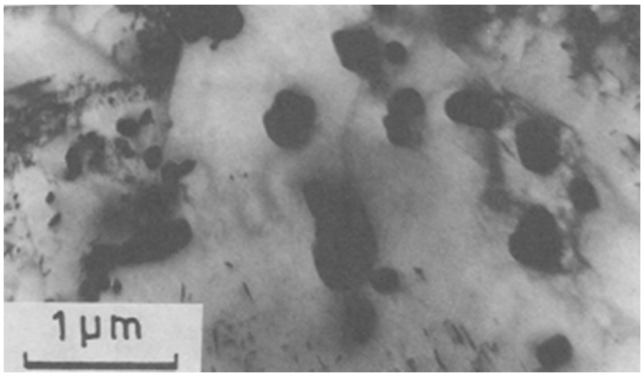

Figure 5.7: *TEM observations on a carbon extraction replica showing globular M_6C carbides, from* [103]

1.2.6 Summary of carbide characteristics

All gathered information regarding the composition, morphology, crystal structure and precipitation site of carbides is summarized in Table 5.1. It appears clearly that all of these carbides exhibit specific properties. In particular, the relative amounts of Fe, Cr and Mo is typical of the nature of carbides, and thus can be used as a means of characterization by EDX measurements on carbon extraction replicas.

Carbide	Morphology	Metallic elements	Nucleation site	Crystal
M_3C	Lenticular, globular	Fe-rich with Cr	Interfaces	Orthorhombic
M_2C (ortho)	Needle-like	Mo-rich with Cr	Laths	Orthorhombic
M_2C (fcc)	Globular	Mo-rich	Laths	fcc
M_7C_3	Rhombus-shaped, rod-like	Cr-rich with Fe	Interfaces	Orthorhombic
$M_{23}C_6$	Rod-like	Fe-rich with Cr	Interfaces/laths	fcc
M_6C	Globular	Mo-rich with Fe	Interfaces	fcc

Table 5.1: *Carbide characteristics from available literature data. "Interfaces" stands for prior austenite grain boundaries and lath boundaries, while "laths" stands for the matrix or dislocations.*

1.3 On the nucleation of carbides

As a general rule, metastable carbides can eventually be replaced by more stable carbides by two different mechanisms:

(i) By *in-situ* transformation: nucleation of new carbides occurs at the interface between pre-existing carbides and the matrix. In some cases, transformation occurs within pre-existing carbides and is triggered by enrichment in solute (direct transformation).

(ii) By separate nucleation: new carbides precipitate elsewhere. This can lead to further dissolution of metastable carbides due to chemical potential gradients.

It is recognized that M_3C carbides can precipitate either from direct transformation of ε-carbide or by separate nucleation, in the latter case, during the decomposition of retained austenite for instance [14]. M_2C carbides are known for precipitating by separate nucleation since cementite accommodates very little molybdenum which then remains in solid solution in the matrix.

Most authors agree that M_7C_3 carbides nucleate at the interface between cementite and matrix. The usual argument supporting this hypothesis is that cementite becomes rapidly enriched in chromium, thus depleting the matrix. Nucleation of chromium carbide M_7C_3 from a chromium depleted matrix appears to be unlikely, while on the other hand the interface between the matrix and the cementite can easily be provided with both chromium and carbon [95, 98]. Pelletier suggested that the occurrence of separate nucleation of M_7C_3 increases with the chromium content in steels [10], and in 3.80 Cr steel these carbides mostly nucleate independently of cementite [111]. Such results are consistent with the previous assumption: In a chromium-rich matrix, M_7C_3 carbides nucleate separately, while in a chromium depleted matrix they nucleate at the cementite/matrix interfaces. Thus, in the studied steel, M_7C_3 carbides are expected to nucleate mostly at the interface

between cementite and matrix; however some separate nucleation might occur, although to a lesser extent.

Baker & Nutting originally suggested that $M_{23}C_6$ carbides form by *in-situ* nucleation, either within the cementite particles or at the interface between cementite and matrix [14]. However, Nutting later considered that these carbides nucleate separately [95]. This assumption might seem contradictory with the previous assessment about M_7C_3 carbides, since $M_{23}C_6$ are chromium carbides too. However, due to their cubic unit cell, they can readily dissolve more iron than M_7C_3 and thus need less chromium to precipitate. This assumption could explain why $M_{23}C_6$ in 2.25 Cr – 1Mo steels are iron-rich as reported in Table 5.1.

M_6C nucleation is believed to happen separately. It was shown that the first M_6C carbides which precipitate contain low amount of molybdenum, and that further dissolution of M_2C releases molybdenum which is then attracted by M_6C carbides [101]. Another hypothesis is that dissolution of M_2C, for instance due to vicinity of $M_{23}C_6$ carbides [15, 17, 102], leads to the release of enough molybdenum in the matrix to trigger nucleation of M_6C. In every case, evolutions of M_2C and M_6C carbides are closely linked to each other.

2. EXPERIMENTAL CHARACTERIZATION OF CARBIDES

Tempering was conducted at four different temperatures: 650°C, 675°C, 700°C and 725°C, for times ranging from so-called 0 hour (as-heated states) to 24 hours. Before investigating the evolution of carbides during such heat treatments, one must find a way to differentiate them. To this aim, thermodynamic calculations were performed in order to determine the carbides stability and their composition at equilibrium. Carbides were then experimentally characterized by means of TEM observations and EDX analyses on carbon extraction, as well as XRD analyses on electroetching extraction residues. More information about the experimental procedures used for each of these techniques can be found in Appendix A. The results are then compared with the literature data and the thermodynamic calculations.

2.1 Thermodynamic calculations

Thermodynamic simulations were performed on ThermoCalc and Matcalc softwares, respectively using the TCFe7 and the mc_fe_v2.022 databases. Stability and chemical composition of carbides at thermodynamic equilibrium were investigated.

The average chemical composition of the steel was chosen with respect of results reported in Chapter II (Table 2.1, quarter-thickness composition). It should be reminded that this composition is only an average one, and thus the local enrichments in the matrix reported in Chapter II cannot be taken into account. Besides, calculations were made for ferritic matrix using only thermodynamic considerations, and do not take potential effects of the nucleation sites into account.

Since none of both databases do not include cubic M_2C, all M_2C carbides as reported in this section are the non-cubic one, represented by their hexagonal cell. M_7C_3 carbides are implemented with their trigonal cell.

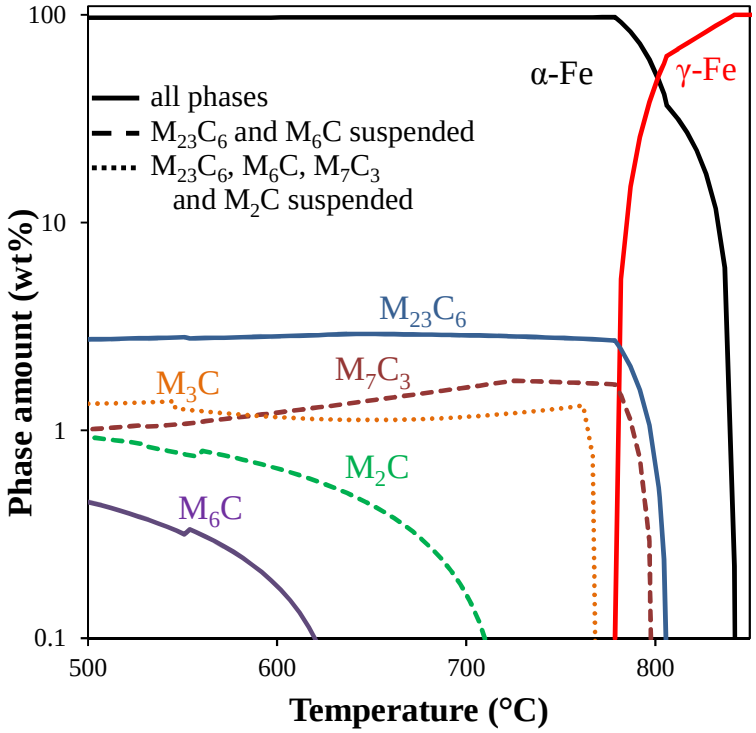

Figure 5.8: *Carbide stability diagram as predicted by Thermocalc*

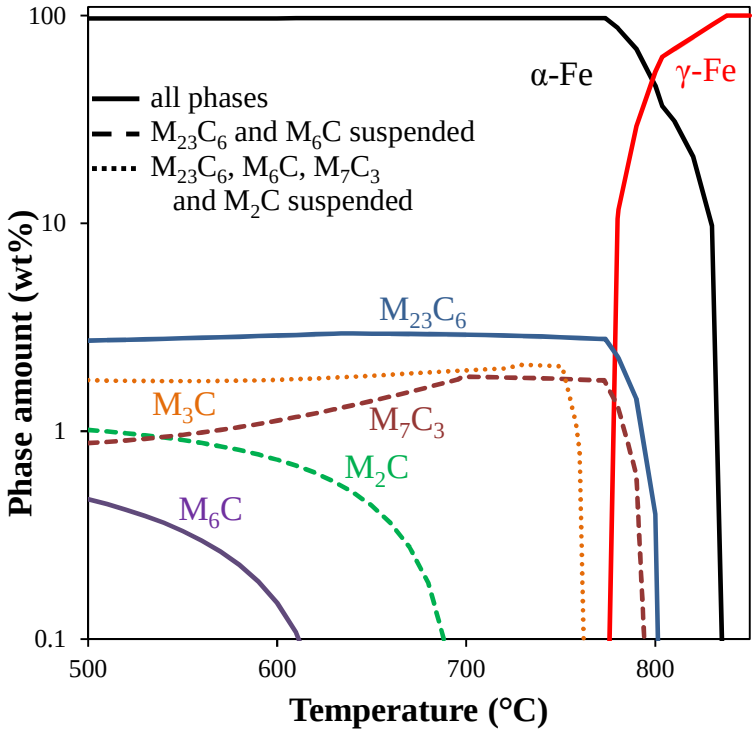

Figure 5.9: *Carbide stability diagram as predicted by Matcalc*

2.1.1 Stability diagram

Carbide stability diagrams calculated with both databases are shown in Figure 5.8 and Figure 5.9, respectively. Equilibrium diagrams (full lines) were calculated considering all possible phases, however only phases of interest are shown. Metastable diagrams were calculated by suspending one or several carbides (dashed and dotted lines). While not perfectly rigorous, this approach allows defining the relative stability of each carbide compared to the others. The reported dissolution temperatures are the ones allowed by the thermodynamics, and therefore do not account for kinetic interactions between carbides. Thus, they must be handled with care. It must also be pointed out that ferrite-austenite intercritical domain temperatures change by a few degrees when some carbides are suspended; this phenomenon is not represented in the figures since it is negligible.

Equilibrium carbides are $M_{23}C_6$ and M_6C. Once suspended, M_7C_3 and M_2C appear, and M_3C only appear if M_7C_3 are suspended. These predictions are consistent with the carbide precipitation sequence reported in section 1.1.1. Good agreement is found between both databases with the exception of the dissolution temperatures which are slightly lower in MatCalc results, as already stated in Chapter II. M_2C carbides are not stable at temperatures higher than 725°C according to ThermoCalc and higher than 695°C according to MatCalc. Thus, these carbides are not expected to be found at the highest studied tempering temperature, namely, 725°C.

According to thermodynamic simulations, M_6C carbides are not expected to be observed during this study: they are only stable below 640°C with ThermoCalc and below 625°C with MatCalc, while the lowest studied tempering temperature is 650°C. These results are in contradiction with the TTP diagram reported by Baker & Nutting, however, simulations performed on MatCalc using their steel chemical composition results in dissolution of M_6C at 580°C. The reason for these differences remains unknown; however the similarities between results obtained using both databases indicate for the considered steel in this study that such difference is unlikely to be due to errors in calculations.

2.1.2 Chemical composition in metallic elements of carbides at equilibrium

The equilibrium chemical composition in metallic elements has been calculated for each carbide at the four tempering temperatures. Only Fe, Cr and Mo were taken into account. For metastable carbides, the composition was calculated by suspending one or several carbides as explained above. Thus, while the composition of $M_{23}C_6$ can be considered as the equilibrium one, it is more accurate to speak about pseudo-equilibrium for M_7C_3, M_2C and M_3C. Figure 5.10 shows calculations performed on both MatCalc and Thermocalc. All considered chemical compositions are reported in weight percents. Good correspondence between results from both databases is obtained, and results can be summarized as follows.

- The cementite is chromium-richer at low temperature (55%), but enriches in iron with increasing temperature until iron becomes predominant. The amount of molybdenum is very low, near 2%, and does not evolve with temperature.
- M_7C_3 carbides are chromium-rich; however, the chromium content decreases with increasing temperature from 65% at 650°C to 50% at 725°C. This chromium depletion comes together with

an enrichment in iron and molybdenum, respectively from 25% at 650°C to 30% at 725°C and from 13% at 650°C to 15% at 725°C.

- At 650°C, $wt\%_{Fe} = wt\%_{Cr} = 40\%$ in $M_{23}C_6$ carbides. With increasing temperature, the iron content increases up to 50% at 725°C while the chromium content decreases (35% at 725°C). The molybdenum content remains stable, around 20%.
- M_2C carbides are very rich in molybdenum (80%) with up to 20% of chromium and almost no iron (1-3%). Their composition remains stable with temperature, with the exception of 725°C where an increase in chromium at the expense of molybdenum occurs when considering the MatCalc predictions. This change in composition is due to the predicted dissolution of M_2C at this temperature.

As a general conclusion, these composition values are in very good agreement with the literature data reported in section 1.2. These results can then be used for helping the experimental characterization, and the MatCalc database appears reliable for further thermokinetic calculations.

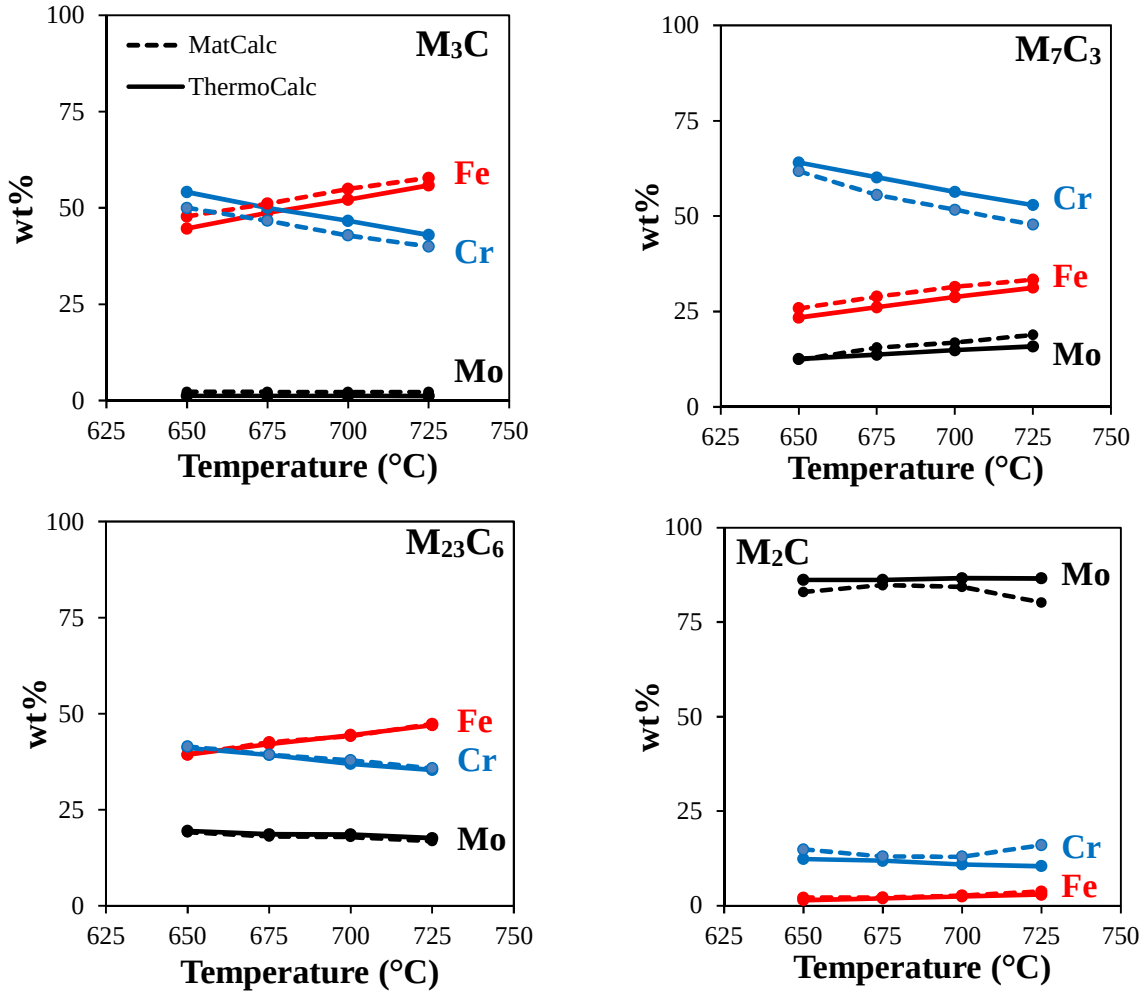

Figure 5.10: *Equilibrium metallic composition of each carbide as a function of temperature. Continuous lines are Thermocalc calculations, dashed lines are MatCalc ones.*

2.2 Experimental characterization

2.2.1 TEM observations, EDX analyses and electron diffraction

From the literature review, it appears clearly that each different kind of carbide exhibits specific crystallographic structure, metallic elements content and morphology (see Table 5.1). Thus, carbides can be identified by means of EDX analyses on carbon extraction replicas. Experimentally analyzed carbides can be categorized into four different groups according to their metallic element content as shown in the example of Figure 5.11: iron-rich, iron-rich with some chromium, chromium-rich with some iron, and molybdenum-rich. When comparing these compositions with the typical composition determined by Moss & Kelly [24] and thermodynamic calculations made using MatCalc for the given temperature (in this case, 675°C), it appears clearly that these four groups are respectively M_3C, $M_{23}C_6$, M_7C_3 and M_2C carbides. In the present study, these four types of carbide were found for almost each tempering condition, with the exception of the as-heated states which will be discussed later. No M_6C carbides were ever found, as predicted by the thermodynamic calculations.

It should be pointed out that the compositions given by Moss & Kelly and reported in Figure 5.11 are mean values based on a literature review, regardless of the thermal history or average composition of the material. Moreover, the equilibrium composition of M_3C carbide is not represented since this carbide is unstable and is unlikely to reach equilibrium.

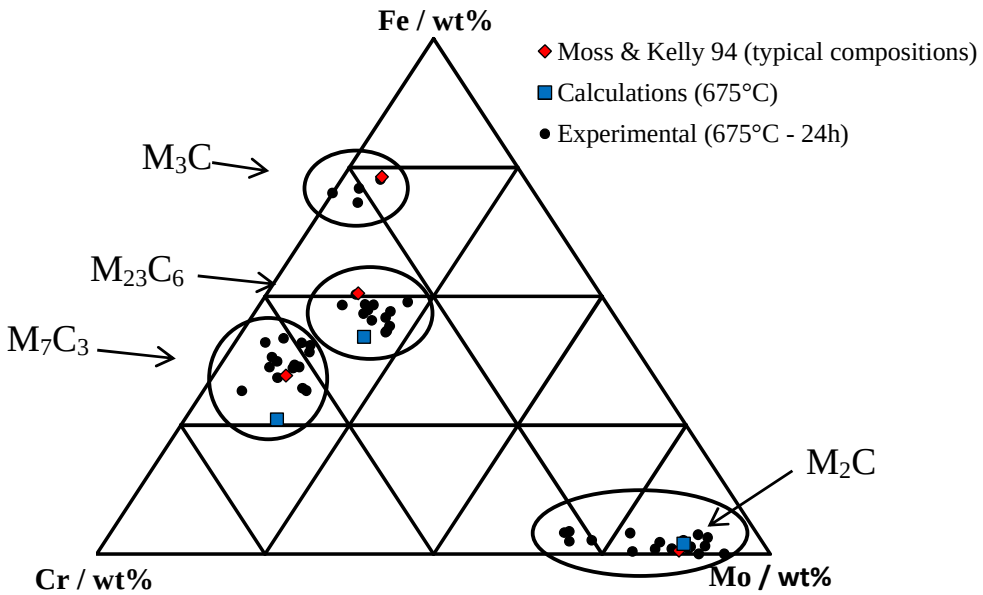

Figure 5.11: *Ternary representation of the chemical content in metallic elements in carbides at 675°C. Calculations were performed with the MatCalc database.*

Morphologies of carbides that were identified by EDX measurements are summarized in Figure 5.12. The length scale in this figure is given for information purpose, as the size of carbides evolves with tempering time and temperature. The carbide morphology is closely related to the nucleation sites.

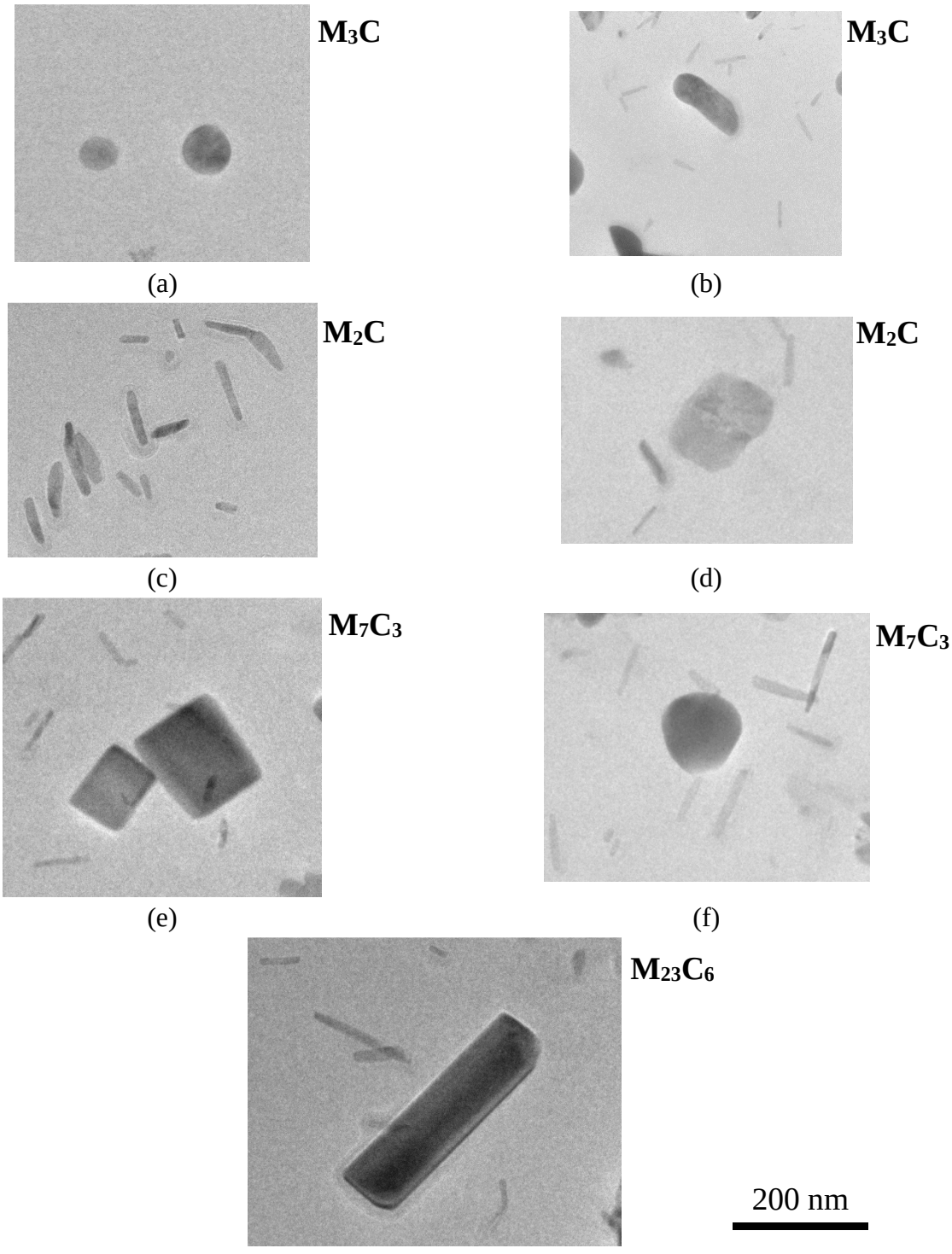

Figure 5.12: *Encountered carbide morphologies: (a) globular M_3C carbides, (b) lenticular M_3C carbide, (c) needle-like M_2C carbides, (d) globular M_2C carbide, (e) rhombus-shaped M_7C_3 carbides (f) globular M_7C_3 carbide and (g) rod-like $M_{23}C_6$ carbide. TEM observations on carbon extraction replicas, identification made by EDX measurements.*

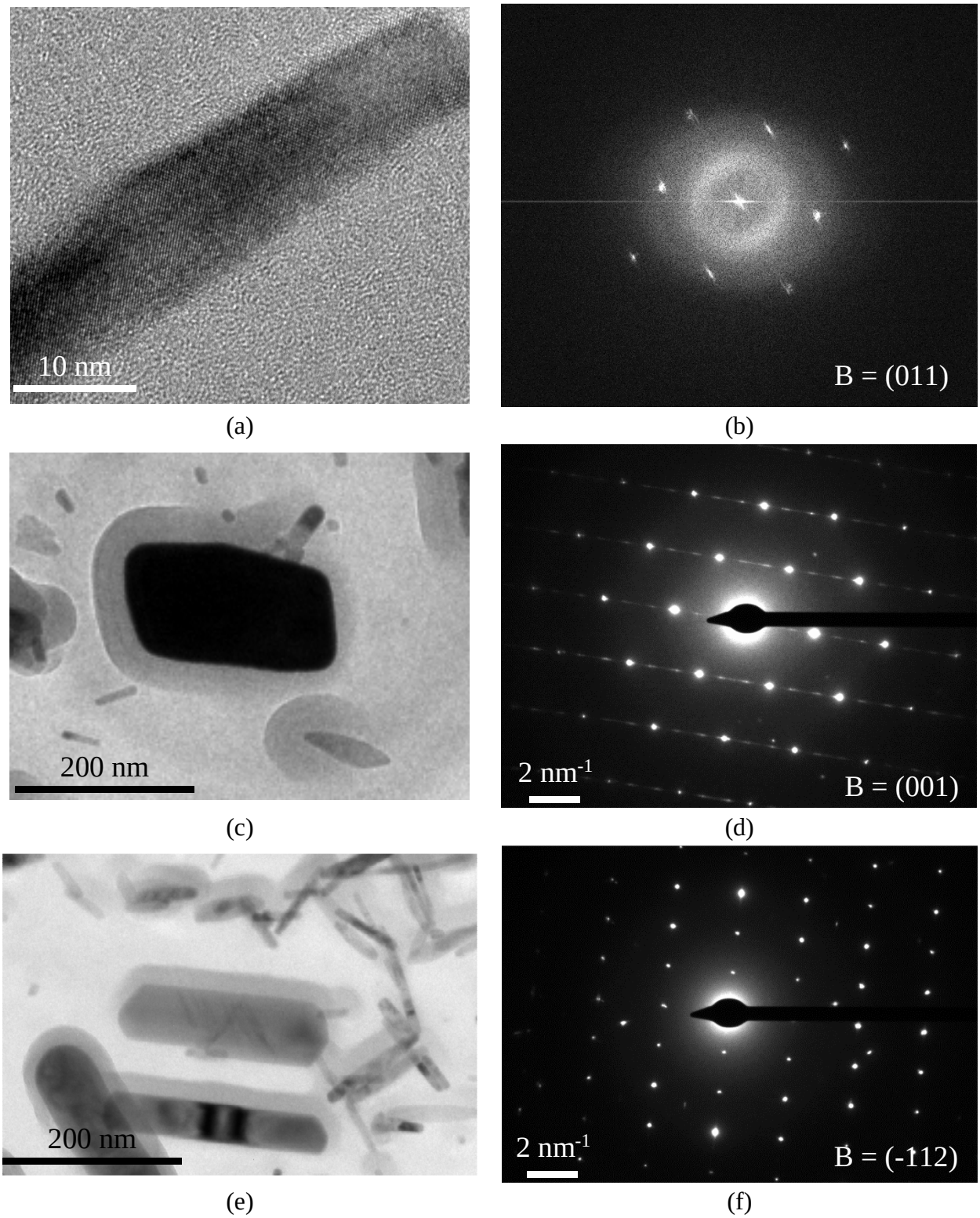

Figure 5.13: *(a) HRTEM image of M_2C carbide, (b) corresponding diffraction pattern, (c) TEM image of a M_7C_3, (d) corresponding diffraction pattern, (e) TEM image of a $M_{23}C_6$ carbide, (f) corresponding diffraction pattern. Observations on carbon extraction replica, tempering: 675°C – 5.5 hours. M_7C_3 and M_2C are identified using their hexagonal unit cells.*

- M_3C are globular or lenticular, depending on the tempering conditions. They may be observed within the matrix but are mostly found at interfaces, particularly in as-heated states and for short durations at low temperature. This specific case will be developed in more detail in section 3.3.1.
- M_2C carbides are needle-shaped or appear as globular particles finely dispersed within the matrix. Needle-shaped M_2C particles are found much more frequently than globular ones. From literature data, one would expect that globular particles are cubic while needles are orthorhombic; this point will be addressed in section 2.2.2.
- $M_{23}C_6$ are rod-like precipitates and are mostly found within the bainitic packets, aligned with the direction of laths. Thus, they seem likely to be located at lath boundaries; however, no complementary observations on thin foils were made to confirm or not this assumption.
- M_7C_3 are rhombus-shaped when found within laths and globular when located at the interfaces. The globular type is predominantly found.

To confirm EDX analyses electron diffraction patterns were obtained for different carbide morphologies, as shown in Figure 5.13. Good agreement is found with EDX characterizations: needles are orthorhombic M_2C, rhombus-likes particles are orthorhombic M_7C_3 and rod-like particles are cubic $M_{23}C_6$. No pattern was taken from M_3C and cubic M_2C due to their rarity.

Properties of carbides as experimentally determined are summarized in Table 5.2. Very good correspondence with the literature review summarized in Table 5.1 is obtained. Thus, TEM-EDX analyses performed on carbon extraction replicas is a fast and efficient way to characterize the nature, size and chemical composition in metallic amount as a function of tempering conditions..

Carbide	Morphology	Typical amount of metallic elements (wt%)
M_3C	Lenticular, globular	70 Fe – 25 Cr – 5 Mo
M_2C	Needles, globular	3 Fe – 22 Cr – 70 Mo
M_7C_3	Rhombus-shaped, globular	37 Fe – 50 Cr – 13 Mo
$M_{23}C_6$	Rod-like	50 Fe – 35 Cr – 15 Mo

Table 5.2: *Carbides morphologies and typical composition as experimentally determined.*

2.2.2 X-Ray diffraction on electroetching residues

X-Ray diffraction on electroetching residues coupled with Rietveld refinements was used in order to confirm the crystal structure and quantify the phase fraction of each type of carbides. Examples of diffraction spectra are given in Figure 5.14.

Rietveld refinements were conducted using crystal structure for carbides gathered in Table 5.3. These crystal structures have been chosen regarding the literature data (Table 5.1).

No cubic M_2C carbides were ever found, thus in the following M_2C carbides will refer to the orthorhombic ones.

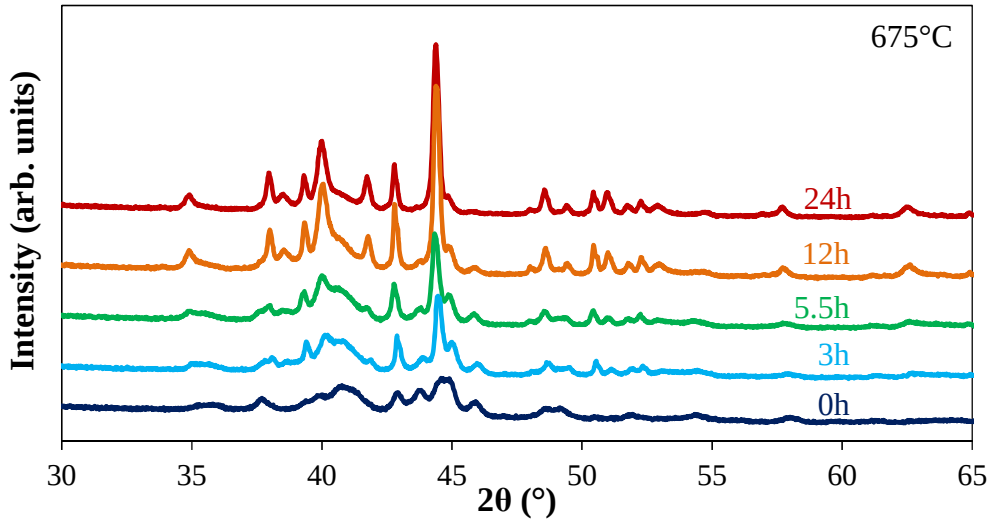

Figure 5.14: *Examples of diffraction spectra obtained after electroetching extraction at 675°C after tempering for different time durations*

Carbide	Space group	*a* (Å)	*b* (Å)	*c* (Å)	Pearson data sheet No.
M_3C	Pnma (62)	5.07	6.74	4.52	1720152
M_2C (ortho)	Pbcn (60)	4.75	6.02	5.20	1715923
M_2C (fcc)	Fm-3m (225)	4.25	4.25	4.25	1503408
M_7C_3	Pnma (62)	4.52	6.97	12.07	1413617
$M_{23}C_6$	Fm-3m (225)	10.60	10.60	10.60	1901808

Table 5.3: *Crystallographic structure used for Rietveld refinements in XRD analyses.*

3. EFFECT OF TEMPERING CONDITIONS ON THE CARBIDE PRECIPITATION

3.1 Experimental results

Before studying the carbide precipitation during isothermal holding itself, the as-quenched state has to be characterized as a starting point. As reported in Chapter IV, it consists of a fully bainitic microstructure with an average prior austenite grain size of 25 µm and an average crystallographic bainitic packet size of 4.8 µm. No carbides were found from TEM observations of carbon extraction replicas. However, XRD analysis shows the presence of retained austenite in this material, equal to 6 wt% according to Rietveld refinements. The presence of retained austenite in such material after quenching has already been observed [10], and is typical of the expected granular bainite microstructure.

Most of the carbon in the material is supposed to be concentrated in the retained austenite particles. The heating rate is set to 0.03°C/s (2°C/min), which means that more than 5 hours are needed to reach the lowest tempering temperature. This long heating step and rather high tempering temperature (> 600°C) should give enough time for retained austenite to decompose into ferrite and

carbides, and for these carbides to start evolving during heating. Thus, it is necessary to study the evolution of microstructure upon heating.

3.1.1 Carbide precipitation upon heating

Figure 5.15 shows partial XRD spectra of bulk samples heated up to 400°C and 600°C respectively and then water quenched, along with the XRD spectrum of the as-quenched, non-reheated state.

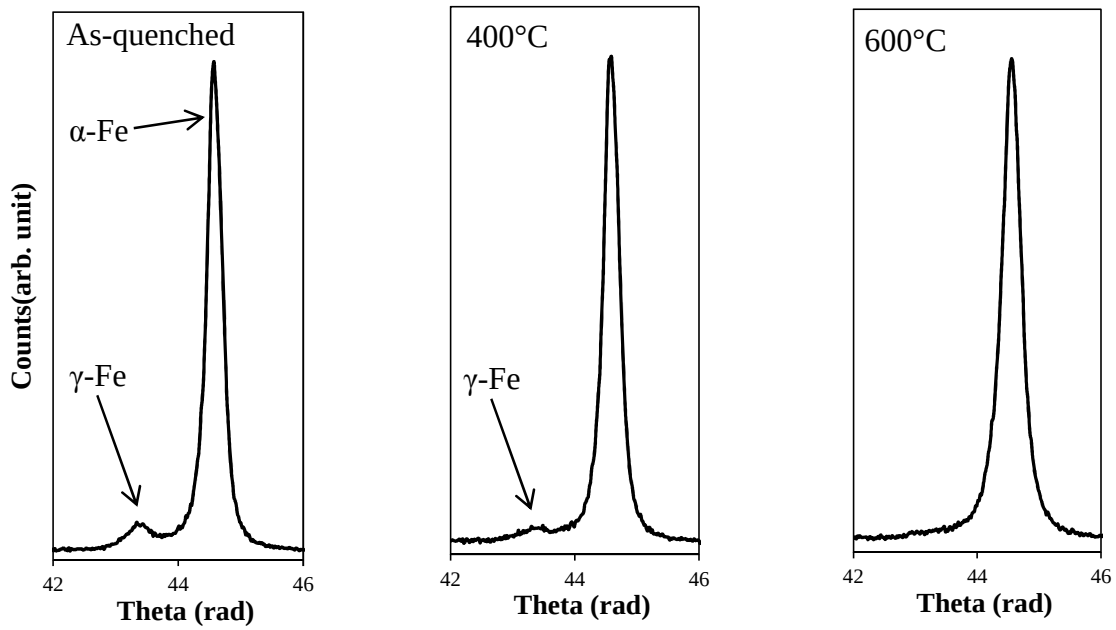

(a) (b) (c)

Figure 5.15: *XRD spectra on bulk samples: (a) as-quenched sample, (b) heated up to 400°C then water quenched, (c) heated up top 600°C then water quenched.*

It appears clearly that austenite has started to decompose at 400°C and that the transformation is entirely finished at 600°C. Observations by TEM of carbon extraction replicas did not reveal the presence of carbides for the sample heated up to 400°C. Either precipitated carbides are too small to be observed or they are too coherent with the matrix to be successfully transferred to the carbon replica. No observations were made for the sample heated up to 600°C.

Figure 5.16 shows SEM observations of carbon extraction replicas of samples heated up to 650°C, 675°C, 700°C and 725°C then water quenched. At 650°C, large clusters of carbides are observed at the interfaces such as prior austenite grain boundaries and lath boundaries. These clusters densified at 675°C, then start to disappear at 700°C and are almost fully dissolved at 725°C. At this temperature, prior austenite grain boundaries are mostly decorated with globular M_7C_3 carbides and few rod-like $M_{23}C_6$. Along with these clusters, some isolated carbides can also be found in the laths for all four states, in an increasing number as the temperature increases.

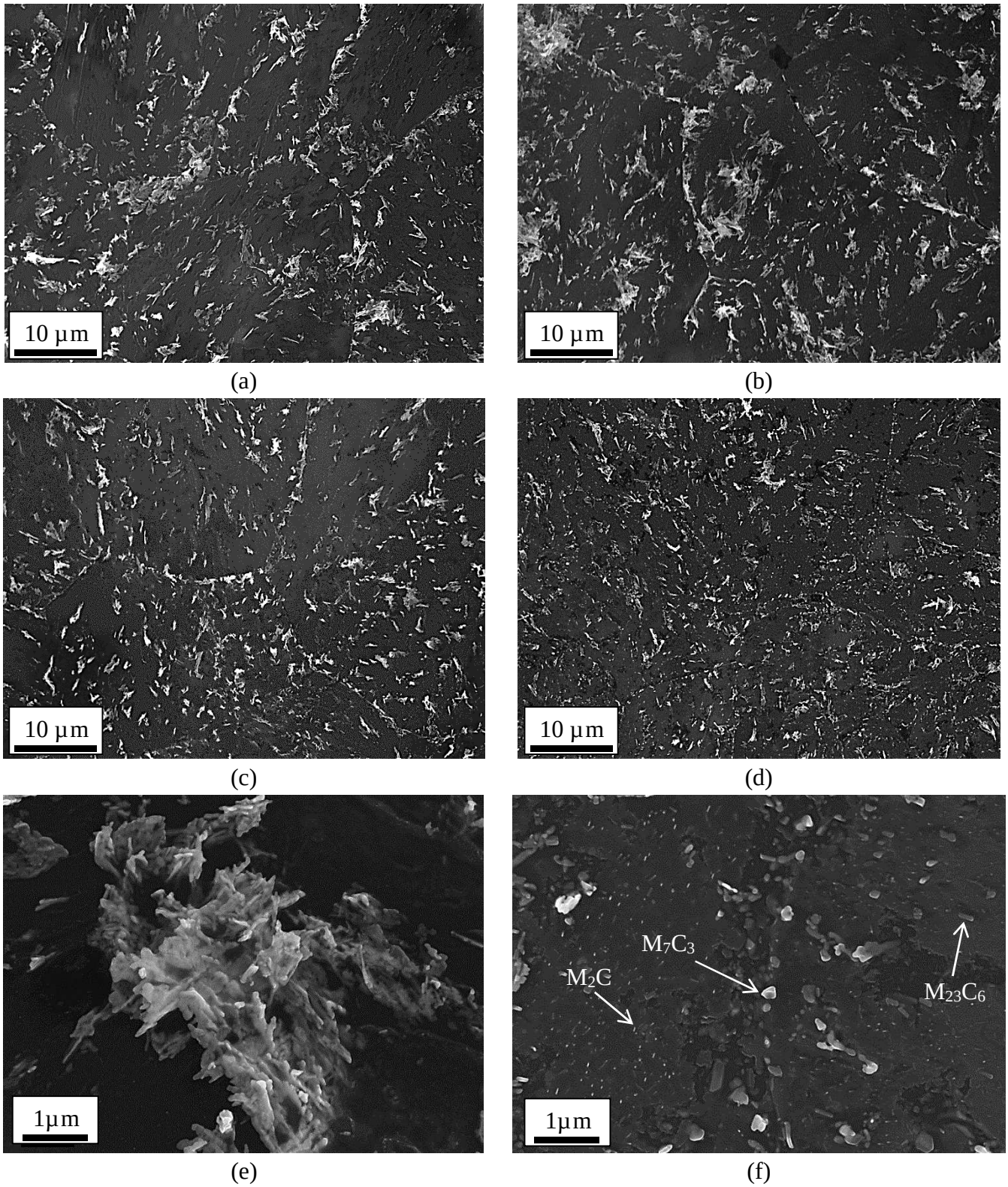

Figure 5.16: *SEM observations on carbon extraction replicas of samples heated then water quenched. (a) 650°C, (b) 675°C, (c) 700°C, (d) 725°C, (e) detail of (b) showing massive cluster, (f) detail of (d) showing M_7C_3 at the prior austenite grain boundaries and M_2C and $M_{23}C_6$ carbides in the matrix*

Figure 5.17 and Figure 5.18 show the chemical composition in metallic elements determined by EDX analyses for clusters and isolated carbides, respectively, along with the typical composition reported by Moss & Kelly [24].

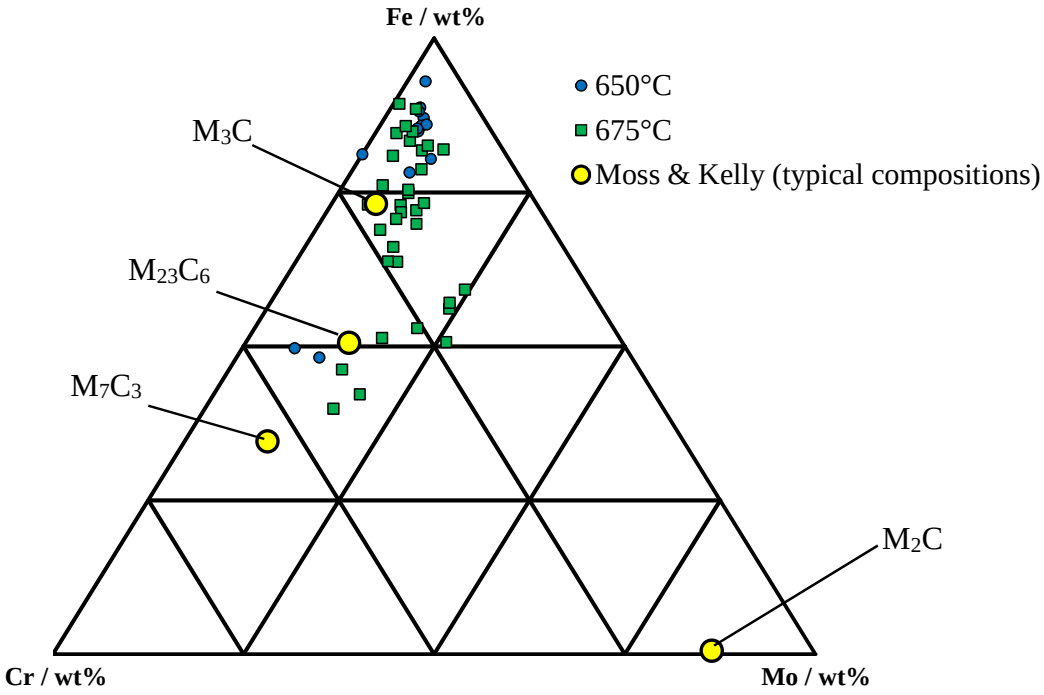

Figure 5.17: *Ternary representation of the metallic chemical content in carbide clusters after heating up to different temperature and water quenching (EDX measurements).*

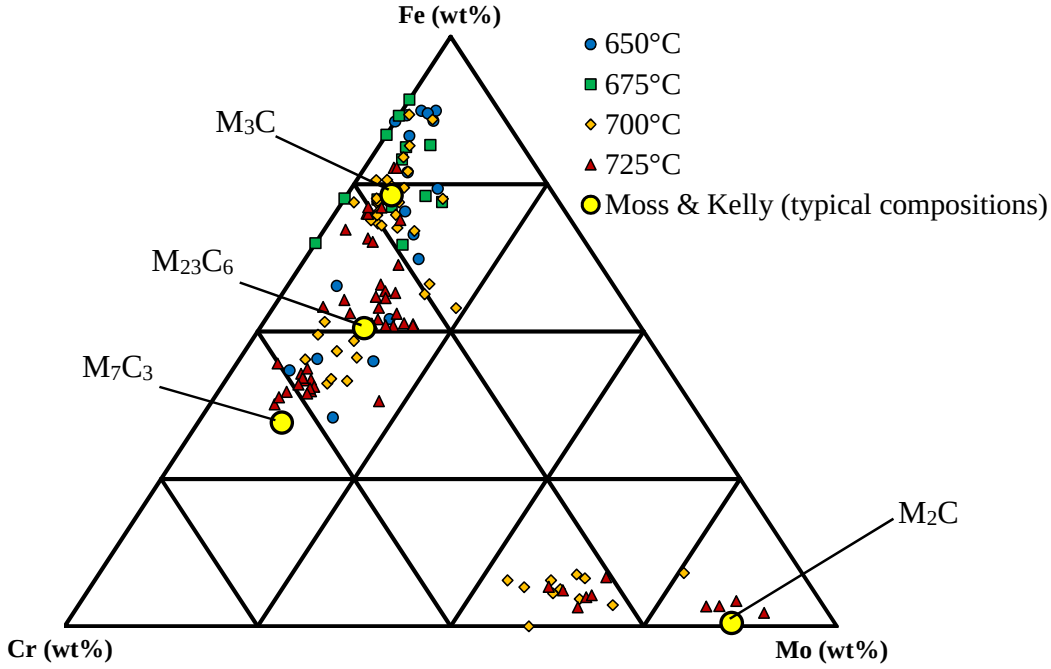

Figure 5.18: *Ternary representation of the metallic chemical content in isolated carbides after heating up to different temperature and water quenching (EDX measurements).*

Many carbide clusters appear to be iron-rich and poor in molybdenum. With increasing temperature, they tend to get enriched in chromium. Moreover, these clusters are not homogeneous in composition in their volume; their chromium content can vary depending on the analyzed region regardless where the analyses were conducted, at the cluster periphery or in their center. On the whole, these clusters remain within the composition range for cementite, and get enriched in chromium with increasing time. This is consistent with the reported "branch-like" cementite resulting from the decomposition of retained austenite in section 1.1.

Isolated carbides are either iron-rich (cementite) or molybdenum-rich (M_2C) or iron-rich with chromium depending on the temperature reached before quenching. Cementite is predominantly found at temperatures lower than 725°C. No measurements were done on M_2C at 650°C and 675°C due to their too small dimensions; moreover, they were rarely seen at 650°C. It is also interesting to notice that M_2C are mostly chromium-rich at 700°C. M_7C_3 and $M_{23}C_6$ carbides are present in all four conditions; however, their composition can only be determined with certainty at 725°C where they are iron-richer than expected. At lower temperature, a whole set of analyzed carbides are too rich in chromium to be $M_{23}C_6$,but not rich enough to be characterized as M_7C_3. Thus, their nature remains uncertain and will be discussed later.

Phase quantification made by Rietveld refinements after heating at 675°C is as follows, in weight percentages: 0.78% of M_3C, 0.17% of M_7C_3, 0.11% of $M_{23}C_6$ and 0.15% of M_2C. The measurements error in relative value is about 2% for cementite, M_7C_3 and M_2C and 5% for $M_{23}C_6$. These results confirm that the observed clusters mostly consist of cementite, although there is a non-negligible amount of other carbides in the material too.

As a conclusion, M_3C, M_2C, M_7C_3 and $M_{23}C_6$ carbides have already precipitated at the end of the heating stage regardless the isothermal holding temperature.

3.1.2 Carbide evolution upon tempering: effect of time and temperature

Evolutions of phase fractions

Figure 5.19 shows the evolution of carbide weight fraction in the material for isothermal and isochronous tempering conditions, respectively at 675°C and for 5.5 hours. Relative measurement error is around 2%.

As already stated, M_3C carbides are predominant at the end of the heating up to 675°C. With further tempering time, they are dissolving. M_7C_3 phase fraction increases during the first 5.5 hours of tempering where it reaches 0.8% of the total material weight. For longer times, it slightly decreases, down to 0.7% after 24 hours. On the other hand, the fraction of $M_{23}C_6$ carbides keeps increasing with time, particularly during the first 3 hours where it reaches 0.38%. M_2C carbides tend to remain stable with a weight fraction around 0.25% up to 24 hours.

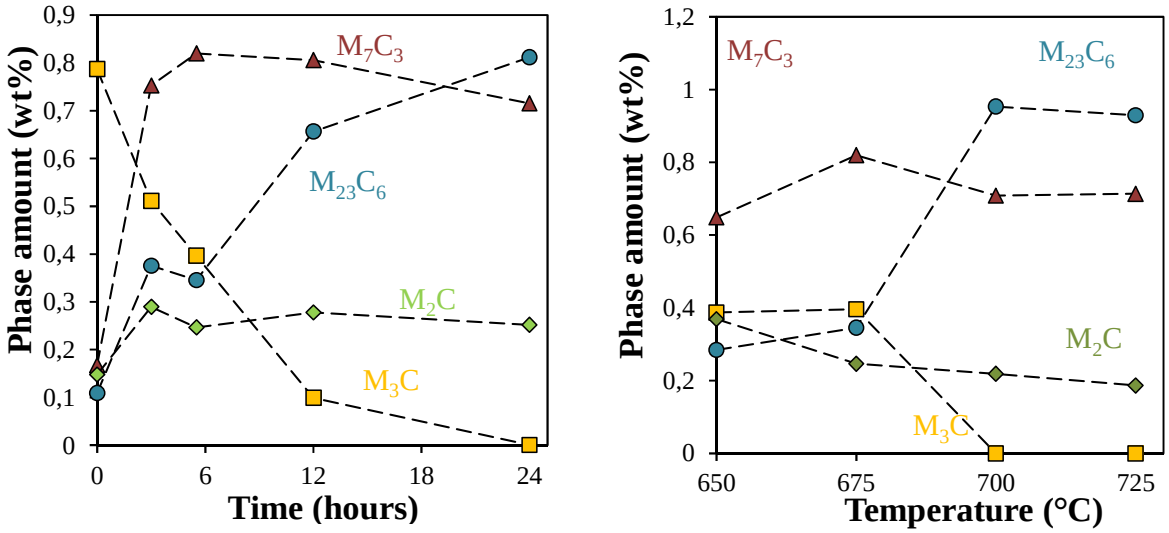

(a) (b)

Figure 5.19: *Evolution of carbides weight fraction during tempering (a) with time at 675°C, (b) at different temperatures after tempering for 5.5h.*

After tempering for 5.5 hours, the weight fraction of cementite is the same at 650°C and 675°C, around 0.4% while it is fully dissolved at 700°C and 725°C. M_7C_3 carbides weight fraction ranges from 0.65% to 0.8%, however their weight fraction does not seem to be directly correlated with the temperature. On the other hand, the $M_{23}C_6$ fraction increases with the tempering temperature, and stabilizes around 0.9% at 700°C. The weight fraction of M_2C at 650°C is 0.4% and it decreases with temperature down to 0.2% at 725°C.

The weight fraction of carbides was also determined after tempering at 725°C for 12 hours. When comparing with tempering at 725°C for 5.5 hours, results are as follows. No cementite is found, the weight fraction of $M_{23}C_6$ increases from 0.9% to 1.1%, the weight fraction of M_7C_3 is decreasing from 0.7% down to 0.5%. The weight fraction of M_2C carbides slightly decreases from 0.19% down to 0.17%.

Evolution of size and morphology

Figure 5.20 shows several TEM micrographs taken from carbon extraction replicas after tempering at different temperatures for 3 hours and 24 hours. Orange arrows point to cementite, green arrows to M_2C carbides, dark blue arrows to $M_{23}C_6$ carbides and dark red arrows to M_7C_3, respectively. Carbides were identified from EDX measurements; the following considerations are based on observations on all twenty metallurgical states.

Cementite clusters remain in the material after 3 hours at 650°C and 675°C, and remnants of these clusters can still be found after 5.5 hours at these temperatures. For longer durations and higher temperatures, these clusters have spheroidized and all observed cementite is globular. Moreover, they become rarer with increasing time and temperature. After tempering for 24 hours, no cementite is ever observed.

M_7C_3 carbides have a fairly constant size, with an equivalent diameter around 100 nm. As already stated, no M_7C_3 was found at 725°C for 24 hours.

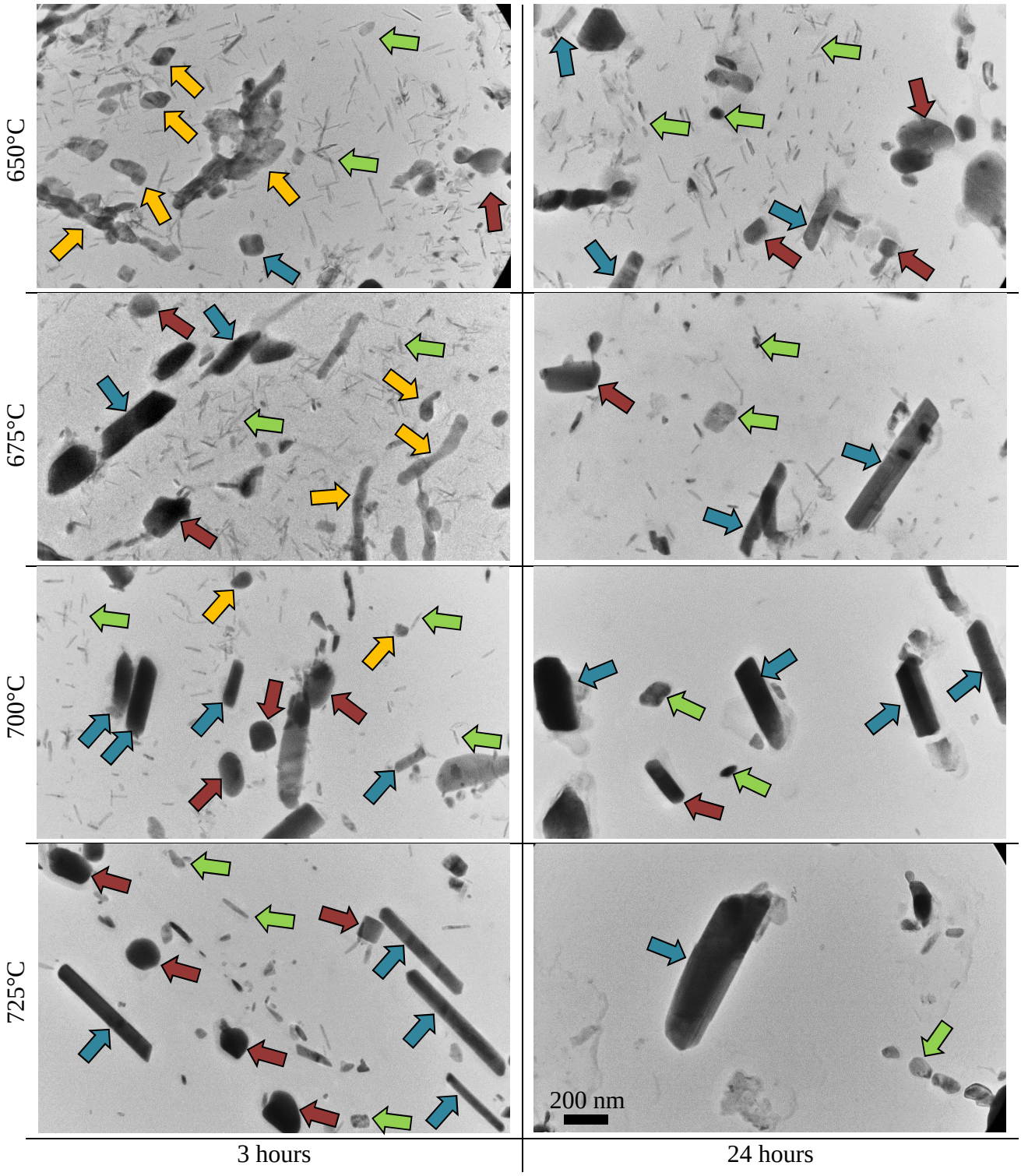

Figure 5.20: *TEM observations on carbon extraction replicas after tempering under various conditions. Orange arrows show M_3C, green arrows show M_2C, pink arrows show M_7C_3 and blue arrows show $M_{23}C_6$.*

$M_{23}C_6$ carbides are hardly seen after 3 hours at 650°C, however they are readily observed in all other tempered states. They tend to grow after longer tempering times and at higher temperatures.

Interestingly, they seem to become longer with increasing temperature, and longer and larger with increasing time.

M_2C carbides are predominantly found as needles for shorter times and at lower temperatures, however globular M_2C can also be found. At 650°C, their number fraction tends to increase with time, while at 675°C it seems to slowly decrease and needles seem to widen. The same phenomenon is observed at 700°C and 725°C for time durations shorter than 12 hours. For longer times, needles are rarely seen while globules are still found, and after 24 hours only globules are observed. The maximal length of needles remains around 100 nm. Moreover, a M_2C-free zone is observed in the vicinity of prior austenite grain boundaries, regardless the tempering conditions. At 675°C, this precipitate-free zone sizes fairly 500 nm, regardless the tempering time.

Evolution of the chemical composition of carbides

The relative amount of metallic elements in M_7C_3, $M_{23}C_6$ and M_2C carbides were analyzed after all 20 heat treatments. Figure 5.21, Figure 5.22 and Figure 5.23 show the evolution of metallic amounts respectively for M_7C_3, $M_{23}C_6$ and M_2C carbides along with their equilibrium composition as predicted by ThermoCalc.

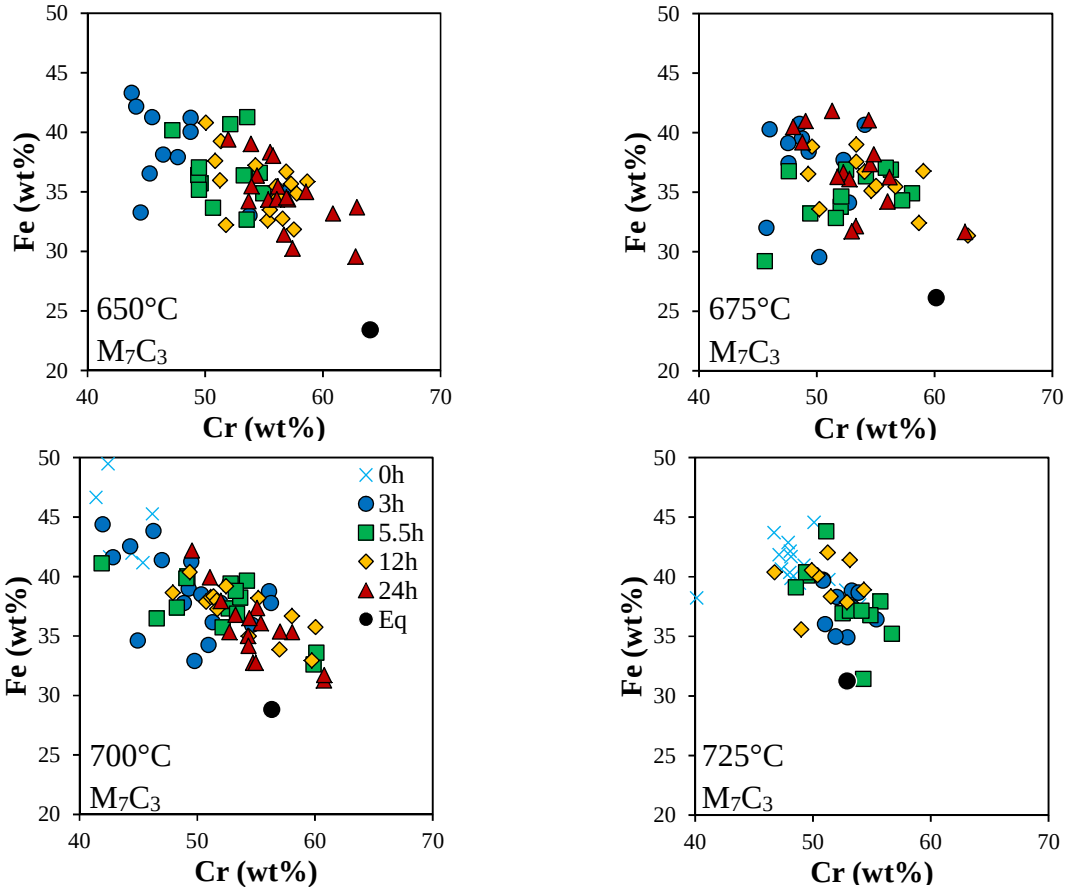

Figure 5.21: *Iron content in M_7C_3 as a function of chromium content for various tempering times at 650°C, 675°C, 700°C and 725°C. Analyses made by EDX measurements on carbon extraction replicas. Equilibrium values are predicted using ThermoCalc.*

For better clarity, compositions are represented by the two major metallic elements, i.e. iron vs. chromium for M_7C_3 and $M_{23}C_6$, and chromium vs. molybdenum for M_2C carbides. Molybdenum content for M_7C_3 and $M_{23}C_6$ and iron content for M_2C remain relatively constant with time and temperature, respectively ranging between 9% and 13%, 13% and 17%; and 2% and 5% in weight. Initial chemical compositions for M_7C_3, $M_{23}C_6$ and M_2C are only shown at 700°C and 725°C for the reasons explained in section 3.1. Each point represents an analyzed particle; the relative error is around 1% for each metallic element.

Analyses for cementite are not represented due to the too low number of analyzed precipitates at temperatures higher than 675°C and time durations longer than 12 hours. After three hours of tempering, their chemical composition remains stable with time and temperature, typically 70% Fe, 25% Cr and 5% Mo, in weight percents. However, at 650°C and 675°C, an enrichment by respectively 12% and 5% in chromium at the expense of iron takes place upon the first 3 hours of tempering.

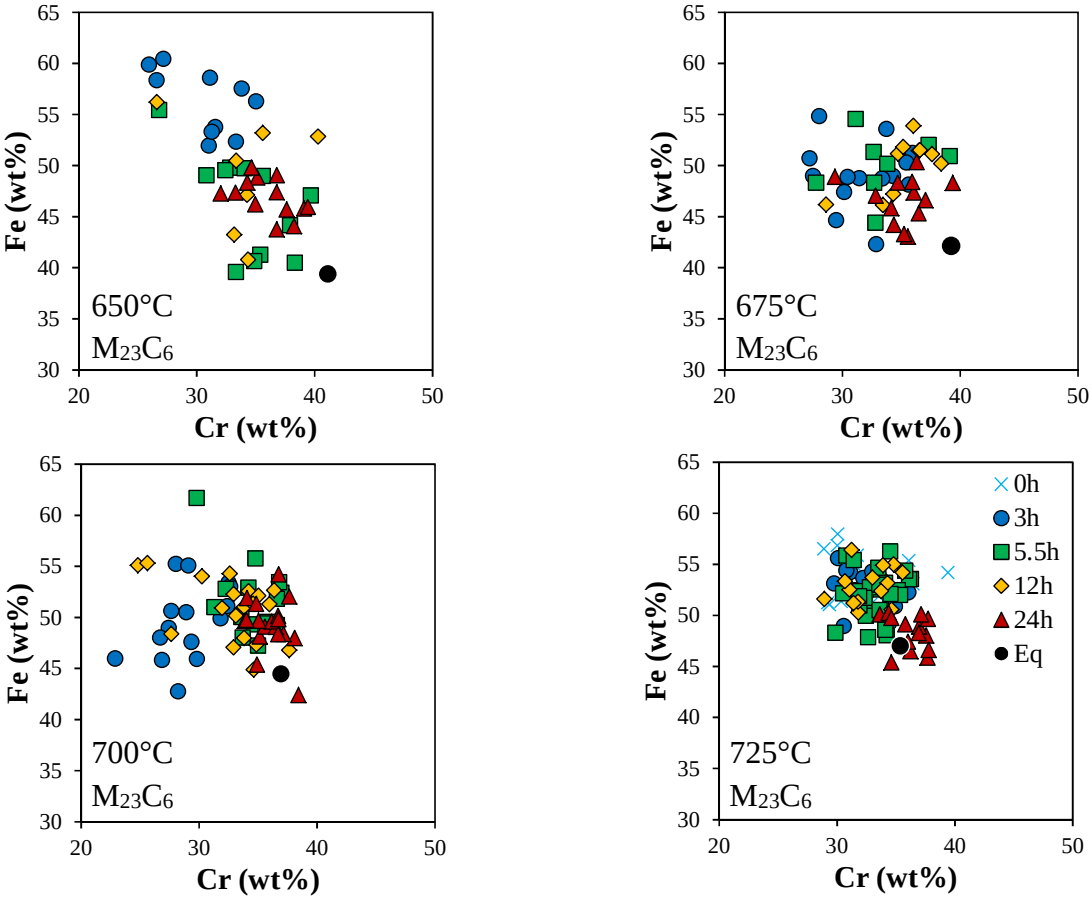

Figure 5.22: *Iron content in $M_{23}C_6$ as a function of chromium content for various tempering times at 650°C, 675°C, 700°C and 725°C. Analyses made by EDX measurements on carbon extraction replicas. Equilibrium values are predicted using ThermoCalc.*

At all temperatures, M_7C_3 carbides become enriched in chromium and depleted in iron with increasing time before stabilizing, which tends to put their chemical composition closer to that of the pseudo-equilibrium one (Figure 5.21). However, this equilibrium composition is never reached. This

is particularly obvious at 650°C and 700°C. Moreover, stabilization seems to occur for shorter times at higher temperature: while the stable composition is not reached after 24 hours at 650°C, the compositions after tempering for 3 hours and 5.5 hours at 725°C remain the same. Interestingly, no M_7C_3 were found at this temperature after 24 hours of tempering. Moreover, at this temperature, M_7C_3 carbides seem to be iron-enriched at the expense of chromium between 5.5 hours and 12 hours, thus moving away from their equilibrium composition. Unlike that of M_7C_3, the chemical composition of $M_{23}C_6$ seems relatively stable with time at all temperatures, with the exception of the first 5.5 hours at 650°C where a clear enrichment in chromium occurs at the expense of iron (Figure 5.22). However, at all temperatures, a slight average enrichment in chromium seems to take place between 3 hours and 24 hours. The chemical composition is always close to the equilibrium one, and becomes closer as the holding temperature is higher. After 24 hours of tempering at 725°C, $M_{23}C_6$ carbides have clearly reached their equilibrium composition.

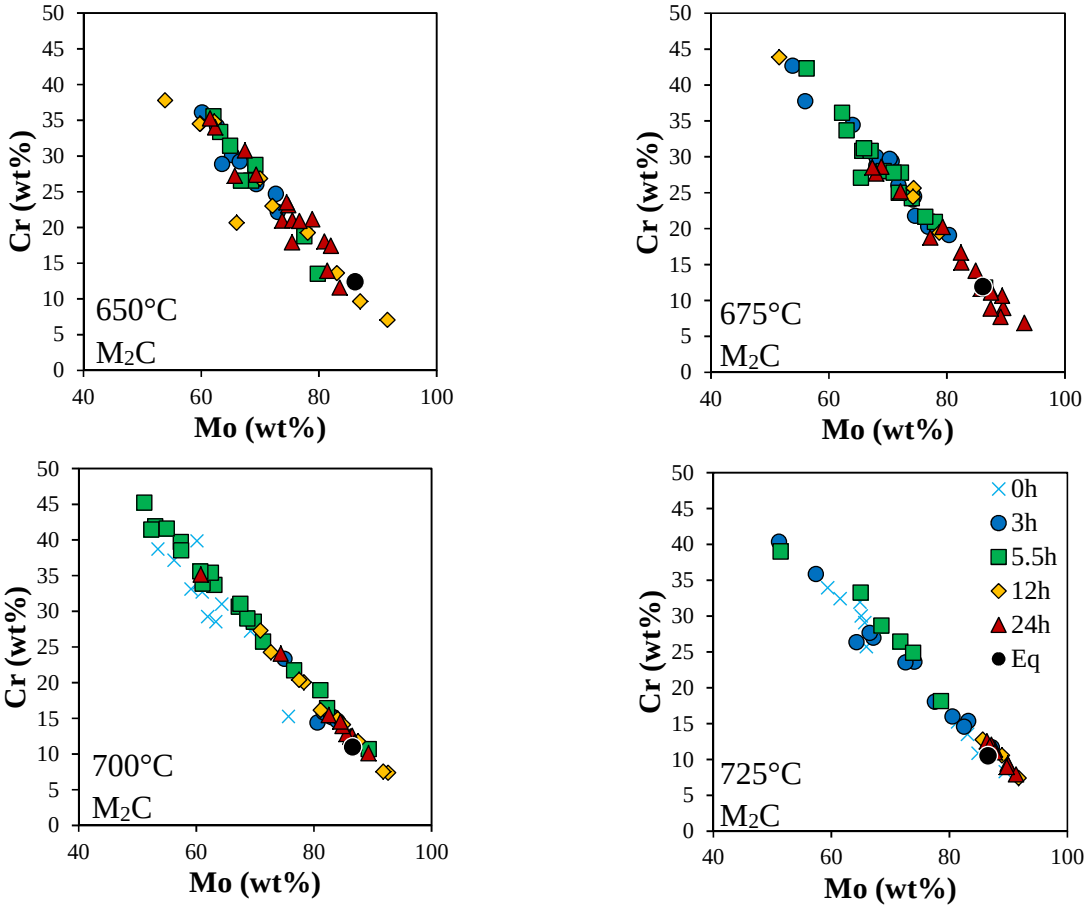

***Figure 5.23**: Chromium content in M_2C as a function of molybdenum content for various tempering times at 650°C, 675°C, 700°C and 725°C. Analyses made by EDX measurements on carbon extraction replicas. Equilibrium values are predicted using ThermoCalc.*

The amount of chromium evolves linearly with the amount of molybdenum for M_2C carbides for all conditions (Figure 5.23). This is due to the very little iron content in these carbides, less than 5 wt%, which only evolves very slightly with tempering time and temperature. M_2C composition is very scattered for short times and low temperatures. For instance, after 5.5 hours of tempering at

700°C, M_2C composition ranges from 50% Mo – 45% Cr to 90% Mo – 7% Cr. A clear correlation is found between the composition and the morphology of M_2C carbides: needles are mostly chromium-richer while globules are molybdenum-richer. However, needles tend to enrich in molybdenum with increasing time too. Like $M_{23}C_6$ carbides, M_2C carbides tend towards their equilibrium composition, and reach it for shorter times as temperature increases.

The general behavior of all three carbides, i.e. enrichment of M_7C_3 and $M_{23}C_6$ in chromium and enrichment of M_2C in molybdenum is in good agreement with the literature review reported in section 1.2.

Evolution of metallic element content in solid solution

By combining the chemical content in carbides obtained by EDX measurements and the phase fraction as determined by Rietveld refinements, one can calculate the amount of iron, chromium and molybdenum contained in carbides and therefore the amount contained within the matrix. These calculations are only valid under the assumption that these atoms are only present in these phases. When considering the phase stability diagrams shown in Chapter II, one should notice that no other secondary phases are expected to contain such elements with the exception of Cr_2N. However, due to their very low phase fraction, they are considered to have a negligible effect on the chemical composition of the matrix.

Normalized amount $N_{x/\varphi}$ of chemical element x in a phase φ was determined using the following equation (5.1):

$$N_{x/\varphi} = \frac{f_\varphi \times wt_M \times wt_{x/\varphi}}{100 \times wt_{tot}} \tag{5.1}$$

where f_φ is the considered phase fraction (in wt%), $wt_{x/\varphi}$ the weight percentage of solute x within this phase (in wt%), wt_{tot} the weight percentage of element in the material (i.e. 2.47 wt% for Cr and 1.11 wt% for Mo) and wt_M the total contribution of metallic elements in the weight of considered carbides (0.93 for M_3C, 0.92 for M_7C_3, 0.95 for $M_{23}C_6$ and 0.93 for M_2C, assuming perfect stoichiometry of metallic elements with respect to carbon). To calculate wt_M, weight percentages are taken as the average metallic content measured by EDX for each type of carbide. For each element x, $\sum N_{x/\varphi} = 1$ as prescribed by mass balance, and the normalized amount of element x in solid solution was calculated as $1 - \sum N_{x/carbides}$.

It should be pointed out that such calculation does not allow the comparison between different phases, but gives the evolution of the amount of metallic elements for one given phase. The evolution of the normalized amounts of chromium and molybdenum with time at 675°C is shown in Figure 5.24. It must be pointed out that this value cannot be calculated at the initial time (as-heated state) due to the lack of reliable EDX measurement of carbide chemistry for this condition. The normalized amounts for isochronous tempering at 5.5 hours are shown in Figure 5.25. The normalized amount of elements in cementite is not represented due to its low weight composition in chromium and molybdenum. Since the average chemical composition of carbides only varies a little,

the evolution of the normalized amount of elements follows the same trend as the evolution of weight fraction.

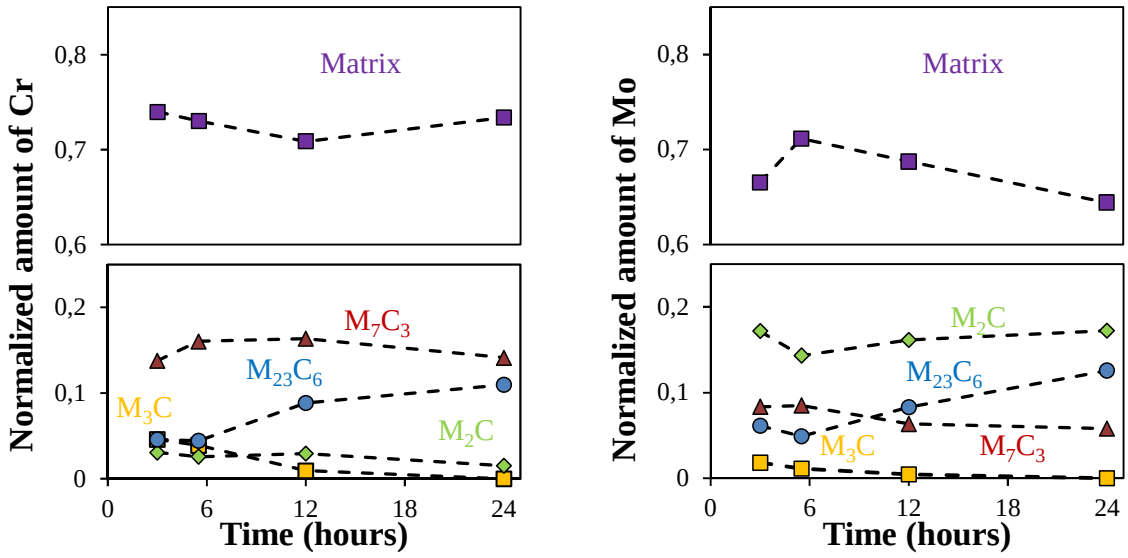

Figure 5.24: *Evolution with time of the normalized amounts of chromium and molybdenum in solid solution (matrix) and in carbides during tempering at 675°C.*

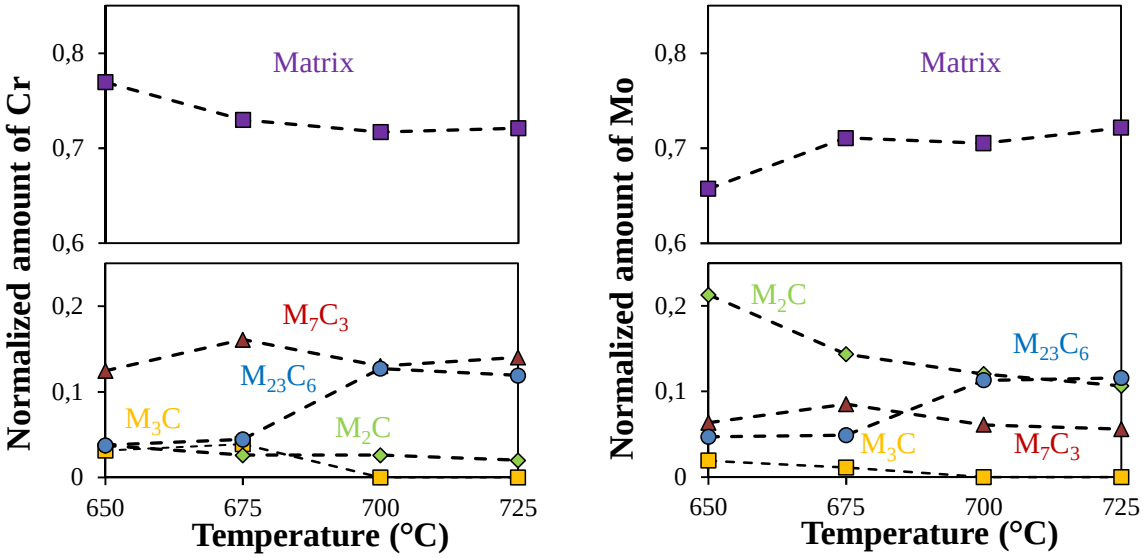

Figure 5.25: *Effect of temperature on the normalized amounts of chromium and molybdenum in solid solution (matrix) and in carbides during isochronous tempering for 5.5 hours.*

For the studied tempering conditions, the normalized amount of chromium in solid solution is almost independent of time and temperature, and remains around 0.75. The normalized amount of molybdenum in solid solution remains around 0.65 at 675°C. Its apparent increase at 5.5 hours is most probably an artifact due to the lower phase fraction measured for M_2C for this tempering time compared to the 3-hour and the 12-hour durations. When increasing the temperature, the amount of molybdenum in solid solution increases due to the dissolution of M_2C. The evolution of amounts of

both molybdenum and chromium in carbides follows the same trend as the evolution of phase fraction, and no remarkable behavior is observed.

3.1.3 Effect of stress-relieving heat treatment on carbides

The effect of a stress-relieving heat treatment (PWHT) at 645°C for 16 hours following a tempering at 675°C for 5.5 hours was studied by means of electro etching dissolution. The heating rate was 0.014°C/s (50°C/h). No TEM observations were made. Table 5.4 shows the comparison of carbides phase fraction before and after PWHT.

	M_3C	**M_7C_3**	**$M_{23}C_6$**	**M_2C**
No PWHT (wt%)	0.40	0.81	0.38	0.25
PWHT (wt%)	0.18	0.94	0.59	0.23

Table 5.4: *Comparison of carbides phase fraction (in wt%) before and after a PWHT at 645°C for 16 hours. Tempering at 675°C for 5.5 hours.*

The PWHT leads to the dissolution of the cementite which transforms into M_7C_3 as well as an increase in $M_{23}C_6$ carbides weight fraction. M_2C carbides weight fraction remains stable.

3.2 Discussion

Based on all these results, the following assumptions can be made on the evolution of carbides during the tempering heat treatment. Propositions of interactions between different carbides will also be discussed.

3.2.1 Evolution of carbides upon tempering heat treatment

M_3C carbides

M_3C carbides precipitate in the form of large clusters upon heating and result from the decomposition of retained austenite between 400°C and 600°C. Since carbide clusters are located at the interfaces, one can safely assume that it is where the retained austenite was located too. No TEM observations on thin foils on the as-quenched sample were made to validate this hypothesis; however, the presence of retained austenite at interfaces is consistent with the expected granular bainitic microstructure.

Clusters rapidly spheroidize with further heating, and have completely disappeared at 725°C. Some of them can still be found after 3 hours of tempering at temperatures lower than 700°C, then they progressively dissolve. As a result, consistently with literature data and equilibrium diagram assessments, cementite is the less stable carbide which precipitates in the material.

M_2C carbides

M_2C carbides have already precipitate at 650°C and then grow upon further heating. They appear to nucleate homogeneously in the matrix, as suggested by their fine distribution and their particular orientation relationship with the matrix. No proof of a potential cubic/orthorhombic transformation upon heating was found, however this latter is expected to happen at lower temperatures as seen in the literature. At 700°C and 725°C, M_2C appear to be relatively unstable as their phase fraction decreases with increasing tempering time, and almost none is observed after 12 hours at these temperatures. In these conditions, only rare globular M_2C are found. This dissolution is likely thermodynamically driven, as suggested by thermodynamic calculations. The increase in stability of globular M_2C might be due to their particular shape, resulting in a better surface/volume ratio compared to needles.

At lower temperatures, their phase fraction remains constant although their number fraction seems to decrease. At the same time, M_2C needles are widening, suggesting that some coarsening might take place. In every case, M_2C becomes molybdenum-richer with increasing time and closer to its equilibrium composition, either by extracting molybdenum from the matrix or by releasing chromium.

M_7C_3 carbides

The evolution of M_7C_3 carbides can be described in three distinct steps: the nucleation and growth upon heating, the increase in phase fraction during the first 5.5 hours of tempering and their dissolution for longer tempering times.

Nucleation and growth upon heating is hinted from X-Ray diffraction and SEM observations. After heating up to 675°C, M_7C_3 are detected in the electroetching powder residues, however, they are not detected by means of TEM observations and EDX analyses. At 700°C and 725°C, M_7C_3 carbides are observable by means of SEM and TEM, although their chemical composition could only be determined at 725°C, and is iron-richer than expected. At lower temperature unidentified carbides are within range of both $M_{23}C_6$ and M_7C_3 composition, as shown by the orange circle in Figure 5.26. These carbides are unlikely to be chromium-rich $M_{23}C_6$ since this would imply a further enrichment in iron that would move away carbides from their equilibrium composition (the red arrow in Figure 5.26). More likely, these carbides are M_7C_3, suggesting they nucleate with a composition far from equilibrium and then enrich in chromium with further heating (blue arrow in Figure 5.26). This increase in chromium content is also observed during the first steps of the isothermal holding stages (for instance, after 5.5 hours at 650°C and after 3 hours at 700°C).

Moreover, the appearance of observable M_7C_3 and their enrichment in chromium seem to coincide with the spheroidization of M_3C clusters, and both are found in the same location (interfaces). Thus, the clusters observed at 675°C could actually consist of a mixture between cementite and iron-rich M_7C_3 in their first stages of growth. Once nucleated, M_7C_3 would then grow by attracting chromium atoms contained in the neighboring cementite and ferritic bainite, triggering the dissolution of cementite. Such *in-situ* transformation of cementite into M_7C_3 is consistent with the literature data reported in section 1.3, and particularly with the proposed mechanism from Inoue & Masumoto [115] who reported that M_7C_3 carbides nucleate at the interface between matrix and

cementite while maintaining crystal orientation relationship with cementite, before growing rapidly towards the cementite crystal.

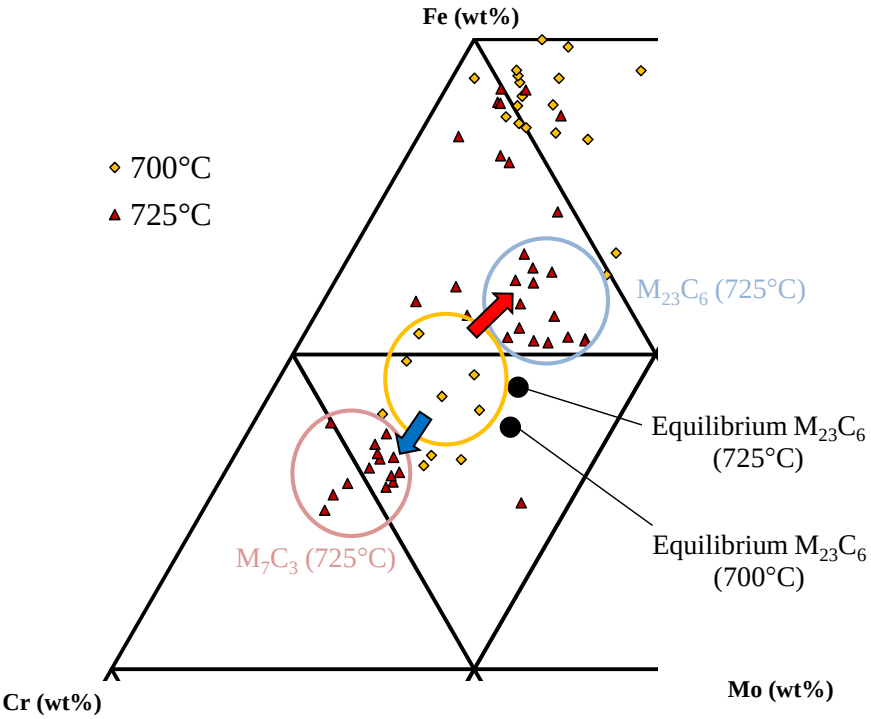

Figure 5.26: *Detailed view of Figure 5.18 illustrating the evolution of carbide chemistry at the end of heating. The orange circle shows the unidentified carbides formed at 700°C, the pink circle highlights the M_7C_3 carbides formed at 725°C and the blue circle $M_{23}C_6$ carbides formed at 725°C. The red and blue arrows respectively represent potential enrichment in iron and chromium.*

It was reported in section 1.3 that the nucleation of M_7C_3 at the cementite/matrix interface was the result of chromium depletion of the matrix. From experimental results, it appears that the total chromium content in the matrix is not negligible and remains constant with time and temperature. Thus, one should expect that M_7C_3 could nucleate separately from the matrix. However the chromium-richer clusters analyzed by EDX after heating up to 675°C contained around 20wt% Cr, which is almost ten times higher than the weight fraction of the matrix (2.47wt% in average without any precipitation). Thus, when accounting for a single cementite particle and its surrounding matrix, the cementite is indeed richer than the matrix, and nucleation of M_7C_3 at this interface still appears to be likely.

During the isothermal step of the tempering, M_7C_3 carbides reach a maximum in phase fraction, which then slowly decreases with increasing tempering time. Increasing the tempering temperature accelerates this final dissolution since no M_7C_3 is observed after 24 hours at 725°C. During the first 5.5 hours of tempering, M_7C_3 carbides enrich in chromium although they never reach their equilibrium composition as calculated from the average composition of the material. It is interesting to notice that after 12 hours at 725°C, a drop in their chromium content occurs before their complete

dissolution after 24 hours. No growth or coarsening seems to occur since their size remains constant, with an equivalent circle diameter of approximately 100 nm.

$M_{23}C_6$ carbides

$M_{23}C_6$ appear to be the equilibrium carbides, since they experience growth with increasing tempering time and temperature while their chemical composition remains stable and close to that calculated at equilibrium. In parallel, the chromium amount in M_2C decreases and M_7C_3 are dissolving.

When looking at Figure 5.24, the constant amount of chromium and molybdenum in solid solution in the matrix indicates that the $M_{23}C_6$ carbides do not attract these elements from the matrix only. On the other hand, the increase in the total amount of chromium in the $M_{23}C_6$ carbides corresponds to the dissolution of the remaining cementite (first 5.5 hours), and then on the dissolution of M_7C_3 carbides. This indicated that the $M_{23}C_6$ carbides experience growth by attracting chromium from less stable carbides, more likely due to a local depletion of chromium in the matrix but only close to the $M_{23}C_6$, leading to a chromium concentration gradient and therefore triggering dissolution of these less stable carbides.

Concerning M_2C carbides, a precipitate-free-zone is sometimes observed at the vicinity of $M_{23}C_6$ particles. Dissolution of these M_2C carbides releases molybdenum in the matrix, and some of it will then diffuse into other M_2C particles, leading to their coarsening and increasing their molybdenum content.

The correlation between growth of $M_{23}C_6$ and dissolution of M_7C_3 is obvious. However, the constant size of M_7C_3 particles suggests that the decrease in their phase fraction is due to a decrease in their number fraction. In other words, dissolution of M_7C_3 is localized. TEM observations show that none or few of these carbides are found near $M_{23}C_6$ carbides for long durations/high temperatures, suggesting that the dissolution of M_7C_3 takes place in the vicinity of $M_{23}C_6$ carbides only, and supporting the abovementioned mechanism.

This evolution of carbide population during tempering is in good agreement with Baker & Nutting's results (with the exception of M_6C carbides) and thermodynamic equilibrium predictions: M_3C is the less stable carbide, M_7C_3 and M_2C are metastable and $M_{23}C_6$ is the equilibrium carbide. An increase in holding temperature seems to accelerate the precipitation sequence, as metastable carbides disappear more rapidly and $M_{23}C_6$ growth is favored.

3.2.2 Summary of precipitation sequence

Based on all previous results and considerations, the microstructural evolution upon tempering heat treatment can be summarized as follows:

- Retained austenite decomposes into ferrite and M_3C clusters during heating. At 600°C, no more austenite remains in the microstructure. Retained austenite was more likely located at the interfaces, especially at prior austenite grain boundaries.

- At 650°C, M_2C carbides nucleate separately from the matrix, likely thanks to the carbon in solid solution within the bainitic laths and in the intralath dislocations. M_7C_3 starts to precipitate at the interfaces between the cementite clusters and the matrix. $M_{23}C_6$ nucleates separately in the matrix. When heating up to 725°C, or when starting the isothermal step at lower temperatures, clusters tend to dissolve due to the diffusion of chromium from M_3C towards M_7C_3. M_2C carbides keep growing.
- For short tempering times, the M_7C_3 phase fraction reaches a maximum value while cementite is dissolving. $M_{23}C_6$ starts to grow, likely due to chromium in solid solution in the matrix. At 700°C and 725°C, M_2C carbides start to dissolve due to their thermodynamic instability.
- For longer tempering times, $M_{23}C_6$ experience growth, leading to progressive dissolution of M_7C_3, decrease in M_2C number fraction and coarsening of M_2C carbides. For isothermal holding times higher than a critical value, only $M_{23}C_6$ carbides remain in the material. This critical value is lower for higher holding temperatures.

This precipitation sequence was successfully reproduced using the thermokinetic software MatCalc. Results from these predictions can be found in Appendix D.

4. CONCLUSION

The four different carbides precipitating in the investigated 2.25 Cr – 1 Mo steel have been identified using literature data, experimental measurements and thermodynamic calculations. Each type of carbide exhibits unique characteristics such as amount of metallic elements, morphology, crystal structure, nucleation site and nucleation conditions. M_3C cementite is the less stable carbide, M_7C_3 and M_2C are metastable carbides and $M_{23}C_6$ is the equilibrium carbide. No M_6C was ever observed.

Precipitation of carbides starts during the heating step, due to the low heating rate that is dictated by the high thickness of the targeted component. From experimental observations, the precipitation sequence was proposed as follows. Cementite (M_3C) precipitates first due to the decomposition of retained austenite. M_7C_3 carbides then nucleate at the interface between cementite and matrix, and grow by attracting both chromium and carbon atoms from their parent M_3C phase. Molybdenum carbides, M_2C, precipitate homogeneously from the matrix, while $M_{23}C_6$ particles are located at dislocations within the bainitic laths. $M_{23}C_6$ experience growth with increasing time and temperature, leading to the dissolution of neighboring less stable carbides: M_2C first, then M_7C_3. These observations were successfully reproduced using a thermokinetic approach, shown in Appendix D.

The effect of a subsequent stress-relieving heat treatment was studied. Using the studied conditions, such heat treatment leads to the dissolution of cementite, as well as an increase in phase fraction of M_7C_3 and $M_{23}C_6$.

These results are to be used in the next chapter in order to understand the effect of the tempering heat treatment on the tensile and impact toughness properties of the considered steel.

Chapter VI: Mechanical properties after tempering

TABLE OF CONTENTS

The effect of the microstructural evolution during the tempering heat treatment and the stress-relieving heat treatment on the final mechanical properties, namely, the hardness, tensile and toughness properties, is reported in this chapter.

This chapter begins with a literature review on the effect of tempering conditions on the mechanical properties of 2.25 Cr – 1 Mo steels. The strengthening mechanisms governing the resistance to plastic deformation at room temperature are highlighted and discussed from results found in the literature. The effect of carbides on toughness is also summarized. In the second part, the mechanical properties of microstructures resulting from tempering heat treatments reported in Chapter V are investigated, as well as the effect of further stress-relieving heat treatment. Hardness measurements have been performed on each of the 24 tempered conditions presented in Chapter V, whereas tensile and impact toughness properties were assessed for tempering conditions of interest.

1. LITERATURE REVIEW: EFFECT OF TEMPERING CONDITIONS ON MECHANICAL PROPERTIES

The following review present results found in the literature concerning the evolution of hardness, tensile properties and toughness as a function of the tempering heat treatment. Results are shown as a function of a Hollomon-Jaffe parameter or Temper Parameter (TP), which gives an equivalence between the tempering temperature (in K) and the tempering time (in hours) such as:

$$\mathrm{TP} = T(\log t + C) \tag{6.1}$$

where C is a constant equal to 20. Assuming that there is a good equivalence between time and temperature, the results should vary uniquely with the TP with almost no noise. If not the case, then no equivalence exists. This latter is likely to be the case, since as seen in Chapter V an increase in

temperature can change the thermodynamic equilibrium, i.e. the nature of carbides that are stable in the material after tempering. Nevertheless, this representation was chosen because, on the one hand, some of the literature results were only reported as a function of the TP, and on the other hand this representation allowed representing a wide range of tempering conditions on a single plot.

Source	Heat treatment	Testing conditions
[116]	940°C – 4h + Air cooled [650, 670]°C – 1.7h, 710°C – [1.7, 9.7, 96]h No information on the heating step	**Tensile:** Room temperature **Toughness** : no information **Hardness**: HV10
[117]	940°C – 2h + Air cooled [640, 680, 720, 780]°C – 2h No information on the heating step	**Tensile:** 6x30mm cylindrical specimens, strain rate: 10^{-3} s^{-1} Room temperature **Hardness**: HV10
[118]	950°C – 2h + Cooled at 0.7°C/s 600°C – [25-500]h, 650°C – [5-470]h, 700°C – [1-150]h No information on the heating step	**Tensile:** Room temperature **Toughness** : no information **Hardness**: HV10
[101]	1100°C – 0.5h + Oil quench 700°C – [0.5-12]h No information on the heating step	**Hardness**: HV30
[4]	920°C – 5h + Cooled at 0.08°C/s Only TP is given	**Tensile:** Room temperature **Toughness** : no information Specimens taken from forgings or plates of thickness ranging from 108 to 450 mm. 10 heats examined.
[84]	920°C – 30 minutes + Water quench [400,500,600,700]°C – 1 hour No information on the heating step	**Toughness:** HV1

Table 6.1: *Heat treatments and testing conditions for results shown in Figure 6.2 and Figure 6.3*

The considered heat treatments and testing conditions are gathered in Table 6.1. The austenitization temperatures can vary between 920°C and 1100°C, and as a first approximation will be considered to have a neglecting effect on the mechanical properties as shown in Chapter IV. Cooling rates are also different but are always resulting in fully bainitic microstructures. However, such change in cooling rates has an impact not only on the bainitic transformation kinetics, as seen in Chapter IV, and thus might have an impact on the bainitic packet size, but also on the distribution of the retained austenite that partly controls carbide precipitation during tempering and therefore the mechanical properties. Finally, no information is given on the heating rate for the tempering heat treatment, although this parameter has a strong influence on the carbide precipitation as seen in Chapter V. It should be pointed out that Murakami [4] and Takahashi [118] only reported their

results as a function of the TP, and the tempering conditions corresponding to a given result remain unknown.

Nevertheless, this literature review does not aim at comparing the different results found in the literature, but at getting a first insight, for a given material, on the effect of tempering time and temperature on the mechanical properties.

1.1 Resistance to deformation and strengthening mechanisms

The strength of a material depends on several microstructural parameters: the unit size of interest (in this case, the bainitic lath size), the dislocation density, the presence of particles such as carbides and the amount of interstitial and substitutional atoms in solid solution. Upon tempering, the bainitic lath size is expected to remain constant with time and tempering since it results from the decomposition of austenite upon cooling. Thus, the observed variations in strength are only due to change in precipitation strengthening, solid solution strengthening and dislocation strengthening. Their effect on the material strength can be summarized as follows:

- Precipitation strengthening is due to the interactions between dislocations and particles, in this case carbides. There are two mechanisms governing this contribution to strengthening: dislocations cutting through particles (shear cutting) and dislocations bowing around particles (Orowan by-passing). Shear cutting occurs for coherent particles only, while Orowan by-passing affects all types of particles. In the case of shearable particles, there is a critical particle size below which dislocations cross particles by only shear cutting mechanism, and by only Orowan by-passing when above.

  In the considered material, M_7C_3 and $M_{23}C_6$ are incoherent carbides and are only concerned by Orowan by-passing, while M_2C are semi-coherent carbides and are thus potentially subjected to both mechanisms. However the critical size for M_2C is 3 nm [119] while their average size upon tempering is larger than 50 nm after heating up to 650°C, thus only Orowan by-passing has to be taken into account. As a conclusion, the contribution to strengthening due to particles in 2.25 Cr – 1 Mo steels is only linked to Orowan by-passing.

  This contribution to strengthening is inversely proportional to the inter-particle distance, for a given volume fraction of particles. Since the inter-particle distance is correlated to the particles size and distribution, growth and coarsening of carbides tends to reduce their strengthening efficiency [107, 120].
- Solid solution strengthening can be due to interstitial atoms (C, N) and to substitutional atoms (Mo, Cr …). Interstitial atoms lead to higher strengthening than substitutional atoms. In a typical granular bainite, carbon atoms are mostly located in the retained austenite, thus they are not in solid solution within the bainite. Moreover, as seen in Chapter V, once precipitation starts the amount of chromium and molybdenum in solid solution remains constant with time and temperature, with the exception of the dissolution of M_2C at high temperature which may result in a release of molybdenum. Based on these observations, solid solution strengthening likely decreases during precipitation and then remains stable. However, the increase in molybdenum in solid solution caused by the dissolution of M_2C might lead to possible strengthening, as pointed out by some authors [94, 107].

- After quenching, bainite exhibits a high dislocation density, in the range of 10^{15} m^{-2} in the studied material as assessed from the B_s temperature (see Appendix D). Strengthening due to dislocations decreases when increasing the tempering temperature. Indeed, higher temperatures lead to faster diffusion, thus the dislocation motion is enhanced and recovery through their annihilation and rearrangement is favored.

Thus, softening due to a change in dislocation density and solid solution chemistry are likely to only happen during the very first stages of tempering, while the growth and dissolution of carbides are responsible for further softening. Such considerations are in good agreement with the work from Parameswaran, who postulated that the evolution of hardness in bainitic 2.25 Cr – 1 Mo steels went through four different stages, as shown schematically in Figure 6.1 [16]. Stage I occurs during the very first beginning of tempering, where softening is due to dislocation recovery. Stage II shows a secondary hardening triggered by the coherency strains due to precipitation of fine, semi-coherent M_2C carbides. Stage III is a further softening, due to precipitation and growth of other incoherent carbides such as M_7C_3 or $M_{23}C_6$ at the expense of M_2C, which on the one hand reduces the strengthening due to M_2C precipitation, and on the other hand depletes the matrix in solid solution elements. The final stage, Stage IV, is a slow softening due to coarsening of incoherent carbides and dissolution of M_2C carbides, which once again reduces the contribution of precipitation to strengthening.

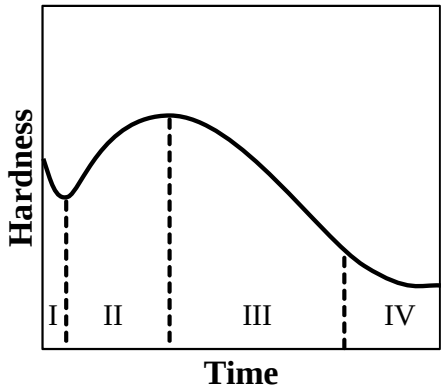

Figure 6.1: *Schematic sketch showing the four stages of hardness evolution with tempering time at a given temperature. From* [16]

Figure 6.2 shows the dependency of tensile properties and hardness on tempering conditions gathered from sources [4, 101, 116–118]. The ultimate elongation is not represented, and varies from 20% for TP = 18700 to 35% for TP = 21600 [116]. One should notice that the results obtained by Murakami et al. [4] are very scattered when represented as a function of TP. This is most likely due to poor equivalence between tempering time and temperature, as well as to the fact that their tensile tests were made on various heats and on components of various thicknesses. Important information given by this figure is that the tensile properties, namely, the yield strength and the ultimate tensile strength, as well as the hardness tend to decrease when increasing the temper parameter, i.e. when increasing tempering temperature and/or time. Evolution of tensile properties and hardness can be divided in three steps, each one of them corresponding to linear variation in strength with the TP.

- At low TP values, i.e. for the two values of LMP ranging from 13000 to 15000, which correspond to 1 hour of tempering at 400°C and 500°C from Chang & Kai [84]. At such low temperatures, no precipitation is expected and softening is thus only induced by recovery of the dislocation structure in bainitic ferrite. This corresponds to Stage I in Figure 6.1.
- At intermediate values of TP, between 15000 and 20000, i.e. after 1 hour at temperatures ranging from 500°C to 700°C according to Chang & Kai [84], 2 hours at temperatures ranging from 640°C to 720°C according to Holzmann [116, 117] and up to 3 hours at 700°C according to Pilling [101]. Compared to Stage I, an additional softening is observed due to the precipitation of incoherent carbides. This corresponds to Stage III.
- At high TP values, higher than 20000, i.e. from 5 hours to 12 hours of tempering at 700°C according to Pilling [101], 2 hours at 780°C and up to 96h at 710°C according to Holzmann [116, 117]. For these tempering conditions, i.e. long durations at any temperature or very short durations at high temperatures, dissolution of M_2C is likely to occur, either due to their thermodynamic instability (above 725°C) or due to growth of incoherent carbides. This corresponds to Stage IV.

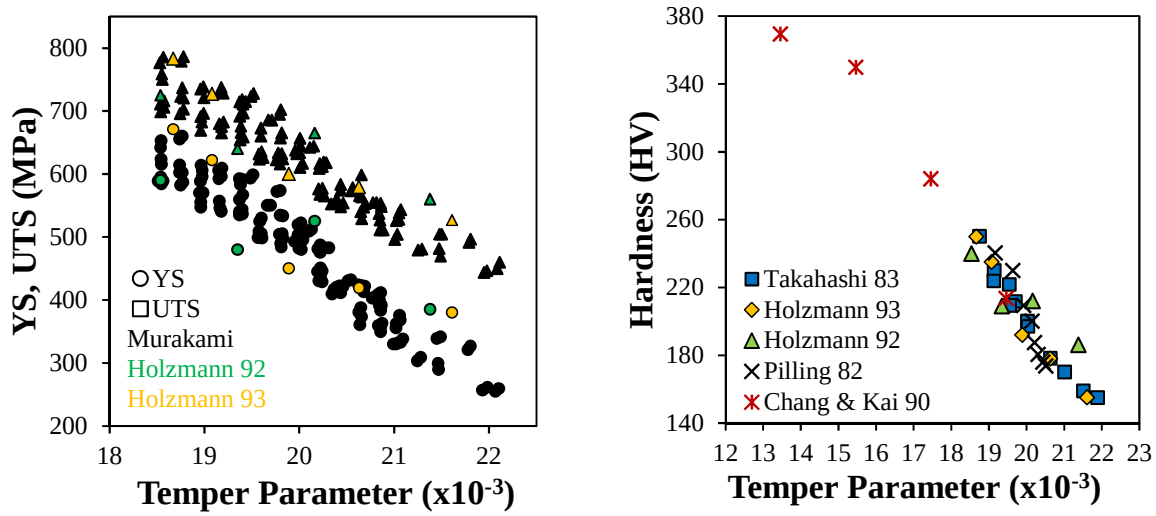

(a) (b)

Figure 6.2: *Relationship between tempering conditions and (a) Yield strength (YS) and ultimate tensile strength (UTS), (b) Vickers hardness of 2.25Cr – 1Mo steels. From* [4, 84, 101, 116–118]

It should be pointed out that the secondary hardening (Stage II) is almost never reported in the literature concerning these materials. This is easily explainable by the fact that incoherent carbides and M_2C carbides precipitate simultaneously, as seen in Chapter V. Thus, phenomena involved in Stages II and III usually happen at the same time. With the exception of secondary hardening, the four stages described by Parameswaran are consistent with the literature data and with the considerations on the evolution of strengthening mechanisms due to the evolution of microstructure as described in Chapter V.

1.2 Toughness properties

In low-alloy steels such as 2.25 Cr – 1 Mo, for a given grain size and matrix microstructure, the resistance to brittle fracture is affected by the carbide size since carbides are known to initiate brittle cleavage failure by particle fracture producing microcracks [120]. 2.25 Cr – 1 Mo steels exhibit good toughness properties due to the fineness of M_2C carbides and moderate prior austenite grain size [121]. Moreover, reports from literature showed that the FATT is not clearly correlated to tempering time and temperature, as shown in Figure 6.3.

Upon certain ageing conditions, phosphorus segregation at prior austenite grain boundaries may take place and may promote intergranular fracture [121–125]. However, due to the very low phosphorus content in the studied material and the relatively short tempering durations, such phenomenon, if happening, can be considered as negligible. Nevertheless, any intergranular facets on fracture surface have to be investigated thoroughly, although it was shown in Chapter IV that intergranular facets on fracture surface for the studied material were likely ductile.

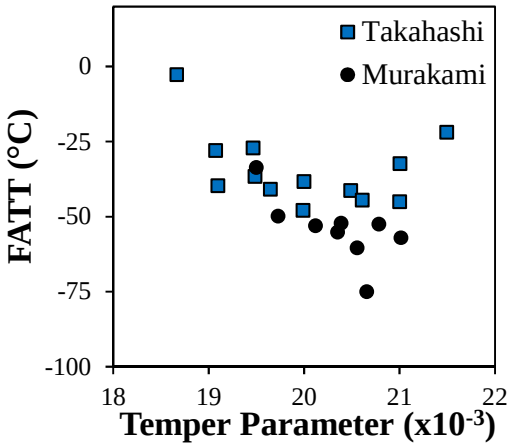

Figure 6.3: *Relation between tempering conditions and FATT of a 2.25Cr – 1Mo steel. From* [4, 118].

As a conclusion, the tensile and hardness properties decrease during the first hours of tempering due to annihilation and rearrangement of dislocations as well as precipitation of carbides, which reduces the amount of solute atoms in solid solution. For longer durations, carbide growth and coarsening are responsible for the softening of the material, since they imply an increasing inter-particle distance while the volume fraction of carbide remains the same. No clear effect of tempering conditions on impact toughness properties has been highlighted regarding literature data.

2. EXPERIMENTAL RESULTS

The effect of the tempering heat treatment, and therefore of the carbide precipitation on the mechanical properties of the material was investigated. Tempering temperatures range from 675°C to 725°C, for durations up to 24 hours with a heating rate at 0.03°C/s. All samples to be characterized by hardness measurements were water quenched after tempering; all specimens used for tensile and toughness tests were air cooled. Due to the geometry of blanks, cooling was fast in both cases: a few

seconds for the water quench, a few minutes for air-cooling. Thus it was assumed that this difference in cooling rates has no effect on the material microstructure.

Hardness values are reported for all 24 tempered states, since this technique requires very little material and time. Mechanisms responsible for the evolution of hardness with tempering are then discussed. Further tensile tests and V-notch Charpy impact tests on small specimens were then conducted for three particular tempering conditions in order to study the effect of tempering time and temperature. Since the reference tempering condition being 5.5 hours at 675°C, as seen in Chapter II, these mechanical tests were also conducted on specimens tempered either at 675°C for 12 hours or at 700°C for 5.5 hours. The effect of the stress-relieving heat treatment following tempering is then briefly investigated.

More information on the experimental procedure followed used in this part of the study can be found in Appendix A.

2.1 Effect of tempering on mechanical properties

2.1.1 Hardness measurements

Figure 6.4 shows the evolution of hardness upon heating and tempering up to 24 hours at 650°C, 675°C, 700°C and 725°C. Upon heating, the hardness remains constant around the as-quenched bainitic hardness, namely, 350 HV, at least up to 400°C. At 600°C, a slight increase in average hardness up to 360 HV is observed; however the uncertainty on this value is 10 HV thus this difference is not significant. At 650°C, the hardness slightly decreases down to 328 HV then a drop down to 298 HV at 700°C takes place. At 725°C, the hardness is 240 HV. Upon tempering, the hardness evolves similarly with time regardless of the tempering temperature, although values are lower for higher temperatures. From the as-heated state to 3 hours of tempering, the hardness drops down and then slightly decreases between 3 hours and 24 hours.

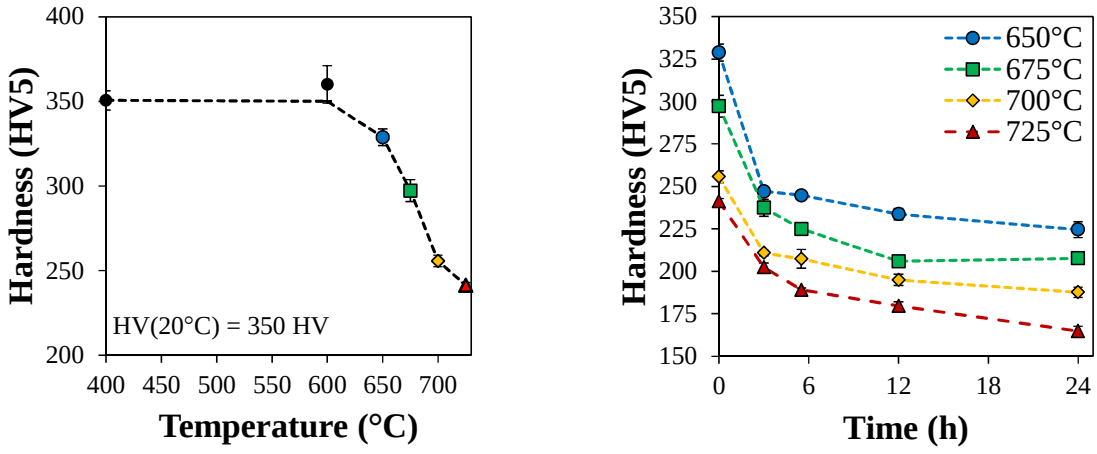

Figure 6.4: *Evolution of hardness (a) upon heating, (b) upon tempering at various temperatures.*

Figure 6.5 shows the variation in hardness during the first 3 hours and between 3 hours and 24 hours as a function of tempering temperature. The drop during the first hours is larger when the tempering temperature is lower, and the remaining loss in hardness remains constant with respect to the tempering temperature, with the exception of tempering at 725°C.

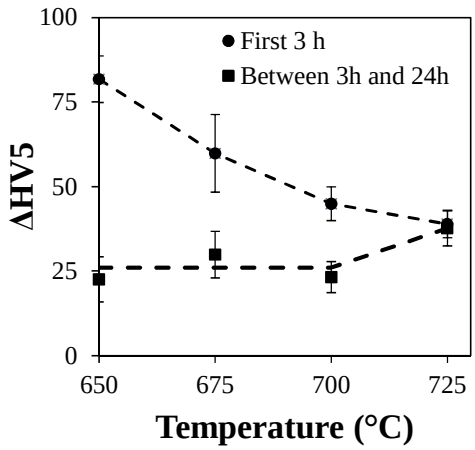

Figure 6.5: *Variation in hardness during the first 3 hours of tempering and between 3 hours and 24 hours as a function of tempering temperature.*

Based on these observations, the evolution of hardness upon tempering can be categorized in three stages: (A) upon heating, (B) during the first 3 hours and (C) during the remaining of the isothermal part of the heat treatment. These stages are consistent with the statements made above based on the literature data, and are to be discussed with respect to Stages I-IV as defined in [16].

Stage A: Evolution of hardness upon heating

First of all, it should be reminded that the as-quenched material contains a non-negligible fraction of retained austenite, around 6 wt%, as reported in Chapter V. However, this retained austenite is fully decomposed into ferrite and cementite at 600°C, where the hardness is close to that of the as-quenched state. Thus, it has no direct effect on the evolution of hardness during heating.

Solid solution chemistry and dislocation density within the matrix can be qualitatively assessed thanks to XRD. The full width at half maximum of matrix diffraction peaks is correlated to the dislocation density [126], and atoms in solid solution distort the matrix, thus changing the lattice parameter *a* and shifting diffraction peaks. It should also be pointed out that change in the lattice parameter can be induced by elastic deformations due to internal stresses. As a first assumption, thes internal stresses will be considered as negligible.

In the case of a bcc structure such as ferrite, the inter-reticular distance decreases for increasing lattice parameter, therefore with the amount of alloy element atoms in substitutional solid solution. The interplanar distance $d(h,k,l)$ in the reciprocal space corresponding to (110) planes is given by equation (6.2).

$$d(1,1,0) = \frac{\sqrt{2}}{a} \qquad (6.2)$$

Figure 6.6 shows the ferrite diffraction peak obtained by Synchrotron X-Ray Diffraction, both before and after heating at 675°C. One should notice that the full width at half maximum decreases and the inter-reticular distance increases when the material is heated. Thus, dislocation recovery and loss of atoms in solid solution take place upon heating. The latter observation is consistent with the observed precipitation of M_2C carbides at 650°C, which are assumed to precipitate within the matrix from carbon and molybdenum atoms in solid solution. However, softening is occurring from 650°C to 675°C, where no major change in carbide precipitation is observed. Thus, this softening is only induced by dislocation recovery. Since the drop in hardness between 600°C and 650°C is similar to the one between 650°C and 675°C (roughly 25HV), one can safely assume that softening due to evolution of the solid solution chemistry is negligible in front of softening induced by recovery of the dislocation structure.

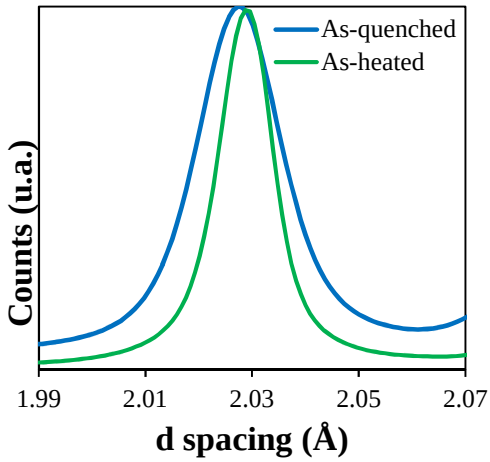

Figure 6.6: *X-Ray Diffraction peaks of the ferritic {110} planes before and after heating up to 675°C followed by water quench.*

Moreover, it should be noted that precipitation of M_2C carbides is supposed to have a positive contribution to strengthening; however the global material hardness is decreasing. Thus, the softening effect due to dislocation recovery is higher than the strengthening effect due to M_2C precipitation.

The drop in hardness between 675°C and 700°C could be explained thanks to the results presented in Chapter V. While both M_7C_3 and $M_{23}C_6$ are detected by X-Ray diffraction at 675°C, they become observable by means of TEM only from 700°C. Thus, a softening effect due to the precipitation and growth of incoherent carbides is likely to take place from 675°C to 725°C.

As a conclusion, Stage A integrates contributions from Stages I and II postulated by Parameswaran [16]. Mechanisms causing the hardness evolution upon heating are summarized in Table 6.2.

Temperature	Mechanisms	Effect
RT → 600°C	Decomposition of retained austenite	Unsignificant
650°C	Loss of carbon and molybdenum in solid solution	Negligible
	Precipitation of M_2C	Hardening
600°C → 725°C	Dislocation recovery	Softening
675°C → 725°C	Growth of M_7C_3 and $M_{23}C_6$ carbides	Softening
Overall		Softening

Table 6.2: *Mechanisms responsible for the hardness evolution upon heating up to 725°C.*

Stage B: Evolution of hardness during the first 3 hours of tempering

Stage B is characterized by a drop of hardness which is more pronounced at lower tempering temperatures than at higher ones. Figure 6.7 shows the ferrite diffraction peak obtained by Synchrotron X-Ray Diffraction after heating up to 675°C and after 3 hours at 675°C, respectively. It appears clearly that the full width at half maximum decreases during this stage, indicating that dislocation recovery is still ongoing. Moreover, when considering the results from Chapter V, both weight fractions of M_7C_3 and $M_{23}C_6$ increase during the first 3 hours of tempering at 675°C, leading to further softening of the material.

The softening effect of temperature can be explained as follows. After heating up to 700°C and 725°C, more dislocations are already annihilated, thus the material is already softer than at lower temperatures. Moreover, M_7C_3 and $M_{23}C_6$ carbides have already started to precipitate, while at lower temperatures, incoherent carbides are still very fine when the heating stops, and only starts to grow during the isothermal step due to dissolution of cementite.

One should also notice that M_2C tends to coarsen after 3 hours at 700°C and 725°C compared to lower temperatures, as seen in Chapter V. Thus, their strengthening effect should decrease with increasing temperature.

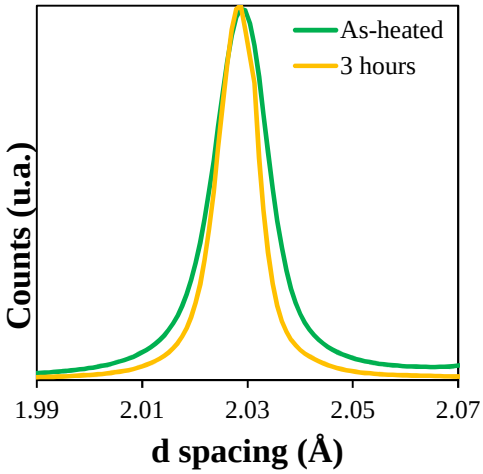

Figure 6.7: *X-Ray Diffraction peaks of the ferritic {110} planes after heating at 675°C and after tempering for 3 hours at 675°C.*

Thus, stage B integrates contributions from Stages II and III postulated by Parameswaran [16].

Stage C: Evolution of hardness between 3 hours and 24 hours of tempering

Upon Stage C, the loss of hardness is similar for temperatures ranging from 650°C to 725°C, namely, 25HV, and is up to 35HV at 725°C, indicating a change in the microstructural evolution at 725°C with respect to lower temperatures.

Based on the results from Chapter V, this range of time durations corresponds to the growth of $M_{23}C_6$, leading to coarsening/dissolution of M_2C carbides, full dissolution of remaining cementite and partial dissolution of M_7C_3 carbides. This phenomenon leads to an increase in inter-particle distance inside bainitic laths, and thus the strengthening contribution due to these carbides decreases. After 24 hours at 725°C, only coarse $M_{23}C_6$ are observed, explaining the stronger softening during Stage C at this temperature.

On the other hand, Figure 6.8 shows the {110} ferrite diffraction peaks obtained by Synchrotron X-Ray Diffraction after tempering at 675°C for times ranging from 3 hours to 24 hours. All peaks are superimposed, thus no significant dislocation recovery is expected to happen.

As a conclusion, microstructural evolutions responsible for softening of the material upon the isothermal part of the tempering treatment are summarized in Table 6.3. All these mechanisms are thermally activated, explaining the decrease in hardness for a given tempering time when increasing tempering temperature. Stage C is thus similar to the stage IV as postulated by Parameswaran [16].

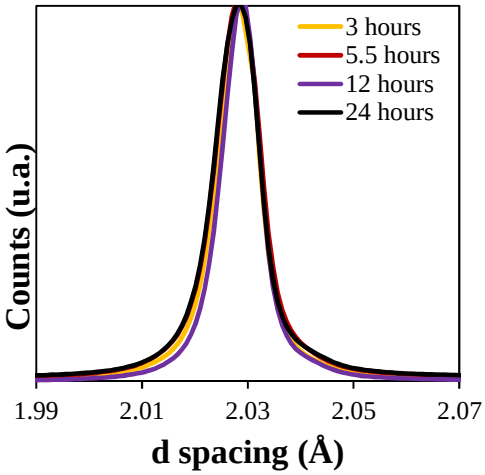

Figure 6.8: *X-Ray Diffraction peaks of the ferritic {110} planes after tempering at 675°C for times ranging from 3 hours to 24 hours.*

Time	Mechanisms	Effect
0h → 3h	Dislocation recovery	Softening
	Precipitation and growth of M_7C_3 and $M_{23}C_6$	Softening
	Coarsening of M_2C (at 700°C and 725°C)	Softening
3h → 24h	Growth of $M_{23}C_6$, coarsening and dissolution of M_2C	Softening

Table 6.3: *Mechanisms responsible for the hardness evolution upon tempering*

As a conclusion on the magnitude of contributions due to microstructural evolutions, the softening induced by loss of atoms in solid solution is negligible compared to of the one due to recovery of the

dislocation structure, and this latter is higher than strengthening induced by precipitation of M_2C carbides. Moreover, softening upon Stage B is higher than upon Stage C, thus the softening due to recovery of the dislocation structure is also higher than the one due to the precipitation of incoherent carbides.

2.1.2 Tensile properties

Tensile testing of small specimens was performed at room temperature with an elongation rate of 5.10^{-4} s^{-1}. Tensile curves for the three selected conditions, namely, 675°C – 5.5 hours, 675°C – 12 hours and 700°C – 5.5 hours are presented in Figure 6.9, along with an enlarged view on the strain hardening zone for all tests. For each condition, two tests were conducted.

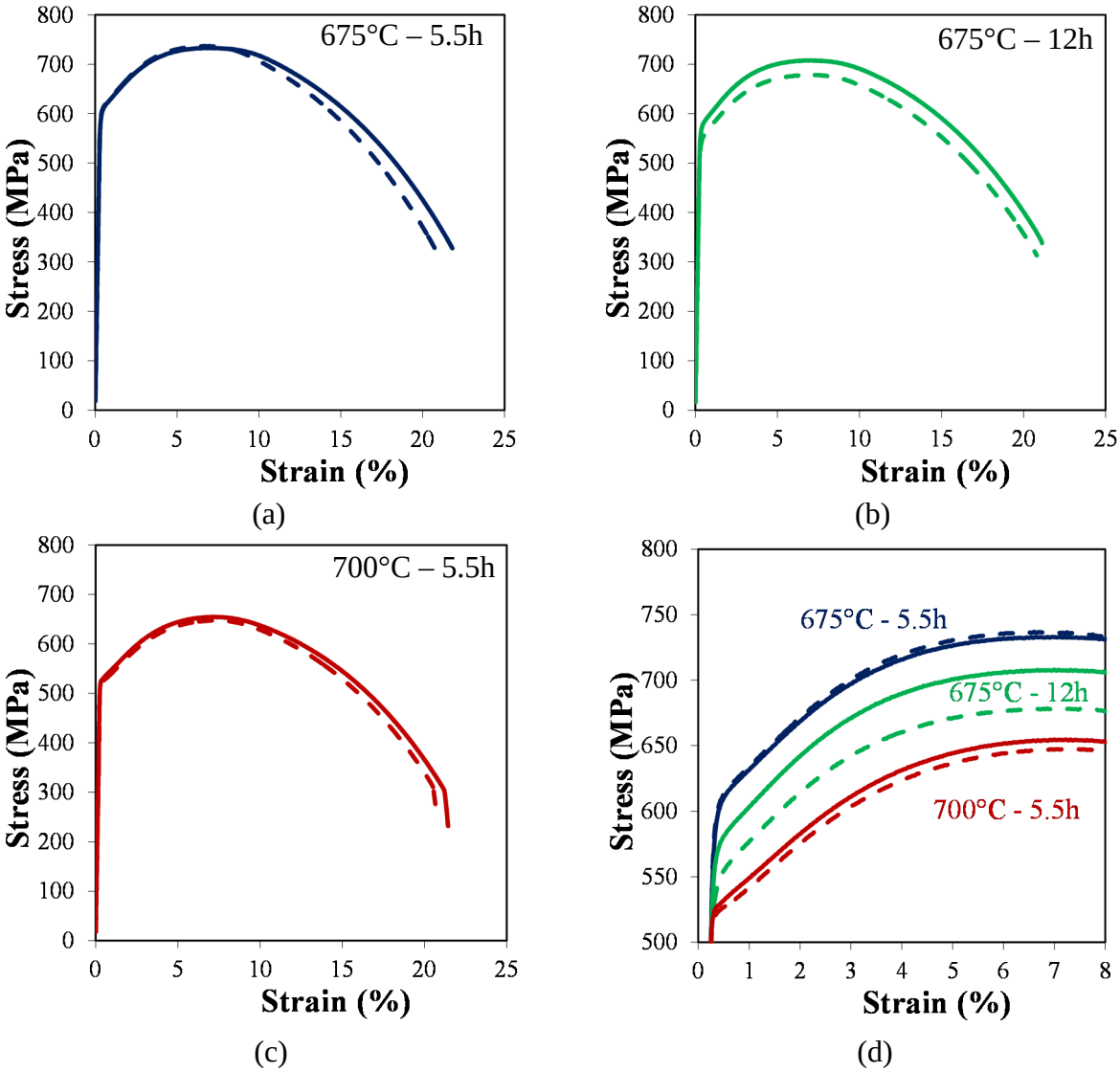

Figure 6.9: *Tensile curves for tempered specimens tempered (a) for 5.5 hours at 675°C, (b) for 12 hours at 675°C, (c) for 5.5 hours at 700°C, (d) enlarged view on the strain hardening zone for each condition.*

It should be pointed out that the tensile tests were conducted without extensometers, thus the elastic part as shown in Figure 6.9 comes from a mathematical correction (from compliance of the tensile machine) made *a posteriori*. The values of yield strength (YS), ultimate tensile strength (UTS), maximum uniform elongation (Ag) and fracture elongation (A) for all six tests are gathered in Table 6.4.

Tempering conditions	**HV5**	**YS (MPa)**	**UTS (MPa)**	**Ag (%)**	**A (%)**
675°C -5.5 hours	225±3	614	737	6.7	20.6
		610	733	7.1	21.7
675°C – 12 hours	206±2	553	678	7.2	20.7
		580	708	7.0	21.0
700°C - 5.5 hours	207±6	526	648	7.3	20.6
		531	655	7.1	21.3

***Table 6.4**: Summary of tensile properties for each tested tempering condition*

The general response to deformation for all three conditions is rather similar: the transition between the elastic domain and the plastic domain is acute, even when the mathematical correction of the Young modulus in not taken into account (i.e. by considering raw data on load vs load line displacement curves). The following strain hardening is moderate (roughly 125 MPa), and all curves are parallel to each other. Necking starts at Ag = 7%, followed by ductile fracture at an elongation of 21%. The yield strength and the ultimate tensile strength decrease with increasing tempering time and temperature. Moreover, increasing the tempering temperature results in a higher loss of tensile properties than increasing the tempering time.

Based on these observations, the effect of tempering conditions on tensile properties can be discussed as follows:

The same tendency for all three tempering conditions with regards of strain hardening and resistance to necking indicates that the same interactions occur between mobile dislocations and forest dislocations. Thus, the dislocation density plays no role in the observed differences. Variations of tensile properties are only induced by the change in the precipitation state, as indicated by the fact that all three conditions are within Stage C as previously mentioned. Carbides can impede dislocation motion, especially in the case of fine, coherent carbides. As seen in Chapter V, for these three tempering conditions, incoherent M_7C_3 carbides remain stable in size but decrease in phase fraction, incoherent $M_{23}C_6$ carbides experience growth and are coarser than M_7C_3 carbides; finally, semi-coherent M_2C carbides are coarsening or dissolving. Growth of $M_{23}C_6$ carbides and dissolution of M_2C carbides result in the general decrease in inter-particle distance which is detrimental regarding the tensile properties.

However, one should notice that the hardness is similar for the 700°C – 5.5h and the 675°C – 12h conditions, namely, 205 HV, while the tensile properties are not the same. As seen in Chapter V, there are more incoherent carbides and slightly less M_2C carbides after 5.5 hours of tempering at 700°C, respectively 0.95 wt% and 0.22 wt%, than after 12 hours of tempering at 675°C, respectively 0.66 wt% and 0.27 wt%. Tensile tests measure the resistance to deformation of the whole sample, at

the opposite of hardness which is only a local measurement. Thus, such slight change in the phase fractions may not affect the local hardness, but may have an impact on tensile properties.

2.1.3 Impact toughness properties

For all three tested temperatures, 14 specimens were tested by V-notch Charpy impact tests, at temperatures ranging from -150°C to 288°C. This latter temperature corresponds to the in-service temperature of a nuclear pressure vessel. Ductile-to-brittle transition curves for all three tested tempering conditions are shown in Figure 6.10, and impact toughness properties are summarized in Table 6.5.

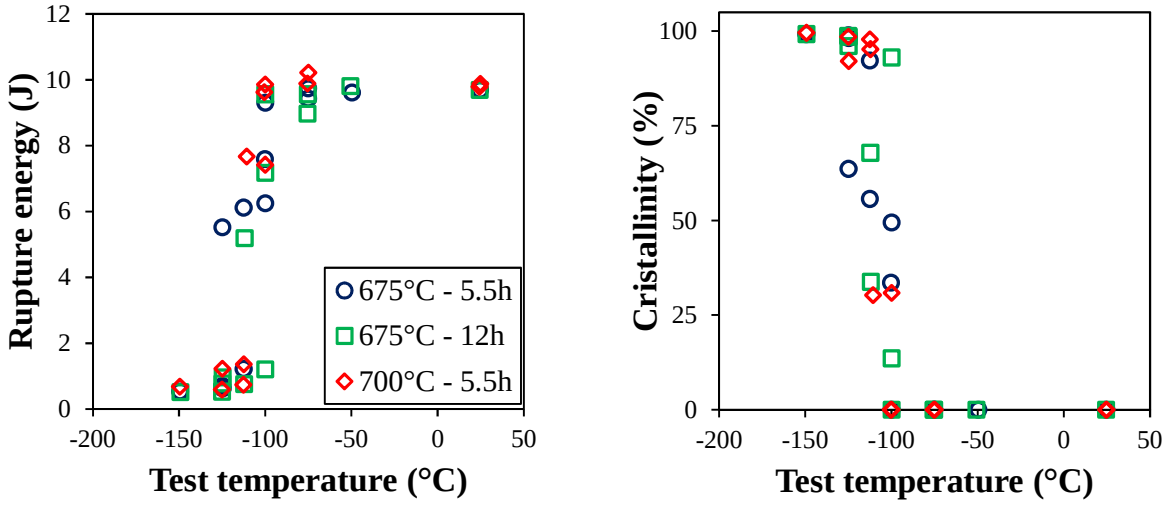

(a) (b)

Figure 6.10: *Ductile-to-brittle transition curves for each tempering condition (a) rupture energy, (b) area fraction of brittle fracture surface*

	DBTT (°C)	FATT (°C)	USE (J)	RE at 288°C (J)
675-5.5	-111	-107	9.55	8.24
675-12	-105	-102	9.66	8.31
700-5.5	-112	-111	9.87	8.31

Table 6.5: *Summary of impact toughness properties for each tested tempering condition*

The evolution of the fracture mode as a function of the testing temperature is rather similar for all three tested tempering conditions, and can be divided in three different zones.

- At low testing temperatures, i.e. below -125°C, rupture is fully brittle and occurs for energy values within a range of 0.5 J. In this temperature domain, fracture occurs by cleavage although patches of intergranular fracture are also observed from time to time, as already stated in Chapter IV and shown in Figure 6.11. Cleavage facets exhibit a wide range of sizes, from 2 µm up to 10 µm, regardless the tempering conditions or the testing temperature. Residual plasticity is sometimes observed close to what appears to be prior austenite grain boundaries, and is likely to be induced by ferrite resulting from the decomposition of retained austenite. No conclusion on the

crack initiation can be drawn from SEM observations; however it is likely due to incoherent carbides, even if they were almost never observed, possibly because located underneath the fracture surface.

- At high testing temperatures, i.e. above -100°C, the rupture is fully ductile, and the dissipated energy is around 9.5 J regardless the tempering treatment. Ductile shear first occurs, roughly over the first millimeter from the notch, before dimples become observable as shown in Figure 6.12. EDX analysis of particles inside these dimples proved that they were MnS.
- A transition between these two regimes occurs for testing temperatures from -125°C to -100°C, where the fracture surface exhibits a ductile crack advance close to the notch, followed by brittle fracture. The ductile and brittle fracture surfaces are similar to the ones described above, namely, a shearing front in the first millimeter and dimples with MnS particles for ductile surfaces, and cleavage with patches of intergranular fracture and local plasticity for the brittle surfaces. DBTT and FATT remain similar regardless the tempering conditions, around -105°C. As already stated in Chapter IV, this transition is very steep, within 20°C, as the fracture energy is distributed into two groups in the vicinity of the DBTT, namely fully brittle fracture of specimens (1-2 J) and brittle-ductile fracture (5-8 J). No physical mechanism can be proposed to explain this bimodality, as fracture surface observations reveal no differences between both energy groups. More detailed investigations about cleavage fracture initiation are needed to clarify this point.

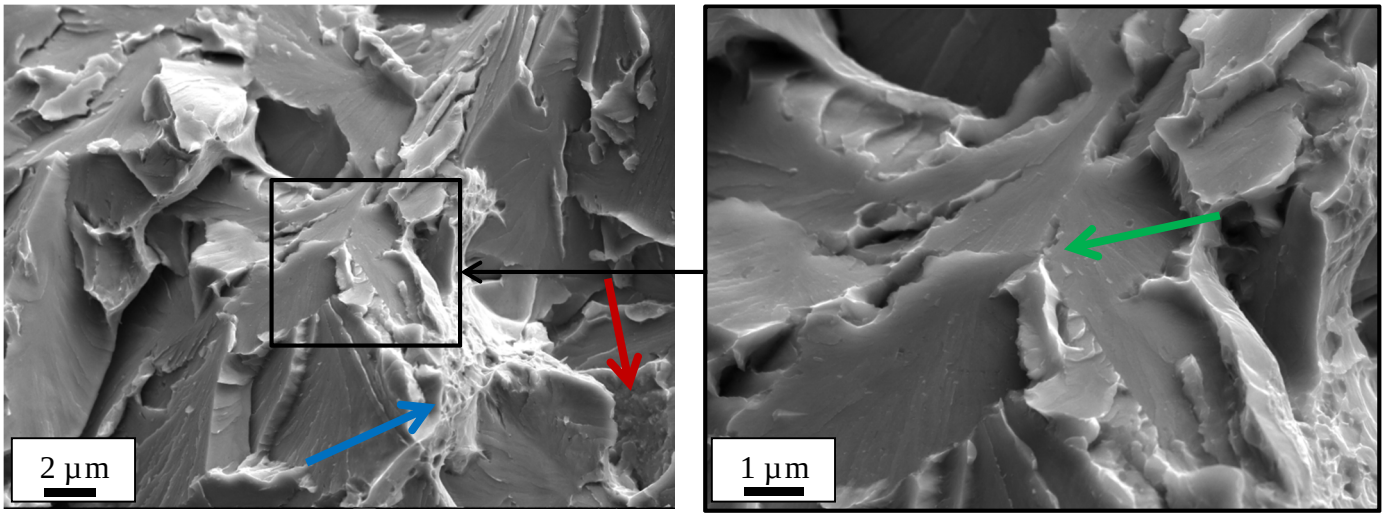

Figure 6.11: *Typical crack initiation site for brittle fracture. Blue arrow shows residual plasticity, red arrow an intergranular patch and green arrow carbides that possibly acted as local crack initiators. Tempering conditions: 675°C – 5.5h, sample tested at -125°C, rupture energy: 0.63 J.*

It appears clearly that the softening previously observed has no impact on the toughness properties. Thus, the change in microstructure induced by a slightly higher tempering temperature or a slightly higher tempering time is not significant enough to impact these properties. However, a major change in microstructure, such as the one observed after 24 hours of tempering at 725°C where all M_2C are dissolved and only large $M_{23}C_6$ carbides remain, is expected to increase DBTT and FATT.

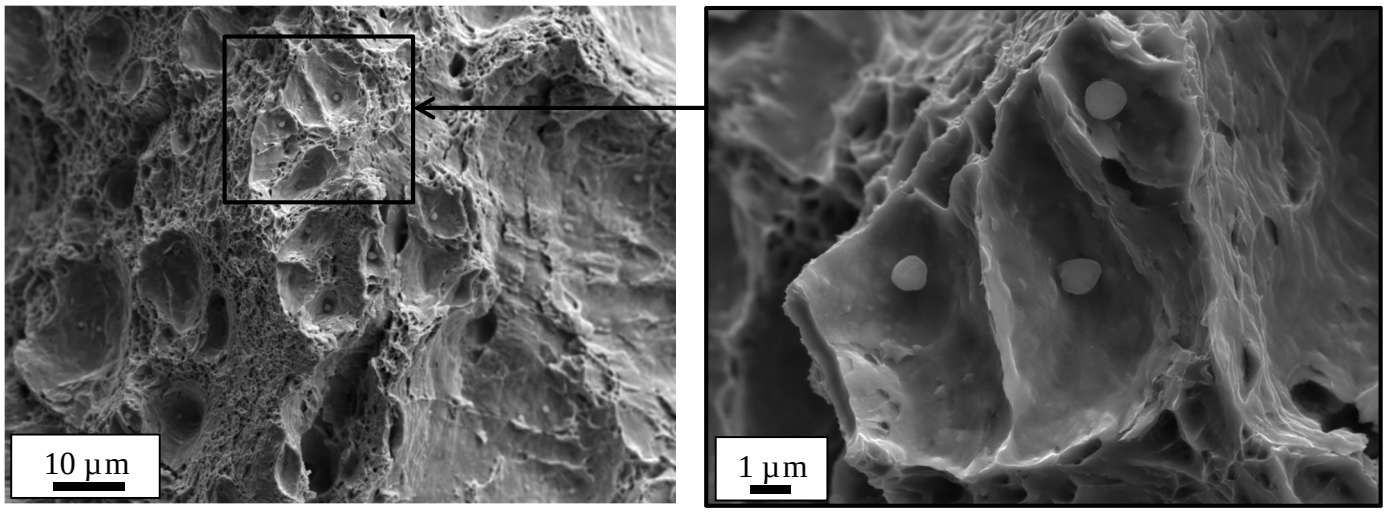

Figure 6.12: *Typical ductile fracture surface. Particles in dimples are MnS. Tempering conditions: 675°C – 5.5h, sample tested at -112.5°C, rupture energy: 6.12 J.*

As a conclusion, the evolution of microstructure upon tempering affects the material strength but not its impact toughness. Moreover, softening during tempering seems to be mostly due to dislocation annihilation, while dissolution of M_2C and growth of $M_{23}C_6$ only has a second-order effect.

2.2 Effect of stress-relieving heat treatment on final mechanical properties

The effect of the final stress-relieving heat treatment (or post-weld heat treatment, PWHT) on mechanical properties has been studied, as the targeted component is made of parts to be joined by welding. Two different stress-relieving heat treatments were tested after tempering at 675°C for 5.5 hours: (A) 645°C – 16 hours, (B) 625°C – 16 hours. The first one corresponds to the PWHT applied on the reference material, and the second one is the one used for the quenched+tempered states in Chapter IV. Results for the latter have already been reported in Chapter IV after austenitization at 970°C – 1 hour. Samples were air cooled after both tempering and stress-relieving heat treatments. The heating rate for both PWHTs was 0.014°C/s (50°C/h).

Figure 6.13 shows the comparison of hardness values before the PWHT and after the PWHT. The stress-relieving heat treatment appears to have none or little effect on the material hardness. These observations are consistent with results reported in Chapter V, where it was shown that the stress-relieving heat treatment only has an impact on the less stable carbides, i.e. M_3C and cubic M_2C, thus no strong change in microstructure is expected during PWHT after tempering. Moreover, the stress-relieving heat treatment is conducted at temperatures lower than the tempering heat treatment, thus no more dislocation recovery should take place.

Figure 6.14 shows the stress-strain curves for the as-tempered states and after any of the two stress-relieving heat treatments. Characteristic tensile properties are summarized in Table 6.6. The yield strength and the ultimate tensile strength appear to decrease after the stress-relieving heat treatment, as well as the maximum uniform elongation. However, the fracture elongation is not affected by this heat treatment, and the temperature of the latter has no effect on the tensile properties.

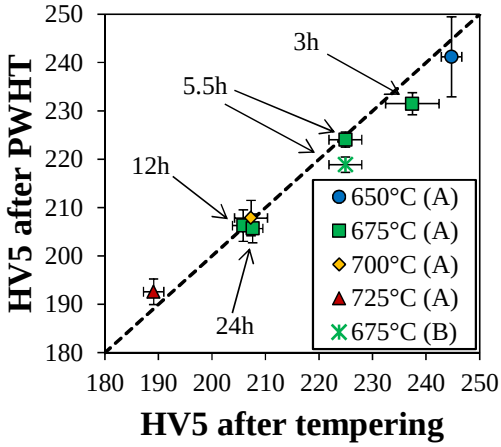

Figure 6.13: *Comparison between hardness before and after PWHT. The 650°C, 700°C and 725°C correspond to 5.5 hours of tempering at these temperatures. A and B refer to the applied PWHT.*

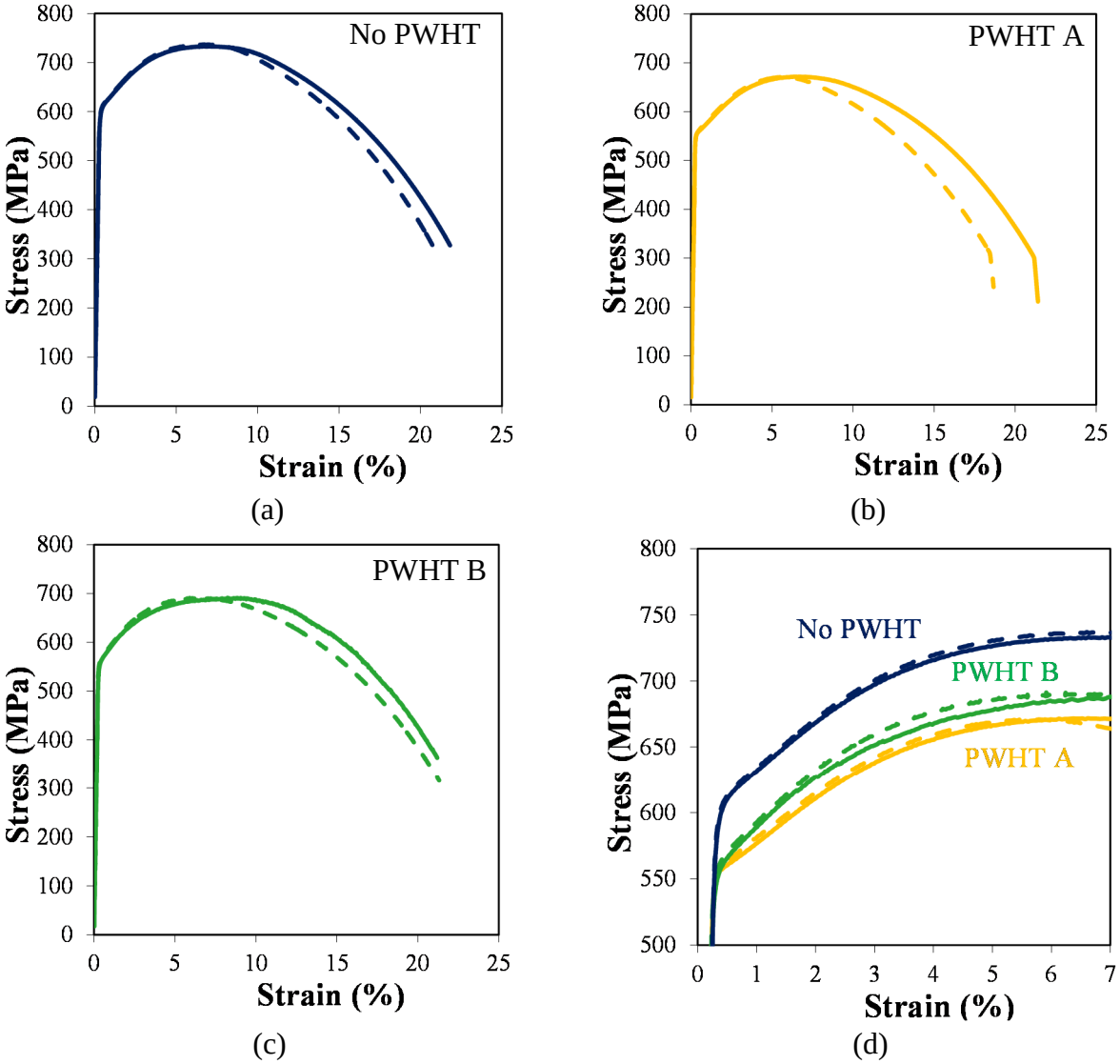

Figure 6.14: *Tensile curves for tempered specimens tempered at 675 °C for 5.5 hours (a) without PWHT, (b) with PWHT A (c) with PWHT B, (d) enlarged view on the strain hardening zone*

Tempering conditions	YS (MPa)	UTS (MPa)	Ag (%)	A (%)
No PWHT	614	737	6.7	20.6
	610	733	7.1	21.7
PWHT A	561	671	5.4	18.5
	560	672	6.3	21.3
PWHT B	565	687	6.0	21.1
	569	691	5.6	21.3

***Table 6.6**: Summary of tensile properties for each tested condition with respect to PWHT*

Since no detailed investigations were made on the microstructure of the stress-relieved specimens, only assumptions can be made, particularly when considering the lack of influence of the stress-relieving heat treatment on hardness. From X-Ray diffraction on electroetching residues, the stress-relieving heat treatment leads to dissolution of cementite and increase in phase fraction of $M_{23}C_6$, M_7C_3, while the weight fraction of M_2C remains constant. Possible coarsening of M_2C carbides might occur, however no TEM observations were made to confirm this hypothesis.

Figure 6.15 shows the rupture energy and the percentage of brittle fracture as a function of the testing temperature for the specimens that were only tempered and the ones which underwent the additional PWHT (A). Tests after PWHT (B) were only conducted at -125°C. Table 6.7 summarizes the impact toughness properties. Results from SEM observations of fracture surfaces are similar to the ones discussed in 2.1.3. The stress-relieving heat treatment does not impact the toughness properties, namely, the FATT, the DBTT and USE either. However, the bimodality of the rupture energy in the ductile to brittle transition range is again evidenced.

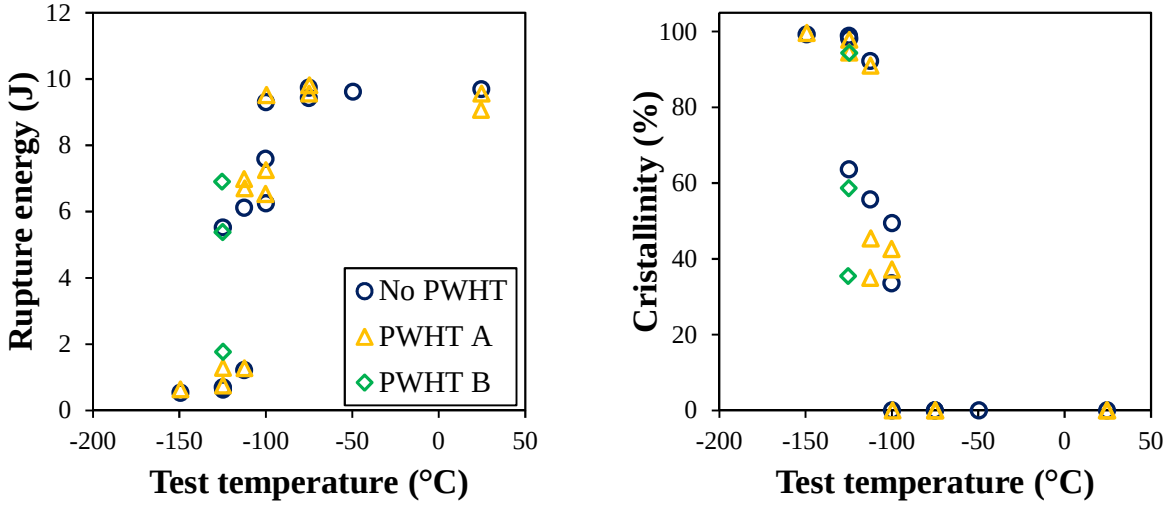

(a) (b)

***Figure 6.15:** Ductile-to-brittle transition curves for specimens tempered at 675°C for 5.5 hours with and without PWHT (a) rupture energy, (b) area fraction of brittle fracture surface*

	DBTT (°C)	FATT (°C)	USE (J)	RE at 288°C (J)
No PWHT	-111	-107	9.55	8.24
PWHT A	-113	-109	9.50	8.46

Table 6.7: *Summary of the effect of PWHT A on impact toughness properties*

2.3 Determination of Temper Parameter coefficient

It is of industrial interest to determine the coefficient *C* in equation (6.1) corresponding to a linear variation of the current experimental values with the Temper Parameter. Indeed, such parameter would allow to rapidly estimate the order of magnitude of mechanical properties for a given tempering time and temperature.

Linear regression by the mean squares method on the hardness values presented in section 2.1.1 with the exception of as-heated states result in an optimized value for *C* of 20.434 (Figure 6.16).

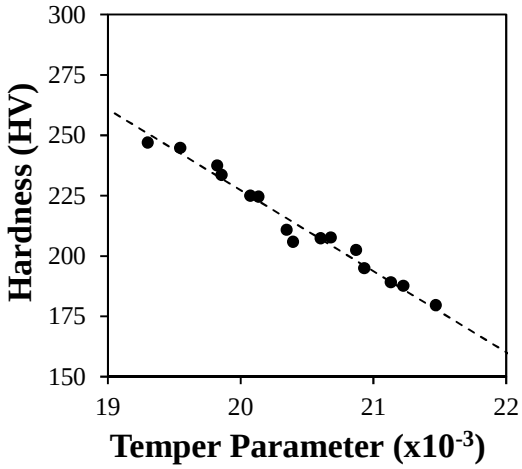

Figure 6.16: *Result of the optimization of the C value of the Temper Parameter on the hardness value*

Using this coefficient *C*, the tensile and impact toughness properties as experimentally determined can be tentatively represented as a function of the Temper Parameter. The addition of a stress-relieving heat treatment can also be represented by adding its equivalent time $t_{eq,PWHT}$ when reported to the prior tempering time t_{temp} at the prior tempering temperature T_{temp}, such as:

$$\mathrm{TP}_{PWHT} = T_{PWHT}(\log t_{PWHT} + C) \tag{6.3}$$

$$\log(t_{eq,PWHT}) = \frac{\mathrm{TP}_{PWHT}}{T_{temp}} - C \tag{6.4}$$

$$\mathrm{TP}_{temp+PWHT} = T_{temp}(\log(t_{temp} + t_{eq,PWHT}) + C) \tag{6.5}$$

Representations of yield strength and ultimate tensile strength, as well as transition temperature and characteristic rupture energy as a function of the temper parameter using C = 20.434 are reported in Figure 6.17 and Figure 6.18. The ultimate elongation is not represented since it does not change

much with tempering conditions. It should also be pointed out that all tested tempering conditions result in values of TP close to each other (between 20 000 and 20 600), and more tests would be necessary to confirm the observed tendencies over a more extended range of values for TP.

Nevertheless, the yield strength and ultimate tensile strength vary linearly with the Temper Parameter, the fit being very satisfactory when the PWHTs are not accounted for. Variation of these properties with the TP, whatever accounting for subsequent PWHT or not, is given in equations (6.6) to (6.9):

No PWHT	$YS\ (MPa) = -0.155 \times TP + 3858$	(6.6)
No PWHT	$UTS\ (MPa) = -0.156 \times TP + 3752$	(6.7)
PWHT	$YS\ (MPa) = -0.124 \times TP + 3083$	(6.8)
PWHT	$UTS\ (MPa) = -0.119 \times TP + 3105$	(6.9)

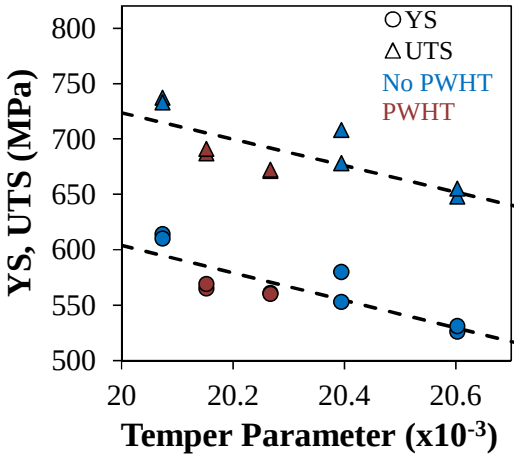

Figure 6.17: *Influence of Temper Parameter on the Yield Strength (YS) and the Ultimate Tensile Strength (UTS)*

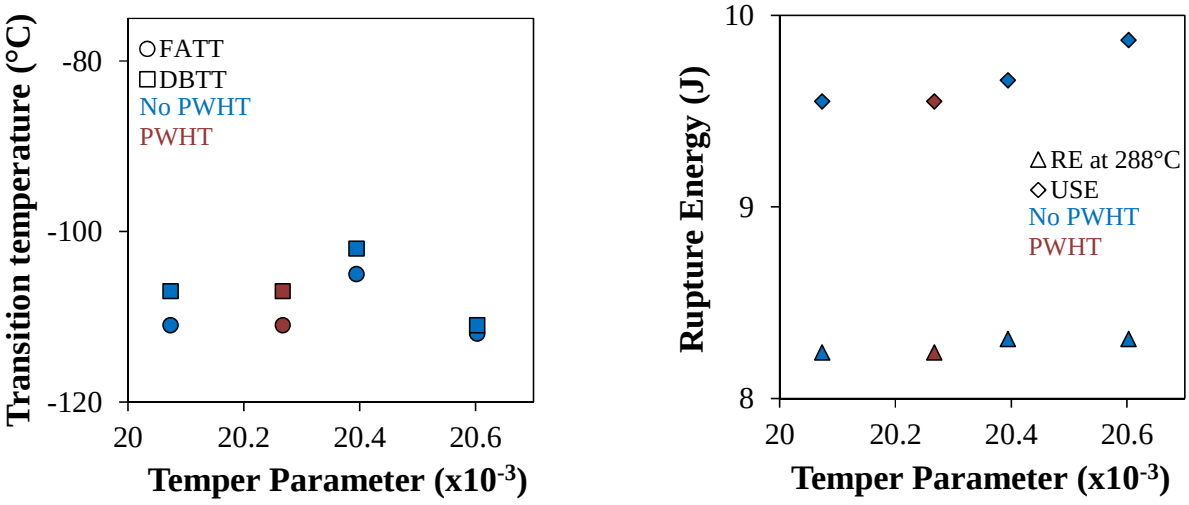

Figure 6.18: *Influence of Temper Parameter on impact toughness properties*

For the tested tempering conditions, impact toughness transition temperatures and characteristic rupture energy appears to remain constant whatever the Temper Parameter, as already stated above.

3. CONCLUSION

Dislocation recovery appears to be the most important microstructural mechanism when considering the softening of the studied material upon tempering. Carbide evolution, such as growth of incoherent carbides and precipitation/dissolution of M_2C, only has a limited effect on hardness. However, tensile properties of fully recovered microstructure prove that the carbide evolution has an impact on the yield strength and the ultimate tensile strength, in a stronger way than expected from hardness measurements. Namely, growth of incoherent $M_{23}C_6$ carbides and dissolution or coarsening of M_2C carbides are detrimental to the tensile properties, for the latter by decreasing the number density of obstacles to dislocation motion.

The stress-relieving heat treatment appears to have no effect on hardness, however an additional softening is observed in tensile tests, once again due to the growth of incoherent carbides. The temperature at which this heat treatment is conducted does not seem to affect tensile properties.

For all tested conditions, no differences were found regarding toughness properties. However, the transition between the brittle fracture and the ductile fracture is very steep, as already stated in Chapter IV. This seems to be characteristic of the studied steel, and further work on the physical origins of this steep transition would be interesting. However, such results show that the studied material exhibits good robustness to tempering and stress-relieving heat treatments in terms of impact toughness, and that these heat treatments should be selected regarding the tensile properties.

A Temper Parameter coefficient C = 20.434 has been determined thanks to hardness values. Acceptable linear variation as a function of the Temper Parameter is found for tensile and impact toughness properties, allowing the prediction of the order of magnitude of these mechanical values for Temper Parameter ranging from 20 000 to 21 000.

Conclusion and outlooks

In this thesis, the effect of heat treatments on the microstructural evolution and mechanical properties of a 2.25 Cr – 1 Mo steel has been investigated using experimental characterization and a modelling approach. The main conclusions from this study are first presented both in terms of under a scientific understanding point of view, then from the industrial angle. Some improvement ways opened by this work are reported at the end of this chapter.

The **material** itself has been first characterized. From thermodynamic equilibrium calculations, and with the exception of carbides, the only secondary phases of interest for metallurgical evolution during heat treatments are aluminum nitrides (AlN) which might affect austenite grain growth, and manganese sulphides (MnS), which act as void nucleation sites for ductile fracture. No major segregations or ghost lines have been highlighted in the material; minor segregations located along the radial-circumferential plane are not expected to affect mechanical and microstructural properties, except for local concentrations of MnS particles. Thus, the chemical composition of the material can be considered as homogeneous in thickness, and no sampling effect was expected in this study. Equivalent cooling rates, corresponding to representative locations across the thickness of the targeted hollow component, were also determined. A first test conducted with an austenitization condition at 920°C for 30 minutes shows insufficient bainitic hardenability, although austenitization at 930°C for 1 hour leads to a fully bainitic structure throughout the thickness.

In order to investigate this phenomenon, the effect of **austenitization** on the **microstructural evolution of austenite** was experimentally investigated, highlighting limited growth at 920°C and 970°C, as well as a slowed down growth at 1020°C. No abnormal growth was ever observed. Thanks to a modelling approach, it was shown that Zener pinning induced by AlN particles has an almost negligible effect on austenite grain growth, while solute drag due to segregation of molybdenum at austenite grain boundaries is likely to induce the observed limited growth.

The effect of austenitization on **final microstructure and mechanical properties** was investigated after cooling at the rates determined above. Coarser austenite grains lead to lower amount of ferrite at lower cooling rates while more martensite precipitates at higher cooling rates. Moreover, ferrite precipitation has higher influence on hardness compared to martensite, at least after tempering. Experimental results confirmed that the austenite grain size is not the only parameter that impacts decomposition of austenite during cooling: at rather low austenitization temperatures, the duration of the isothermal stage has also to be accounted for. This is more likely due to enrichment of austenite grain boundaries in molybdenum with time.

The **carbide precipitation sequence** was characterized upon both heating up to the temperature of interest and the isothermal step of tempering. Precipitation of carbides starts during the heating step, due the low heating rate that is dictated by the high thickness of the targeted component. From experimental observations, a precipitation sequence was proposed as follows. M_3C cementite precipitates first from the decomposition of retained austenite that stems from the incomplete bainitic

transformation. M_7C_3 carbides then nucleate at interfaces between cementite and matrix, and grow by attracting both chromium and carbon atoms from their parent M_3C phase. Molybdenum carbides, M_2C, precipitate homogeneously in the matrix, while $M_{23}C_6$ are located at dislocations within the bainitic laths. $M_{23}C_6$ experience growth with increasing time and temperature, leading to the dissolution of neighboring less stable carbides. The subsequent stress-relieving heat treatment leads to a full dissolution of remaining cementite and increase in phase fraction of M_7C_3 and $M_{23}C_6$.

Thanks to these results, **the effect of the microstructural evolution upon tempering on hardness, tensile and impact toughness properties** has been determined. Dislocation recovery appears to be the most important microstructural mechanism when considering softening of the studied material upon tempering. Carbide evolution, such as growth of incoherent carbides and precipitation/dissolution of M_2C, only has a limited effect on hardness. However, tensile properties of fully recovered microstructures prove that the carbide evolution has an impact on the yield strength and the ultimate tensile strength, in a stronger way than expected from hardness measurements. Dissolution and coarsening of M_2C carbides are detrimental to the tensile properties by decreasing the number of obstacles impeding the dislocation movement. Further stress-relieving heat treatment decreases the yield strength and the ultimate tensile strength while the hardness remains constant. These contradictory results have not been explained, and further experiments should be conducted in order to clarify this phenomenon. For all tested conditions, no differences were found regarding toughness properties.

From the above results, the following points of interest for the industrial application were highlighted:

- Minor segregations only have little effect on the microstructural and mechanical properties of this material.
- There is no need to further add aluminum for controlling the austenite grain growth, since limited growth at low temperatures is due to another phenomenon than pinning by AlN particles.
- An optimal austenitization condition leading to both constant austenite grain size and fully bainitic microstructure within the thickness of the component has been determined, namely, 970°C – 1 hour. However, the studied material is robust with respect to austenitization parameters. It may experience a wide range of austenitization conditions resulting in a fully bainitic microstructure and similar tensile and impact toughness properties, namely, 1 hour at temperatures ranging from 920°C to 1000°C.
- For the tested tempering conditions and specimen geometry, carbide precipitation during tempering has only an effect on the tensile properties and none on impact toughness. Thus, the tempering condition could be selected by only considering the tensile properties at first glance. Moreover, mechanical properties are not significantly sensitive to the temperature at which the stress-relieving heat treatment is conducted.
- From a practical point of view, a Temper Parameter coefficient of 20.434 (formally similar to a Larson-Miller parameter) gives good time-temperature equivalence for the studied material concerning the effect of tempering conditions on yield and tensile strength at room temperature.

Outlooks

To further refine our understanding of microstructural development during heat treatments and of its influence on resulting mechanical properties, several issues still need to be addressed.

Interactions between **growing austenite grains** have not been taken into account in the model used for underlying the mechanisms responsible for austenite grain growth. Some further work in this direction would be useful, and may result in a lower contribution of solute drag, thus in a lower estimate of the binding energy between molybdenum atoms and austenite grain boundaries.

Quantitative measurements of the **molybdenum segregation** at prior austenite grain boundaries and at prior ferrite/austenite interphases, for instance by means of STEM or atom probe tomography, would confirm or invalidate the hypothesis of a solute-drag like effect taking place during the decomposition of austenite into ferrite upon cooling.

The **bainitic matrix** itself has not been extensively characterized, and much work is needed on this particular topic in order to fully understand microstructural evolution of the material during heat treatments. Mainly, the effect of austenitization conditions and cooling rate on decomposition of austenite into bainite upon cooling has not been studied. This matter is likely to have an effect on the carbide precipitation during tempering, since it might induce change in the amount or spatial distribution of retained austenite within the bainitic matrix, bainitic lath size and dislocation density.

Further TEM observations after the **stress-relieving heat treatment** would improve the understanding of the slight softening effect induced by this heat treatment on tensile strength, but not on hardness. **Interactions between recovery of dislocation structure and precipitation** would also be interesting to study in this material.

Finally, it would be interesting to refine the **selection of the heat treatment** based on a sample geometry more representative of that of industrial-scale components, in order to better take the effect of **thickness** on microstructural development and resulting mechanical properties into account, particularly for the carbide precipitation, since the tempering time is not the same all across the thickness.

Mechanical tests using **standard-sized specimens** are also needed in order to fully characterize the material, particularly with regard to the RCC-M standards, once the heat treatment has been determined. A more detailed study of the toughness behavior of the material would also be of interest, particularly in order to understand the observed **bimodality of the ductile-to-brittle transition curves**.

References

1. Trautwein, A., Mayer, H., Gysel, W., & Walser, B. (1982). “Structure and mechanical properties of 21/4Cr-1Mo cast steel for pressure components with wall thickness up to 500mm.” In G. S. Sangdahl & M. Semchysen (Eds.), *Application of 21/4Cr-1Mo steel for thick-wall pressure vessels* (pp. 189–207). Denver, Colorado: ASTM.

2. Pillot, S., Chauvy, C., Corre, S., Coudreuse, L., Gingell, A., Héritier, D., & Toussaint, P. (2013). “Effect of temper and hydrogen embrittlement on mechanical properties of 2,25Cr–1Mo steel grades – Application to Minimum Pressurizing Temperature (MPT) issues. Part I: General considerations & materials’ properties.” *International Journal of Pressure Vessels and Piping*, *110*, 17–23.

3. Pillot, S., Chauvy, C., Corre, S., Coudreuse, L., Gingell, A., Héritier, D., & Toussaint, P. (2013). “Effect of temper and hydrogen embrittlement on mechanical properties of 2,25Cr–1Mo steel grades – Application to Minimum Pressurizing Temperature (MPT) issues. Part II: Vintage reactors & MPT determination.” *International Journal of Pressure Vessels and Piping*, *110*, 24–31.

4. Murakami, Y., Nomura, T., & Watanabe, J. (1982). “Heavy-section 21/4Cr-1Mo steel for hydrogenation reactors.” In G. S. Sangdahl & M. Semchysen (Eds.), *Application of 21/4Cr-1Mo steel for thick-wall pressure vessels* (pp. 383–417). Denver, Colorado: ASTM.

5. Orr, J., Beckitt, F. R., & Fawkes, G. D. (1978). “The physical metallurgy of chromium-molybdenum steels for fast reactor boilers.” In *Ferritic steels for fast reactor steam generators.* (pp. 91–109). London, UK: British Nuclear Energy Society.

6. Manna, G. (2004). *Factors limiting the in-service lifetime of CrMoV steels and weldments for pressure equipment*. PhD dissertation, University of Wales Swansea, United Kingdom.

7. Copeland, J. F. (1976). “Influence of Sulfur Content on the Fracture Toughness Properties of 2 1/4 Percent Cr-1 Percent Mo Steel.” *Journal of Pressure Vessel Technology*, *98*(2), 135–142.

8. Andrén, H.-O., Cai, G., & Svensson, L.-E. (1995). “Microstructure of heat resistant chromium steel weld metals.” *Applied Surface Science*, *87-88*, 200–206.

9. Dawson, K. (2012, July 1). *Dissimilar metal welds*. PhS dissertation, University of Liverpool, United Kingdom.

10. Pelletier, M. (1981). *Study of structural transformations occuring in low carbon chromium-molybdenum ferritic steels: influence of small additions of vanadium and molybdenum*. PhD dissertation, Paris-Sud University, Orsay, France. In French.

11. Klueh, R. L. (1982). “Chromium-molybdenum steels for fusion reactor first walls — a review.” *Nuclear Engineering and Design*, *72*(3), 329–344.

12. Wada, T., & Eldis, G. T. (1982). “Transformation characteristics of 21/4Cr-1Mo steel.” In G. S. Sangdahl & M. Semchysen (Eds.), *Application of 21/4Cr-1Mo steel for thick-wall pressure vessels* (pp. 343–361). Denver, Colorado: ASTM.

13. Suresh, S., Zamiski, G. F., & Ritchie, R. O. (1982). “Fatigue crack propagation behavior of 21/4Cr-1Mo steels for thick-wall pressure vessels.” In G. S. Sangdahl & M. Semchysen (Eds.), *Application of 21/4Cr-1Mo steel for thick-wall pressure vessels* (pp. 49–67). Denver, Colorado: ASTM.

14. Baker, R. G., & Nutting, J. (1959). “The Tempering of 2.25Cr–1Mo. Steel after Quenching and Normalising.” *Journal of the Iron and Steel Institute*, *7*, 257–268.

15. Cane, B. J. (1976). “Creep-fracture initiation in 2¼%Cr-1%Mo steel.” *Metal Science*, *10*(1), 29–34.

16. Parameswaran, P., Vijayalakshmi, M., & Raghunathan, V. S. (2003). “The influence of prior microstructure on tempering stages in 2.25Cr-1Mo steel.” *High Temperature Materials and Processes*, *21*(5), 251–267.

17. Mitchell, D. R. ., & Ball, C. . (2001). “A quantitative X-ray diffraction and analytical electron microscopy study of service-exposed 2.25Cr–1Mo steels.” *Materials Characterization*, *47*(1), 17–26.

18. Nishizaka, Y., Hara, Y., Hori, A., Tsukahara, H., Miyano, K., Wada, T., & Cox, T. B. (1985). “Changes in microstructure and mechanical properties of Cr-Mo reactor vessel steels during long-term service.” *Journal of Pressure Vessel Technology*, *107*(3), 285–294.

19. Cheruvu, N. S. (1989). “Degradation of mechanical properties of Cr-Mo-V and 2.25Cr-1Mo steel components after long-term service at elevated temperatures.” *Metallurgical Transactions A*, *20*(1), 87–97.

20. Sato, S., Matsui, S., Enami, T., & Tobe, T. (1982). “Strength and temper embrittlement of heavy-section 21/4Cr-1Mo Steel.” In G. S. Sangdahl & M. Semchysen (Eds.), *Application of 21/4Cr-1Mo steel for thick-wall pressure vessels* (pp. 363–383). Denver, Colorado: ASTM.

21. Guttmann, M., Dumoulin, P., & Wayman, M. (1982). “The thermodynamics of interactive co-segregation of phosphorus and alloying elements in iron and temper-brittle steels.” *Metallurgical Transactions A*, *13*(10), 1693–1711.

22. Song, S. H., Faulkner, R. G., & Flewitt, P. E. J. (2000). “Quenching and tempering-induced molybdenum segregation to grain boundaries in a 2.25Cr–1Mo steel.” *Materials Science and*

Engineering: A, *281*(1-2), 23–27.

23. Scott, T. E. (1982). “Pressure vessels for coal liquefaction - an overview.” In G. S. Sangdahl & M. Semchysen (Eds.), *Application of 21/4Cr-1Mo steel for thick-wall pressure vessels* (pp. 7–25). Denver, Colorado: ASTM.

24. Moss, C. J., & Kelly, P. M. (1994). “The mechanisms and detection of embrittlement in Cr-Mo pressure vessel steels.” *Fatigue & Fracture of Engineering Materials and Structures*, *17*(3), 369–380.

25. Wanagel, J., Hakkarainen, T., & Che-Yun, L. (1982). “Hydrogen attack in thick-section 21/4Cr-1Mo steels at elevated temperatures.” In G. S. Sangdahl & M. Semchysen (Eds.), *Application of 21/4Cr-1Mo steel for thick-wall pressure vessels* (pp. 93–108). Denver, Colorado: ASTM.

26. Marini, B., Averty, X., Wident, P., Forget, P., & Barcelo, F. (2015). “Effect of the bainitic and martensitic microstructures on the hardening and embrittlement under neutron irradiation of a reactor pressure vessel steel.” *Journal of Nuclear Materials*, *465*, 20–27.

27. Miller, M. K., Pareige, P., & Burke, M. G. (2000). “Understanding Pressure Vessel Steels.” *Materials Characterization*, *44*(1-2), 235–254.

28. Huang, H., Radiguet, B., Todeschini, P., Chas, G., & Pareige, P. (2011). “Atom Probe Tomography characterization of the microstructural evolution of a low copper reactor pressure vessel steel under neutron irradiation.” *MRS Proceedings*, *1264*, 1264–BB05–18.

29. Meslin, E., Lambrecht, M., Hernández-Mayoral, M., Bergner, F., Malerba, L., Pareige, P., … Almazouzi, A. (2010). “Characterization of neutron-irradiated ferritic model alloys and a RPV steel from combined APT, SANS, TEM and PAS analyses.” *Journal of Nuclear Materials*, *406*(1), 73–83.

30. Nikolaev, Y., Nikolaeva, A., & Shtrombakh, Y. I. (2002). “Radiation embrittlement of low-alloy steels.” *International Journal of Pressure Vessels and Piping*, *79*(8-10), 619–636.

31. Shtrombakh, Y. I., Gurovich, B. A., Kuleshova, E. A., Frolov, A. S., Fedotova, S. V., Zhurko, D. A., & Krikun, E. V. (2015). “Effect of Ni content on thermal and radiation resistance of VVER RPV steel.” *Journal of Nuclear Materials*, *461*, 292–300.

32. Blagoeva, D. T., Debarberis, L., Jong, M., & ten Pierick, P. (2014). “Stability of ferritic steel to higher doses: Survey of reactor pressure vessel steel data and comparison with candidate materials for future nuclear systems.” *International Journal of Pressure Vessels and Piping*, *122*, 1–5.

33. Ghiya, S. P., Bhatt, D. V., & Rao, R. V. (2009). “Stress relief cracking in advanced steel material - Overview.” *Lecture Notes in Engineering and Computer Science*, *2177*(11737-1740).

34. Klueh, R. L., & Swindeman, R. W. (1986). “The microstructure and mechanical properties of a modified 2.25Cr-lMo steel.” *Metallurgical Transactions A*, *17*(6), 1027–1034.

35. Ishiguro, T., Murakami, Y., Ohnishi, K., & Watanabe, J. (1982). “A 21/4Cr-1Mo pressure vessel steel with improved creep rupture strength.” In G. S. Sangdahl & M. Semchysen (Eds.), *Application of 21/4Cr-1Mo steel for thick-wall pressure vessels* (pp. 129–147). Denver, Colorado: ASTM.

36. Kar, R. J., & Todd, J. A. (1982). “Alloy modification of of thick-section 21/4Cr-1Mo steel.” In G. S. Sangdahl & M. Semchysen (Eds.), *Application of 21/4Cr-1Mo steel for thick-wall pressure vessels* (pp. 228–255). Denver: ASTM.

37. Berthet, J. A., Blondeau, R., Catelin, D., Cheviet, A., & Roux, J. H. (1982). “Data obtained on industrial production plates 150 to 500 mm (6 to 20 in.) thick in chromium-molybdenum steel.” In G. S. Sangdahl & M. Semchysen (Eds.), *Application of 21/4Cr-1Mo steel for thick-wall pressure vessels* (pp. 148–166). Denver: ASTM.

38. Swift, R. A. (1982). “Effects of composition and heat treatments on the mechanical properties of a 300-mm-gage 21/4Cr-1Mo steel plate.” In G. S. Sangdahl & M. Semchysen (Eds.), *Application of 21/4Cr-1Mo steel for thick-wall pressure vessels* (pp. 166–189). Denver, Colorado: ASTM.

39. Ghosh, A. (2001). “Segregation in cast products.” *Sadhana*, *26*(1-2), 5–24.

40. Abbruzzese, G., Heckelmann, I., & Lücke, K. (1992). “Statistical theory of two-dimensional grain growth—I. The topological foundation.” *Acta Metallurgica et Materialia*, *40*(3), 519–532.

41. Lücke, K., Heckelmann, I., & Abbruzzese, G. (1992). “Statistical theory of two-dimensional grain growth—II. Kinetics of grain growth.” *Acta Metallurgica et Materialia*, *40*(3), 533–542.

42. Burke, J. E., & Turnbull, D. (1952). “Recrystallization and grain growth.” *Progress in Metal Physics*, *3*, 220–292.

43. Uhm, S., Moon, J., Lee, C., Yoon, J., & Lee, B. (2004). “Prediction model for the austenite grain size in the coarse grained heat affected zone of Fe-C-Mn steels: considering the effect of initial grain size on isothermal growth behavior.” *ISIJ International*, *44*(7), 1230–1237.

44. Beck, P. A., Kremer, J. C., Demer, L. J., & Holzworth, M. L. (1947). “Grain growth in High-Purity Aluminum and in an Aluminum-Magnesium alloy.” *Transactions of the Metallurgical Society of AIME*, *175*, 372–400.

45. Miranda, R. M., & Fortes, M. A. (1989). “Austenite grain growth, microstructure and hardness in the heat-affected zone of a 2.25 Cr-1Mo steel.” *Materials Science and Engineering: A*, *108*, 1–8.

46. Hu, H., & Rath, B. B. (1970). “Time exponent in isothermal grain growth.” *Metallurgical Transactions*, *1*(11), 3181–3184.

47. Andersen, I., & Grong, Ø. (1995). “Analytical modelling of grain growth in metals and alloys in the presence of growing and dissolving precipitates—I. Normal grain growth.” *Acta Metallurgica et Materialia*, *43*(7), 2673–2688.

48. Humphreys, F. J., & Hatherly, M. (2004). *Recrystallization and Related Annealing Phenomena*. *Acta Metallurgica et Materialia*. Elsevier.

49. Pous-Romero, H., Lonardelli, I., Cogswell, D., & Bhadeshia, H. K. D. H. (2013). “Austenite grain growth in a nuclear pressure vessel steel.” *Materials Science and Engineering: A*, *567*, 72–79.

50. Smith, C. S. (1948). “Introduction to grains, phases, and interfaces - an interpretation of microstructure.” *Transactions of the Metallurgical Society of AIME*, *175*, 15–51.

51. Manohar, P. A., Ferry, M., & Chandra, T. (1998). “Five decades of the Zener equation.” *ISIJ International*, *38*(9), 913–924.

52. Ashby, M. F., Harper, J., & Lewis, J. (1969). “The interaction of crystal boundaries with second-phase particles.” *Transactions of the Metallurgical Society of AIME*, *245*(8), 413–420.

53. Ringer, S. P., Li, W. B., & Easterling, K. E. (1989). “On the interaction and pinning of grain boundaries by cubic shaped precipitate particles.” *Acta Metallurgica*, *37*(3), 831–841.

54. Dimitrov, O., Fromageau, R., & Dimitrov, C. (1978). *Recrystallization of Metallic Materials*. (Haesner, Ed.). Stuttgart.

55. Lücke, K., & Detert, K. (1957). “A quantitative theory of grain-boundary motion and recrystallization in metals in the presence of impurities.” *Acta Metallurgica*, *5*(11), 628–637.

56. Hillert, M. (1999). “Solute drag, solute trapping and diffusional dissipation of Gibbs energy.” *Acta Materialia*, *47*(18), 4481–4505.

57. Hillert, M., & Sundman, B. (1976). “A treatment of the solute drag on moving grain boundaries and phase interfaces in binary alloys.” *Acta Metallurgica*, *24*(8), 731–743.

58. Cahn, J. W. (1962). “The impurity-drag effect in grain boundary motion.” *Acta Metallurgica*, *10*(9), 789–798.

59. Barcelo, F., & Brachet, J. C. (1994). “Image-analysis measurements of prior austenitic grain-size of 9Cr - 1Mo martensitic steels in function of the austenitization conditions.” *Revue de Métallurgie-CIT*, *91*(2), 255–266.

60. Gjostein, N. A., Domian, H. A., Aaronson, H. I., & Eichen, E. (1966). “Relative interfacial energies in Fe-C alloys.” *Acta Metallurgica*, *14*(12), 1637–1644.

61. Shahandeh, S., & Militzer, M. (2013). “Grain boundary curvature and grain growth kinetics with particle pinning.” *Philosophical Magazine*, *93*(24), 3231–3247.

62. Maalekian, M., Radis, R., Militzer, M., Moreau, A., & Poole, W. J. (2012). “In situ measurement and modelling of austenite grain growth in a Ti/Nb microalloyed steel.” *Acta Materialia*, *60*(3), 1015–1026.

63. Rath, M., & Kozeschnik, E. (2013). “Coupled grain growth and precipitation modeling in multi-phase systems.” *Materials Science Forum*, *753*, 357–360.

64. Banerjee, K., Militzer, M., Perez, M., & Wang, X. (2010). “Nonisothermal Austenite Grain Growth Kinetics in a Microalloyed X80 Linepipe Steel.” *Metallurgical and Materials Transactions A*, *41*(12), 3161–3172.

65. Nieuwland, H. C. D., Kawaguchi, S., Tsukada, H., Suzuki, K., Sato, I., Taira, J., & Kusuhashi, M. (1985). “Development of thick wall 2.25Cr-1MoNiNb steel forgings for steam generators of fast breeder reactors.” *Nuclear Engineering and Design*, *84*(2), 123–146.

66. Bodnar, R. L., Ohhashi, T., & Jaffee, R. I. (1989). “Effects of Mn, Si, and purity on the design of 3.5NiCrMoV, 1CrMoV, and 2.25Cr-1Mo bainitic alloy steels.” *Metallurgical Transactions A*, *20*(8), 1445–1460.

67. Wilson, F. G., & Gladman, T. (1988). “Aluminium nitride in steel.” *International Materials Reviews*, *33*(01), 221–226.

68. Bouet, M. (2000). *The effect of molybdenum in silicon-manganese-niobium TRIP steels*. PhD dissertation, McGille University, Montreal, Canada.

69. Enomoto, M., Maruyama, N., Wu, K. M., & Tarui, T. (2003). “Alloying element accumulation at ferrite/austenite boundaries below the time–temperature–transformation diagram bay in an Fe–C–Mo Alloy.” *Materials Science and Engineering: A*, *343*(1-2), 151–157.

70. Maruyama, N., Smith, G. D. W., & Cerezo, A. (2003). “Interaction of the solute niobium or molybdenum with grain boundaries in α-iron.” *Materials Science and Engineering: A*, *353*(1-2), 126–132.

71. Fletcher, H. A., Garratt-Reed, A. J., Aaronson, H. I., Purdy, G. R., Reynolds Jr, W. T., & Smith, G. D. W. (2001). “A STEM method for investigating alloying element accumulation at austenite–ferrite boundaries in an Fe–C–Mo alloy.” *Scripta Materialia*, *45*(5), 561–567.

72. Ham, J. L. (1945). “The rate of diffusion of molybdenum in austenite and ferrite.” *Transactions*

of the American Society for Metals, *35*, 331–361.

73. Enomoto, M., White, C. L., & Aaronson, H. I. (1988). "Evaluation of the effects of segregation on austenite grain boundary energy in Fe-C-X alloys." *Metallurgical Transactions A*, *19*(7), 1807–1818.

74. Liu, Z.-K. (1997). "The transformation phenomenon in Fe-Mo-C alloys: A solute drag approach." *Metallurgical and Materials Transactions A*, *28*(8), 1625–1631.

75. Faulkner, R. G. (1987). "Combined grain boundary equilibrium and non-equilibrium segregation in ferritic/martensitic steels." *Acta Metallurgica*, *35*(12), 2905–2914.

76. Faulkner, R. G., Song, S. H., & Flewitt, P. E. J. (2013). "Determination of impurity–point defect binding energies in alloys." *Materials Science and Technology*, *12*(11), 904–910.

77. Purdy, G. R., Reynolds Jr, W. T., & Aaronson, H. I. (1999). "Analysis of the solute drag-like effect on thickening kinetics of grain boundary ferrite allotriomorphs in Fe-C-Mo alloys." In M. Koiwa, K. Otsuka, & T. Miyazaki (Eds.), *Solid-Solid Phase Transformations* (pp. 1461–1465). Kyoto: The Japan Institute of Metals.

78. Hoerner, M., Eberhart, M., & Speer, J. (2015). "Ab-initio calculation of solute effects on austenite grain boundary properties in steel." In W. Poole, S. Christensen, S. Kalidindi, A. Luo, J. Madison, D. Raabe, & X. Sun (Eds.), *3rd World Congress on Integrated Computational Materials Engineering*. Hoboken, NJ, USA: John Wiley & Sons, Inc.

79. Toda-Caraballo, I., Capdevila, C., Pimentel, G., & De Andrés, C. G. (2013). "Drag effects on grain growth dynamics." *Computational Materials Science*, *68*, 95–106.

80. Rancel, L., Gómez, M., Medina, S. F., & Gutierrez, I. (2011). "Measurement of bainite packet size and its influence on cleavage fracture in a medium carbon bainitic steel." *Materials Science and Engineering: A*, *530*, 21–27.

81. Gourgues, A. F., Flower, H. M., & Lindley, T. C. (2000). "Electron backscattering diffraction study of acicular ferrite, bainite, and martensite steel microstructures." *Materials Science and Technology*, *16*(1), 26–40.

82. Bouyne, E. (1999). *Propagation et arrêt de fissure de clivage dans l'acier 21/4Cr-1Mo*. PhD dissertation, ENSMP, Paris, France. In French.

83. Bhadeshia, H. K. D. H. (2001). *Bainite in Steels second edition*. London: Institute of Materials.

84. Chang, H. J., & Kai, J. J. (1990). "The effects of thermal treatment on the microstructure and tensile properties of 2.25Cr-1Mo steel." *Scripta Metallurgica et Materialia*, *24*(11), 2101–2106.

85. Chen, J., Tang, S., Liu, Z., & Wang, G. (2013). "Influence of molybdenum content on

transformation behavior of high performance bridge steel during continuous cooling." *Materials & Design*, *49*, 465–470.

86. Junhua, K., Lin, Z., Bin, G., Pinghe, L., Aihua, W., & Changsheng, X. (2004). "Influence of Mo content on microstructure and mechanical properties of high strength pipeline steel." *Materials & Design*, *25*(8), 723–728.

87. Reynolds, W. T., Li, F. . Z., Shui, C. K., & Aaronson, H. I. (1990). "The Incomplete transformation phenomenon in Fe-C-Mo alloys." *Metallurgical Transactions A*, *21*(6), 1433–1463.

88. Wu, K. M., Kagayama, M., & Enomoto, M. (2003). "Kinetics of ferrite transformation in an Fe-0.28mass%C-3mass%Mo alloy." *Materials Science and Engineering: A*, *343*(1-2), 143–150.

89. Kinsman, K. R., & Aaronson, H. I. (1967). *Transformation and hardenability in steels*. Arbor, MI: Ann Climax Molybdenum Co.

90. Aaronson, H. I., Reynolds, W. R., & Purdy, G. R. (2004). "Coupled-solute drag effects on ferrite formation in Fe-C-X systems." *Metallurgical and Materials Transactions A*, *35*(4), 1187–1210.

91. Hutchinson, C. R., Zurob, H. S., & Bréchet, Y. (2006). "The growth of ferrite in Fe-C-X alloys: The role of thermodynamics, diffusion, and interfacial conditions." *Metallurgical and Materials Transactions A*, *37*(6), 1711–1720.

92. Militzer, M., Pandi, R., & Hawbolt, E. B. (1996). "Ferrite nucleation and growth during continuous cooling." *Metallurgical and Materials Transactions A*, *27*(6), 1547–1556.

93. Suehiro, M., Liu, Z.-K., & Ågren, J. (1996). "Effect of niobium on massive transformation in ultra low carbon steels: a solute drag treatment." *Acta Materialia*, *44*(10), 4241–4251.

94. Jayan, V., Khan, M. Y., & Hussain, M. (2003). "X-ray investigation of solid solution partitioning in 2.25Cr-1Mo steel after extended elevated temperature service in power station." *Materials Science and Technology*, *19*(11), 1546–1552.

95. Nutting, J. (1998). "The Structural Stability of Low Alloy Steels for Power Generation Applications." In IOM Communications (Ed.), *Advanced Heat Resistant Steels for Power Generation* (pp. 1–20). San Sebastian, Spain.

96. Thomson, R. C., & Bhadeshia, H. K. D. H. (1994). "Changes in chemical composition of carbides in 2.25Cr-1Mo power plant steel. Part 1: Bainitic microstructure." *Materials Science and Technology*, *10*(3), 193–203.

97. Výrostková, A., Kroupa, A., Janovec, J., & Svoboda, M. (1998). "Carbide reactions and phase equilibria in low alloy Cr–Mo–V steels tempered at 773–993 K. Part I: Experimental

measurements.” *Acta Materialia*, *46*(1), 31–38.

98. Yang, J. R., Huang, C. Y., Yang, C. N., & Horng, J. L. (1993). “Microstructural examination of 2.25Cr-1Mo steel steam pipes after extended service.” *Materials Characterization*, *30*(2), 75–88.

99. Yu, J. (1989). “Carbide stability diagrams in 2.25Cr-1Mo steels.” *Metallurgical Transactions A*, *20*(8), 1561–1564.

100. Leitnaker, J. M., Klueh, R. L., & Laing, W. R. (1975). “The composition of eta carbide phase in 2 1/4 Cr-1 Mo Steel.” *Metallurgical Transactions A*, *6*(10), 1949–1955.

101. Pilling, J., & Ridley, N. (1982). “Tempering of 2.25 Pct Cr-1 Pct Mo Low Carbon Steels.” *Metallurgical Transactions A*, *13*(4), 557–563.

102. Murphy, M. C., & Branch, G. D. (1971). “Metallurgical changes in 2-25 CrMo steels during creep-rupture test.” *Journal of the Iron and Steel Institute*, *209*(JUL), 546–561.

103. Gope, N., Chatterjee, A., Mukherjee, T., & Sarma, D. S. (1993). “Influence of long-term aging and superimposed creep stress on the microstructure of 2.25Cr-1Mo steel.” *Metallurgical Transactions A*, *24*(2), 315–326.

104. Jayan, V., Mandal, P. K., Hirani, M., & Sanyal, S. K. (1999). “X-ray investigation of carbide precipitation in 2.25Cr-1Mo steel for predicting remaining life of boiler components after extended service in fossil fuel fired power stations.” *Materials Science and Technology*, *15*(11), 1308–1316.

105. Kim, C. S., Park, I. K., & Jhang, K. Y. (2009). “Nonlinear ultrasonic characterization of thermal degradation in ferritic 2.25Cr–1Mo steel.” *NDT & E International*, *42*(3), 204–209.

106. Parameswaran, P., Vijayalakshmi, M., Shankar, P., & Raghunathan, V. S. (1993). “Influence of carbon content on microstructure and tempering behaviour of 2 1/4 Cr 1 Mo steel.” *Journal of Materials Science*, *28*(20), 5426–5434.

107. Bišs, V. A., & Wada, T. (1985). “Microstructural changes in 1Cr-0.5Mo steel after 20 years of service.” *Metallurgical Transactions A*, *16*(1), 109–114.

108. Parthé, E., & Sadogopan, V. (1963). “The structure of dimolybdenum carbide by neutron diffraction technique.” *Acta Crystallographica*, *16*(3), 202–205.

109. Swift, R. A. (1971). “The mechanism of stress relief cracking in 21/4Cr-1Mo steel.” *Welding Journal*, *50*(5), S195–S200.

110. Nagakura, S., & Oketani, S. (1968). “Structure of transition metal carbides.” *Transactions of the Iron and Steel Institute of Japan*, *8*(5), 265–294.

111. Dyson, D. J., & Andrews, K. W. (1969). “Carbide M7C3 and its formation in alloy steels.” *Journal of the Iron and Steel Institute, 207*, 208–219.

112. Fruchart, R., & Rouault, A. (1969). “Twin crystals of orthorhombic isomorphous Cr7C3, Mn7C3, Fe7C3 carbides.” *Annales de Chimie France, 4*(3), 143–145.

113. Abdel-Latif, A. M., Corbett, J. M., & Taplin, D. M. R. (1982). “Analysis of carbides formed during accelerated aging of 2·25Cr–1Mo steel.” *Metal Science, 16*(2), 90–96.

114. Benvenuti, A., Bontempi, P., Corti, S., & Ricci, N. (1996). “Assessment of material thermal history in elevated temperature components.” *Materials Characterization, 36*(4-5), 271–278.

115. Inoue, A., & Masumoto, T. (1980). “Carbide reactions (M3C→M7C3→M23C6→M6C) during tempering of rapidly solidified high carbon Cr-W and Cr-Mo steels.” *Metallurgical Transactions A, 11*(5), 739–747.

116. Holzmann, M., Man, J., & Vlach, B. (1993). “Upper-nose temper phenomena and transition behaviour of fracture toughness of 2.25Cr-1Mo pressure vessel steel.” *Scripta Metallurgica et Materialia, 29*(12), 1633–1638.

117. Holzmann, M., Vlach, B., & Man, J. (1992). “The effect of microstructure on the mechanical and brittle fracture properties of 2 1/4 Cr-1Mo steel.” *Welding International, 6*(11), 912–919.

118. Takahashi, E., & Iwai, K. (1982). “Omission of intermediate postweld heat treatment (PWHT) by utilizing low-temperature PWHT for welds in pressure vessels.” In G. S. Sangdahl & M. Semchysen (Eds.), *Application of 21/4Cr-1Mo steel for thick-wall pressure vessels* (pp. 418–450). Denver, Colorado: ASTM.

119. Yu, X. (2012). *Multi-scale characterization of heat-affected zones in martensitic steels*. Dissertation, Ohio State University, USA.

120. Norris, S. D., & Parker, J. D. (1996). “The effect of microstructure on fracture mechanisms of 2·25Cr1Mo low alloy steel, part B: the influence of carbides.” *International Journal of Pressure Vessels and Piping, 67*(3), 329–337.

121. Zhang, J. G., Noble, F. W., & Eyre, B. L. (1991). “Comparison of effects of aging on fracture of 9Cr–1Mo and 2·25Cr–1Mo steel Part 1 Quenched and tempered material.” *Materials Science and Technology, 7*(3), 218–223.

122. Ding, R. G., Rong, T. S., & Knott, J. F. (2005). “Phosphorus segregation in 2.25Cr1Mo steel.” *Materials Science and Technology, 21*(1), 85–92.

123. Khan, S. A., & Islam, M. A. (2007). “Influence of prior austenite grain size on the degree of temper embrittlement in Cr-Mo steel.” *Journal of Materials Engineering and Performance,*

16(1), 80–85.

124. Wada, M., Fukase, S., & Nishikawa, O. (1982). “Role of carbides in the grain boundary segregation of phosphorus in a 2.25 Cr-1 Mo steel.” *Scripta Metallurgica*, *16*(12), 1373–1378.

125. Shen, D. D., Song, S. H., Yuan, Z. X., & Weng, L. Q. (2005). “Effect of solute grain boundary segregation and hardness on the ductile-to-brittle transition for a Cr–Mo low-alloy steel.” *Materials Science and Engineering: A*, *394*(1-2), 53–59.

126. Gubicza, J., Ribárik, G., Goren-Muginstein, G. ., Rosen, A. ., & Ungár, T. (2001). “The density and the character of dislocations in cubic and hexagonal polycrystals determined by X-ray diffraction.” *Materials Science and Engineering: A*, *309-310*, 60–63.

127. Béchade, J.-L., Menut, D., Doriot, S., Schlutig, S., & Sitaud, B. (2013). “X-ray diffraction analysis of secondary phases in zirconium alloys before and after neutron irradiation at the MARS synchrotron radiation beamline.” *Journal of Nuclear Materials*, *437*(1-3), 365–372.

128. Kozeschnik, E. (2012). *Modeling Solid-State Precipitation*. Momentum Press.

129. Svoboda, J., Fischer, F. D., Fratzl, P., & Kozeschnik, E. (2004). “Modelling of kinetics in multi-component multi-phase systems with spherical precipitates.” *Materials Science and Engineering: A*, *385*(1-2), 166–174.

130. Russell, K. C. (1980). “Nucleation in solids: The induction and steady state effects.” *Advances in Colloid and Interface Science*, *13*(3-4), 205–318.

131. Zajac, S., Komenda, J., Morris, P., Dierickx, P., Matera, S., & Penalba Diaz, F. (2005). *Quantitative structure-property relationships for complex bainitic microstructures*. *Report EUR 21245EN*. Technical Steel Reseach, European Commission.

132. Fu, L. M., Wang, H. R., Wang, W., & Shan, A. D. (2011). “Austenite grain growth prediction coupling with drag and pinning effects in low carbon Nb microalloyed steels.” *Materials Science and Technology*, *27*(6), 996–1001.

Appendix A: Experimental procedures

TABLE OF CONTENTS

Experimental procedures used for this study are developed in detail in this appendix.

1. HEAT TREATMENTS

1.1 Austenitization in an induction furnace

Austenitization temperature and cooling rate have a strong influence on the as-quenched microstructure. Moreover, a considerable amount of samples had to be austenitized and quenched for the study of tempering conditions. As a result, a furnace which can heat treat several samples with an accurate control of sample temperature was needed.

An induction furnace (Figure A.1.a) and a specimen holder (Figure A.1.b) were designed and manufactured by S. Gailliègue at the Centre des Matériaux. This furnace allows heat treatment of eight mini-Charpy blanks at the same time or, alternatively, of one sample for selective dissolution at a time. Heat treatments were performed under argon atmosphere. A K-thermocouple was spot-welded on each blank for temperature monitoring; the furnace was controlled by one of them.

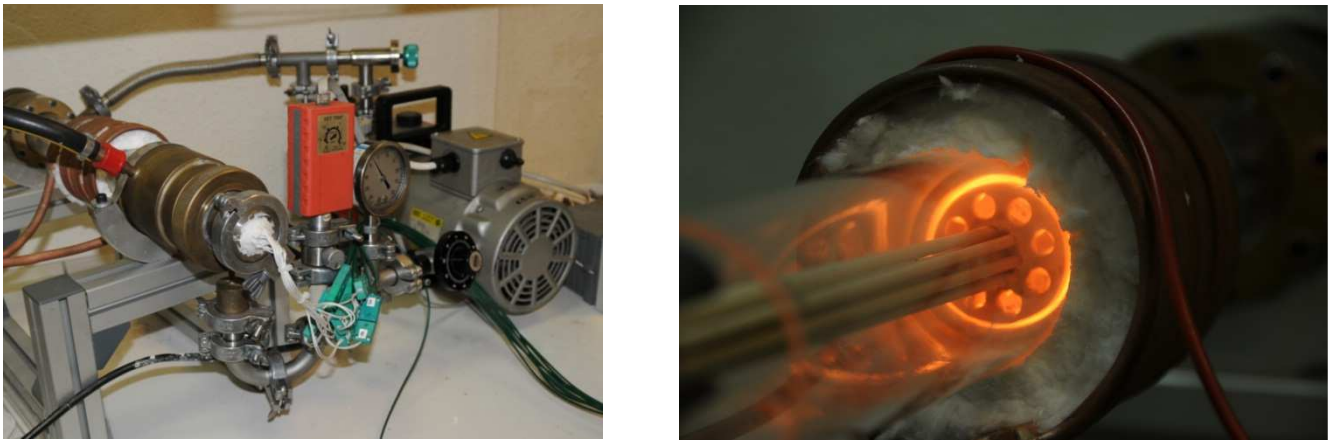

(a) (b)

Figure A.1: *(a) Induction furnace and (b) specimen holder during a heat treatment.*

Figure A.2 shows the longitudinal and azimutal thermal profiles of the surface of a blank specimen during isothermal soaking at 970°C. A satisfactory temperature gradient (± 5°C) is observed in the vicinity of the sample center. Both extremities of samples are placed in the specimen holder which is made of silica, thus explaining the lower temperature at the blank ends. The azimutal thermal gradient is rather low, with a maximum difference of 10°C. This thermal profile guarantees a homogeneous microstructure around the notch after machining the blanks to mini-Charpy specimens.

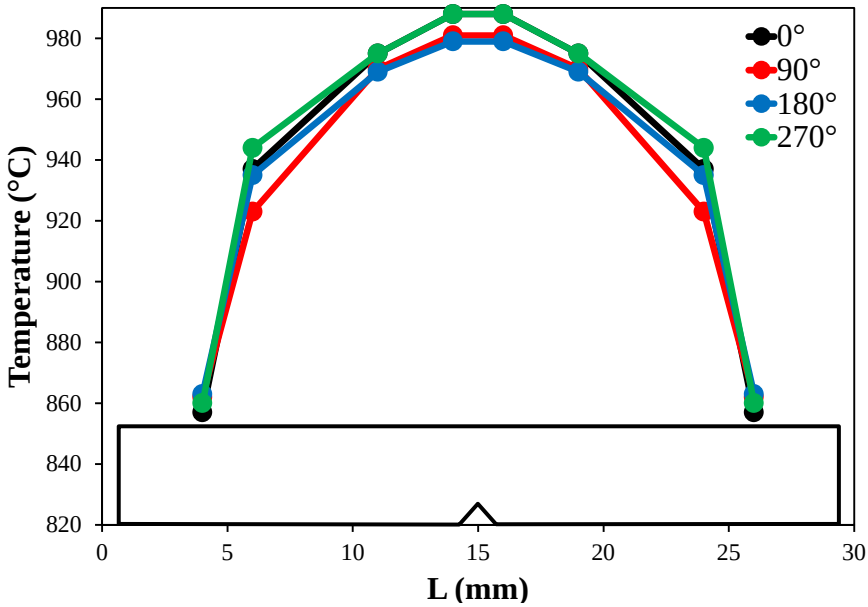

Figure A.2: *Longitudinal and azimutal thermal profile of a sample measured during isothermal step. A schematic drawing of the mini-Charpy specimen (same scale) is superimposed.*

Typical heat treatment acquisition data is shown in Figure A.3. Small deviations from the prescribed values of temperature are observed when the material passes the ferromagnetic-paramagnetic transition (Curie temperature) and during the decomposition of austenite into bainite. A cooling rate of 0.5°C/s is applied between 970°C and 400°C as required.

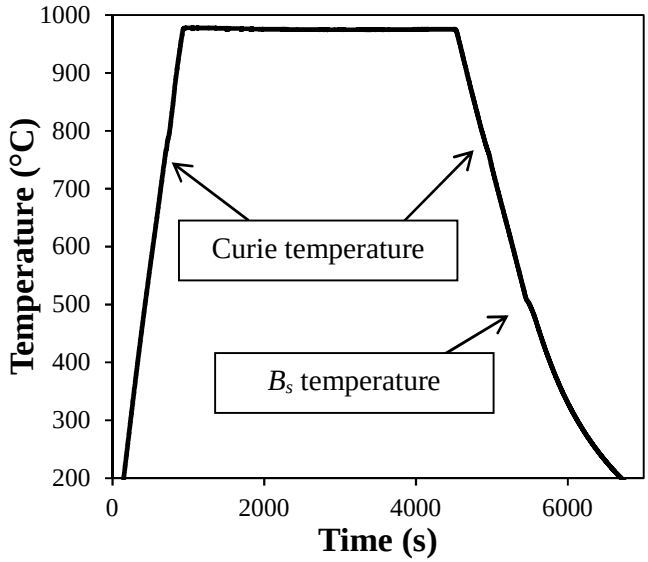

Figure A.3: *Typical temperature data recorded during an austenitization heat treatment*

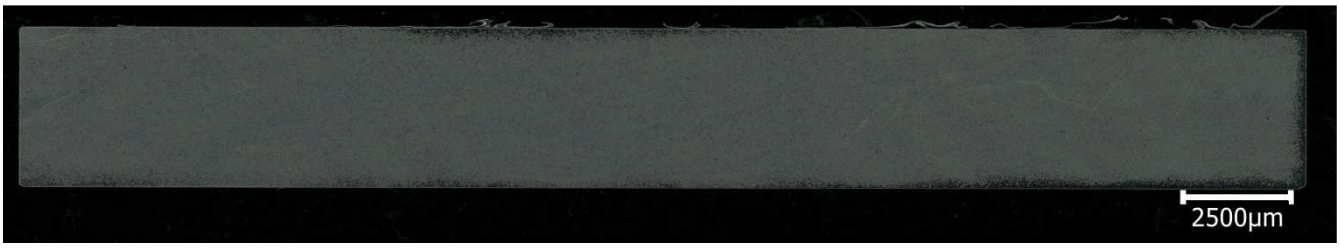

(a)

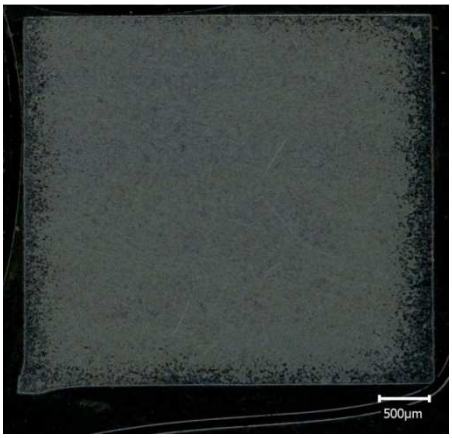

(b)

Figure A.4: *Optical macrographs of a heat treated sample (a) longitudinal section, (b) cross-section. The bluish regions near edges belong to the decarburized layer.*

To further validate the heat treatment procedure, a heat-treated sample was analyzed by means of optical microscopy and hardness measurements. Its microstructure appears to be fully bainitic. The thickness of the ferrite layer due to decarburization does not exceed 500 µm at its most, and thus will be removed after machining to mechanical testing specimens (Figure A.4). The hardness values, between 340 and 360 HV5, are consistent with the as-cooled bainitic microstructure of these samples

(Figure A.5). The longitudinal temperature gradient does not impact the longitudinal hardness profile.

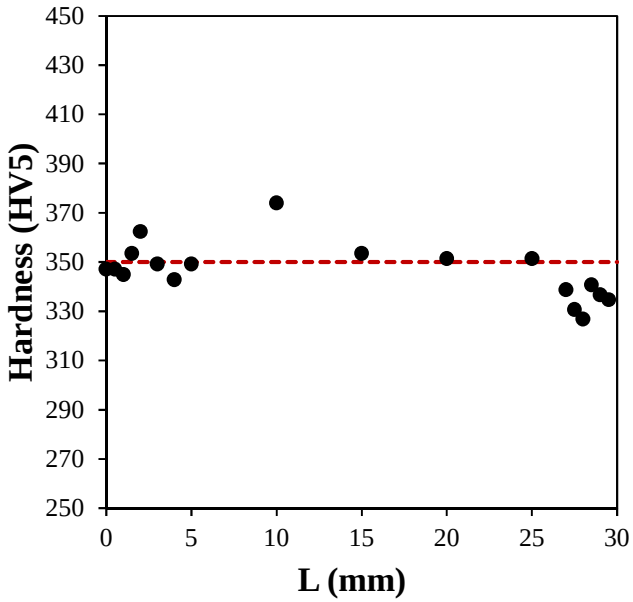

Figure A.5: *Hardness longitudinal profile of a heat-treated sample. The red line corresponds to the fully bainitic hardness as seen in Chapter 2.*

1.2 Tempering

After austenitization, the blanks were tempered under Helium atmosphere with a heating rate of 2°C/min. A water quench followed the isothermal holding. Similar cooling conditions were used for the post weld heat treatment (PWHT), but with a heating rate of 1°C/min.

Tempering and PWHT were conducted either in a Pyrox furnace or in an Adamel tubular furnace, depending on the batches.

2. MICROSTRUCTURAL OBSERVATIONS: MICROSCOPY AND MICROANALYSIS

2.1 Optical microscopy: metallographic observations and austenite grain size measurements

All images were taken by using a LEICO Reichert Jung MeF3A optical microscope; the image acquisition and processing software is analySIS docu.

2.1.1 Metallographic observations

Unless specified otherwise, a 2% Nital etching (2% nitric acid in ethanol) was used to reveal the microstructure. Images were taken at three different magnifications: x10, x20 and x50.

2.1.2 Austenite grain size measurements

In the studied steel, austenite is not stable at ambient temperature, thus no direct observation of austenite grains is possible. To address this issue, a dedicated heat treatment was applied: after austenitization thermal holding step, the sample was quenched in the dilatometer down to, and held at an intermediate temperature, after which a final quench was applied down to room temperature. Cooling rate for these quench is 50°C/s. Intermediate holding lead to partial decomposition of austenite into ferrite, with a greater contribution from nucleation over that of growth. The objective was to precipitate small ferritic grains at austenite grain boundaries. The final quench transformed the residual austenite into martensite. These isothermal conditions were chosen using the TTT diagram established in parallel of the CCT diagram for the 920°C – 30 minutes austenitization condition (Figure A.6). It appeared that a step cooling at 625°C for 48 hours (~170 000 seconds) would give satisfactory results. The microstructure was then revealed by dipping samples for a few seconds into a solution of 5 grams of sodium disulfite in 100 mL of water. This tinting etchant colors ferrite in dark brown and martensite in light brown.

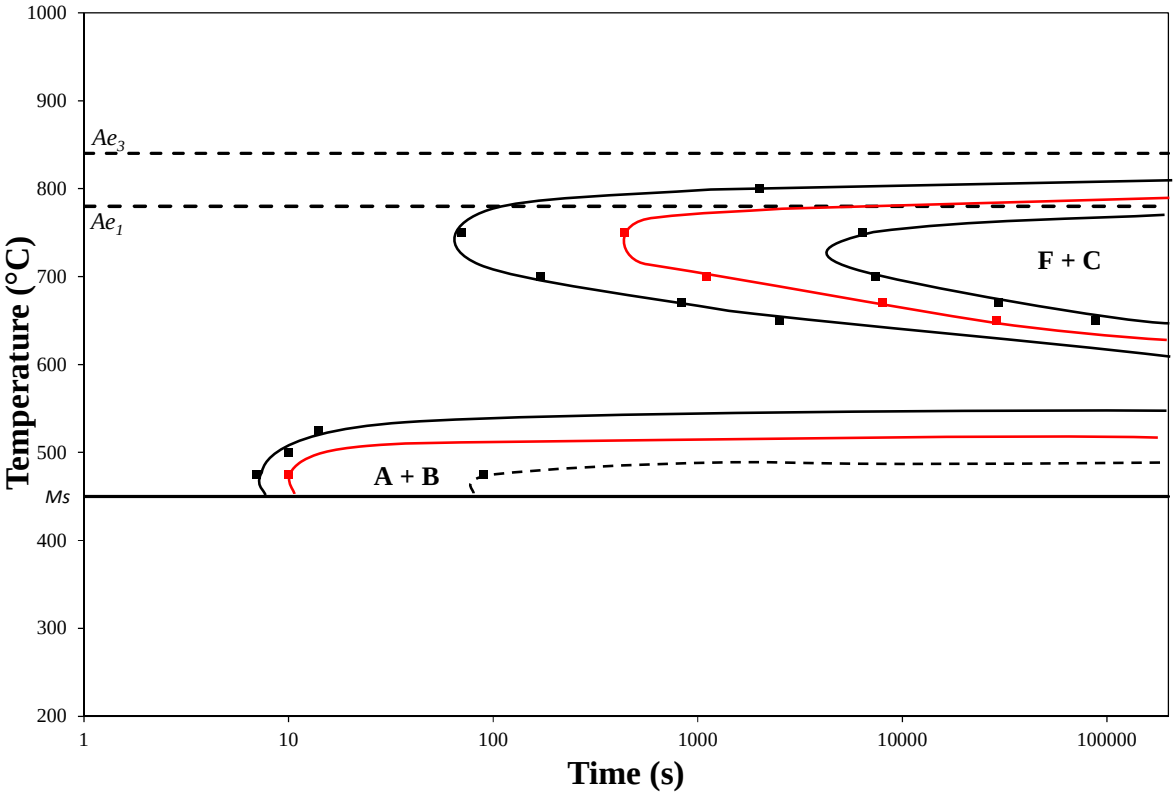

Figure A.6: *TTT Diagram of the studied steel after an austenitization at 920°C for 30 minutes. A: austenite, B: bainite, F: ferrite, C: carbides.*

It should be kept in mind that the TTT diagram was obtained after an austenitization at 920°C for 30 minutes. Since applied step cooling implies localized ferritic transformation at austenite grain boundaries, any increase in austenite grain size obviously affects the precipitation of ferrite. Any increase in grain size will then shift the ferritic transformation domain towards higher temperatures and times. For larger austenite grains, it means that less ferrite nucleates thus austenite grain

boundaries are not so well defined. For smaller austenite grains, there is a high risk that ferritic grains grow at the expense of austenite grains, partly masking their original morphology, so that no measurements can be done. Since this is a time consuming technique (each sample requires 4 days of work, including more than 2 days in the dilatometer), all austenitization conditions were first followed by the same step cooling. When this method was suspected to be inefficient, i.e. when small austenite grain sizes were expected, another methodology was used. Samples were quenched at 50°C/s to room temperature right after the austenitization step, and then lightly etched with Villela etchant.

A least six images were taken for each austenitization condition. The magnification was selected according to the grain size: for coarse grains as the ones obtained after austenitization at 1120°C, images were taken using a x10 magnification. Otherwise, a x20 magnification was used. Austenite grain size was then measured using the Visilog software. Each grain was measured individually and then the average grain size was calculated. Table A.1 summarizes the number of austenite grains analyzed for each studied austenitization condition.

	0 min	**5 min**	**15 min**	**30 min**	**60 min**	**120 min**
920°C	76	106	170	157	209	162
970°C		220	963	177	834	229
1020°C	56	121	261	238	253	172
1070°C	61		95		209	
1120°C	71	113	135			

Table A.1: *Number of austenite grains analyzed for austenite grain size determination*

2.2 Scanning electron microscope: carbon extraction replicas, EBSD and fractography

All SEM observations were done with a 15 kV acceleration voltage.

2.2.1 Observation of carbides on carbon extraction replicas

Scanning electron microscopy was used qualitatively to analyze the carbide location, size and number fraction after tempering. Carbon extraction replicas were prepared from metallographic samples as follows:

- After polishing, samples were slightly etched with a 2% Nital solution.
- A carbon layer was deposited in an Edwards AUTO 306 thermal evaporator. A grid was then cut at the surface of the carbon layer.
- An electrolytic dissolution of the matrix was conducted. The chemical composition of the solution was 100 mL acetylacetone, 10 g tetramethylammonium chloride in 900 mL of methanol, and the potential was set to 1.3 V at room temperature. At the end of the process, thin carbon films were floating in the solution.
- These thin films were then washed in ethanol and deposited into a 3 mm diameter copper grid.

All observations were done on a JEOL JSM7001F SEM.

2.2.2 EBSD

All information regarding EBSD measurements has been reported in Chapter IV, section 2.3.1.

2.2.3 Fractography

After being mechanically tested, mini-Charpy specimens were put in a dessicator in order to prevent from oxidation their fracture surface. Observations were done:

- On a Cambridge S260 SEM for the study of the reference material.
- On a LEO 1450VP SEM for the study of austenitization effects.
- On a JEOL JSM7001F SEM for the study of tempering effects.
  MnS particles were identified using EDX microanalyses.

2.3 Carbide characterization using transmission electron microscopy

All TEM observations were made on carbon extraction replicas by using a FEI Tecnai F20 TEM with a 200 kV acceleration voltage. Images were acquired with an Orius camera with a 1 second exposure time using DigitalMicrograph software.

EDX analyses were performed with an α-tilt of 12° and a counting time of 15 s. Spectra were processed using TIA software; only Fe, Cr and Mo elements were taken into account for the quantitative analyses. No thickness correction was applied.

2.4 Quantification of segregations using electron probe microanalysis

All information regarding the electron probe microanalysis measurements have been reported in Chapter II, section 3.

3. CHARACTERIZATION OF CARBIDES USING X-RAY DIFFRACTION TECHNIQUES

3.1 X-Ray diffraction and sample preparation by selective dissolution

The diffractometer used in this study was a Brüker D8 Advance in the Bragg-Benato mode, using a θ-2θ configuration. The X-Ray generator was an anticathode CuKα (λ = 1.540598 Å), using a voltage of 40 kV and an intensity of 40 mA. A LynxEye detector with a 3° opening was used, with discrimination in energy ranging from 0.19 to 0.25 V. Acquisition was made as follows: Angular domain 2θ ranging from 13° to 140° with a step of 0.02°; 10s acquisition per angular step.

For bulk analyses, samples were polished down to 1 µm diamond paste in order to remove the strain-hardened surface layer.

For quantitative measurements of the carbide phase fractions, analyses were made on powder obtained after electrolytic dissolution of the matrix. Experimental protocol was as follows: 100 mm long rods with a diameter of 10 mm were dipped in a solution of 90% methanol – 10% HCl under Argon sparging and electric current. Typical duration for electroetching extraction was 5 hours. Once the matrix was dissolved, the remaining solution was filtrated using a Buchner funnel with filters which holes size 200 nm maximum. Several filtrations were done for each experiment. Once the precipitates were separated from the solution containing the dissolved matrix, filters were dried for half a day. The obtained powder was then analyzed by X-Ray diffraction.

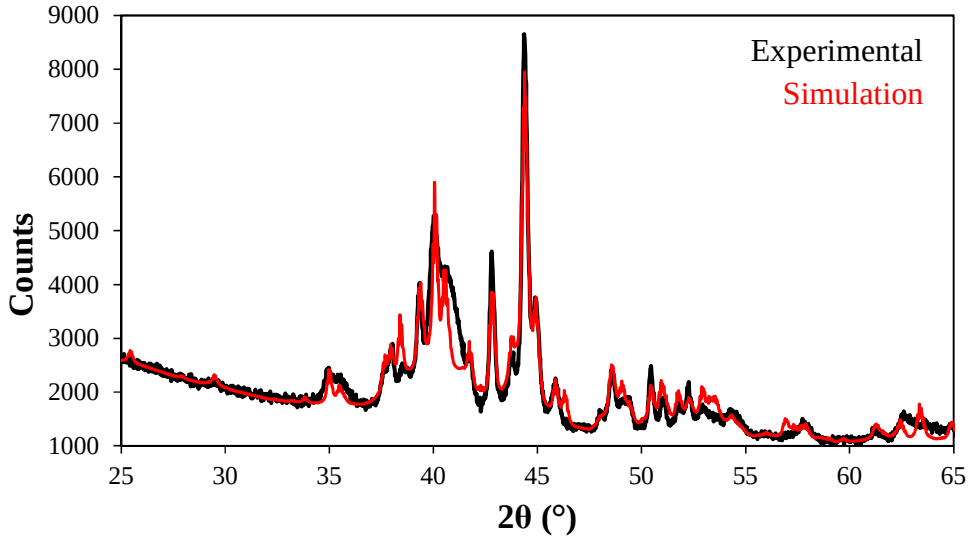

Figure A.7: *Comparison between experimental diffraction diagram and a simulated one using Rietveld refinements. Tempering condition is 675°C – 5.5h. Crystal data are the ones given in Chapter V*

Rietveld refinements were performed using FullProf software in order to evidence additional phases, refine lattice parameters and quantify phase fractions. This method consists in calculating a pattern from the known structural information: the nature of the phases, atomic positions and nature of the atoms at each site according to the structure prototype. The calculated pattern is compared with the experimental (observed) one and the parameters defining the calculated pattern are iteratively refined by a non-linear least-square method in order to obtain the best agreement between both patterns. Example of Rietveld refinements is given in Figure A.7.

3.2 Synchrotron X-Ray diffraction

X-Ray Diffraction (XRD) analyses (MARS beamline, synchrotron SOLEIL facility) were performed on thin foils in transmission mode at 16.7 keV, equivalent to a wavelength of 0.742515 Å. Acquisition and data reduction are extensively described in [127].

Thin foils thickness was 100 µm maximum, with a final polishing using a 4000-grit SiC papers.

4. THERMAL PROPERTIES

4.1 Characterization of phase transformations using dilatometry

All dilatometric studies were made using either of different modified DT1000 by AET Technologies, which present the same characteristics except that one of facilities manufactured allows using larger samples. CCT diagram (Chapter II), TTT diagram (section 2.1.2 of this appendix) and austenite grain size measurements (Chapter III) were determined using 12x2x2 mm^3 samples, while the study on phase transformation upon cooling after different austenitization conditions (Chapter IV) was made on 30x3x4 mm^3 blanks primarily dedicated to mechanical testing, and which geometry is reported Chapter II.

An S-thermocouple was spot-welded onto the sample surface in order to measure the temperature during the tests. Thermal cycle program, control and acquisition were made with the DAQFactoryRuntime software.

All tests were carried under Helium atmosphere in order to limit decarburization at high temperatures (i.e. austenitization temperatures). At lower temperatures (i.e. step cooling temperatures), tests were conducted under secondary vacuum when the step duration was longer than 4 hours. Cooling was applied either using Helium injection inside the furnace for cooling rates higher than 1°C/s, or by Helium sweeping around the furnace for lower cooling rates.

The transformation kinetics and the measurement of transformation temperatures were determined thanks to the dilatometric curves $dL/L = f(T)$ (Figure A.8). When no transformation occurs, the material expansion dL/L is proportionally related to the temperature T by the thermal expansion coefficient of the considered phase. Upon phase transformation, the material experiences a contraction or an expansion, depending on the crystallographic structure of the considered phases. In such case, the transformation start and end temperatures T_1 and T_2 were characterized using the tangent method as shown in Figure A.8. Kinetics of decomposition of phase φ was determined at each temperature T using the lever rule method as shown in Figure A.8, such as $\%\varphi(T) = AB(T)/AC(T)$.

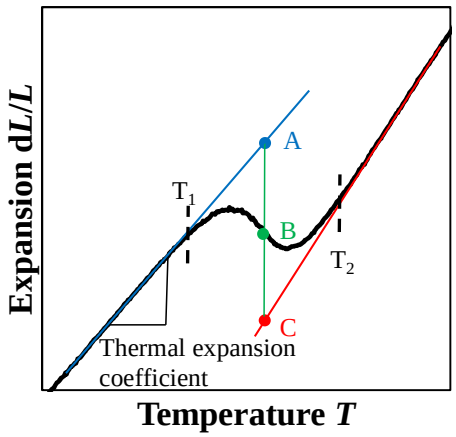

Figure A.8: *Determination of phase fraction, transformation temperatures and dilatation coefficient using dilatometric curves.*

4.2 Determination of ferrite-austenite transformation temperatures using calorimetric measurements

Temperatures Ac_1 and Ac_3 reported in Chapter II for heating rates of 0.02°C/s and 0.2°C/s were determined using a calorimeter from the SETARAM brand. These tests were conducted with three 12x2x2 mm^3 samples put inside an alumina crucible under an Argon atmosphere. One test was done for each heating rate. Temperatures of interest were determined using the tangent method as explained above for the dilatometric curves.

4.3 Determination of the thermal diffusivity using Laser flash analysis

The laser flash analysis is a technique used for measuring the thermal diffusivity of metals. It consists in heating a side of a sample by short energy pulse and measuring the response in temperature on the opposite side. The heat equation is then resolved using the temperature measurements, the geometry of the sample and the energy pulses characteristics.

Measurements were done in a Flash 1000 equipment which allows the determination of the thermal diffusivity at temperatures ranging from 20°C to 1000°C under Helium atmosphere. Heating was provided by a Nd-phosphide laser delivering short energy pulses (< 200 µs); the temperature was measured thanks to an infrared sensor (MCT type). In order to ensure an homogeneous centering of the laser beam on the sample, a graphite diaphragm was placed in front of the sample and the pulse duration was controlled by pockels cells. Samples were 12 mm diameter disks with a 2 mm thickness. Experimental results were processed using the Blitz software developed by Influtherm.

5. MECHANICAL TESTING

5.1 Hardness and nanoindentation

All macrohardness measurements were made at room temperature using a Wolpert V Testor 2 durometer by applying a 5 kg load during 10 seconds. Reported values are the average over 5 measurements per sample.

Nanoidentation measurements were made on a CSM Instruments equipment using a Berkovich indentor, as reported in Chapter II. The conversion from the material resistance to deformation H_{IT}, expressed in Pascal, into HV value is as follows. The material resistance to deformation is a function of the applied load F and of the projected contact area between the penetrator and the sample A_p such as:

$$H_{IT} = \frac{F}{A_p} \tag{A.1}$$

where F is the applied load and A_p the projected contact area between the penetrator and the sample. A_p is a function of the maximum indentation depth h_{max} and is calibrated with a material of known hardness.

In Vickers indentation tests, a 136° diamond pyramid is pressed onto the surface of the sample being tested. The Vickers hardness number obeys a relationship between the diagonal of the indent left by the penetrator, d, the applied load F, the angle between the axis of the diamond indenter and the three faces, α and the standard gravity, g_n such as:

$$\mathrm{HV} = \frac{2F.\sin(\alpha)}{g_n \,.\, d^2} \tag{A.2}$$

For standard Vickers measurement, $\alpha = 68°$. The diagonal length d is linked to A_p by:

$$d^2 = 2A_p \tag{A.3}$$

And $sin(\alpha)$ can be expressed as:

$$\sin(\alpha) = \frac{A_p}{A_c} \tag{A.4}$$

where A_c is the area of contact between the penetrator and the sample. Then, the HV_{IT} number, which is the converted HV number from H_{IT}, can be written as:

$$\mathrm{HV_{IT}} = \frac{F.A_p}{A_p.A_c.g_n} = \frac{\mathrm{H_{IT}}.A_p}{g_n.A_c} \tag{A.5}$$

For a modified Berkovich penetrator, $\alpha = 65.27°$. Then the relation between HV_{IT} and H_{IT} is:

$$\mathrm{HV_{IT}} = 0.0926\ \mathrm{H_{IT}} \tag{A.6}$$

Hardness measurements in H_{IT} and converted values in HV_{IT} are given below (Table A.2 and Table A.3). Comparative study on calibration materials showed that converted Vickers number is systematically overestimated by 7% compared to values directly obtained from Vickers measurements. Since measurements in Table 2 were made in order to compare nanoindentation measurements to actual hardness measurements, this 7% correction was applied. Detailed experimental results are reported in Table A.2 and Table A.3, whereas corrected values and interpretations are reported in Chapter II.

Calibration materials were provided by MPA Hannover. Their references are as follows: MPA-H-7175.0911, MPA-H- 7176.0911, MPA-H- 7177.0911, MPA-H- 7178.0911, MPA-H- 7179.0911, MPA-H- 7180.0911.

H_{IT}	Enriched region (A)	Depleted region (B)	Enriched region (C)	Depleted region (D)
Average (GPa)	3.0	3.1	2.9	3.2
Standard Deviation (GPa)	0.1	0.1	0.1	0.1
Minimum (GPa)	2.8	2.9	2.5	3.0
Maximum (GPa)	3.2	3.4	3.2	3.4

HV_{IT}	Enriched region (A)	Depleted region (B)	Enriched region (C)	Depleted region (D)
Average	277	290	271	298
Standard Deviation	8	10	12	10
Minimum	260	269	232	278
Maximum	296	315	296	314

***Table A.2*:** Hardness values for enriched and depleted areas, in GPa (H_{IT}) and HV numbers *(*load: 15 mN, average value given for 60 measurements).

H_{IT}	Enriched region (A)	Depleted region (B)
Average (GPa)	2.6	2.7
Standard Deviation (GPa)	0.1	0.04
Minimum (GPa)	2.4	2.7
Maximum (GPa)	2.7	2.8

HV_{IT}	Enriched region (A)	Depleted region (B)
Average	240	250
Standard Deviation	10	5
Minimum	222	250
Maximum	250	260

$HV_{IT, corrected}$	Enriched region (A)	Depleted region (B)
Average	225	234
Standard Deviation	8	3
Minimum	207	233
Maximum	232	241

***Table A.3**: Hardness values for enriched and depleted areas, in GPa (H_{IT}) and HV numbers before and after correction (load: 400 mN, average value over for 5 measurements)*

5.2 Tensile tests

Tensile tests were conducted at room temperature on cylindrical specimens machined from the blanks presented in Chapter II. The geometry of these specimens was as follows: gage region of 10 mm in length and 2 mm in diameter, as shown in Figure A.9.

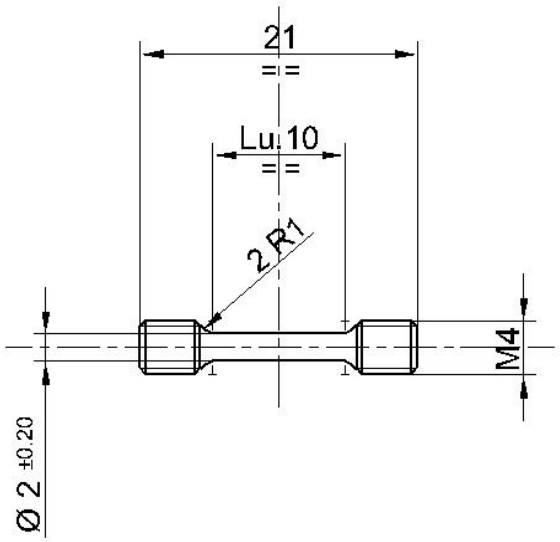

Figure A.9: *Schematic drawing of the specimen used for tensile tests*

Tests were conducted on an INSTRON tensile machine. As no extensometer was used, a displacement correction was applied after the tests to remove the contribution of the load line compliance from the load line displacement measurements. The average deformation rate was 5.10^{-4} s^{-1}.

5.3 Impact toughness tests

Impact toughness tests were conducted on V-notch Charpy reduced specimens as already presented in Chapter II. Geometry of specimens is 3x4x27 mm^3. An instrumented Zwick Roell Amsler equipment with a capacity of 50 J was used. This installation was equipped with a climatic chamber (-180°C to 650°C) with mechanical transfer from the storage room to the equipment. Impact speed of the hammer is 3.83 $mm.s^{-1}$.

The rupture energy was determined by the difference between the potential energy of the initial and the final positions of the hammer.

The crystallinity (percentage of brittle fracture) was determined from the force-displacement curve of the test, as shown in Figure A.10. Characteristic forces were as follows: Plastic flow force F_{gy}, maximal force F_m, brittle cracking initiation force F_{iu} and cracking stop force F_a. The crystallinity Cr(%) was then calculated from equation (A.7) (equation C2 from ISO 14556 standard).

$$Cr(\%) = 100 \times \frac{(F_{iu} - F_a)}{2 - F_m - F_{gy}} \tag{A.7}$$

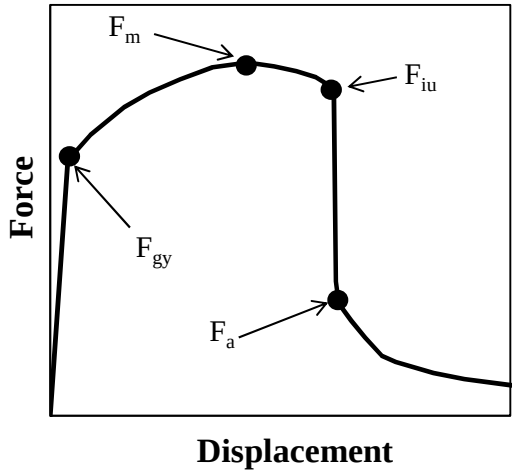

Figure A.10: *Definition of characteristic forces used for the crystallinity calculation. The contribution from elastic waves to the curve has been removed for clarity.*

Appendix B: Thermokinetic calculations

TABLE OF CONTENTS

The Matcalc software, developed by E. Kozeschnik et.al, allows modeling nucleation and growth of precipitates in multicomponent systems. The following information are taken from references [128, 129].

1. NUCLEATION IN MULTICOMPONENT SYSTEMS

The nucleation rate J of a family of precipitates of same shape, interfacial energy with the matrix and chemical composition is given by the multicomponent classical nucleation theory as:

$$J = Z\beta^* N_c \exp\left(\frac{-G^*}{k_B T}\right) \exp\left(-\frac{1}{2Z^2\beta^* t}\right) \tag{B.1}$$

where Z is the Zeldovitch factor, β^* the atomic attachment rate, N_c the number of available nucleation sites, k_B the Boltzmann constant and G^* the nucleation energy barrier. All these factors are described subsequently.

1.1 Nucleation energy barrier

The nucleation energy barrier for a spherical particle is given by:

$$G^* = \frac{16\pi\gamma_k^3}{3(\Delta G_{vol})^2} \tag{B.2}$$

where γ_k is the interfacial energy of particle k and matrix, and ΔG_{vol} the specific free energy change on nucleus formation, given by:

$$\Delta G_{vol} = -\frac{d_{chem}^{P}}{v^{M}} + \Delta G_{vol}^{el} \tag{B.3}$$

where d_{chem}^{P} is the chemical driving force for the precipitate phase and v^{M} the matrix molar volume. ΔG_{vol}^{el} is the elastic energy per unit volume associated with the mean elastic stress field around an ellipsoidal inclusion using an Eshelby approach, due to an isotropic volume change during precipitation, and is expressed as:

$$\Delta G_{vol}^{el} = \frac{E_M}{9(1-\nu_M)} \cdot \left(\frac{v^P - v^M}{v^M}\right)^2 \tag{B.4}$$

where E_M and ν_M are respectively the matrix elastic Young's modulus and Poisson's ratio and v^P is the precipitate molar volume.

The interfacial energy is expressed as:

$$\gamma_k = \frac{n_s . z_{\mathrm{S,eff}}}{N_A . z_{\mathrm{L,eff}}} . \Delta h_{sol} \tag{B.5}$$

where n_s is the number of atoms per unit area of interface, $z_{\mathrm{S,eff}}$ is the effective number of broken bonds across the interface counted per interface atom, N_A Avogadro's number, $z_{\mathrm{L,eff}}$ the effective coordination number and Δh_{sol} the enthalpy of solution. $z_{\mathrm{S,eff}}$ and $z_{\mathrm{L,eff}}$ parameters are determined using the Generalized Broken-Bond approach, which is well described in literature [128].

1.2 Number of available nucleation sites

Nucleation can occur at different types of sites:

For homogeneous nucleation, each atom in the bulk is assumed to be a potential nucleation site. The number of sites per unit volume in the system N_0 is thus evaluated from equation (B.6).

$$N_0 = \frac{N_A}{v^M} \tag{B.6}$$

Around dislocations, nucleation is due to compressive and tensile stress fields close to dislocation cores. In this case, each single atom along the dislocation core represents a potential nucleation site, so that, per unit volume:

$$N_{disl} = \frac{\rho}{a_M} \tag{B.7}$$

where ρ is the dislocation density and a_M the matrix mean interatomic distance.

At grain boundaries and subgrain boundaries, nucleation is possible due to the disturbed nature of the interface. The potential number of nucleation sites at grain boundaries can be estimated based on a geometrical model representing the polycrystalline grain morphology. The geometrical object which presents the most resemblance with an equiaxed grain while perfectly tiling space is the so-called Kelvin tetrakaidecahedron, a solid shape with eight hexagonal faces and six square faces as shown in Figure B.1.

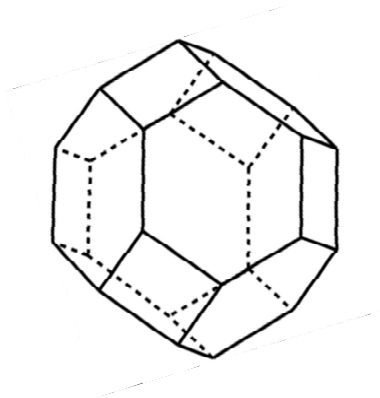

Figure B.1: *Tetrakaidecahedron object*

For a polycrystalline structure composed of n_G equally sized tetrakaidehedra par unit volume, the potential number of nucleation sites at grain boundaries N_{GB}, at triple junctions N_{GT} and at the grain boundaries corners N_{GC} are:

$$N_{GB} = \frac{n_G}{2}\frac{A}{a_M^2} \tag{B.8}$$

$$N_{GT} = \frac{n_G}{3}\frac{L}{a_M} \tag{B.9}$$

$$N_{GC} = \frac{n_G}{4}\,C \tag{B.10}$$

where A is the total grain boundary area, L is the total length of grain boundaries and C is the total number of corners, each for a single grain.

1.3 Zeldovich factor

The Zeldovich factor accounts for the probability for an exact critical cluster whether to grow or to dissolve [130]:

$$Z = \left[-\frac{1}{2\pi k_B T}\left(\frac{\partial^2 \Delta G_{vol}}{\partial n^2}\right)_{n^*}\right]^{1/2} \tag{B.11}$$

where n and n^* are the number of atoms in the embryo and in a critical cluster, respectively.

1.4 Atomic attachment rate

The atomic attachment rate represents the rate at which atoms forming the precipitate attach to the critical cluster. It can be expressed as:

$$\beta^* = \frac{4\pi(r^*)^2}{a^4 v^M}\left[\sum_{i=1}^{n}\frac{(c_{ki}-c_{0i})^2}{c_{0i}D_{0i}}\right]^{-1} \tag{B.12}$$

where c_{ki} is the mean concentration of element i in the precipitate, c_{0i} is the concentration of element i in the matrix and D_{0i} is the diffusion rate of element i in the matrix. r^* is the critical radius, such as:

$$r^* = -\frac{2\gamma_k}{\Delta G_{vol}} \tag{B.13}$$

2. MEAN-FIELD EVOLUTION EQUATIONS FOR PRECIPITATE GROWTH

The MatCalc precipitation model is based on the work of Svoboda et al [129]. This model is based on the Onsager thermodynamic extremal principle (TEP), which postulates that a thermodynamic system evolves towards equilibrium in such a way that it produces maximum entropy or the maximum Gibbs free energy dissipation. Under several assumptions, the total Gibbs energy of the system G can be expressed by means of state parameters q_i, and the rate of the total Gibbs energy dissipation rate Q can be expressed by means of q_i and $\dot{q}_i$:

$$\frac{\partial G}{\partial q_i} = -\frac{1}{2}\frac{\partial Q}{\partial \dot{q}_i} \tag{B.14}$$

2.1 System description

The system consists of a supersaturated solid solution (the matrix), from which precipitate will form. Each phase in the system is assumed to consist of s substitutional and p interstitial elements, with $n = s + p$. Let N_i be a fixed number of moles of component i in the system, m the number of precipitates in the system, r_k the radius of precipitate k, u_{ki} the mean site fraction of element i in the precipitate and u_k a structural factor defining the stoichiometry of the precipitate k in terms of substitutional and interstitial elements. The molar volume of interstitial elements p is considered to be negligible in front of the molar volume of substitutional elements s, and is set to zero.

The mean concentration of element i per unit volume in the precipitate k, c_{ki}, can be introduced as:

$$c_{ki} = \frac{u_{ki}}{v_s} \tag{B.15}$$

where v_s is the partial molar volume of substitutional elements components in precipitates.

The number of moles of component i in the matrix is calculated from the mass-balance as follows:

$$N_{0i} = N_i - \frac{4\pi}{3} \sum_{k=1}^{m} r_k^3 c_{ki} \tag{B.16}$$

The mean concentration c_{0i} of element i in the matrix is given as:

$$c_{0i} = \frac{N_{0i}}{v_s \sum_{j=1}^{s} N_{0j}} \tag{B.17}$$

Thus, in this system, state parameters for application of the TEP are the mean chemical concentration per unit volume c_{ki} and the radius r_k of precipitates. The parameters for the matrix are fixed by mass balance.

2.2 Total Gibbs energy and its dissipation rate in the system

The total Gibbs energy in the system is expressed as:

$$G_{tot} = \sum_{i=1}^{n} N_{0i}\, \mu_{0i} + \sum_{k=1}^{m} \frac{4\pi r_k^3}{3} \left(\lambda_k + \sum_{i=1}^{n} c_{ki}\, \mu_{ki} \right) + \sum_{k=1}^{m} 4\pi r_k^2\, \gamma_k \tag{B.18}$$

where μ_{0i} and μ_{ki} are chemical potentials of element i respectively in the matrix and in the precipitate, λ_k is the strain energy. In this equation, the first term describes the Gibbs energy of the matrix by summing up the contributions from alloying elements i in the matrix. The second term is the Gibbs energy of the precipitates, where the specific mechanical energy λ_k due to volumetric misfit is taken into account. The third term describes the energy due to the formation of the precipitate-matrix interfaces.

During the system evolution, the excess Gibbs energy can be dissipated by three processes:

Migration of interfaces, due to the growth or shrinkage of a precipitate. This process can be written as:

$$Q_1 = \sum_{k=1}^{m} \frac{4\pi r_k^2}{M_k} \left(\frac{dr_k}{dt} \right)^2 \tag{B.19}$$

where M_k is the mobility of the interface. Here, $1/M_k$ can be interpreted as a friction coefficient. Its product with the square interface velocity is the specific energy that is dissipated by the motion of the precipitate-matrix surface.

Diffusion inside the precipitate, due to the evolution of the chemical composition of the precipitate during the precipitation reaction. Considering atoms entering or leaving the precipitate in the course of growth and shrinkage are deposited or removed uniformly over the precipitate volume, and thus involve diffusion of atoms inside the precipitates, the diffusive flux j_{ki} of element *i* inside the precipitate *k* is expressed as follows:

$$j_{ki} = -\frac{r}{3}\frac{dc_{ki}}{dt} \tag{B.20}$$

with $0 \leq r \leq r_k$. The total energy dissipation rate is expressed such as:

$$Q_2 = \sum_{k=1}^{m}\sum_{i=1}^{n}\int_0^{r_k}\frac{4\pi r^2 RT}{c_{ki}D_{ki}}\, {j_{ki}}^2\, dr \tag{B.21}$$

where D_{ki} is the diffusion rate of alloying element *i* in precipitate *k*. Like the inverse of the mobility mentioned before, $1/D_{ki}$ plays the role of a friction coefficient. Once equation (B.21) is solved, the Gibbs energy dissipation rate is given by:

$$Q_2 = \sum_{k=1}^{m}\sum_{i=1}^{n}\frac{4\pi r_k^5 RT}{45c_{ki}D_{ki}}\left(\frac{dc_{ki}}{dt}\right)^2 \tag{B.22}$$

Diffusion inside the matrix, due to the long-range transport of atoms towards or away from the precipitate caused by the evolution of the precipitate size. Let us assume that the fluxes of atoms in the matrix are once again uniformly deposited or removed within a sphere of radius *Y*, in analogy to the diffusive transport inside the precipitate. The diffusive flux J_{ki} in the matrix is given by:

$$J_{ki} = \left(\frac{dr_k}{dt}(c_{0i} - c_{ki}) - \frac{r_k}{3}\frac{dc_{ki}}{dt}\right)\left(\frac{r_k^2}{r^2}\,\frac{Y^3 - r^3}{Y^3 - r_k^3}\right) \tag{B.23}$$

with $r_k \leq r \leq Y$. The first term in equation (B.23) represents the transinterfacial diffusional flux whereas the second one is the geometrical parameter assuring mass conservation of the spherical system matrix-precipitate. The Gibbs energy dissipation rate is given by:

$$Q_3 = \sum_{k=1}^{m}\sum_{i=1}^{n}\int_{r_k}^{Y}\frac{4\pi r^2 RT}{c_{0i}D_{0i}}{J_{ki}}^2\, dr \tag{B.24}$$

Assuming that $Y \gg r_k$ i.e. the distance between individual precipitates is sufficiently large, then:

$$Q_3 = \sum_{k=1}^{m} \sum_{i=1}^{n} \frac{4\pi r_k^3 RT}{c_{0i} D_{0i}} \left(\frac{dr_k}{dt}(c_{ki} - c_{0i}) + \frac{r_k}{3} \frac{dc_{ki}}{dt} \right)^2 \tag{B.25}$$

The total Gibbs energy dissipation rate is therefore given as the sum of contributions from equations (B.19), (B.22) and (B.25):

$$Q = Q_1 + Q_2 + Q_3 \tag{B.26}$$

By applying equation (B.14) to the system, the following set of equations is obtained:

$$\frac{\partial G}{\partial r_k} = -\frac{1}{2} \frac{\partial Q}{\partial \dot{r_k}} \ (k = 1, \dots, m) \tag{B.27}$$

$$\frac{\partial G}{\partial c_{ki}} = -\frac{1}{2} \frac{\partial Q}{\partial \dot{c_{ki}}} \ (k = 1, \dots, m; i = 1, \dots n) \tag{B.28}$$

2.3 Evolutionnary equations

Resolving equations (B.27) and (B.28) leads to a linear system of equations for the time derivatives of state variables $\dot{r_k}$ and $\dot{c_{ki}}$:

$$\sum_{j=1}^{n-1} A_{ij} \dot{q}_j = B_i \tag{B.29}$$

where A_{ij} and B_i parameters are expressed in literature [128, 129]. In other words, this set of equation describes the evolution of radius and chemical composition of each precipitate k for each step of time. Time-integration of the evolution equations is performed using the Numerical Kampmann-Wagner approach, where the precipitate distribution is treated in terms of discrete size classes for precipitates *k* of identical radius and chemical compositions.

Appendix C: Chemical composition of carbides after heat treatments involving different austenitization conditions

The chemical composition of carbides as determined by EDX measurements after the three austenitization temperature-duration couples presented in Chapter IV, followed by cooling at 0.3°C/s, tempering at 675°C for 5.5 hours and stress-relieving heat treatment at 625°C for 16 hours are presented in Figure C.1.

After these heat treatments, M_7C_3, $M_{23}C_6$ and M_2C carbides are found in the material. No cementite is expected, since it was shown in Chapter V that further stress-relieving heat treatment results in its full dissolution. The differences between the three austenitization conditions have no significant effect on the chemical composition of carbides after the final heat treatments.

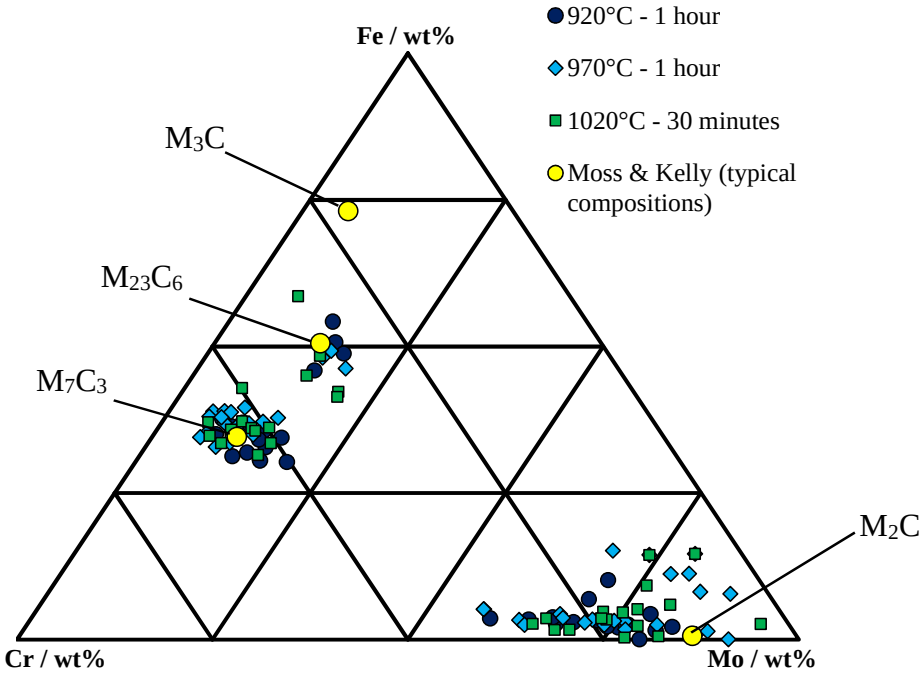

***Figure C.1**: Carbide chemical composition in metallic elements after three different austenitization conditions, followed by cooling at 0.3°C/s, tempering at 675°C for 5.5 hours and stress-relieving heat treatment at 625°C for 16 hours.*

Appendix D: Thermokinetic modelling of the carbide precipitation sequence

TABLE OF CONTENTS

In order to test the assumptions made on the nucleation of M_7C_3 carbides and the growth of $M_{23}C_6$ carbides, thermokinetic calculations were performed in order to reproduce the experimental observations.

1. GENERAL FRAMEWORK

The general framework of the MatCalc precipitation model has already been reported in Appendix B.

2. MODEL ASSUMPTIONS

The chemical composition of the system was set up regarding the quarter-thickness composition presented in Chapter 2. The system was represented as follows.

2.1 Matrix

Bainite can be represented in this framework as elongated ferritic subgrains (laths) which share similar crystallographic orientations within the grain (packet), where a carbon partitioning occurs between the (perfect) crystal lattice and the dislocations. First simulations were conducted with such a representation of the matrix. However, the results proved to be highly sensitive to the lath size, the which value has not been determined precisely. Thus, the matrix was simulated at a larger scale,

where so-called grains are prior austenite grains and so-called subgrains are the bainitic packets. The assumption lying behind this representation of bainite is that the total dislocation density in the material is partly due to the low-angle lath boundaries in a given packet. Thus, no difference is made between carbide precipitation at intralath dislocations and at lath boundaries. Moreover, the presence of retained austenite at interfaces cannot be directly taken into account. Instead, calculations were carried out with carbon trapped at subgrain boundaries, i.e. at bainitic packet boundaries. For comparison purposes, calculations were also performed with carbon trapped at dislocations. In such case, the relative evolution of carbide phase fraction was the same, but the kinetics was not satisfactorily represented.

The dislocation density in the matrix, ρ, was determined according to the empirical equation (D.1) given by Zajac et al [131], where B_s is the bainite start transformation temperature in the case of isothermal transformation, in Kelvin. As a first assumption, this temperature will be taken as the one in the case of continuous cooling. As seen in Chapter IV, for the considered cooling rate of 0.3°C/s, B_s = 520°C, $\rho \sim 1\text{x}10^{15}$ m^{-2}. This order of magnitude seems reasonable when considering a bainitic microstructure.

$$\log_{10}(\rho) = 9.28480 + \frac{6880.73}{B_s} - \frac{1780360}{{B_s}^2} \qquad (D.1)$$

2.2 Carbides

Carbides to be considered in calculations were selected according to reported experimental observations, i.e. M_3C, M_7C_3, $M_{23}C_6$ and M_2C. The nucleation stages were represented in the model by considering literature data and discussions from Chapter V: cementite transforms from ε-carbides, M_7C_3 nucleates at the interface between cementite and the matrix, and $M_{23}C_6$ and M_2C nucleate on their own. From experimental results, cementite was assumed to nucleate from the retained austenite around 500-600°C. However, such transformation cannot be taken into account in these calculations. Thus, in order to simulate nucleation of cementite at these temperatures, ε-carbides were artificially added to the system, and set up to transform into cementite upon heating at the experimentally observed temperature.

The chemical composition of the nucleus is a key parameter for modelling precipitation of carbides. Cementite and M_7C_3 carbides are not concerned by this parameter since they result from the transformation of pre-existing carbide; no control on their nucleus composition can be made. M_2C and $M_{23}C_6$ nuclei composition were calculated under an ortho-equilibrium assumption. The model calculates the chemical composition by assuming that the precipitates nucleate with their equilibrium composition. For $M_{23}C_6$ carbides, such assumption is in good agreement with experimental measurements. For M_2C carbides, this assumption is more representative of the experimental results than a para-equilibrium composition, which assumes that the nucleus composition is the same as the one of the matrix, except for carbon.

Nucleation sites were chosen according to the results from experimental observations: M_2C carbides were assumed to precipitate homogeneously within the laths, $M_{23}C_6$ carbides were assumed

to precipitate at dislocations since these latter partly correspond to actual lath boundaries, and cementite and M_7C_3 carbides (and therefore ε-carbides in these calculations) were assumed to precipitate both at dislocations and at subgrain boundaries (SGB).

A shape factor was applied to M_3C, M_2C and $M_{23}C_6$ precipitates due to their particular geometry, respectively branch-like, needle-like and rod-like. The shape factor for branch-like and rod-like was set to 5; the one for needle-like was set to 10.

2.3 Nucleation and growth parameters

It should be pointed out the abovementioned hypotheses alone, coupled with the default parameters in MatCalc, result in calculated phase fraction and size within the right order of magnitude. However, the precipitation/dissolution of carbides is not well described. For instance, $M_{23}C_6$ carbides grow very slowly at 650°C, while no more M_7C_3 are present after only 1 hour at 725°C. Moreover, the balance between nucleation and growth for $M_{23}C_6$ do not describe accurately the experimental results. Thus, several parameters were adjusted in order to change the temperature at which carbides start to precipitate and their nucleation rate. The chosen values for these parameters are only guessed ones, since no information is available from literature, to the author's knowledge. However, these slight changes result in better agreement with experimental data.

- The critical radius of carbides is the minimum size of a carbide embryo that is stable and begins to grow (i.e., minimum nucleus size). Decreasing the value of this parameter results in a higher nucleation rate, and nucleation occurs at lower temperature. This parameter was set to 0.5 nm for all carbides with the exception of M_7C_3 for which it was set at 0.55 nm in order to increase the transformation temperature for the $M_3C \rightarrow M_7C_3$ reaction. Note that these values may even be lower than the size of the crystal unit cell (that contains a lot of atoms, though, for some carbides).
- Nucleation rates can be decreased by decreasing the nucleation constant, resulting in a lower number fraction of carbides. The default value of this parameter is 1; its value was decreased down to 0.5 for M_7C_3 carbides in order to reduce the rate of transformation from cementite, and down to 0.4 for $M_{23}C_6$ carbides in order to avoid a too massive precipitation upon heating.

Summary of all nucleation conditions and values of model parameters for all types of carbides is made in Table D.1.

	M_3C	**M_7C_3**	**M_2C**	**$M_{23}C_6$**
Nucleation sites	Same as ε-carbides	M_3C surface	Matrix	Dislocations
Nucleus composition	Direct transformation from ε-carbides	M_3C	Ortho-equilibrium	Ortho-equilibrium
Critical radius (nm)	0.5	0.55	0.5	0.4
Nucleation constant	1 (default)	0.5	1 (default)	0.3
Shape factor	5 (rod)	1 (sphere)	10 (needle)	5 (rod)

Table D.1: *Summary of nucleation mechanisms and carbide model parameters*

Heat treatments numerically applied in the simulations were chosen in accordance with the experimental ones, namely, a heating step at 0.333°C/s (2°C/min), then an isothermal holding for times up to 30 hours, followed by a quench at 100°C/s in order to simulate the water quench. No evolution of carbides occurs during this quench, thus they will not be discussed. Temperatures for the isothermal step range from 650°C to 725°C.

3. COMPARISON WITH EXPERIMENTAL RESULTS AND DISCUSSIONS

3.1 Evolution of carbide phase fractions

The evolution of carbide phase fraction with temperature during heating up to 725°C is shown in Figure D.1. Since ε-carbides are only taken into account in order to simulate the precipitation of cementite at 520°C, they are not represented in this figure. From results given by the model, 80% of cementite is located at dislocations, which is in good agreement with experimental results, since in this model dislocations also account for lath boundaries.

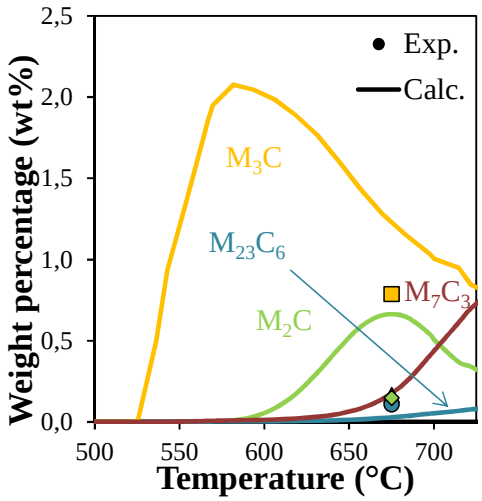

Figure D.1: *Evolution of carbide phase fraction upon heating*

Slight differences are found between experimental measurements and calculations, especially regarding the precipitation of M_2C carbides which is too strong, however at higher temperature their phase fraction decrease down to 0.3 wt% due to the precipitation of M_7C_3 carbides. Despite these slight differences, rather good agreement is found.

The evolution of phase fraction with time during the isothermal step at 650°C, 675°C, 700°C and 725°C is shown in Figure D.2. General good agreement is found with the experimental results. However, in the calculations M_7C_3 precipitate too rapidly, leading to a too fast dissolution of cementite and a too high phase fraction of M_7C_3. At temperatures 700°C and 725°C, growth of $M_{23}C_6$ is slowed down due to the too stable M_7C_3 carbides. Moreover, at these temperatures, M_2C carbides are dissolving rapidly due to the too low dissolution temperature predicted for M_2C carbides as already stated in section 2.1.1 of Chapter V, while experimentally this dissolution happens for

longer times. Such change in the thermodynamic equilibrium conditions might explain the differences between model predictions and experimental measurements. Slight differences at other temperatures are also observed: M_7C_3 carbides appear to be too stable, while M_2C carbides precipitate too massively at low times, as already stated. However, the general trend is respected.

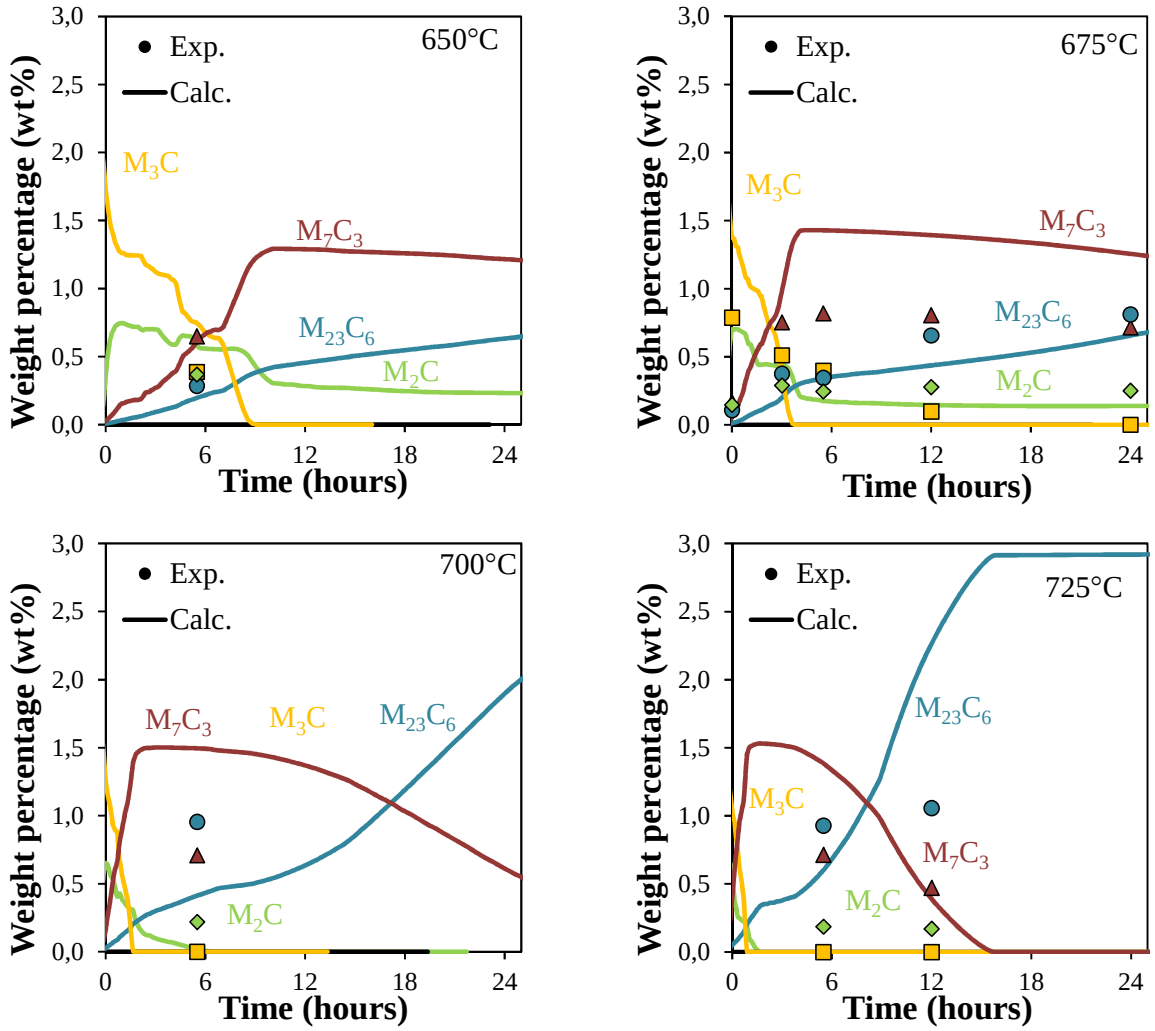

Figure D.2: *Evolution of carbide phase fraction upon isothermal holding at different temperatures.*

3.2 Size evolution of carbide

The evolution of the characteristic dimensions of carbides with holding time at several temperatures is shown in Figure D.3. The characteristic dimension is the mean diameter for M_7C_3 carbides and the mean length for elongated M_2C, $M_{23}C_6$ and M_3C carbides. Experimental measurements were made from TEM observations, for an average number of 15 measurements per carbide per tempering condition. These dimensions are likely to obey a log-normal distribution, explaining the high standard-deviations for $M_{23}C_6$. It should be pointed out that the calculated number density of carbides remains stable between their nucleation upon heating and their final

dissolution. Thus, growth is the only phenomenon that occurs during isothermal holding and that accounts for the change in phase fraction.

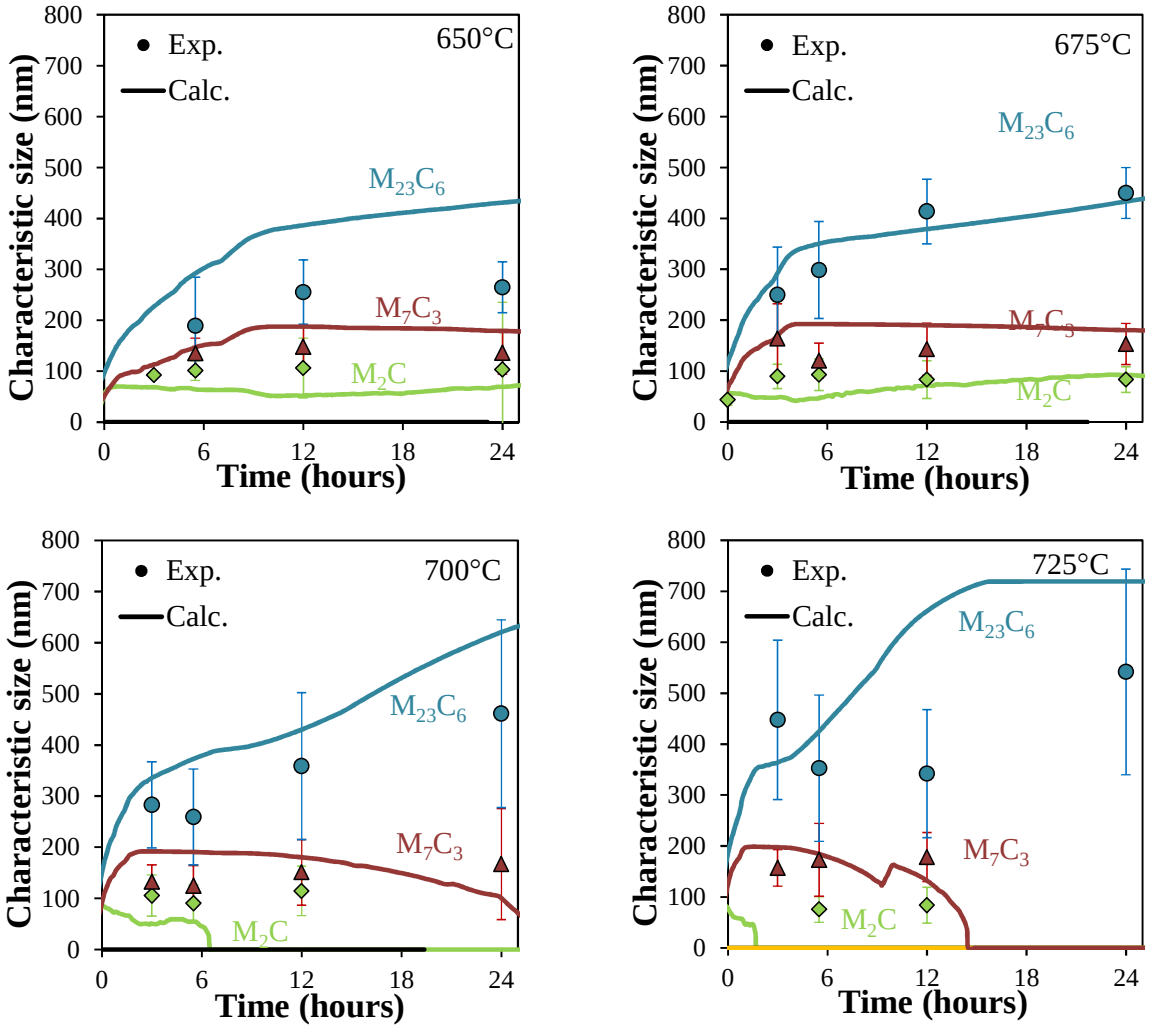

Figure D.3: *Evolution of carbide characteristic dimension during the isothermal holding step.*

Very good agreement is found for M_7C_3 and M_2C carbides. The general trend for $M_{23}C_6$ carbides is fairly well represented; however one should notice that their growth appears to be too rapid. This is due to a bad balance between nucleation and growth of these carbides using the chosen parameters: in the calculations, less carbides are precipitating but they are growing faster when compared to experimental observations.

3.3 Amount of elements in solid solution

A comparison between the normalized amounts of both chromium and molybdenum in solid solution and in the carbides at 675°C is shown in Figure D.4.Good agreement is found, except for the molybdenum content after 3 hours, once again due to the too extensive precipitation of M_2C carbides predicted during the first hours of tempering by the model. Calculations for the normalized amount of chromium at 675°C for times up to 80 hours (Figure D.5) shows that the increase in chromium

content in $M_{23}C_6$ due to its growth is approximately balanced by the chromium release by M_7C_3 particles during their dissolution, with a minor contribution from the matrix. This is in good agreement with the discussions made in Chapter V.

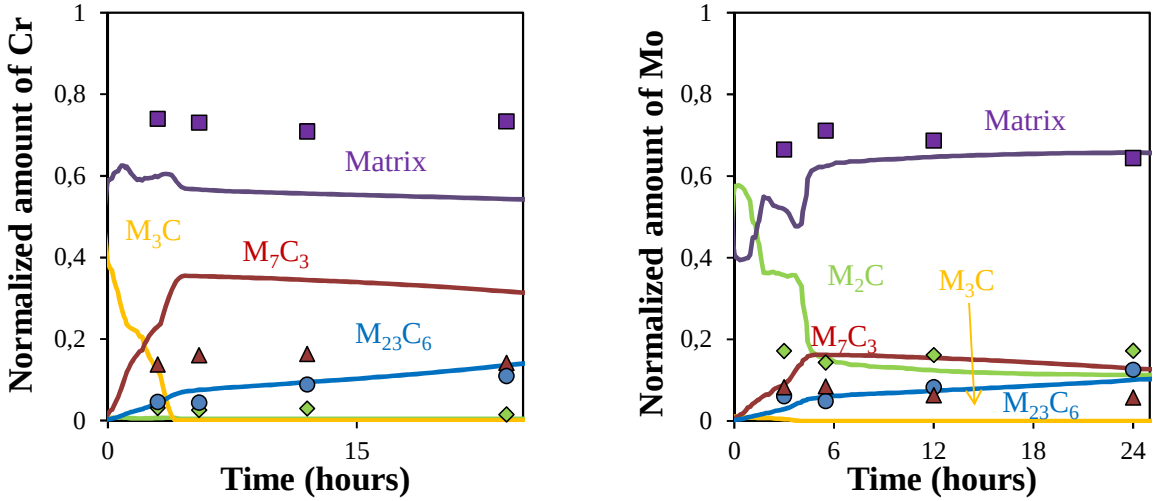

Figure D.4: *Evolution with time of the normalized amount of carbide forming elements in matrix solid solution and in the carbides at 675°C for: (a) chromium; (b) molybdenum*

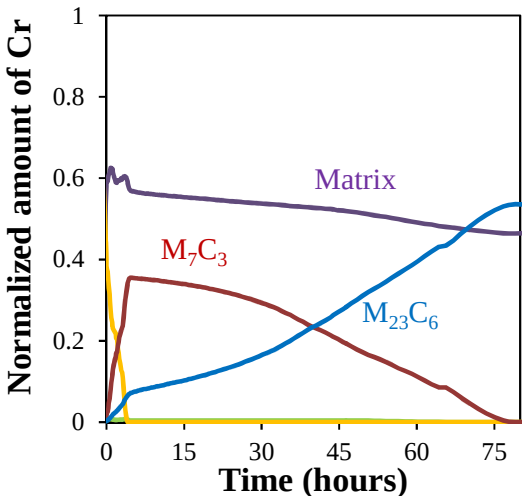

Figure D.5: *Evolution with time of the normalized amount of chromium in matrix solid solution and in the carbides at 675°C as calculated for holding for up to 80 hours.*

3.4 Limitation of the model: evolution of the chemical composition of carbides

The more significant difference between model predictions and the assumptions derived from experimental results is the relative amounts of metallic elements in cementite and M_7C_3 carbides. Cementite as calculated is chromium-richer than experimentally measured, around 40 wt.% vs. 15-25 wt.%, and M_7C_3 carbides nucleate in a chromium-rich composition with a further enrichment in iron, while experimentally it was shown that they nucleate with an iron-rich composition, then

undergo chromium enrichment. It should be pointed out that no differences in carbide composition for times longer than 3 hours are found between measurements and calculations.

Regarding cementite, this is due to their nucleation mechanism in the model, which is the direct transformation from ε-carbides. Experimentally, they result from decomposition of retained austenite, thus their composition is somehow inherited from this phase. Regarding M_7C_3, these contradictory observations can be explained by two ways:

- Calculation models for the nucleus composition do not reflect the reality.
- $M_{23}C_6$ and M_7C_3 are actually chromium-rich, but the presence of cementite in their vicinity induces an error on the measurement by TEM observations.

While the second explanation appears very likely when considering small M_7C_3 carbides located in cementite clusters, the experimentally observed enrichment in chromium of M_7C_3 carbides during the isothermal holding is clearly established experimentally and contradictory to model predictions. It is then more likely that the calculations of the nucleus composition do not represent the reality.

3.5 Effect of stress-relieving heat treatment

Calculations were performed to further assess a subsequent stress-relieving heat treatment (PWHT) at 645°C for 16 hours after a tempering at 675°C for 5.5 hours, the cooling rate applied after tempering was 1°C/s and the heating rate for the PWHT was set to 0.014°C/s (50°C/h). No changes happened upon this additional heat treatment: the phase fraction and size of carbides remain the same. However, predictions cannot be fully compared to experimental observations, since no cementite is predicted after 5.5 hours of tempering at 675°C, while the PWHT only affects cementite as experimentally stated. Nevertheless, the stability of other carbides is in good agreement with experimental results.

4. CONCLUSION

Experimental observations are rather successfully reproduced using the nucleation conditions based on the experimental discussion, i.e. nucleation of M_7C_3 carbides at the surface of cementite and separate nucleation of $M_{23}C_6$ and M_2C carbides from inside the matrix. The growth of $M_{23}C_6$ and the dissolution of M_7C_3 carbides are interrelated due to chromium diffusion. Further stress-relieving heat treatment does not influence the carbide chemistry or distribution.

Evolution microstructurale d'un acier 2.25 Cr – 1 Mo au cours de l'austénitisation et du revenu : croissance des grains austénitiques, séquence de précipitation des carbures et effets sur les propriétés mécaniques.

RESUME : Ce travail traite de l'optimisation des propriétés en traction et en résilience d'un acier 2.25 Cr – 1 Mo par le contrôle de sa microstructure via des traitements thermiques appropriés. Ainsi, les transformations de phases ayant lieu au cours de l'austénitisation, de la trempe et du revenu doivent être correctement appréhendées. Des observations en microscopies électroniques à balayage et en transmission, ainsi que des analyses par diffraction des rayons X, ont été effectuées afin de caractériser et de modéliser la microstructure de l'acier à chaque étape du traitement thermique. L'évolution de la phase austénitique lors de l'étape d'austénitisation, ainsi que son influence sur la microstructure après trempe, ont été étudiées. La croissance du grain austénitique a été modélisée afin de comprendre ses mécanismes sous-jacents, en particulier le phénomène de croissance limitée observé aux plus basses températures. L'effet des conditions d'austénitisation sur la décomposition de l'austénite ainsi que sur les propriétés mécaniques du matériau après trempe et revenu a été étudié expérimentalement. Une condition d'austénitisation optimale a été déterminée et utilisée pour étudier la précipitation au revenu. La précipitation des carbures a été étudiée pour différents temps et températures de revenu. La séquence de précipitation suivante a ainsi été mise en évidence : la cémentite M_3C précipite en premier, suivie des carbures M_2C et M_7C_3 ; les carbures à l'équilibre étant les $M_{23}C_6$. Enfin, l'influence de la précipitation des carbures sur les propriétés mécaniques de l'acier a été étudiée. Les propriétés en traction sont particulièrement sensibles aux conditions de revenu dans le domaine d'étude, alors que les propriétés en résilience restent stables.

Mots clés : Aciers bainitiques, carbures, austénitisation, croissance de grain, revenu, propriétés en traction, résilience

Microstructural evolution of a 2.25 Cr - 1 Mo steel during austenitization and temper: austenite grain growth, carbide precipitation sequence and effects on mechanical properties

ABSTRACT : This work aims at optimizing tensile and toughness properties of a 2.25Cr – 1Mo steel by controlling its microstructure through heat treatments. To this aim, phase transformations during austenitization, quenching and tempering have to be understood. Quantitative microstructural analyses were performed by means of SEM, TEM and XRD to characterize and model metallurgical evolution of the steel at each step of the heat treatment. The evolution of austenite during the austenitization stage, and its influence on the resulting as-quenched microstructure were thoroughly investigated. Austenite grain growth was modelled in order to understand its mechanisms, including the limited growth phenomenon observed at lower temperatures. The effect of austenitization conditions on further decomposition of austenite and on mechanical properties after quenching + tempering was experimentally determined. An optimal austenitization condition was selected and applied to study the tempering stage. Carbide precipitation was studied for various tempering temperatures and amounts of time. M_3C carbides precipitate first, followed by M_2C and M_7C_3; $M_{23}C_6$ are the equilibrium carbides. The influence of carbide precipitation on mechanical properties was studied. Tensile properties are closely linked to the tempering conditions in the range investigated, while impact toughness remains stable.

Keywords : Bainitic steels, carbides, austenitization, grain growth, temper, tensile properties, impact toughness

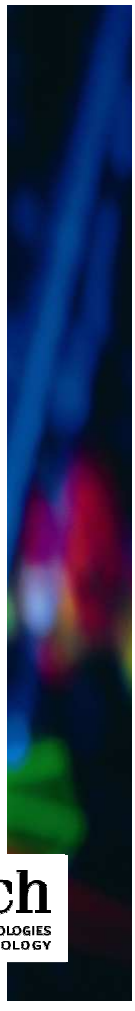

MINES ParisTech

ParisTech
INSTITUT DES SCIENCES ET TECHNOLOGIES
PARIS INSTITUTE OF TECHNOLOGY